MICRO-STRUCTURE BASED MULTI-SCALE THERMO-MECHANICAL CHARACTERIZATION OF PORTLAND CEMENTS

A Dissertation work
Submitted in Partial Fulfilment of the requirements

For the Award of the Degree of

DOCTOR OF PHILOSOPHY

in

CIVIL ENGINEERING

By

Harsha Praneeth Pavani
(Roll No. 714111)

Under the guidance of

RESEARCH SUPERVISOR

Dr. T. P. Tezeswi
Assistant Professor

DEPARTMENT OF CIVIL ENGINEERING

NATIONAL INSTITUTE OF TECHNOLOGY

WARANGAL - 506 004, (T.S.), INDIA

March – 2020

MICRO-STRUCTURE BASED MULTI-SCALE THERMO-MECHANICAL CHARACTERIZATION OF PORTLAND CEMENTS

A Dissertation work
Submitted in Partial Fulfilment of the requirements

For the Award of the Degree of

DOCTOR OF PHILOSOPHY

in

CIVIL ENGINEERING

By

Harsha Praneeth Pavani
(Roll No. 714111)

Under the guidance of

RESEARCH SUPERVISOR

Dr. T. P. Tezeswi
Assistant Professor

DEPARTMENT OF CIVIL ENGINEERING

NATIONAL INSTITUTE OF TECHNOLOGY

WARANGAL - 506 004, (T.S.), INDIA

March-2020

NATIONAL INSTITUTE OF TECHNOLOGY
WARANGAL

CERTIFICATE

This is to certify that the thesis entitled "**Micro-structure based multi-scale thermo-mechanical characterization of Portland cements**" being submitted by **Mr. Harsha Praneeth Pavani (Roll No: 714111),** for the award of the degree of **DOCTOR OF PHILOSOPHY** to the Faculty of Engineering and Technology of **NATIONAL INSTITUTE OF TECHNOLOGY, WARANGAL** is a record of bonafide research work carried out by him under my supervision and it has not been submitted elsewhere for award of any degree.

Dr. T. P. Tezeswi
Thesis Supervisor
Assistant Professor
Department of Civil Engineering
National Institute of Technology
Warangal (T.S.) - INDIA.

Dedicated to

My

Beloved Parents

Mr . Sanjeeva Rao . P & Mrs . Latha Mangesh

&

Sister

Mrs . Manogna . P

ACKNOWLEDGEMENTS

A great man once said “Don’t confuse momentum with progress” and hope everyone has this confusion. In this journey of Ph.D. of four years I had plenty of these moments of momentum and few traces of progress, and this hold good to the rest of my life. Failures are very hard on your mind, they make you sad, and however in this journey I understood they cause disappointment. All these things which make the journey much harder than it intended to be, and all this effort is worth remembering. I understood it is very hard to find a light house in the midst of these failures, and I take a great pride in acknowledging those people who bestowed faith and trust in me, more than my belief of what I have on myself.

I would like to thank research supervisor Dr. T. P. Tezeswi, Assistant professor, Department of Civil Engineering, National Institute of Technology, Warangal, who has given an opportunity and freedom to embark on this memorable journey of Ph.D. for which I am deeply indebted to, and without his moral support and valuable insights I could not have come this far.

I would sincerely like to thank Dr. M. Raja Vishwanathan, Department of Humanities & Social Sciences, National Institute of Technology, Warangal and DSC member Prof. P. Rathish Kumar, Department of Civil engineering, National Institute of Technology, Warangal who bestowed faith in me and directed me in the right direction when I seriously doubted the capabilities of my judgment of my research work. I remember every single interaction and moral support he induced in me to arrive at this juncture.

I take this great opportunity to express my profound gratitude to Prof. M. Chandrasekhar, Professor and Head, Department of Civil Engineering, Chairman of Department Scrutiny Committee, and also to the members of DSC committee Prof. Rajesh Kumar, Department of Civil Engineering, Dr. Satish Ben, Department of Mechanical Engineering, for their valuable suggestions and constructive criticism at various stages of the investigation.

My sincere thanks are due to the senior Professors and faculty of Structures division Prof. C. B. Kameswara Rao, Prof. G. Rajesh Kumar, Prof. T. D. Gunneswara Rao and all the faculty of Civil Engineering Department for the encouragement throughout the work.

I would like to thank my friends Mr. Aditya Kamineni, Mr. Jaya Krishna, Dr. Uday Kala, Mr. Suminder Meerwal, Mr. E. R. Ramudu, Mr. Dinesh naidu, Mr. Vijay, Mr. Ravikanth Reddy, Mr. Kiran Kumar, Mrs. Umi Tahira Kathoon, Ms. Thanushri Soni, Mr. Murali Krishna, Mr. P. Yugendar, Mr. Praveen Kumar, Mr. V. Guru Prathap Reddy for their moral support.

A very special debt of deep gratitude to my uncle to whom I look as my ideal and a deep knowledge about life and values Mr. K. Prasadh and aunt Mrs. K. Prasana, who transformed my vison about life with their modesty and simplicity.

The author gratefully acknowledges the help given by all the persons who have directly or indirectly supported the work.

- Mr. Harsha Praneeth Pavani

ABSTRACT

In this study thermal behaviour are investigated for the three grades of Cement PPC, OPC-43 and OPC-53 that are procured from the retailers in the market are investigated. Three cubes of 50x50x50 mm^3 are cast with *w/c* of 0.33 for each grade of cement for their respective temperatures. The chemical oxide concentrations and particle size distribution are determined, using X-ray fluorescence (XRF) and Particle size analysis (PSA). The development of various phases with the increase in hydration and temperatures are monitored using X-ray diffraction (XRD), Fourier Transformation Infrared (FTIR) and Fourier Transformation Raman spectroscopy (FTRS). The deterioration of various phases with the increase in temperatures, are monitored using Thermal analysis (TA). From TA, four critical regions *i.e.* 100 °C, 400 °C, 500 °C and 800 °C apart from ambient temperature are analysed. The elemental concentrations of Carbon, Hydrogen, Nitrogen, Oxygen, and Sulfor are determined using CHNS-O elemental analysis at 100 °C and 800 °C.

The chemical and physical tests conducted on the PPC, OPC-43 and OPC-53 samples 50 x 50 x 50 mm^3 indicate that PPC samples exhibit a superior compressive strength under thermal loads. TA studies indicate that heat flow taking place in PPC samples is lower when compared to OPC-43 and OPC-53. The samples made of PPC were able to withstand external loads at 800 °C, while OPC-43 and OPC-53 failed to do so at 500 °C. As PPC having higher concentrations of Fly Ash (FA), while OPC-43 and OPC-53 have less concentrations of FA. To understand the superior behaviour in compressive strength of PPC samples under thermal loads, with respect to OPC. The evolution of meso and micro structure pores was captured using Computer Tomogrpahy (CT), at the critical temperatures obtained from TA .

CT studies indicate larger diameter of pores, greater than 10 mm exists in all the samples. The generation and evolution of new pores in hydrated samples at elevated temperatures is a continuous process. Higher pore distribution and interconnectivity of these pores at elevated temperatures is the primary reason for the disintegration of OPC-43 and OPC-53 samples was captured. With the increasing temperatures, number of inaccessible pores in the samples has also increased at macro and micro-scale. Hence, CT is a better alternative for estimation of porosity in the samples of larger sizes over traditional methods. The usage of PPC cements is recommended over OPC-43 and OPC-53 for superior thermal behaviour.

CONTENTS

Chapter-4

List of Figures

List of Tables

Abbreviations & Acronyms

AEA	Air entrained admixture
AFt	Alumina ferric oxide tri-sulfate
AFm	Alumina ferric oxide mono-sulfate
CH	Calcium hydroxide
CT	Computer tomography
C_3A	Tri-calcium aluminate
C_3S	Tri-calcium silicate
C_2S	Di-calcium silicate
C_4AF	Tetra-calcium aluminium ferrate
CAH	Carbo Aluminate hydrate
CSH	Calcium silicate hydrate
CHNSO	Carbon, hydrogen, nitrogen, sulfur, and oxygen
DSC	Differential scanning calorimetry
DTA	Differential thermal analysis
DTD	Differential dilatometry
ESEM	Environmental scanning electron microscopy
FA	Fly ash
FTIR	Fourier transform infrared spectroscopy
FTRS	Fourier transform Raman spectroscopy
GoC	Grade of cement
GGBFS	Ground granulated blast furnace slag
HRCT	High resolution computer tomography
LSCM	Laser scanning confocal microscope
MIP	Mercury intrusion microscopy
NND	Nearest neighbour distance
OPC	Ordinary Portland cement
PC	Portland cement
PSA	Particle size analysis
PPC	Pozzolana Portland cement
PSD	Particle size distribution

ROI	Region of interest
SF	Silica fume
SEM	Scanning electron microscopy
TA	Thermal analysis
TEM	Transmission electronic microscopy
TGA	Thermogravimetric analysis
UPV	Ultrasonic pulse velocity
w/c	Water cement ratio
XRD	X-ray diffraction
XRF	X-ray fluorescence

Chapter-1

Introduction

Chapter-1
Introduction

1.1. Background/Motivation

As per ASTM C 150 Portland Cement is defined as *"hydraulic cement (cement that not only hardens by reacting with water but also forms a water-resistant product) produced by pulverizing clinkers which consists essentially of hydraulic calcium silicates, usually containing one or more of the forms of calcium sulfates as an inter ground addition."*

It is not an exaggeration to say that along with food and clothing the next material that is mostly used by mankind is concrete and the consumption of Portland Cements (PC) exceeded 3 billion tons (van Oss H. G. *et al.* 2002). India is the second-largest consumer of Portland cement (PC) in the world after China; the production of fly ash from thermal power plants is expected to reach 140 metric tons by 2020 (Senapati M.R, 2011). As a result, recent research has focused on discovering better means of utilizing fly ash. Accordingly, the substitution of 15-35% fly ash in PC was found to be a suitable alternative. Prior to the use of fly ash as a constituent substitution, three grades of cement (GoC), i.e., Ordinary Portland Cement-33 (OPC-33), OPC-43, and OPC-53, were most commonly used throughout India. However, several studies conducted on PC, with a partial replacement of fly ash, concrete members have indicated a improvement in durability, gradual increase in compressive strength, and lower heat of hydration *etc*. These properties are very crucial in increasing the life span of the structures, hence the production of Portland Pozzolana Cement (PPC) has gained some significance, and due to its advantages over OPC-33. The OPC-33 was replaced with Portland pozzolana cement (PPC). The fire accidents taken place in tunnels: Channel (1996), Tauren &

Mont-blanc (1999), Saint gothard (2001), Kaprun (2000), and WTC in USA (Masse S. *et al.* 2002). Research indicates that the temperature and duration of fire to which concrete is subjected, leads to changes in the texture, morphology of concrete in addition to spalling, cracking, and reduction in the mechanical properties and elastic wave velocity (Georgali *et al.*2005; Kim *et al.*2013).

Concrete is one of the most crucial and complex materials in civil engineering applications. The constituent materials in concrete are relatively cheap and easy to obtain, and all these materials should blend together for a superior performance. In concrete, coarse aggregate gives volume to concrete and fine aggregate fills the voids present in between these coarse aggregates. The most crucial ingredient in concrete is the PC, which binds aggregate in the concrete by inclusion of water. Once water is added to unhydrated PC, the hardening takes place in the concrete. PC is initially a mixture of major chemical oxides such as Calcium oxide (CaO), Silicon di-oxide (SiO_2), Aluminium oxide (Al_2O_3), Iron oxide (Fe_2O_3) and some other minor oxides such as Magnesium oxide (MgO), Potassium oxide (K_2O), etc. Alite (Tricalcium silicate) is the major composition (40-70% of mass) of a clinker, it has hexagonal crystal, which reacts very quickly with water and helps in gaining the early strength in 28 days. The major phases present in PC with their mass percentages and crystal structure are shown in Table 1.1. Belite is the second major constituent (15-45% of mass) of a clinker, it is not as reactive

Table 1.1. Major Phase concentrations of Portland cement

Sl. No.	Phase	Mass percent(%)	Crystal structure
1	Alite	40-70	Hexagonal
2	Belite	15-45	Monoclinic
3	Aluminate	1-15	Cubic (Or) Orthorhombic
4	Ferrite	0-18	Dendritic

as Alite, and contributes to later strength more than 28 days. Tricalcium aluminate constitutes 1-15% of clinker, it has cubic or orthorhombic form and is highly reactive with water. Ferrite constitutes 0% and 18% of clinker and it has dendritic prismatic forms these appear to bind the silicate crystals. Periclase and Free Lime occur in lesser quantities. Alkali Sulfates and calcium Sulfates, which effect the hydration of concrete can also be found in clinker. Arcanite, Aphthitalite, Calcium Langbeinite, Sodium Anhydrite are also found in clinker (Miller,1996). Additionally (Taylor,1997) Alkali Sulfates and Sulphate phases like Thenardite

in high Na/K clinkers and possibly anhydrite in some high SO_3 are observed long crystal perimeters within the voids. Their average rate of disappearance over the first few days or weeks of hydration and their overall reactivities usually decrease in the order: $C_3A>C_3S>C_4AF>C_2S$. The inclusion of water triggers the hydration process which is important in the formation of two crucial hydrated products in PC which are Portlandite ($Ca(OH)_2$) and Calcium Silicate hydrate (CSH). Among these two major hydrated gels formed during the hydration, CSH gel is an amorphous material. Due to its amorphous nature of CSH the identification and quantification of this phase becomes more complicated, However researchers indicated the Tobermorite-9Å, Tobermorite-11Å, Tobermorite-14Å, Jennite etc. where 9Å, 11Å, 14Å refers to the characteristics basal spacing of 9.3, 11.3 and 14Å (Merlino S. *et al.* 1997, 1999). While Portlandite is a detectable phase which can be observed during X-ray diffraction (XRD) analysis.

Cement is a complex composite material and the behaviour of cement when exposed to higher temperatures effects the overall response of the concrete as it is a binding material. The mechanical properties of cement vary very suddenly at elevated temperatures because of its heterogeneous nature at multiple scales. All the constituents that forms PC start to deteriorate nonlinearly with respect to changes in temperature. The constituents that has the least amount of strength at lower temperatures, most severely affects the mechanical properties. Chemical changes also lead to physical changes. These physical changes with increase in temperature of concrete, increases the stiffness of concrete and cause a reduction in the mechanical properties, thereby not serving the intended purpose. The two major reason the temperature affects the functionality of concrete:

(a) Mechanical properties of concrete are temperature sensitive and each constituent's behaviour to temperature are different (Lee J. *et al.* 2009).

(b) Phase transformation of constituents at different temperatures.

Hence the response of concrete under elevated temperatures must be understood from both mechanical and chemical point of view (Lee J. *et al.* 2009). Concrete loses 40 - 60% of its strength when exposed to a temperature of 500 °C. Cement paste is the most important constituent that is exposed to fire because it acts a matrix (Buchanan A. H. *et al.* 2002). Stiffness of concrete increases with increase in temperature, because of temperature has a direct effect on mechanical properties, making concrete more brittle. Type of aggregate and

cement paste affects the thermal properties of concrete, while the increase in stiffness with increase in temperature, and causes a reduction in the phase transformation of constituents at different temperatures (Lee J. *et al.* 2009). Concrete mechanical properties do change with the GoC and since cement is a binding material in concrete its behaviour effects the mechanical properties at the concrete scale. When the concrete is subjected to fire loads the hydrated cement starts to shrink and then starts to spall there by losing its load bearing capacity.

To predict the outcomes of concrete during its exposure to fire, requires a greater understanding of transformation that the member undergoes during the fire. The physio-chemical changes taking place in the concrete at both micro and macro scale, and the radical changes taking place due to heat at the boundaries of the phases at micro and macro scales need to be understood. Changes occurring in the phases such as Portlandite, Calcite, CSH and microstructure changes in the non-evaporable water and micro pores was evaluated (Piasta J. 1984). To understand the behaviour of concrete subjected to higher temperatures, a need exists for understanding physio-chemical changes involved during the exposure to these temperatures. These phenomena include chemical reaction, phase transformation, and deformation due to heat that occur at microscopic scale of particular phases of concrete compounds. Multiple analytical methods have been applied to investigate thermal behaviour of hardened cement paste, however these methods are conducted on the pulverised cement powder samples.

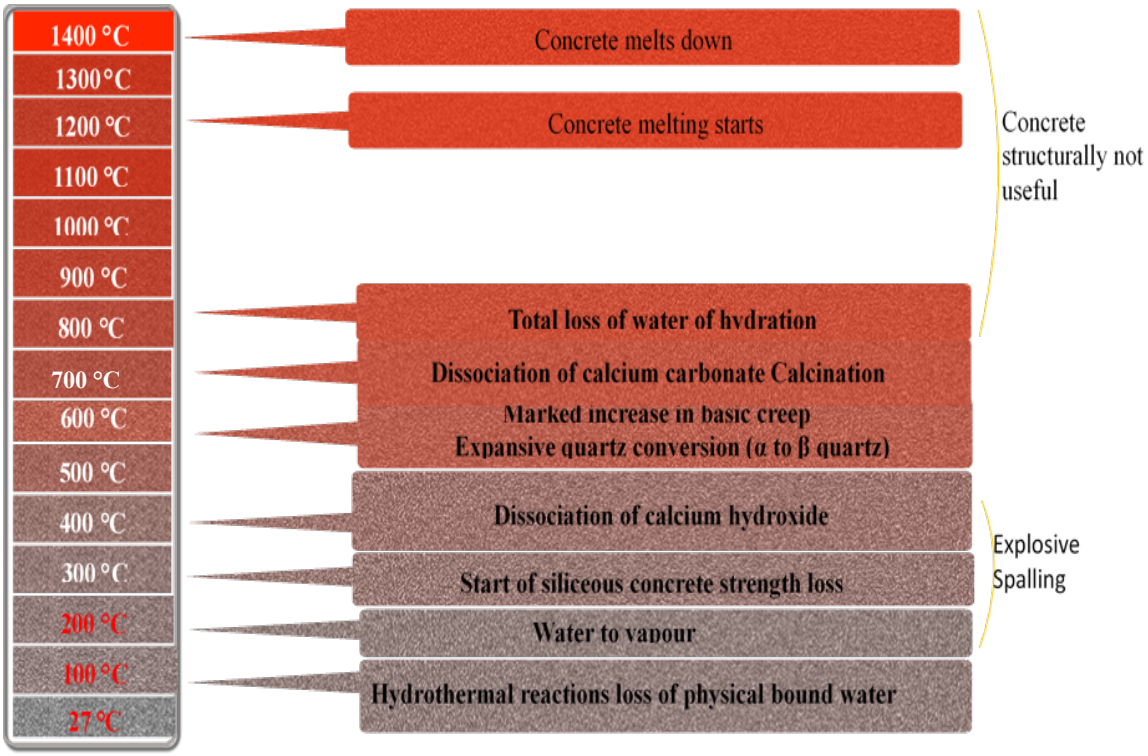

Figure 1.1. Effects of increasing temperature in concrete at various stages (Kodur V., 2014).

Fire response of concrete structural members is dependent on the thermal, mechanical, and deformation properties of concrete. These properties vary significantly with temperature and also depend on the composition and characteristics of concrete batch mix as well as heating rate and other environmental conditions. Effects of fire on the thermal properties of concrete at various stages of increasing temperatures is shown in Figure 1.1. Effects of temperature on concrete at 20 °C, 105 °C and at 800 °C is shown in Figure 1.2. At 20 °C there is some percentage of free water + physically and chemically bound water present in the concrete, however as the temperature reaches 105 °C, the free water and physically bound water evaporation leads to the formation of pores and the internally stresses, as this evaporated water should flow out of the concrete. Finally when the concrete reaches the 850

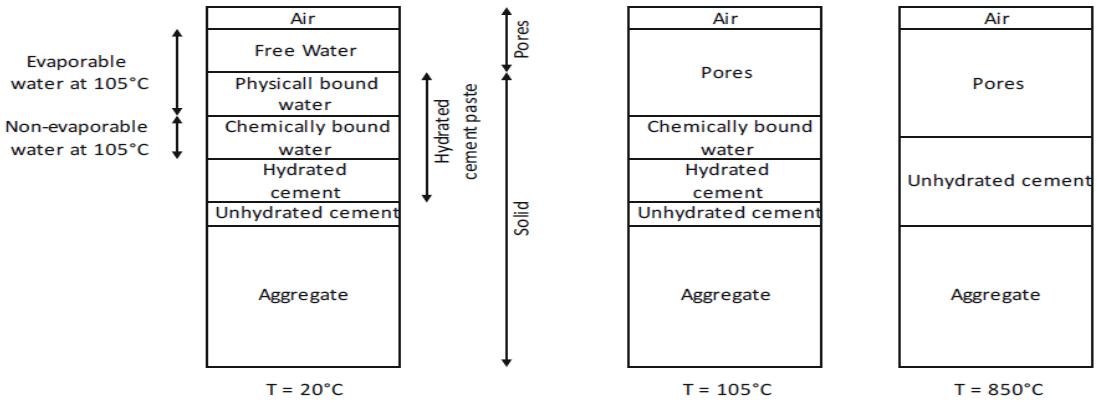

Figure 1.2. Different type of water inside concrete at different temperatures levels (Ichikawa Y. 2000)

°C, the chemically bound water is also and at this point the internal stresses due to the evaporation of the water is every high, which damages the concrete. An increase in the concentration of unhydrated cement and pores in the sample (Ichikawa Y. 2000).

The micro structure of cement is governed by the mechanical and transport properties. Hence when a concrete structure is subjected to elevated temperatures it induces mechanical damage and chemical transformation also takes place. The pore diameters of 0.001 µm to 1000 µm estimated from Mercury intrusion porosimetry (MIP), however due to the limitations of the tests the predictably of pore sizes is also limited (Zhang Q. *et al.* 2011). At temperatures of 30 ºC and 100 ºC a chemical bound water is lost, at 180 ºC to 300 ºC the chemically bound water from CSH and CH is lost, 450 ºC to 550 ºC the Portlandite dehydrati-

on takes place, 600 ºC to 700 ºC the calcite and CSH decomposes. All the chemical changes causes the coarsening of pore structure, which initiates the cracks at the surface and the core of the specimen and internally causes the shrinkage of concrete, and the variation in the thermal expansion of aggregate and mortar. The research in the past regarding the fire damaged concrete members, indicated that re-curing of the damaged concrete through water or in humid environment imitates the recovery process (Henry M. *et al.* 2016).

1.2. Objective and outline

The current thesis focuses on understanding which Grade of Cement performs better under the thermal loads among the three Grade of cements, that is currently used in India. As mentioned earlier PPC, OPC-43 and OPC-53 are commonly used, while OPC-53 is most commonly used because of its superior compressive strength. So the primary focus of this thesis is to determine, which Grade of cements has superior behaviour under the thermal loads. As these PC has different ratios of chemical composition and particle size distribution (PSD) and varying quantity of fly ash.

The scope is limited to characterizing the internal micro and meso structure changes taking place in the three PC with varying PSD and chemical compositions. To differentiate these PC various physical, chemical and bond behaviour studies were also compared. The specific objectives are:

- Evaluation of the characteristics of hydration products of various cements at room temperature.
- Studying the influence of elevated temperatures on hydration of ordinary Portland and Portland Pozzolana cement.
- Quantification of the physical changes at meso-level (porosity and pore network) in different types of cement under various high temperatures.
- Estimation of the interconnected porosity in hydrated cements at elevated temperatures based on micro tomography studies.

1.3. Limitations

The current studies consider only the hydrated PC samples, as the PC binding property are adversely effected, with the increasing temperatures. The effects of coarse aggregate, fine aggregates, mineral and chemical admixtures are not considered in this study. The temperature loads were simulated in a muffle

furnace and the rate of loading is constant, and temperatures for which the samples are exposed is restricted from room temperature (27 ºC) to 800 ºC beyond which the binding properties of PC is lost. However, the samples exposed to these temperatures are brought down to room temperatures at the time of carrying out the tests, except for the thermal analysis.

1.4. Thesis organization

The thesis is organized into 7 chapters:

Chapter 1. A brief introduction of concrete and its thermal behaviour during its exposure to elevated temperature was shown. The organisation of the thesis and the limitation of this research work is presented.

Chapter 2. Literature review of the work conducted so far by other researchers to understand the behaviour of Portland cements, mortar and concrete subjected to various temperature ranges is summarised based on the characterization method and gaps are identified.

Chapter 3. "Characterisation of PC at different stages of hydration" Three GoC are commonly used in India. PC in India are classified into three different GoC and their difference in terms of physical, chemical classification are studied and discussed at different stages of hydration *i.e.* 3 days, 7-days, 14 and 28 days of hydration .

Chapter 4. "Thermal characterisation of Portland Cements at elevated temperatures" Thermal behaviour for the three GoC are analysed using thermal analysis and at the critical temperature regions chemical and spectroscopy tests were conducted and results were discussed at the temperatures of room temperature, 100 ºC, 400 ºC, 500 ºC and 800 ºC.

Chapter 5. "Determination of porosity and pore network at mesoscale" Four critical temperature ranges are identified and the porosity and pore network present in the hydrated PC samples are studied using high resolution computer tomography (HRCT). 2D and 3D analysis was carried at temperatures of room temperature, 100 ºC, 400 ºC, 500 ºC and 800 ºC from the obtained images.

Chapter 6. "Determination of porosity and pore network at Micro-scale" from the tests of thermal analysis at the critical temperature regions, micro tomography tests are conducted on various hydrated PC samples exposed to these temperatures at micro scale using micro tomography and the results and observations are discussed. 2D and 3D analysis was conducted from the obtained images at temperatures of room temperature, 100 ºC, 400 ºC, 500 ºC and 800 ºC.

Chapter 7. "Conclusions and scope of future research" conclusions are drawn from all the tests conducted and the findings of this research work are discussed in detail. The outcomes of these tests are consolidated for all the three GoC.

1.5. Additional comments

- Harsha Praneeth, T.P. Tadepalli, Ashish k Agarwal "Thermal behaviour of PPC and OPC-53 when exposed to elevated temperatures." *Advances in cement research* (DOI: 10.1680/jadcr.18.00066).
- Harsha Praneeth, T.P. Tadepalli, Ashish k Agarwal "Evolution of Pore Network in Portland Cement at Elevated Temperatures Using High Resolution and Micro X-ray Computer-Tomography" in *Magazine of concrete research* (DOI: 10.1680/jmacr.18.00321).
- Harsha Praneeth, T.P. Tadepalli, Ashish k Agarwal "Estimation of porosity and pore distribution in hydrated Portland cement at elevated temperatures using synchrotron micro tomography" in *Journal of advanced concrete technology* (DOI:10.3151/jact.17.34).

The results from the current study have been split and organized into seven chapters, along with some unpublished work.

Chapter-2

Literature review

Chapter-2

Literature Review

2.1. General

Pure flint aggregate used in concrete is not a suitable aggregate under fire (Barret; 1854), a quick sudden drop in thermal gradient is one of the primary reason for spalling of concrete during the exhaustion of fire at the time firefighting (Ingle; 1866). The first committee was formed in 1903 for understanding the behaviour of concrete under fire, considered that spalling caused due to fire is related to fire resistance. (Woolson; 1905) observed as concrete is exposed to fire on one side, liquid water start to come out of the sample on the unexposed side. Concrete prepared with Basalt aggregate used in concrete has superior behaviour under thermal loads (Gary; 1911-1918), compared to Quartz aggregate (Hull; 1920). A step by step mechanism was postulated by (Preston and White; 1934) in describing spalling and it is defined as "Spall is a perfectly flaked shaped piece, and it is a thin one wave, namely, in a direction perpendicular to the original face. (Hasenjager; 1935) listed out critical stages of spalling in concrete during fire:

(a) Rapid heating of concrete.
(b) Exceeding the tensile strain by unilateral strain.
(c) Volume change taking place in concrete, which leads to rapid structure change.
(d) Water vapour and gasses present in cement paste and aggregate are liberated.

With the passing of time and increase technology, the behaviour of concrete under the thermal loads has gained significance. Many studies have emerged, which determine various constituents present in PC, listed as follows in Table 2.1.

2.2. Thermal analysis and XRD

Piasta J. *et al.* 1984.

Cement paste was subjected to a temperature of 20-800 °C and the transformation taking place in microstructure and phase composition was investigated using thermal analysis, XRD. The concentration of Calcite remained static at 8.6% up to 200 °C; as the temperatures reached the ranges of 200-500 °C a

constant increase was observed by 15.7%. At the temperatures beyond 500 °C a continuous reduction in Calcite was observed, due to the disassociation. As TGA analysis is not structural dependent while XRD

Table 2.1. Techniques used for determining various properties in PC.

Sl. No	Tests Name	Purpose
1	PSD	determine the size of the Portland cements and admixtures.
2	XRF	determining the elemental and chemical oxides of present in cements and admixtures
3	XRD	determining chemical oxide and phase concentrations present in cements and admixtures.
4.	FTIR	determining organic, polymeric, and, in some cases, inorganic materials to observe the chemical composition.
5.	FTRS	determining organic, polymeric, and, in some cases, inorganic materials to observe the chemical composition.
6.	CHNSO Analysis	determining elemental composition such as Carbon, Hydrogen, Nitrogen, Sulfur, and Oxygen concentration
6.	TGA	determining the weight change taking in the material as a function of increasing temperature
7.	DTA	determining the exothermic and endothermic reactions taking place in the material, due to heat flow
8.	DSC	determining the exothermic and endothermic reactions taking place in the material, due to heat flow
9.	HRCT	determining the internal structure in the third dimension at meso scale
10.	MCT	determining the internal structure in the third dimension at micro scale

method monitors changes in the structure to the extent of its crystallisation degree. Hence the increase observed in the intensity of Portlandite is less than 300 °C is due recrystallization in amorphous hardened cement pastes. While the variation of Portlandite above 500 °C determined by XRD and TGA shows an evidence in the formation of amorphous Portlandite. The grains of unhydrated cement at 100 to 400 °C decreases, which is found by the decrease in the intensity of β-Belite and Alite.

Piasta J. 1984.

The deformation phases due to heat in hardened cement pastes at temperatures ranging 20 °C to 800 °C. The **Table 2.2** showing the parameters of major phases found in PC; thermal analysis tests were also conducted. The deformations occurring due to heat are measured using thermal dilatometry (TD), change in velocity using differential dilatometry analysis (DTD) and

chemical process taking place using DTA was measured simultaneously on the individual phases of cement. At temperatures of 20 °C to 900 °C no endothermic peaks were found for the major phases of cement except for β - C_2S. The β - C_2S has a weak endothermic peak at 630 °C to 700 °C which is related to the Polymorphous transformation of α - C_2S. The C_3A phase has the lowest thermal expansion while C_3S and C_4AF precedes it and this expansion is linear while that of β -C_2S it is non-linear at the temperatures of 600 °C - 700 °C. The thermal expansion in PC is linear until 600 °C and then increases with constant acceleration with the increasing temperatures.

Table 2.2. Basic properties of the major phases of PC

Mineral	**Density (g/cm^3)**	**CaO (weight %)**	**Blain SSA (cm^2/g)**
C_3S	3.15	1.82	2940
β -C_2S	3.23	0.002	3010
C_3A	2.95	1.81	2920
C_4AF	3.72	0.80	2900

Sha W. *et al.* 1999.

Thermal behaviour of hydrated PC as a function of time are investigated using DSC and XRD. Three endothermic peaks were observed for the phases of CSH, De-hydroxylation of Portlandite, De-carbonation of Calcite, and the peaks of Ettringite, C_4AH_{13}, and Fe_2O_3 solid solution were also observed. Water reacts with C_3S and C_2S in forming CSH, and Portlandite which are the primary hydration products as shown in Equations 2.1 & 2.2:

$$2C_3S + 6H \rightarrow C_3S_2H_3 + 3CH \text{ ---------} \quad (2.1)$$

$$2C_2S + 4H \rightarrow C_3S_2H_3 + CH \text{ ----------} \quad (2.2)$$

The $C_3S_2H_3$ is an approximate representation of CSH, while gypsum undergoes a quick reaction to produce C_4AH_{13} and this reacts with calcium sulphate present in gypsum to form Ettringite. The ferrite phase present in cement reacts with gypsum to form ettringite substituted with gypsum. An increase in the size of the peak is an indication of the desorption of capillary water, present in silica-lime gel. The de-hydroxylation of Portlandite from DSC data is in sync with the XRD data at 635 ºC which confirms these reactions. The hydration of C_3A and Ferrite are observed in four smaller peaks, while the peaks in the ranges of 165-205 ºC & 255-300 ºC are peaks Ettringite C_4AH_{13} which are the reaction products of C_3A. The concentration of iron-substituted Ettringite and formation of Fe_2O_3, which are the products of Ferrite observed at 155 ºC and 390 ºC.

Handoo S.K. *et al.* 2002.

Samples prepared using OPC are subjected to temperatures ranging from 27 °C - 1000 °C at an interval of 100 °C for a duration of 5 hours. XRD, TG/DTA, are conducted for estimating the mineralogical changes, and the physical changes are measured using ultrasonic pulse velocity (UPV). XRD analysis carried at the core and surface of the samples indicate, a gradient is observed for Portlandite and Calcite at surface and core of the sample. As the changes in Portlandite and calcite intensity is more severe at the surface than the at the samples core. Thermal analysis carried at the surface and core of the sample indicates that severe damage exists at the surface rather than the core of the sample, while the concentration of Portlandite at surface and core were almost same as obtained from TG and similarly from XRD analysis, at temperatures greater than 700 °C Portlandite phase was not noticed.

Lucia A. *et al.* 2005.

Cement pastes subjected to temperatures ranging from room temperature to 800 ºC using thermal analysis. The exposure of hydrated paste to extreme certainly temperature leads to irreversible decomposition reaction and also causes changes in mineralogical composition. The thermal decomposition is analysed using TGA and DTG curves. The bound and evaporable water escapes at 30 to 105 ºC, while at 120 ºC the evaporable water is completely lost. The decomposition of phases such as Gypsum, Ettringite takes place at 110 to 170 ºC along with loss in water from Carbo Aluminate hydrate (CAH). At 180 to 300 ºC bound water is lost by decomposition of CSH and CAH. Dehydroxylation of Portlandite at 450 to 550 ºC, while the decarbonation of calcite takes place at 700-900 ºC. The weight loss of CSH, Portlandite, Calcite is estimated as shown in Table 2.3.

Table 2.3. Weight loss in major phases of hydrated PC.

Phase	Ref	100ºC	200ºC	300ºC	400ºC	500 ºC	600ºC	700ºC	800ºC
CSH	79.83	54.09	41.82	20.13	10.68	12.16	8.22	11.21	0.00
Portlandite	9.05	25.51	28.25	44.61	37.91	26.56	27.59	57.01	88.76
Calcite	11.12	20.41	29.92	35.25	51.41	61.28	64.19	31.78	11.24

Stepkowska E.T. *et al.* 2005.

Two PC with different specific surface area and compressive strength i.e. OPC-33 and OPC-43 prepared with a w/c = 0.40 and hydrated for one month. After the hydration, specimens are tested for a period of 1 year and 5-6 years as they were in contact with air. These pastes were

tested using static heating, TGA, DTA, DSC, and XRD analysis. The XRD analysis indicated a continuous reduction in Portlandite peak and completely disappeared after 450 ºC. The calcite peak which is initially broad and small, has gradually increased mainly after the disappearance of Portlandite. While the calcite peak lowered at 600 ºC and disappeared completely beyond 700 ºC. The variation in the Portlandite with ageing was observed which has exceed the standard d(001) = 4.958 Å, this was higher in OPC-33 paste since it has higher carbonation when compared to OPC-43 pastes. The peaks of XRD are dependent on the quality and age of the pastes.

Mohamed H. 2006.

Thermal effects of samples prepared with lime stone and Fly ash (FA) are studied at the temperatures of 250 ºC, 450 ºC, 650 ºC and 850 ºC. Changes in phase's are studied using XRD, DSC for the lime stone and fly ash pastes. The specimens are prepared with OPC and then the cement is partially replaced by a weight percentage of 0, 10, 20 and 30, while the lime stone was replaced with weight percentages of 5, 10, 15 and 20. The w/c is the normal consistency values of the cement, and the mixed samples were placed in moulds of 25.4 x 25.4 x 25.4 mm^3 and the wet curing periods were for 28 and 366 days. Increase in compressive strength was observed for the samples exposed to temperatures of 250 ºC due to the formation of additional hydration of un-hydrous grains, as a result of autoclaving (this phenomenon takes place at temperatures ranging 105 ºC to 250 ºC),this process causes the deposition of CSH into the pores. The specimens prepared by FA has shown superior compressive strength properties at 650 ºC in comparisons to OPC pastes. The acetone used for pre-treatment has lowered the expansion, however after wetting the specimen's, reaction was same as the unreacted pastes.

Black L. *et al.* 2006.

The hydration process in C_3A is studied using XRD analysis, while the C_3A reactions in the presence and absence of gypsum was monitored. The hydration of C_3A is the fastest among the four major phases of cement and is responsible for flash setting. As C_3A in in contact with water it gives to needle like hexagonal hydrates C_4AH_{19} and C_2AH_8 under an $Al(OH)_3$ gel is believed to be formed. In order to control this reaction gypsum is added ($CaSO_4.2H_2O$, $C\bar{S}H_2$) to cement which gives a dense coherent structure called Ettringite (also known as Aft)($Ca_6Al_2(SO)_3(OH)_{12}.26H_2O$, $C_6A\bar{S}_3H_{32}$ is formed on the surface of the C_3A grains. Ettringite is stable until the presence of sulfates is greater than 2/3, however once it falls down below it which converts in to monosulfates ($Ca_4Al_2O_6(SO_4).14H_2O$, $C_4A\bar{S}H_{14}$) also called AFm

which can react with the unhydrated C3A that gives rise to monosulfate until the C_3A or sulfate is consumed.

Arioz O. 2007.

Concrete prepared of different *w/c* ratios were studied using DTA technique, for which four kinds of cement mixes were prepared using PC. The weight loss increased with the increase in temperature, the weight loss is 45% at 1200 °C, an abrupt weight loss takes place after 800 °C and until then it is smooth, which has an adverse effects on the mechanical properties of concrete. The loss of chemically bound water in CSH is the reason for the concrete losing its binding property.

From the thermal analysis the following observations were made:

114 °C - dehydration of physically bound water in causes an endothermic peak.

300 °C – exothermic peak due to release of gasses.

490 °C – endothermic peak due to CH.

740 °C – endothermic peak to dehydration of CSH.

1097 °C – exothermic peak causes by generation of new phases.

The intensity of the yellow colour increased with increase in the exposure time, up to 600 °C green colour was observed, and 800 °C to 1000 °C red colour was observed.

Luis P. E. 2011.

This research article focuses on silica fume (SF) cement based material which has low water hydration and porosity. The XRD analysis was carried to monitor the hydration taking place in the samples, along with TG/DTA and DSC analysis. TG/DTA is also helpful in interpreting the effects of mineral admixtures such as SF, FA *etc.* in pozzolanic mineral interactions. Three samples were analysed (a) cement paste, (b) cement-silica paste and (c) cement-silica paste with water entrained. The first endothermic peak of cement paste is observed at 150 ºC which is caused by the dehydration of CSH that correspond to TGA. The mass loss at this instant is due to weakly bound water present in the solid gel at ≈ 110 ºC. The endothermic peak at 410 ºC is due to the dehydration of Portlandite, followed by a mass loss. Minor peak observed at 800 ºC due to uncontrolled carbonation. A new approach was adopted for determining the Pozzolanic activity of silica fume, based on the differentiation of phases such as CH and CSH by TG

measurements. A good correlation exists between TGA and DTA for estimating the CH phase, while the XRD method has a poor correlation because of poor crystalline phase existing in CH.

Qi Zhang *et al.* 2011.

In the current article the cement paste samples are subjected to temperatures of 100 ºC to 1000 ºC and the rate of heating was 5 ºC/min and cooled to room temperature. Experimental investigations are carried for the samples using environmental TGA. No abrupt change in capillary pores was observed until 400 ºC, however weight loss was observed. After 400 ºC weight loss reduced and the pores of capillarity expanded drastically.

Gallucci E. *et al.* 2013.

The effects of temperature on concrete and its effects on the hydration of PC and there contribution in the microstructure development was studied. CSH is very sensitive to temperatures and there is an increase in the density in the temperature ranges of 5 ºC to 60 ºC. The temperature does not have an effect on the final degree of hydration, while the porosity increase is very minor, than measured for AFm phases rather ettringite. The Figure 2.1 showing the thermal analysis of samples at various stages of hydration. The increase in the density of CSH is often associated with a reduction in the amount of structural bound water. From the thermal analysis, for the temperatures between 80 ºC – 420 ºC there is a weight loss caused to the dehydration of CSH, AFt and AFm phases. The water present in Portlandite is lost at 420 ºC – 550 ºC, the weight loss caused by de carbonation of calcite is at the temperatures of 600 ºC – 780 ºC and any weight loss between 780 ºC – 1050 ºC is due to CSH.

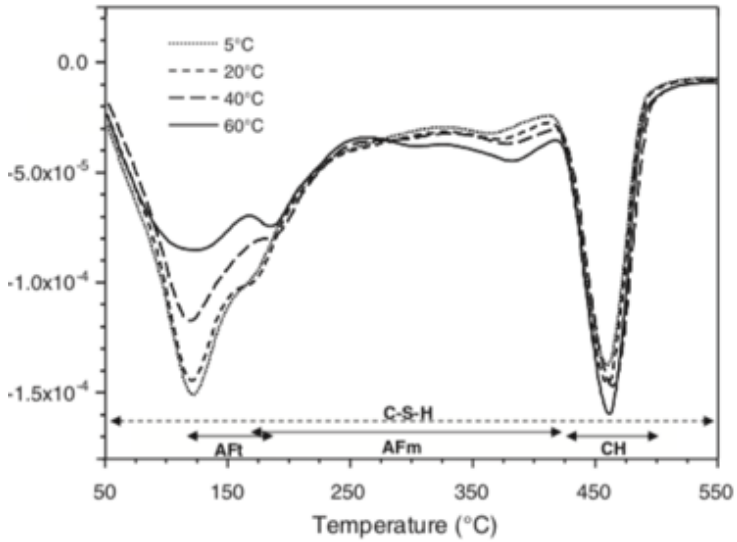

Figure 2.1. TGA analysis of hydrate assemblage of 90 days cured specimens at various degree of hydration

Kim K. Y. *et al.* 2013.

The mortar specimens are subjected to temperatures of 1000 ºC, and XRD tests are conducted. The XRD studies indicated that the Portlandite concentration did not alter much at temperatures of 25 ºC - 400 ºC; and not a significant decrease till 600 ºC, however a drastic decrease after 700 ºC was observed. An increase in the concentration of CaO due to the decomposition of Portlandite, which happens due to hydrolysis of moisture at temperature exceeding 500 ºC and partial decomposition of calcite exceeding 900 ºC.

Michael H. *et al.* 2016.

The rehydration reactions taken place in fire damaged cementitious material subjected to recurring using water, and the qualitative and quantitative data is assessed. The chemical changes and physical changes taking place in the cement pastes subjected to a temperature of 600 ºC and re-cured, by doing so the rehydration mechanism taking place in the fire damaged cement paste was monitored. XRD studies indicated that the recurring of the cement paste samples displayed a connectivity in the pore network, this can be attributed towards the rehydration of CaO and Portlandite. A variation in the chemical analysis of hydrated and rehydrated cements was observed this can be due to the C_2S phase which a play a significant role in CSH gel formation during the initial stages of water re curing of the sample. A variation in the rehydration reaction differed with the initial hydration process in two ways and this was also observed through the chemical analysis.

2.3. Microscopy studies

Piasta J. 1984.

The deformation of phases due to heat in hardened cement pastes at temperatures ranging 20 °C to 800 °C and SEM tests is conducted. Ettringite expansion is short and least due to heat until 50 °C, and the shrinkage is higher. The micro cracks are higher among the unhydrated clinker grains and the paste at 400 °C; at 500 °C complete destruction of unhydrated grains takes place which were observed under SEM. The Portlandite crystals in cement paste are compact crystals and crystal structure is very fine, while lager crystals are also observed and spaced uniformly. The growth of Portlandite crystals can be observed until 200 °C, while the micro cracks are formed at 300 °C at Portlandite and between the laminas. The growth of Portlandite carbonisation was found at 200 °C - 500 °C.

Abell A.B. *et al.* 1999.

The research article focused on determining the pore structure using MIP and image analysis is used for validation of the samples at room temperature. The SEM images indicates a variation in the porosity values CSH at an earlier and later stage, which means that CSH gel is formed at initial stages of hydration is porous than the CSH gel formed at later stages. Mortar samples of two *w/c* ratios i.e. 0.4 and 0.6, and the specimens were compacted with a pan vibrator and water cured for 14 days, while the specimens of ~ 10 mm dia x 20 mm long were drilled and oven dried.

Handoo S.K. *et al.* 2002.

Samples prepared using OPC are subjected to temperatures ranging from 27 °C - 1000 °C at an interval of 100 °C for a duration of 5 hours. The morphological changes SEM tests were conducted on the specimens exposed to elevated temperatures. The specimens collected from the core and surface are analysed using SEM. Samples at temperatures of 200 °C did not indicate any change in morphology; at 300 °C deformation of Portlandite and CSH phases, and the transformation of Portlandite to calcite was observed. As the temperatures reached 500 °C micro cracks are observed because of the increase in porosity and changes in Portlandite and CSH. At 600 °C and 800 °C micro cracks are well spread across the sample with further increase in porosity and disrupted boundaries of CSH.

Diamond S. 2000.

Air voids present in concrete, mortar and cement pastes are spread in the scale of 10 μm - 500 μm and this contributes to the major portion of the pore volume. Few tests were done under optical microscopy to determine the air void sizes in the samples and these values ranged from 150 μm to 10 μm, while the air content lied in between 1 - 2.5% of the pastes volume, which is in between 0.02 to 0.05 cm^3/g this indicates that the percentage of air pores is very less, except for the mixtures mixed under vacuum.

Gallucci E. *et al.* 2007.

The cement paste samples are prepared with CEM I 42.5 PC (OPC) and with a *w/c* = 0.5, the paste is injected with a syringe in to a glass tube of diameter 600 μm. The samples hydration was monitored for 1, 3, 7, 14, 28 and 60 days and different samples. The article focused on the

anhydrous reactions and porosity, and the capillary porosity enabled the study of connectivity and tortuosity existing in the pores network. Since the variation in the beam-matter interactions there was a difference in the X-ray projection and SEM-BSE images have a similar phase contrast:

(a) the brightest phases which is indication of the highest density are of anhydrous unreacted cement grains are observed in X-ray CT and SEM-BSE analysis.

(b) The gray colour phases belong to 'inner' CSH and undifferentiated hydration products.

(c) Light gray phase belongs to Portlandite.

(d) Darkest phase is of porosity.

Georgali G. *et al.* 2005.

The core of the samples collected from fire damaged concrete was investigated using optical microscopy. The suitability of optical microscopy equipment for samples exposed to thermal loads, for understanding the microstructure of concrete and aggregate pastes, cement paste separation from aggregates, and cracks and voids at microscale, as well as crack pattern quantification were analysed. The petrographic-microscopic examination indicate a parallel cracking at the core axis, this indicates larger internal cracking due to shrinkage, caused by sudden heating and cooling cycle.

Qi Zhang. *et al.* 2011.

In the current article the cement paste samples are subjected to temperatures of 100 ºC to 1000 ºC and the rate of heating was 5 ºC/min and cooled to room temperature. Experimental investigations are carried for the samples using environmental scanning electron microscopy (ESEM). The images obtained from ESEM were analysed to estimate the hydrated volume fractions. The grey level histograms are plotted for images obtained from ESEM are shown in Figure 2.2. Microstructure variations in cement pastes were not observed and the CSH had a gel morphology from 30 ºC - 400 ºC, for the images of 105 ºC - 400 ºC four peaks were observed which indicates capillary pores, low (low dense CSH) and high (high dense CSH and CH) density hydrates, and clinker. Cracks were observed in the samples from 500 ºC – 800 ºC, and the pores which are isolated were connected, hence the peaks of CSH and CH merged to a single peak (*i.e.* low and high density peaks merged to dehydration product having a similar density). At 1000 ºC CSH and CH transferred to crystalline phase while the pores expanded drastically, histogram of three peaks was observed where the intensity of the hydrated and clinker peaks is very low *i.e.* 2 peaks were observed.

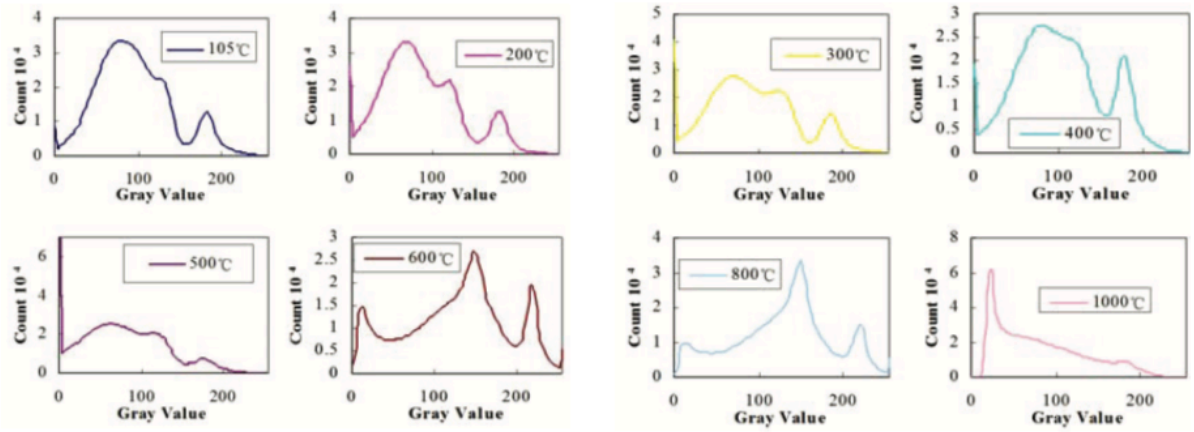

Figure 2.2. Histogram of BSE images obtained for heated cement pastes at different temperatures.

The BSE images obtained from ESEM were analysed using threshold technique in image processing, till the temperatures of 30 ºC - 500 ºC, four phases were observed, and from 600 ºC to 1000 ºC three phases were observed, and from this it is observed that growth in area of the pores fraction is slow till 400 ºC and then a rapid increase is observed and the decomposition of CH at 400 ºC to 500 ºC there is a decrease in the area of the hydrated phases which is continuous.

Kwang Y. K. *et al.* 2013.

The mortar specimens are subjected to temperatures of 1000 ºC, and the internal pore structure evolution with respect temperature is monitored using SEM to study the physical and chemical changes taking place in the specimen. SEM investigation indicated a richer formation of CSH and Portlandite at 25 ºC to 300 ºC, and the shape of them is a cotton cloud and hexagonal plate. At temperatures exceeding 450 ºC the breakdown of Portlandite, the cotton cloud remained intact however the hexagonal plates start to separate which is an indication of microstructure being deformed. At 700 ºC, the hydrated phases start to decomposes and this increases the density of pores due to the decomposed CSH gel. At 1000 ºC most of the hydrated products start to decompose, while melting of aggregates and minerals takes place, and minor portion of Portlandite remains unaffected. No cracks were observed in the surfaces of sample until 500 ºC, however a fracture at the edge of the specimen of 20 mm length was visible at 600 ºC.

Zhang W.M. *et al.* 2010.

Laser scanning confocal microscope (LSCM) is used to produce a series of 2D images of the cross section. For the image segmentation the thresholding was used for grouping the image pixel by checking pixel intensity against the set of threshold. The threshold 2D images are reconstructed to 3D for visualisation of the pore morphology. The samples were cast with OPC

CEM II 42.5 with a w/c = 0.60, and the pastes were cast into mould of 30 mm x 30 mm x 30 mm. After the desired curing of 90 days the slices of 1mm thick were cut, the cut slices were placed in acetone to prevent the changes in microstructure and hydration process. The specimens were vacuum dried and were place in a low viscus epoxy which was doped in a florescent material. LSCM is a very useful method for investigation of 2D pore structure in cement based material (CBM). The pore structure and the matrix of the CBM can be predicted accurately into 3D by reconstructing the 2D slices, by interpolation of grey level and image segmentation technique. The paper focused on the process of 3D reconstruction of the 2D slices and the threshold process adopted to separate the pores and the matrix, while it this study was not focused on quantifying it.

Luis P. E. 2011.

Silica fume (SF) cement based material which has low water hydration and porosity is analysed using SEM. The SEM technique is more suited for low water and porosity systems, while this technique failed in differentiation of hydration phases. The microstructure and pore structure used to investigate at this scale and it is homogeneous, while the change in morphology can be differentiated at sub-microscopic scale. Understand porosity at macro-scale of 2D slices, is not useful in obtaining the pore depressions hence a 3D approach is useful for obtaining an in depth understanding of pore network. At *w/c* = 0.3 and silica fume modified cement ratio of 0.15 the complete conversion of CH to CSH was not possible. The long term hydration the Pozzolanic activity is not significant and it is negligible after 3 days in a sealed hydration environment.

Kim K. Y. *et al.* 2013.

The mortar specimens are subjected to temperatures of 1000 ºC, and the internal pore structure evolution with respect temperature is monitored SEM. The studies pertaining to fire induced cracks are scarce due to the limitation in visualizing the internal structure by naked eye, and hence many numerical modelling has emerged with time. SEM investigation indicated a richer formation of CSH and Portlandite at 25 ºC to 300 ºC, and the shape of them is a cotton cloud and hexagonal plate. At temperatures exceeding 450 ºC the breakdown of Portlandite, the cotton cloud remained intact however the hexagonal plates start to separate which is an indication of microstructure being deformed. At 700 ºC, the hydrated phases start to decomposes and this increases the density of pores due to the decomposed CSH gel. No cracks were observed in the surfaces of sample until 500 ºC, however a fracture at the edge of the specimen of 20 mm length was visible at 600 ºC. While the fractures are spread across consequent slices over 5-7 layers at

700 ºC which indicate the depth of the fracture, and fracture width of 0.3-0.5 mm. The fracture initiation took place at the surface of the samples at extreme temperatures, and fractures were easy to be identified after 800 ºC, and they were extensively developed at 1000 ºC.

2.4. Conventional methods to determine porosity

Piasta J. *et al.* 1984.

Cement paste was subjected to a temperature of 20-800 °C and the transformation taking place in microstructure and phase composition was investigated using MIP. An increase in porosity was observed at 300 °C to 500 °C, that is due to the increase in the number of pores of diameter of 500 nm. Liberation of water caused by the decomposition of Portlandite and carbon dioxide separated from $CaCO_3$ at 700 °C.

Chan Y. N. *et al.* 1999.

Porosity of both the normal strength concrete (NSC) and high strength concrete (HSC) are determined using the MIP. The pores of diameter greater than 1.3 μm might be the reason forth increase in the permeability in the hydrated cement paste (HCP). Tests were conducted on HSC and NSC for compressive and split tensile strength at 1200 °C. The failure pattern for both concrete is similar, and the critical region of temperatures was from 400 °C to 800 °C. HSC permeability related durability was analysed when the concrete is exposed to extreme temperatures. HSC has a better behaviour to fire in the ranges of 20 °C - 400 °C, while most of the compressive strength is lost at temperatures beyond 600 °C. At 800 °C most of the compressive strength is lost for both type of concrete, hence a need for research needs to be carried at the temperature ranges of 400 °C - 800 °C.

Abell A.B. *et al.* 1999.

The research article focused on determining the pore structure using MIP and image analysis is used for validation of the samples at room temperature. The intrusion into pores was carried using a wood's metal which penetrates and gets deposited as solid in the pores. This research revealed that the pores are of irregular geometry which is confirmed by substituting the pores with intruding liquid which remains as solid in the pores present in the mortar specimens, were as MIP assumes the pores are of regular geometry. While the woods MIP (WMIP) values are in sync MIP values, while the estimation of pores diameter is larger in the case of WMIP. The

volume fraction estimated using MIP and WMIP are in good agreement which were estimated using image analysis. The image analysis indicates a greater diameter of larger pores than MIP.

Diamond S. 2000.

MIP method of determining porosity in cement pastes, mortar and sometimes concrete has become a in-house method, and many research articles were published till data by varying the age and water cement ratios of mixes. This method is not even close in predicting the actual pores present in the system that it measures. The process of MIP method is very simple, a specimen is dried for removing the existing fluids present in the pores, and then weighed. Then mercury (Hg) is introduced in to the chamber until it fills the chamber. Since Hg cannot wet the surface of the specimen, pressure is applied in proper increments, and Hg intrusion is monitored. Hence the pressure steps and the volume of Hg intruded in to the pores provides the PSD. The major of advantage of this method is the repeatability of the data. This process does not produce any data, and for which a suitable model needs to be used, and for which Washburn equation is used for estimating the cylindrical pore diameters calculated at each pressure step using the equation 2.1:

$$d = -\left(\frac{4*g*cos\theta}{P}\right) \text{ ---------- } (2.1)$$

were cylinders diameter is ‘d’; Hg surface tension is ‘g’; Hg contact angle on solid is ‘θ’; and the pressure applied is ‘P’.

The major drawback that this method suffers from is that it represents how the Hg intrudes into the specimen however not governed by the actual pores present. The Washburn equation assumes the pores are cylindrical and the they are accessible from surface of the sample. The pressure required for filling the pores diameter cross section is estimated using Washburn equation, only if the mercury is accessible to the pore, which proves the process is fundamentally flawed. The estimation of the pore size distribution is also effected with the w/c ratio and the duration of hydration that the samples underwent. The samples were often set to a lot of pressure so that new fractures are caused because of the pressure, there by misleading data is produced. The Figure 2.3 showing the comparison of 28 days paste which was mixed in vacuum with water to cement ratio of 0.4, the pore size distribution of using image analysis is spread up to 10 μm while the MIP has shown a pore volume double than the image analysis which is shown in the Figure. 2.3 below and even the size of these pores is < 0.2 μm. Air voids

present in concrete, mortar and cement pastes are spread in the scale of 10 μm - 500 μm and this contributes to the major portion of the pore volume. An attempt was deliberately made to make a design mix entrained with air voids and image analysis has easily identified the entrained air voids while MIP failed to do so.

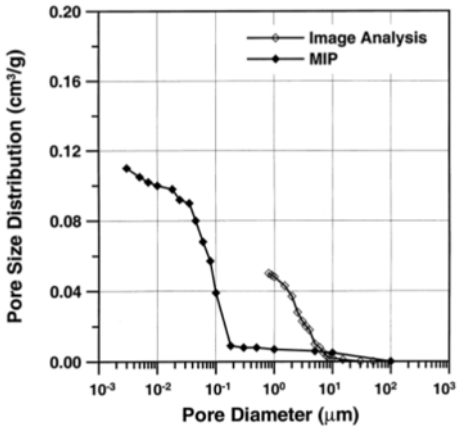

Figure 2.3. Pore size distribution estimated using MIP and image analysis of the same samples which is vacuum mixed, 28 days old with w/c of 0.40.

Handoo S.K. *et al.* 2002.

Samples prepared using OPC are subjected to temperatures ranging from 27 °C - 1000 °C at an interval of 100 °C for a duration of 5 hours. The physical changes are measured using ultrasonic pulse velocity(UPV) were conducted on the specimens exposed to elevated temperatures. The UPV results showed a decrease in velocity from 4.05 to 0.33 km/s at temperatures of 100 °C to 700 °C, along with concrete deterioration. At temperature's exceeding 300 °C the velocity reduces significantly, and at 800 °C pulse could not pass through the specimens indicating a complete failure of the specimen. The compressive strength results were not affected until the specimens temperature reached 400 °C, while the concrete specimens compressive strength decline after 600 °C.

Neville A. 2003.

w/c ratios affect the strength parameters of concrete, hence if there is a undesirable reduction in compressive strength a need to quantify the w/c ratio exists. The direct method of fluorescence microscopy which was used as a standard method by noridc organisation, has been studied. This method requires a reference standard with a range of mixes of specific ingredients and their curing history is also to be known. A recent study using this method stated that the w/c ratio of unknown sample can be determined to an accuracy of ± 0.02, and from this research the claim is found to be untrue.

Vodak F. *et al.* 2004.

Porosity **(P)** was determined using MIP on sample volumes of 0.5 cm^3, of hardened cement paste obtained by drilling from the concrete specimen, and also compressive strength **(S)** of unsealed concrete cubes are determined at temperature ranges of 25 °C to 280 °C, once brought down to room temperatures. Concrete can resist the heat caused due to natural hazard, however continuously subjecting the member to these thermal loads will cause the deterioration of CSH, CA gels and Portlandite are disintegrated, and these physiochemical changes that leads to catastrophe. The concrete consists of various types of pores such as gel pores whose sizes vary from 0.5-10 nm; capillary meso pores vary from 10-5000 nm and macro pores. The capillary gel pore effect is neglected in S(P) relation, and the annealing process does not have an effect on porosity. An effect of compressive strength with 27 days and 90 days of hydration at different temperatures was shown. Changes of porosity with respect to temperature are shown in Figure 2.4.Drying process increases the compressive strength at 100 °C and 200 °C. Bound

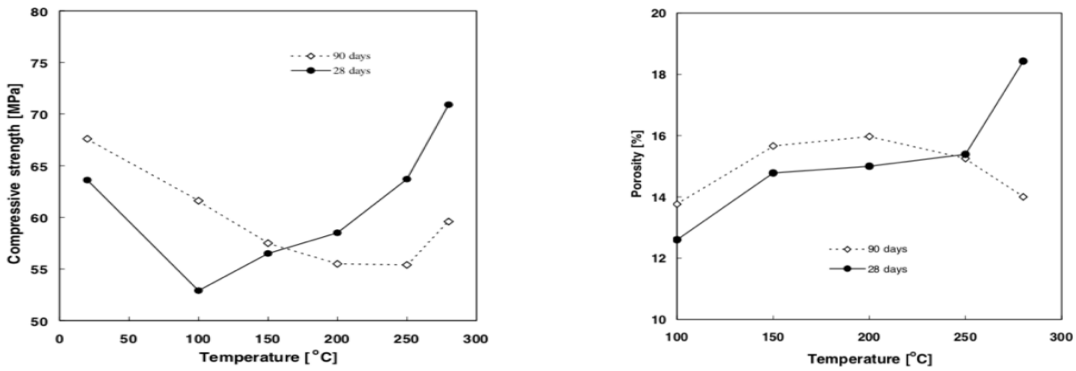

Figure 2.4. Relation between compressive strength, temperature and porosity.

water starts to release at 180 °C, the thermal incompatibility of hardened cement paste and aggregates causes micro cracks in the member.

Qi Zhang *et al.* 2011.

In the current article the cement paste samples are subjected to temperatures of 100 ºC to 1000 ºC and the rate of heating was 5 ºC/min and cooled to room temperature. Experimental investigations are carried for the samples using MIP. The images obtained from ESEM were analysed to estimate the hydrated volume fractions. The dehydration of CSH and Portlandite takes in to thinly dispersed crystalline particles as the temperatures reached 1000 ºC. While an increase in pore connectivity with an increase in temperature. The porosity observed by MIP is greater than ESEM and this is due to the difference in the techniques that these testing methods adopt and hence the ESEM technique could not estimate the pores smaller than the resolution.

The capillary pores of sizes > 1µm are very similar from 105 ºC -400 ºC, at 500 ºC temperatures the capillary pores of diameter > 0.001 µm, and gel pores < 0.01 µm increased drastically due the decomposition of CH.

Gallucci E. *et al.* 2013.

The effects of temperature on concrete and its effects on the hydration of PC and there contribution in the microstructure development was studied. The modification taking place in CSH, by isothermal curing and at the temperatures ranging 5 ºC to 60 ºC. The increase in the temperature of 5 ºC to 60 ºC a slight change in the C/S ratio and CSH was observed, and this was associated with polymerization in the higher degree silicate chains, while there is increase in apparent density by 25% and decrease in the bound water content. The increase in the density is due to the difference in nanoscale packing of CSH. The porosity is higher in hydrated cement pastes specimens cured at elevated temperatures, due to the changes in the CSH density. CSH is very sensitive to temperatures and there is an increase in the density in the temperature ranges of 5 ºC to 60 ºC.

Qiang Zeng. *et al.* 2016.

Two cement paste samples with *w/c* of 0.3 and 0.5 were analysed for porosity at different stages of hardening *i.e.* 7, 28, 90 and 180 days using MIP and nitrogen adsorption/desorption (NAD) method. MIP is useful in predicting the pore sizes across larger ranges while NAD can predict the size of pores lesser than 70 nm. The macro pores ≤ 2 nm, meso pores ≤ 2-70 nm and capillary pores ≥ 70 nm were estimated in the HCP. The characterisation of specific surface area (SSA) and PSD was estimated using MIP-NAD method is helpful in predicting the evolution of pore structure in relation to hydrates filling and CSH growth. The pore volume and SSA growth is related to the growth of CSH while the filling of hydrates is captured using MIP pore volume. As the samples are subjected to freeze-drying cycle for testing under the MIP and NAD tests, we can only estimate the low density CSH and not the high density CSH. With the increase in *w/c* ratio there is an increase in lower density of CSH and reduction in the high density CSH. With evolution of hydration process the capillary pores that exists initially are occupied by free water, but they will be filled by hydrates. The higher *w/c* also dominates the filling of hydrates in the meso-pores, while such a filling is encountered by high density CSH growth with lower *w/c* ratio.

2.5. Spectroscopy studies

Ghosh S.N. *et al.* 1974.

The major clinker phases present in cement pastes were synthesised in 20 grams quantities by

Table 2.4. Absorption peaks from IR analysis in cement paste.

Phase	Adsorption
C_3S	995; 903 s,br; 846 sharp; 798 sh; 692 w; 520 s
β-C_2S	995; 972; 940; 845 s; 815 sh; 690 w; 668 w; 565 s,sh; 520 s; 500 s; 440 m; 360 s
γ- C_2S	950 m; 865 s; 845 sh; 820 s; 787 w; 765 w; 741 s; 707 s; 610 w, br; 580 m; 540 sh; 522 m; 510; 465 m; 411 m; 385 w
C_3A	894 s; 865 s; 845 sh; 820 s; 787 w; 765 w; 741 s; 707 s; 610 w, br; 580 m; 540 sh; 522 m; 510; 465 m 411m; 385 w
C_6AF_2	693 s, br; 605 s; 554 s, br
br - broad; sh - shoulder; s - strong; m-medium; w - weak	

using $CaCO_3$, SiO_2, Al_2O_3 and Fe_2O_3 mixed in stoichiometric proportions and were fired in an electric furnace at appropriate temperatures and the tests were carried in Infrared spectroscopy (IR). γ-C_2S was synthesized by controlled heating for stable β-C_2S. The absorption peaks observed for major phases of cement at different wave number is shown in Table 2.4. C_3S, β-C_2S, γ-C_2S and rarely α^{l}-C_2S belong to the orthosilicate groups. $Ca_3O[SiO_4]$ is the structural formula for C_3S, hence the stretching of Ca-O, stretching and bending of Si-O indicate the C_3S phase that are found in the IR region at different wavenumbers. The relative proportion of Alite and Belite phases occur in the range of 800 - 1000 cm^{-1} are important.

John B. 1977.

The carbon-di-oxide present (CO_2) in the atmosphere reacts with hydrated or hydrating cement compounds in the presence of moisture content, hence higher concentrations of CO_2 the rate of carbonation is also high. This carbonation increases the weight of concrete and causes shrinkage. Raman Spectroscopy (RS) testing method was adopted to find the traces of carbonation present in cement products. Ettringite (ν_1SO_4) peak was observed at 1015 cm^{-1}, after 24 hours a peak at 1090 cm^{-1} of Calcite was observed. Sulphate band at 1015 cm^{-1} which is formed due to ettringite has its intensity diminished to 1010 cm^{-1} i.e. gypsum. This indicates that a larger quantity of ettringite has decomposed to calcite and gypsum due to carbonation, however as the time progress there is no ettringite band i.e. 1015 cm^{-1}. Silica gel like alumina gel did not produce any peaks. RS can be used to monitor the effects of progressive carbonation on the phases of CSH and ettringite in cement compounds as well as white cement.

Ghosh S. N. *et al.* 1980.

A review article stating the applications of IR and RS in cement and concrete was carried. The

various polymorphic forms of C_2S is shown in Table 2.5. For Alite and Belite a strong peak is absorbed at 840 and 838 cm^{-1} which are related to the Si-O bond in the $[SiO_4]^{4-}$ unit. The formation of Portlandite is a resultant of all these phases formed in the region of 500 & 900 cm^{-1}. The IR bands observed in PC are similar to the peaks observed in the regions of 925, 885-895, 520 and 465 cm^{-1} to that of Alite, while the wave numbers of 965-985, 845-850 cm^{-1} of Belite are also observed in PC. The various polymorphic forms of C_3A and there wave numbers were shown in Table 2.6. As the C_3S was hydrated the wave numbers of 700 to 1200 cm^{-1} was not observed. The phases of Plombierite CSH (I), Tobermorite and Techaranite are similar to one another, however they varied in comparison to the similar phases such as xonotlite.

Table 2.5. IR wavenumbers of various forms C_2S phase.

α	*α¹*	β	*γ*
510 , 550, 840, 930, 1000,1150	500, 515, 550, 850,935, 980, 1150	500, 520, 540,845, 870, 890,920, 1000, 1170	440, 455, 495,515, 565,815,855,920,930950, 1150.

The IR and RS phases of the calcium sulphate such as gypsum, Anhydrate and hemihydrate are shown in Table 2.7.Ettringite $Ca_6Al_2(SO_4)_3.32H_2$) which is related to symmetrical stretching of vibrational wavelength $[SiO_4]^{2-}$ and the table showing the wavenumbers of ettringite and sulfate are shown in Table 2.8. Calcium Carbonate peaks at 1413 cm^{-1} caused by C-O stretching, 712 and 873 cm^{-1} along with the minor bands at 1800 and 2510 cm^{-1} due to C-O bending. Portlandite at 3640 cm^{-1} because of O-H stretching, the peaks at 974 cm^{-1} of CSH caused due to $[SiO_4]^{4-}$ stretching vibration. The band at 1111 cm^{-1} due to vibration stretching of $[SiO_4]^{2-}$, sharp peak at 3409 cm^{-1} because of stretching vibration and some weak organic bands at 2850 and 2925 cm^{-1} because of methyl and methylene groups. Peaks of silica are observed at 204, 464, 695, 1158 cm^{-1} intense band at 464 cm^{-1} because of vibration stretching of Si-O vibration of $[SiO_4]^{4-}$ in the quartz, bands at 401 and 806 has shifted by 10 cm^{-1}.

Table 2.6. IR wavenumbers of C_3A in various crystal forms.

C_3A	**Chemical composition**			**700 - 900 cm^{-1}**	**< 700 cm^{-1}**
	CaO	**Al_2O_3**	**Na_2O**		
cubic	60.57	37.4	2.42	894,862,842,816, 804,788,742,710	626,593,525,512, 460, 431, 415.
Orthorhombic	59.04	37.5	3.8	904, 861, 824, 801, 745,716	592, 540, 510,473, 431, 417
Tetragonal	57.52	37.22	4.83	879, 862, 790, 732, 723.	597, 537, 523, 494, 430, 416
Monoclinic	56.3	37.38	5.7	922, 874, 794, 735, 724	609, 598, 537, 522, 492, 432,416

Table 2.7. IR & RS wave numbers of various phases of calcium sulphate.

Gypsum	**IR**	602, 667, 1004, 1120, 1148, 1623, 1638, 3410, 3500, 3555.
	RS	414, 494, 622, 624, 676, 1010, 1114, 1138, 1144.
Hemihydrate	**IR**	602,660, 1008, 1094, 1115, 1155, 1623, 3560,3615
	RS	438, 494, 602, 636, 676, 1018, 1132,1150,1174
Anhydrate	**IR**	593, 612, 675, 1130, 1158
	Raman (soluble)	438, 498, 604, 636, 678, 1020, 1131,1150, 1172
	Raman (Insoluble)	420, 500, 611, 630, 679, 1020, 1116, 1134, 1166

Table 2.8. IR spectra wavenumbers of monsulphate and Ettringite.

Monosulphate	Ettringite
850, 1100, 1170, 1600, 3100-3500, 3540, 3675	855, 1120, 1640,1675, 2190,3420, 3635

Bonenon D. *et al.* 1994.

C_3S polymorphs is due to out-of-plane Si-O bending ν_4, while there was a shift to higher energy for commercial C_3S.The main band of C_2S is due to asymmetric Si-O stretching ν_3. The C_3S has monoclinic polymorph at temperatures of 980-1070 °C, triclinic polymorph at 980 °C-stable, and hexagonal polymorph temperatures exceeding 1070 °C. C_3S polymorphs differ by ionic bond length and coordinate numbers which produces different RS. Low-symmetry triclinic polymorph can be observed by a peak at 541 cm^{-1} and a small shoulder at 714, 798, and broad bands at 925 and 1340 cm^{-1}, which is caused by out of plane asymmetrical bending of SiO_4-ν_4. Synthetic monoclinic phase exhibits three bands and the band at 593 cm^{-1} interferes with the triclinic band and the other two weak bands at 938 and 1361 cm^{-1}.

Ping Yu. *et al.* 1999.

The specimens of Tobermorite-11Å, Tobermorite-14Å, Jennite are prepared while the C/S ratios of 0.41-1.85 and the H_2O concentration decreased with the increasing C/S ratios. The phases of Tobermorite-11Å, Tobermorite-14Å, Jennite are the crystalline phases with C/S ratios of 0.8, 0.9 and 1.4. The C/S ratio of 0.41-1.85, the CSH phases of Tobermorite-11Å, -14

Å and Jennite have a similar structure which are analysed using far, mid and near IR and these tests provide an insight into the OH and H_2O environments. The stretching of Si-O bonds at the wavenumber of 950-1100 cm^{-1} is due to the shift towards the lower wave number which indicate the decreasing polymerisation, and slowly shifts to higher wave number which indicates the increasing of Jennite structural environments. The H atom is bonded to O atom in the crystalline solids, this reduces the OH bond strength there by its vibration frequency. The Jennite has a weak band 3740 cm^{-1}, which is of Si-OH and a broad band at 3140 cm^{-1} this is due to the stretching of OH bond present at the interlayers and surface-absorbed water molecules. The Tobermorite 11Å has two broad bands due to stretching of OH bands similar to the frequency ranges of Jennite.

Stepkowska E.T. *et al.* 2005.

Two PC with different specific surface area and compressive strength i.e. OPC-33 and OPC-43 prepared with a w/c = 0.40 and hydrated for one month. After the hydration, specimens are tested for a period of 1 year and 5-6 years as they were in contact with air. These pastes were tested using static heating and tested using mass spectroscopy. The thermal expansion values of hydrated phases of the specimens was higher than that of the values reported in literature. The Portlandite that contains OH^- are substituted with CO_3^{2-} with ageing and these have twice bigger diameter, which causes an increases in the d(001) spacing, which increases the thermal expansion and reduction in the decomposing temperature. However, for calcite there were some OH^- which are smaller than CO_3^{2-} hence they does not undergo any change in the d(104) spacing, this results in lower temperature of energy for decomposition.

Black L. *et al.* 2006.

The hydration process in C_3A is studied using RS, while the C_3A reactions in the presence and absence of gypsum was monitored. The hydration of C_3A is the fastest among the four major phases of cement and is responsible for flash setting Peaks at 506 cm^{-1} (ν_1 [AlO_4^{5-}]) and 754 cm^{-1} (ν_3 [AlO_4^{5-}]) are observed for pure C_3A polymorph. Upon hydration raman bands are observed at 510 and 825 cm-1, due to the formation of C_4AH_{19}. Hemi-carbo-aluminate and mono-carbo-aluminate are formed due to carbonation, which is formed because of CAH, this was observed because of the characteristic bands ν_1 [CO_3] at 1060 and 1067 cm^{-1}. Hydrogarnet (540 cm^{-1} (ν_1 [AlO_4^{5-}]) is formed from C_4AH_{19} 510 (ν_1[AlO_4^{5-}]) this observed by the disappearance of band.

Ylmen R. *et al.* 2009.

Alite and Belite are crucial in building up the strength in PC, as these two calcium silicate pahses are produced at temperatures of 800 ºC. When the samples are subjected to IR rays the atoms or group molecules existing on the larger molecules absorb different wavelengths of IR lighting depending on the type of that constitute the molecules or group, its geometry and immediate surroundings. The chemical changes taking place in hydrated pastes in monitored using diffuse reflective (DR)-FTIR. At first 30 minutes rapid and slow recrystallization of sulphates was observed. A broad absorption hump that is observed at 970 – 1100 cm^{-1} formed after 60 minutes of hydration is due to polymeric silica.

Li Q. *et al.* 2012.

The effects of elevated temperature from 150°C – 700°C, with concrete samples prepared by substituting 10%, 30% and 50% GGBFS to the weight of cement. The parameters such as mass loss, carbonation depth, E and compressive strength was determined. The mass loss is less than 8% observed at under 700 °C for GGBFS concrete and which is similar to concrete prepared by OPC. The depth of carbonation is higher for concrete prepared from higher concentration of GGBFS, compared to lower concentration of GGBFS. While the depth of carbonation at 300 °C is twice for GGBFS when compared with OPC. A significant reduction of *E* was observed until the temperatures of 300 °C, while the reduction in GGBFS concrete is certain. The *E* decreased with the increase in temperature and also with the increase in GGBFS concentration in OPC concrete.

Kim Y. K. *et al.* 2013.

The mortar specimens are subjected to temperatures of 1000 ºC, and the internal pore structure evolution with respect temperature is monitored using X-ray CT to study the physical changes taking place in the specimen. The studies pertaining to fire induced cracks are scarce due to the limitation in visualizing the internal structure by naked eye, and hence many numerical modelling has emerged with time. Since the pores are hardly connected in cementitious materials, the vapour present at the surface is easy to escape thought the pore existing at the surface rather than the pores at the centre. The macro pores are estimated using X-ray CT because of the limitation in resolution, while these pores are most predominant. The analysis at macro scale was able to capture the physical pores, and the damage caused due to their

evolution, leading to strength reduction. Without the study at micro scale and nanoscales studies the failure has been captured.

Horgnies M. *et al.* 2013.

FTIR is not used as a quantifying tool, the intensity of certain bands such as Portlnaidte, can vary as per the content present in the sample. Since it is not possible to make the relation between intensity or area of the IR bands and specific ratios. The bands such as silica or calcium can be erased or underestimated because of the presence of certain higher intensity in IR bands. The interpretation of the spectra can be disturbed because of the presence of water present in the hydrated sample. The wavenumber of 900-950 cm^{-1} and 883-938 cm^{-1} is double peak, which is due to Si-O asymmetric stretching vibrations that represent the C_3S and C_2S phases.

Piasta J. *et al.* 1984.

Cement paste was subjected to a temperature of 20-800 °C and the transformation taking place in microstructure using FITR. The grains of unhydrated cement at 100 to 400 °C decreases, which is found by the decrease in the intensity of β-Belite and Alite. From IR spectroscopy at 20 °C a maximum wide adsorption band of 980 cm^{-1} is of the silicate phase, while a narrower band at 873 cm^{-1} is due calcite, and with increase in temperatures the silicate phases shifted towards lower wavenumber. An adsorption band appeared at 512 cm^{-1} at 500 °C while the silica bands splits into 3 adsorption bands of 1000, 920 and 847 cm^{-1} at 700 °C and 800 °C. A decrease in the pore percentage ranging from 5-10 nm in regard to pores of 25-75 nm, along with the capillary pores of radii greater than 150 nm. A shift of 980 cm^{-1} towards lower wavenumber is due to depolymerization of SiO_4^{-4} anion caused by the liberation of chemically bound water. New belite bands observed in the region of 500 to 700 °C is due to the changes taking place in the gel structure phases of Belite.

2.6. Mechanical Properties studies

Li M. *et al.* 2004.

This paper discussed the advantages of NSC over HSC at 200 °C, 400 °C, 600 °C, 800 °C and 1000 °C. The heat load was applied in an oil furnace. Compressive tests, split tensile strength and bending tests are conducted on the 3 GOC. The thermal parameters such as specific heat, diffusivity, thermal conductivity, co-efficient of thermal expansion of HSC is similar to NSC. So the larger specimens have shown higher compressive strengths, compared to smaller

samples. Hence the parameters such as temperature, strength grade, water content, specimen size, temperature and elevated speed effects the thermal behaviour of concrete under elevated temperatures. As the specimen size is larger, the loss in strength is less, and larger specimens are need to be investigated under fire. The effect of water content at temperatures of 800 °C is not significant, and the effect of water content at temperatures less than 500 °C needs investigation.

Xia J. *et al.* 2004.

This review article constitutes the research carried form past 20 years in china. The comparison study was carried out on the research analysis initiated in determining the mechanical behaviour of concrete before and after exposing to fire. The effects of fire on the strength, E, and peak strain, μ, yield strength, bond behaviour between concrete and rebar were studied. A difference in the response of HSC and NSC was found, while the relative E of HSC is lower than NSC at certain temperatures. Various cooling cycles has various effects on the mechanical properties of concrete, the samples cooled under water initiates a loss in compressive strength in comparison to sample cured under air. In comparison with concrete, the sensitivity of the rebar is higher. Concrete under extreme temperature has a better performance during the heating, in comparison to after heating. The bond behaviour is effected on the type of rebar between concrete and steel behaviour, while the reduction in bond strength is observed in plain bars when compared to deformed bars. A need to further investigate the performance of HSC and high performance concrete (HPC) in china.

Georgali G. *et al.*, 2005.

The mechanical properties were determined for concrete samples subjected to elevated temperature. The reduction in compressive strength by 70% is an indication that specimens reached 700 °C. The surface of the sample turned to grey, which indicates that temperatures have surpassed 800 °C. As surface temperatures reached 950 - 1000 °C, while the temperatures surrounding the bar reached 800 °C this is used for determining crack density measurement. Gaps formed due to separation of hydrated paste or pulverisation of aggregates is an indication that temperatures reached 1000 °C.

Fabien D. 2012.

The samples were prepared at the following heating cycles duration of 24, 8, 6, 3 hours for

temperatures of 150 °C, 300 °C, 600 °C and 900 °C for a heating rate of 3 °C/min. Increase in the mechanical properties by replacing the GGBS with PC was observed, an inclusion of GGBFS by 50% of PC yielded a compressive strength (residual) similar to initial strengths, however a replacement of 80% replacement of GGBS in PC decreased the 28 days initial strength. Loss in compressive strength at temperatures below 300 °C was observed for all the sample irrespective of the cement mix, which is due the dehydration of CSH. At 450 °C to 550 °C inclusion of GGBFS also limits the rehydration process after cooling due to Portlandite decomposition, which leads to an increase in volume, hence risk of cracking in concrete is avoided. The replacement of GGBFS to PC is found to be a suitable alternative for increasing the durability of the structures exposed to fire.

Arioz O. 2007.

Four kinds of cement mixes were prepared using PC, river aggregate and crushed lime stone of 15 mm and cubes of 70 x 70 x 70 mm^3 were prepared and the samples were exposed to temperatures ranging from 200 °C - 1200 °C at an interval of 200 °C. The weight loss in the concrete prepared by river gravel aggregate is low. A noticeable drop in compressive strength took place after the concrete is subjected to thermal loading. A residual compressive strength

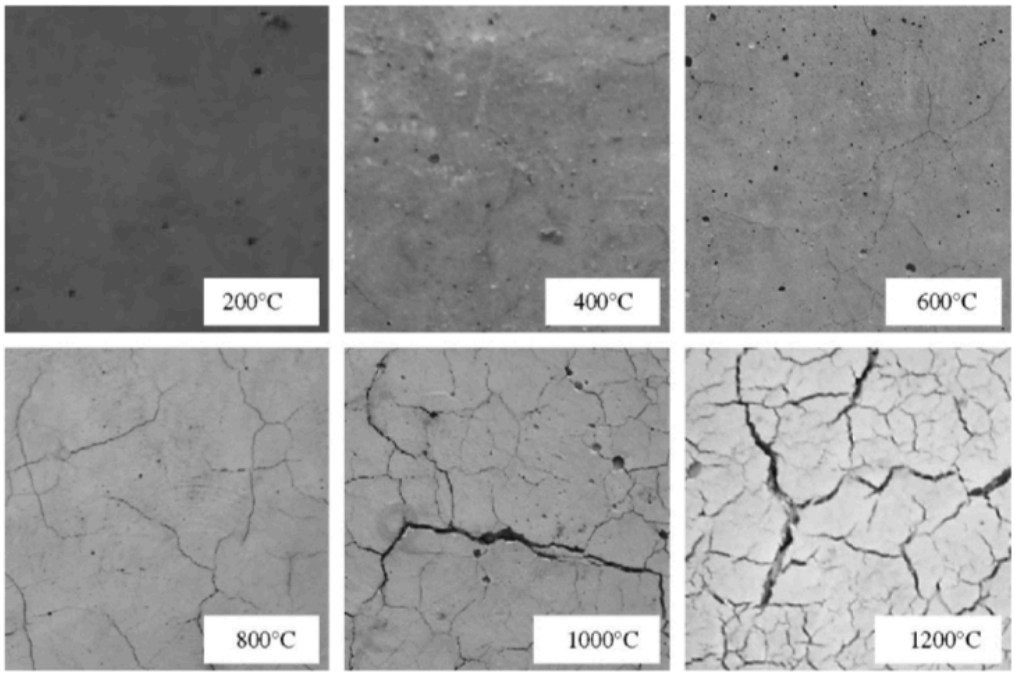

Figure 2.5. Images of concrete surface exposed to different temperature.

of 90% is observed at 600 °C, while the upper limit is 80% and other researchers have got much lesser average values. The expansion of aggregate plays a major role in the reduction of compressive strengths, hence concrete made of lime stone aggregate is prone to less damage than concrete made of siliceous aggregates. At temperatures below 500 °C the type of aggregate effects are negligible. Loss in strength is due to the increase in weight loss. The physical changes in the samples are shown in Figure 2.5. Until the sample losses 10% of its weight the loss in strength is 70%, while the loss is weight is 30% the loss in strength is 90%. The concrete relative strength decreased with increase in temperature and the concrete prepared by river gravel aggregate was severely affected. As concrete is exposed to severe thermal loads during its exposure to fire, the thermal exposure effects the serviceability of the structure.

Hager I. 2013.

The inter alia, aggregate type, concrete composition, w/c ratio, and pozzolana inclusion effects the thermal behaviour. While the rate of heat loading, and it's duration also plays a critical role. As the temperature is increased the water vapour evaporation, dehydration of CSH gel, and decomposition of the calcium hydroxide and calcium carbonate *etc.* takes place along with the Changes in aggregate. The phase changes taking place is dependent on the CaO/ SiO_2, amount of finer particles and the state of temperature and pressure levels present the sample. When the temperatures are above 100 C and the sample C/S ≈ 1.5, in this environment the various forms of calcium silicates are formed, which is porous and week. Temperatures greater than 100 °C, with C/S ≈ 1 a 1.5 to 1 Tobermorite gel is formed and Xonolite and hillebrannite are formed at 180 °C and 200 °C. Due to dehydration the cement paste has a partial damaged structure at 105 °C. Portland decomposed to CaO and H_2O at 500 °C - 550 °C.

2.7. 3D Microstructure studies

Wong R.C.K. *et al.* 2005.

The paper focused on CT as a suitable method for estimating the air contents present in concrete as a suitable NDT method. The NSC (30 Mpa) and HSC (90 Mpa for these samples silica fume was added) samples, were subjected separately to a load of 50% of the estimated compressive strength and the load was released and then the distorted sample was placed under CT scan. The similar plan adopted for both the samples at 85% of the estimated compressive strength value. The analysis of the CT data for NSC and HSC are compared with the undistorted sample. The NSC samples has an air content of 4.2% and while for HSC it was 2.1% estimated using pressure method, form this the statement that HSC concrete has lesser air voids was proven.

Sine HSC uses SF during the preparation, which causes a lesser sizes of pores. The values estimated includes the collapsible air voids in the cement pastes, but not the microspores present in the aggregates. The internal changes in microstructure of NSC are very different in comparison to HSC, in NSC the air voids merged and also increased in size, were as there was not a significant increase in air voids of HSC.

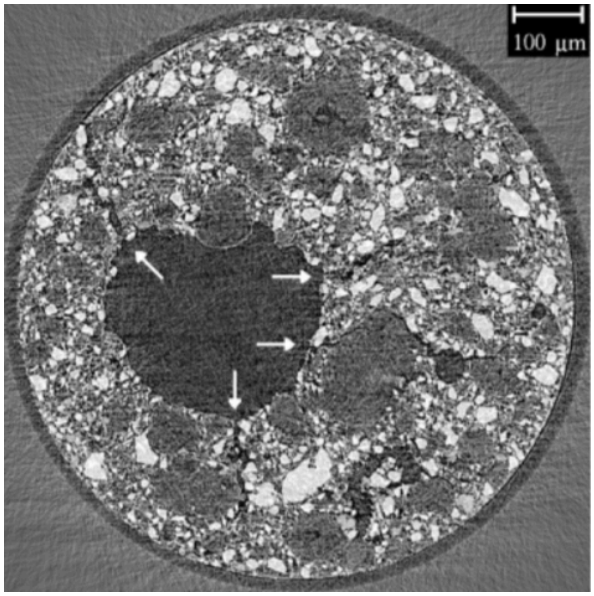

Figure 2.6. Cross section of a sample with w/c of 0.36 at 31.5 hours of hydration.

Helfen L. *et al.* 2005.

The samples were prepared using CEM I 42.5R-HS which is a rapid hardening cement denoted by 'R' that produces early strength while it offers higher resistance to sulphate attack, this is achieved by lower concentration of C_3A i.e. ≤ 5% which is denoted by 'HS'. The hydration period of samples varied from 4 - 8 hours, for samples of w/c of ≈ 0.30 the data was obtained after 4 hours while for w/c ≈ 0.5 it is 8 hours. The evolution of hydrated PC for two samples at w/c of 0.97 and 0.41 while the micro crack formation for lower concentrations of w/c of 0.36

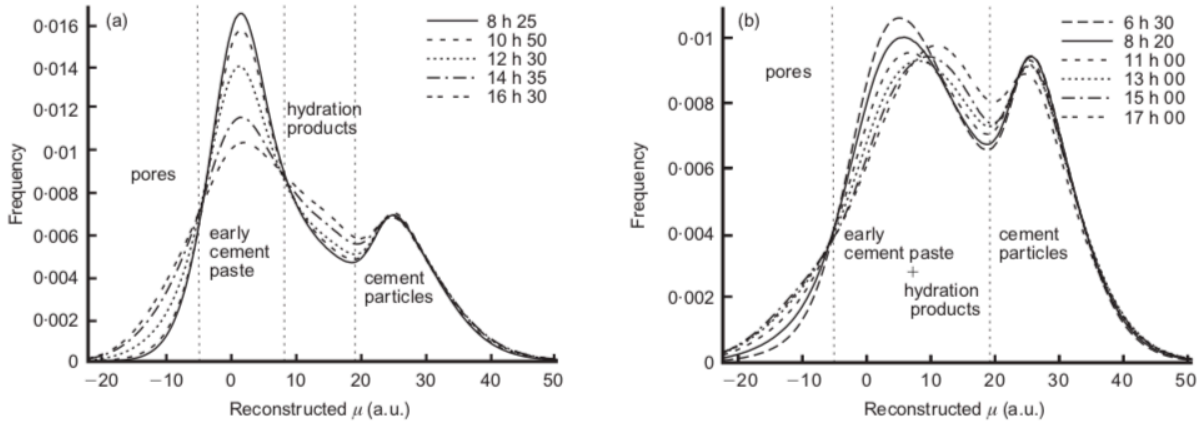

Figure 2.7. 3D histograms of the images at various stages of hydration at w/c of 0.97, sample with w/c of 0.41(left) and 0.35 bin sizes (right).

were also presented, as shown in Figure 2.6. The changes in the hydrated cement pastes at different time frames of different w/c ratio is shown in Figure 2.7. and their growth in the gray scale can also be observed. The gray colour images obtained can be used to obtain the phases depending upon the intensity of the gray colour. A decrease in volume fraction of pores at early stages of hydration and rich-hydration product was determined and the quantification micro porosity was possible. The images revealed that higher amounts of pore connectivity at micro meter scale with the progress of hydration, and it is more severe in the case of water-rich cement pastes. Using X-ray CT the percolation pore structure can also be captured and measured in 3D if provided higher image resolution was possible.

Lu S. *et al.* 2006.

Four different types of concrete mixtures were analysed using X-ray micro tomography with a spatial resolution of 1 and 4 μm. The visualisation of pore system is characterised in terms of connectivity and size distribution. The 3D constructed micro tomography images showing the

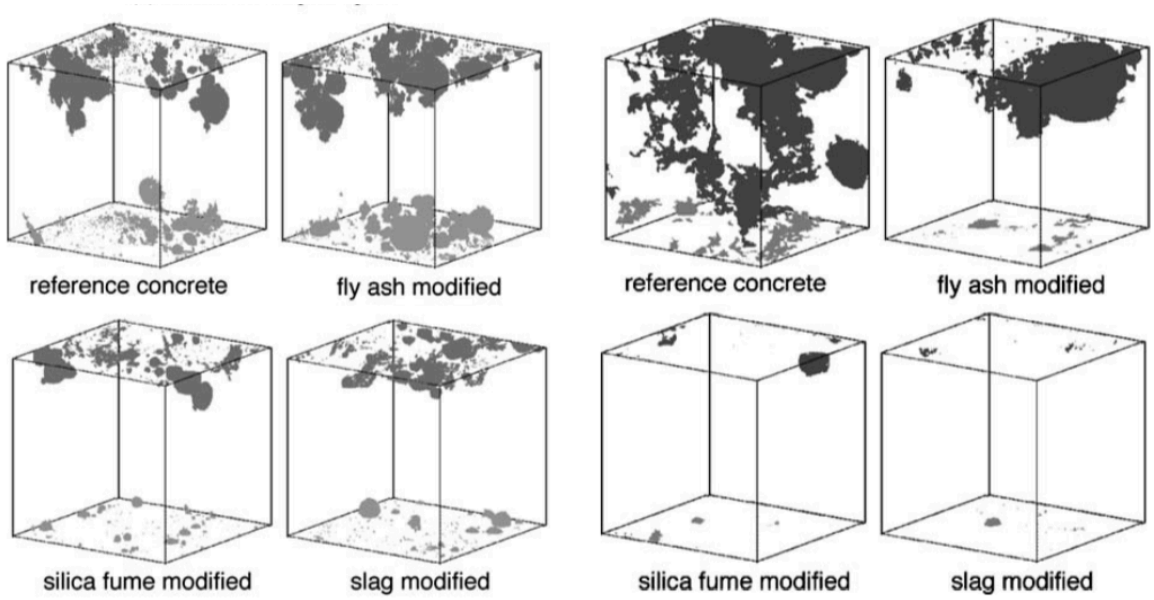

Figure 2.8. connected pores spaces observed in the specimens using micro tomography at a resolution of 4 μm (right) and 1 μm (left).

pore connectivity at 1 μm and 4 μm, shown in Figure 2.8. From the scans it was observed that no pore connectivity exists at a pore diameter of 1 μm. Since there was no pore connectivity, disconnected pore distance was measured. Disconnected pore distance is the minimum distance between the connected pore network at the top and bottom of the sample. However, with the limited image scale resolution, no crucial values were reported regarding the disconnected pore distance. With the limited study it was observed that the admixtures have led to increase in the disconnected pore distance, and a reduction in chloride permeability was observed.

Gallucci E. *et al.* 2007.

The cement paste samples are prepared with CEM I 42.5 PC (OPC) and with a *w/c* = 0.5, the paste is injected with a syringe in to a glass tube of diameter 600 µm. The samples hydration was monitored for 1, 3, 7, 14, 28 and 60 days and different samples were analysed using the X-ray CT images which is due to the limitation X-ray CT availability, and the obtained 2D images are built into 3D and the changes taking place in the hydration were estimated qualitatively and morphologically. As a single sample was not analysed in X-ray CT there were problems in problems corresponding to homogeneity of the samples as different samples were scanned. From this analysis the reduction in the concentration of unreacted cement content and the size of the particles was bee estimated. The pore network both geometrical and morphological parameters that actually exists and how they evolve with the hydration time can be captured. The second advantage being the addition of third dimension in analysing the connectivity.

Valentini L. *et al.* 2011.

The samples are prepared by using CEM I 52.5 OPC cements and the *w/c* of 0.5 and the second sample was prepared by using superplasticiser of 2% weight of cement and a w/c of 0.37. The hydration periods for the samples with superplasticizer are 8 and 58 hours, while the samples without admixture are of 9 and 58 hours. Quantitatively measuring the microstructure is fundamental to assess the durability and performance of the end product. Obtaining the microstructure without hindering the internal structure is of at most importance. By adopting this approach, the estimation of Ettringite volume fraction locally in hydrating cement paste and 3D map was constructed. From this study how the addition of superplasticizer reduces the rate of hydration is shown and also assuming the effects of error due to poor time resolution is negligible. However, despite of all the limitation mentioned in the study the X-ray CT method is still advanced method in assessing the microstructural changes which take place in CBM.

Artioli G. *et al.* 2010.

XRD micro tomography (XRD-CT) technique for the hydrating cement pastes for monitoring the microstructure evolution and formation of phases in 3D is a non-invasive image approach. Comparison of gray scale during the hydration of cement paste at different time periods was monitored. While the grayscale histogram has shown an increase in the Ettringite concentration for the time period of 9 hours and 58 hours and this was also in good agreement with XRD analysis using Rietveld analysis. The CEM I 52.5 GOC is mixed with a *w/c* = 0.50 and the pastes was poured in to 500 µm capillary glass tube. The XRD –CT method can be applied for

3D investigation of cement pastes, and the major advantage being the capacity to assess the distribution of amorphous phases. The evolution of Ettringite in hydrated cement pastes and mortar samples was possible. By increasing the beam size, larger crystals can be captured but that will compromise the spatial resolution. The size of the peaks decreased with the progress of time which is related to unreacted cements, while the increase in peaks indicated the increase in hydrated products. The peaks generated by porosity have a lower range of grey value and this overlaps with the hydration products grey level.

Han J. *et al.* 2012.

The changes in the volume of microstructure characteristics and defects in mesoscale of cement pastes before and after carbonation, are investigation was carried in a 3D scale. The carbonation reaction which include the changes of micro structure in hardened cement pastes using 3D X-ray CT. Micro cracks were observed at the interior portion of the specimens prepared by carbonation with *w/c* = 0.53, while many micro cracks were observed on specimen's surface. This is due the shrinkage of CSH and stresses generated due to the shrinkage of CSH, is greater than the tensile strength, which is the reason for the propagation of micro cracks from the external to the internal portions of the cement pastes for samples prepared at *w/c* of 0.53. The grey scale values that represent the density, and they also increased with the increase in *w/c* ratio. a clear increase in the grey value of the samples at the external surface due to the carbonation was observed for samples of *w/c* = 0.53. The reason for such increase in the density, is the generation of calcite is greater than the combined concentration of Portlandite and CSH. While no changes were observed in the samples prepared by w/c of 0.35 and 0.23 after the carbonate reactions.

Kim K. Y. *et al.* 2012.

The air voids are spread spatially across the CBM, influence's the mechanical response when subjected to thermal and mechanical loading. The accurate estimation of spacing factor in material is crucial for evaluating the freeze-thaw durability. For assessing the frost-susceptibility of CBM there is need for understanding the air void parameters such as air content and spacing factor. The air entrained admixtures (AEA) were used to distribute air voids in matrix, however such a method of analysing is still the old way and confined to 2D analysis. Three sample types are prepared consisting a single sample of non-AEA and two samples of AEA. CT method is very beneficial for visualizing the internal structure that is very hard to quantify in engineering applications. The in practise method for determining the spacing factor is truly a 3D measure, while it was used for 2D. From the current study it was observed that the line traverse method over estimates the spacing factor, in comparison to values obtained by

statistical spacing of paste-voids. The limitation of CT imaging is the specimen size, since the void size used for estimating spacing factor is less than 100 μm, however the characterisation technique by using CT images is found promising.

John L. P. *et al.* 2012.

For commercial applications of alkali activated binders durability is an important aspect, and to achieve this the microstructure and pore network plays an engaging role. Micro tomography test were conducted on specimens of sodium meta-silicate activated with fly ash/slag blends. The 2D images are aligned in to 3D for separating the pore and solid regions then the tortuosity of pores is estimated using random walker method. The specimens prepared by alkali activated binders, and the evolution of microstructure and pore network was analysed for the first 45 days of curing. The samples are prepared by alkali silicate activation of FA, and GGBFS, while the blends were made of 100% of GGBFS, 100% FA 75% of GGBFS, 25% FA and GGBFS, 50% FA and GGBFS, 25% GGBFS and 75% FA while the water binder ratio was 0.40 and the specimens of 1mm in size were analysed. The impact of curing time and the effects of various binder composition has an effect on the pore network and microstructure, in the process of hydration and hardening. The tortuosity of pore network, and decrease in porosity were mainly effected by longer curing time and high slag content, while this is much effective in at 50% higher slag contents. Which is an indication C-A-S-H space gel dominate the alkali activated binder at slag content of 25% and 50%, while the samples that contains slags of 25% or less the N-A-S-(H) are dominating, this formation does not bind the chemically bound water hence the pore network extent is not severe.

Kim K. Y. *et al.* 2012.

3D representation of air void parameters was carried out using X-ray micro tomography on three specimens that has different air void systems. Sensitivity analysis was performed of the sample on the number of traverse lines for a single section and number of sampling sections across the height of specimen considered. Convergence was rapid for a single section with the increase in number of traverse lines, with the limitations of unacceptable variations across multiple sections. The analysis on the CT images indicate that this method is suitable to capture the variations in the air-void parameters formed due to the variations of the AEA. The advantages of using this are (a) no pre-treatment of the specimens (b) the representativeness of the specimens can be increased by optimising the sample effects (c) useful in quantifying the heterogeneity of distribution in air-voids. The limitations of the study are regarding the size of

the samples since the samples with aggregates cannot be scanned and special care is to be taken for accommodating the aggregate to represent the volume of the aggregate present in the concrete sample.

Kim K. Y. *et al.* 2013.

The mortar specimens are subjected to temperatures of 1000 ºC, and the internal pore structure evolution with respect temperature is monitored using X-ray CT. The studies pertaining to fire induced cracks are scarce due to the limitation in visualizing the internal structure by naked eye, and hence many numerical modelling has emerged with time. The increase in temperature effects the water present in the inter pore and intra pores starts to evaporate, and the vapour tries to escape, with the increasing temperatures these effects are very adverse. Since the pores are hardly connected in cementitious materials, the vapour present at the surface is easy to escape thought the pore existing at the surface rather than the pores at the centre. The macro pores are estimated using X-ray CT because of the limitation in resolution, while these pores are most predominant. The analysis at macro scale was able to capture the physical pores, and the damage caused due to their evolution, leading to strength reduction. Without the study at micro scale and nano scales studies the failure was been captured.

Wan k. *et al.* 2014.

Local porosity distribution in cement pastes were determined in terms of frequency and spatial using dual CT scanning method for the 3 specimens prepared by 3 different *w/c* ratios. The porosity of the samples is also determined using MIP, and gravimetric method, and compared to the CT method. The dual CT scanning method overcomes the limitation of, not depending on the spatial resolution, and the determination of 3D porosity which is not possible by traditional analytical methods, while it is also a NDT method and it can also be applied to cement pastes, mortar and concrete as well. The variation in the heterogeneity was observed using probability method for all the 3 *w/c* ratios. The porosity map of the RVE size has decreased with w/c ratio and later increased with the w/c ratio. The probable local porosity is estimated on different pore sizes, and was observed that heterogeneity of the RVE size or probe size increases the degree of hydration or *w/c* ratio. CT method used to estimate the porosity distribution and average porosities are consistent with gravimetric results, and they are larger when related to MIP results.

Michael H. *et al.* 2014.

The effects of heating and re-curing on the microstructure of cement pastes is analysed using X-ray CT. The re-curing had significant recovery effects on the pores at microstructure by reducing the inter connection between the pore space and the recovery happening in the sample at 7 days of water curing. Heating has caused cracks at the interface of mortar-aggregate, while bridging cracks were formed between aggregate and voids. There is 1.5 times increase in total pore volume, and this increased the connectivity of the void space by 3.5 times. This phenomenon is due to the cracks occurred because the process of heating has joined the isolated pores there by reducing the pore space relative to the pore-heating process. The rate of pore connectivity in the re-cured samples after 28 days of re-curing has shown higher connectivity, while the pore volume remained the same. No significant changes in the microstructure took place due to the recurring in air, however there is a noticeable increase in the mean pore size was observed due to the air voids formed at the surface.

Anton D. P. *et al.* 2014.

A single specimen is scanned for a resolution ranging from 5 µm, 10 µm, 20 µm, 40 µm, 60 µm, 80 µm,100 µm and varying scan time for a scan duration of 1 hour and 5 min. The image segmentation is carried by 2D and 3D analysis for estimating the voids area, void volume porosity, and volumetric porosity analysis. It was observed that the voids of smaller size are still present in the sample, since the voids sizes are very much dependent on the resolution. The detection of voids is dependent on the resolution, higher the resolution and smaller will be the detectable voids. Shorter scan period (5 min) is also helpful in extracting crucial data in terms of porosity, when comparing to higher scan periods. When large number of samples are present, and are to be compared to one another the fast scan is good enough to produce crucial data. For scanning under a smaller resolution, the smaller voids can be detected, however the larger voids became much larger for such a smaller field of view.

Parisatto M. *et al.* 2015.

The evolution of hydration taking place in Portland cement binder using X-ray CT as a non-invasive technique. The imaging process such as 2D and 3D image analysis of an undisturbed hydrated samples at the hydration of periods of ~ 1.5 hours to 3 days. Using this analysis, the evolution taking place during the early stages of hydration, porosity and unreacted clinker that is present in the sample was monitored successfully by comparing the 2D slices and the 3D volume of the samples. The CSH development at the expense of the pores and grains of

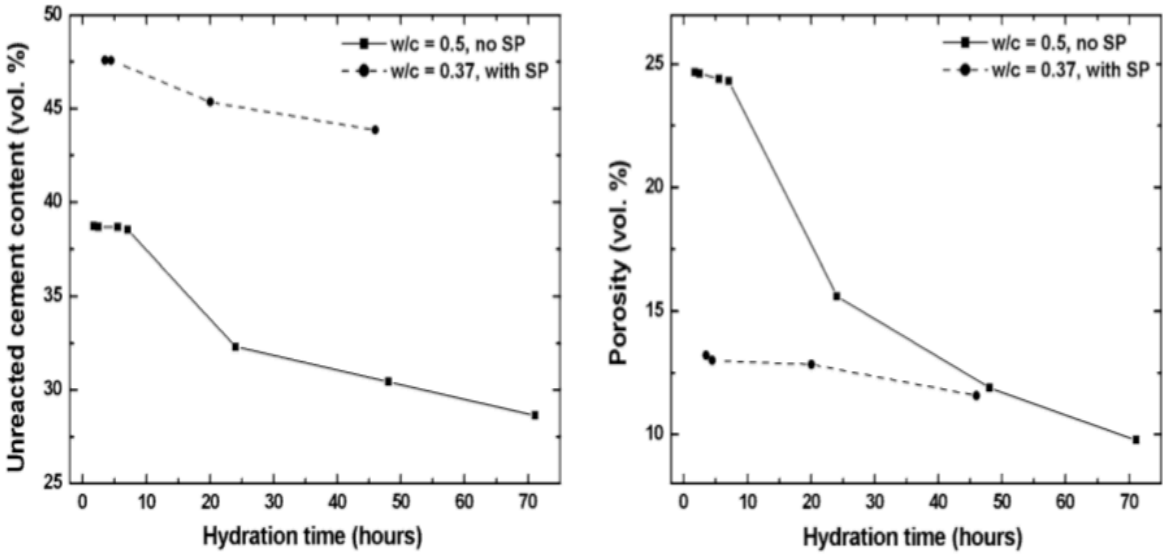

Figure 2.9. Evolution of the unreacted clinker (left) and porosity (right) volume fraction of the samples with and without admixtures at different stages of hydration.

anhydrous clinker was captured by comparing the 2D slices and 3D data sets at different stages of hydration which was helpful in analysing the in-situ evolution of microstructure. The estimation of porosity and the unreacted clinker was quantified. The figure showing the variations in the volume fraction of unreacted cement clinker and porosity at different stages of hydration is shown in Figure 2.8.

Elen E. B. *et al.* 2015.

In order to achieve better spatial resolution for conducting the studies on the microstructure of pores present in matrix of PC, there is a need for the researchers to used samples of smaller size specimens. So the selection of an appropriate sample specimen is required, and this sample performance can be related to the entire volume. This article focuses on selecting various region of interest (ROI) in the specimen of size 20 mm x 40 mm, and the variations in the porosity was analysed using X-ray micro tomography. The porosity obtained from micro tomography was also compared with the helium and mercury pycnometer. The porosity estimated at different ROI is the same for the specimen at 7 days of hydration, while the specimens porosity is more at the outer layers for a hydration period of 28 days. Micro tomography and pycnometer are capable of yielding the results, however the sample preparation techniques should be reassessed for drying the material.

Bronislava M. *et al.* 2015.

The sizes of pores, and their distribution not only effects the porosity, they also predict the outcomes of physical and mechanical properties together. The air entrainment presents in traditional concrete and air

entrained concrete is not adoptive, as the entrainment in concrete is not always helpful, and air content beyond 2% increases is useful in resisting to water and chemical thawing. The pores are categorised as shown in Figure 2.9. were the pores of less than1.25 nm are micro-pores, while 1.25 nm to 25 nm are meso-pores, greater than 25 nm to 5000 nm macro-pores and pores between 5000 nm to 50000 nm are large pores. The air content and micro-pore air content is determined in fresh concrete using pressure method and air void analyser while the average pore diameter and specific surface of air voids is estimated using microscopic analysis and CT methods.

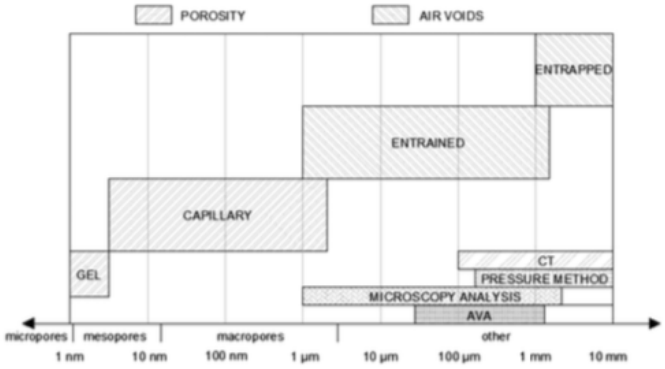

Figure 1: Example of pore size in concrete
Slika 1: Primer velikosti por v betonu

Figure 2.10. Categorisation of various pores in concrete at different scales.

This paper focused on determination of porosity on the surface of concrete to a depth of 40-60 mm obtained from the specimens, as this effects the durability of the whole structure. Variation in the results can be observed due to limitations in the detection capabilities of pore sizes using each approach, and the sizes used for each method. The CT method uses the concept of image reconstruction and the parameters of stereoscopic microscope can be detected. The obtained pore values are not in sync with the other test methods because of the limitation in the detection capabilities. For the test methods such as stereoscopic microscope and CT scan variation in the pore results were observed due to the difference in automatic and manual detection. AVA and stereoscopic microscope method used for detection air voids in aerated concrete, both the methods have under predicted the values. The CT method has better detection capabilities to estimate the air-pore content, provided a suitable interpretation algorithm is applied for filtering the detected voids from the scan. While detecting the pore characteristics of concrete it is better to initially decide what type and size of pores are being detected and then to choose a suitable technique.

Libor S. *et al.* 2015.

This study aimed at monitoring the changes taking place in concrete internal structure of varying composition before and after subjecting the samples to different thermal loads. Eight samples of different PC and aggregates were exposed to temperatures of 600 ºC and 900 ºC, and these samples were scanned

before subjecting them to these temperatures. Variation in the damage behaviour exists in the samples prepared with different mix proportions. Basalt aggregate was used for preparing the samples, as this aggregate has higher résistance to elevated temperatures, and artificial light weight aggregate was also used which is produced from the expanded clay and this aggregate is thermally stable to the temperatures

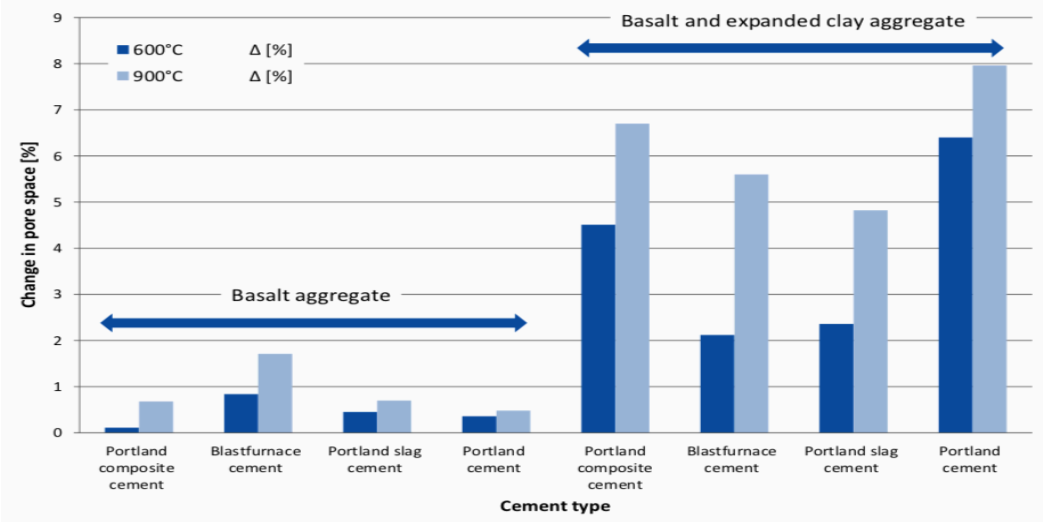

Figure 2.11. Change in pore spaces of different concrete samples prepared by basalt aggregate and light weight aggregates at 600 ºC and 900 ºC.

of 1050 ºC. The changes in pores space of the different samples were shown in Figure 2.11. The type of cement and aggregate has an effect on the thermal behaviour of the member, as it affects the resistance of concrete. The radial cracks produced in concrete of the samples prepared from blast furnace and Portland slag cement and separation of cracks were found across the aggregate grains with the samples prepared by PC and Portland composite cement with lime stone. The severity of the samples effected by 900 ºC is more compared to 600 ºC. Higher content of water in the aggregates of expanded clay in the preparation of concrete, which has caused the penetration of water in to the matrix at elevated temperatures and this has effected the integrity of the matrix. The micro X-ray CT has shown promising results and also the visualisation of the crack pattern inside the concrete at elevated temperatures. This method of analysis has provided the researchers, an insight into the failure mechanism of different samples exposed to extreme temperatures.

Rivera O.G. *et al.* 2016.

Hierarchical approach was adopted for designing a material that should be a thermally stable material by using materials such as alkali activated slag, FA and metakaolin, while the prepared specimen's values were compared with PC mixtures and monitored using CT. The study carried on 3 different alkali activated mortars in comparison to 2 different OPC mixes. The samples prepared by FA mortar mix has the superior behaviour at 650 ºC, when compared to other samples. The three alkali activated mortars had superior quality in dissipating heat, while the samples of FA has shown the dissipation of heat until 565 ºC in the

50 mm samples without any signs of thermal cracking. The pore size distribution has helped the FA samples to show a better behaviour to extreme temperatures. The test data of CT revealed that the initial porosity of alkali activated FA mortar samples has the least porosity in comparison to OPC and the pores of diameter 20 μm - 50 μm has 66% of the porosity.

Liu Z. et. al. 2016.

The research article focused on monitoring the water migration in unsaturated in situ pastes. The adsorption values obtained from the X-ray CT scan are compared with the gravimetric method and MIP methods. Two samples one with 0% and the other with 10% of slag to the weight of cement were prepared, with a *w/c* = 0.35. The water uptake process has a rapid growth at initial time, and slows down over a period of time and finally it gets stable. While the reduction in the concentration of slag in the cement paste, percolation of water accelerated. CT method is helpful in not only quantifying the penetrated water evolution, however it can also predict the changes taking place in the mass of capillary water adsorption. A non-linear relation exists between the depth and adsorption of water with square root of time. The MIP results predict an average diameter of pores as 26.8 nm and 16.9 nm assuming the pores are cylindrical and open ended for slag inclusion of 0% and 10% to the weight of cement samples.

Anton du Plessi. 2016.

The application of industrial X-ray CT is an emerging area of science in understanding the samples internal structure, with sample sizes varying from 1mm – 300 mm of diameter. The industrial CT have higher resolution capabilities in comparison to medical CT. Four objects used in the industry i.e. steel turbine, titanium casting, cylindrical concrete cube, and concrete block reinforced with metal fibers. The medical CT scan whose scan time is 5 to 10 seconds per object, while the industrial CT scan time for object varied from 1 to 2 hours. The medical CT is capable of producing useful data with a lesser scan time periods mainly for large number of samples were the resolution is moderate, and the major advantage being the capability to scan larger objects when compared to industrial CT scans. While the data sets produced are small and easy to process for obtaining crucial data using medical CT. The limitation of the sample size used in industrial CT, and for these smaller samples and low density these can produce better quality images than medical CT. Larger samples can be scanned using medical CT and with the limitation of moderate image resolution. The medical CT data is not good enough for industrial testing, but can be crucial for analysing larger critical components that cannot be tested under industrial CT.

Su Y. M. *et al.* 2016.

Concretes damage was evaluated due to fire using NDT methods such as acoustic emission and CT methods. The concrete cylinders which are moist cured for 20 days were subjected to temperatures of 400 ºC and 600 ºC for 1 hour in a furnace. The cylindrical samples are prepared with a *w/c* = 0.45,

superplasticizer and AEA for improving workability and not effecting the properties of hardened concrete. Through visual inspection it was inferred that concrete cylinders of siliceous aggregates at 400 ºC, part of the aggregate has turned to pink colour, while cement pastes completely changed their colours at 600 ºC. Surface cracks were not predominant at cross section and length of the cylinder at 400 ºC, however they very well spread at 600 ºC and effected the concrete. From CT scan data the sample at 400 ºC there was not a significant change in voids while at 600 ºC the voids were well spread, and most of the voids also healed due to recurring and in most of the segments up 2% of the voids were healed. The moisture curing had good effect in curing the samples subjected to temperatures of 600 ºC compared to curing by air. At 400 ºC the increase in the voids sizes is lesser compared to 600 ºC, and the air curing did not help in re-curing the voids. The visual inspection of the CT images is not possible and the visual inspection could not find most of the changes because of the smaller size of voids, and higher is the number of slices obtained from the scan.

Michael Henry. *et al.* 2016.

The physical changes taking place in the cement pastes subjected to a temperature of 600 ºC and re-cured, by doing so the rehydration mechanism taking place in the fire damaged cement paste was monitored using CT scan studies were carried, the CT scan revels that temperatures cause the cracks to propagate in the radial and vertical direction of the cement paste. The recurring of the cement paste samples displayed a connectivity in the pore network, this can be attributed towards the rehydration of CaO and Portlandite. A variation in the chemical analysis of hydrated and rehydrated cements was observed this can be due to the C_2S phase which a play a significant role in CSH gel formation during the initial stages of water re curing of the sample. The CT scan analysis was able to capture the interconnection of the crack in the sample. The heating caused cracks in the specimen which are formed due to the shrinkage of the hydrated and un hydrated products. The supply of water caused the growth in the crack spaces in the form of connectivity of network, and this happened at 28 days of re-curing.

Eva Lubloy. *et al.* 2017.

Fire damaged concrete was assessed using CT, and to understand the capabilities of CT technique possess, two case studies were conducted (a) sample collected from the tunnel and exposed to fire (b) fire test on a scale of 1:1 reinforce concrete building. The concrete cylindrical sample was collected from the tunnel and it fire loaded using hydrocarbon fire in a horizontal furnace for a period of 2 hours to temperatures of ~ 1100 ºC. CT study is a suitable study for understanding the buildings damaged due to fire, because the fire loads causes change in porosity and reduction in weight, and these changes can be monitored using CT. Calibration of measurements were carried for validating the methodology, for estimating the changes pertaining to porosity, and density in the concrete samples subjected to fire. The cement matrix, aggregates, and air inclusions were removed,

while the porosity increased and the pores of smaller sizes has also evolved. The increase in the porosity and production of smaller pores sizes caused the reduction in material density. The CT scan method was able to identify the damage caused by concrete due to fire loads at temperatures beyond 500 ºC. Hence the 500 ºC is very crucial for structures, and after these temperatures the stability of concrete is lost.

Koodallor P. *et al.* 2017.

The microstructure deterioration in cement pastes under acid environment are analysed using micro tomography. The cement paste specimens of 10 x 10 x 60 mm^3 were cast and the specimens are placed in an accelerated static based leaching test with a periodic abrasion action while the cement paste *w/c* = 0.40. The micro tomography tests was helpful for understanding the kinetic degradation due to acid attack was analysed quantitatively and qualitatively. The depth of alteration and brevity of the damage depends on the acids type and concertation. A protective layer of gypsum with silica-alumina gel was formed when the specimen was subjected to acid attack of sulfur for the concentration of 1%, because of this protective layer the alteration depth is of 437 μm which is the least among other acid attack. As lesser depth of penetration was observed 86.16% of the final area was decalcified. In the acid environment of hydrochloric and acetic acid the leaching effect is prominent and the final reaming area was 62.78% and 6.5%. The citric acid effect is more severe and a rapid loss of the outer layer, and mass was lost, even though the depth of alteration is less than 499 μm a thickness of 78.43% was lost.

Lu H. *et al.* 2018.

The potential of X-ray CT to estimate the entrained air void parameters in concrete is studied. A series of 6mm diameter cores are obtained from 100 mm diameter cylinders from a payment, by doing so the samples collected, represent the air contents present in the system, and these samples are scanned under as resolution of 7.5 μm/pixel. A step by step approach is proposed to for eliminating the difficulties involved in thresholding the voids (i.e. voids formed due to air and in aggregate) and solid, the separation of bubbles closer to each other. Using the 3D reconstruction of X-ray CT images, the air content and specify surface was estimated and by using this data the powers spacing factor was estimated. The representative of the sample with the volume of concrete was also assessed. This method is suitable in determining the spacing factor and specific surface, however due to the limitation of the sample size this method is not suitable for determination of air content present in the bulk of the sample. The air voids will have a spherical solidity closer to '1' while voids in aggregate it is closer to '0'. The voids that are clustered is often caused by the resolution of X-ray CT scan and the method to separate the clustered voids was also presented and the spherical solidity of the voids is shown in Figure 2.12. The minimum diameter of voids that can be

estimated are in the range of 20 µm - 40 µm, due to which the comparison of air voids estimated by other methods might be of smaller size.

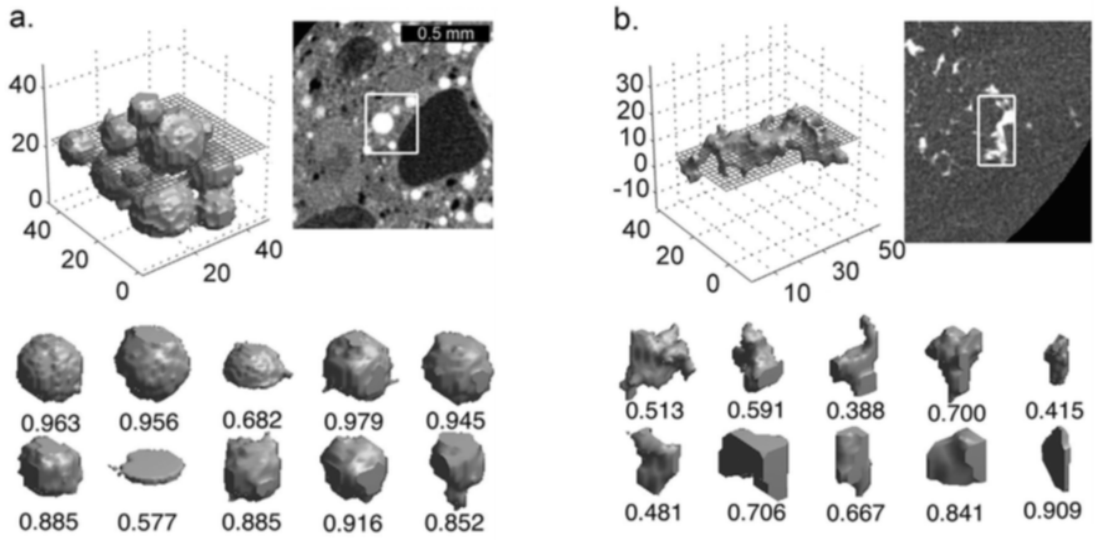

Figure 2.12. Coalesced voids and there solidity values after separating using watershed (a) Entrained air voids (b) voids in aggregate.

2.8. Summary of literature review

Literature relating to the thermal studies on concrete, mortar and cement samples has been investigated and organized on the basis of analysis techniques. Several studies involving usage of XRD, FTIR, FTRS, Mass spectroscopy, Optical microscopy, SEM, TGA, DTA, DSC, MIP etc. testing facility have been conducted to understand the overall response of the concrete material in general. However, all these studies are limited to 2D studies and smaller sized samples. The recent studies have shown the importance of understanding the 3D structures of the material, using computer tomography. In the current literature the application of computer tomography in the studies related to thermal behaviour is lacking, along with observed as mentioned below:

- Effects of particle size distribution and variations in chemical compositions on the thermal behaviour of PC have not been studied.
- Variations in the elemental concentrations of Carbon, Hydrogen, Nitrogen, and Oxygen concentrations due to elevated temperatures have not been studied.
- Variations in the chemical concentrations and their effects on the absorbance spectrum of FTIR and FTRS spectrum have not been studied.
- Evolution of Pores, Pore network, Pore connectivity, Porosity due to the effects of thermal loads in the samples of dimensions greater than 20 mm have not been studied.

- Evolution of internal pore structure and their distribution across the sample with an increase in the thermal loads.
- The existence of interconnectivity and inaccessible pores present in the sample needs to be found.
- Effects of thermal loads on the internal structure of the hydrated cement samples need to be captured using computer tomography.
- The maximum diameter of pore estimated using traditional methods is not greater than 0.83 ± 0.17 mm since the sample dimensions analysed are smaller, however the largest diameter of pores which can exist in a sample needs to be found.

Addressing these gaps would be useful in understanding the thermal behaviour of concrete, and a step towards making concrete a better performing material under thermal loads.

Chapter-3

Characterization of Portland cement at different stages of hydration

Chapter-3

Characterization of Portland cement at different stages of hydration

3.1. General

The material properties and characteristics of a heterogeneous material like PC, are primarily governed by Particle size distribution (PSD), and the elemental concentrations, chemical oxides, phase composition and their proportions existing in the ordinary cement (OC). Four major oxides *i.e. CaO*, SiO_2, Al_2O_3, Fe_2O_3 and minor oxides *MgO, Na_2O, K_2O, SiO_2 etc.* are commonly used in PC. In order to quantify the major phases present in PC, from the chemical oxide concentrations obtained from XRF analysis, Bogue has developed an equation, according to which, the range of C_3S is around 60-65% and C_3A + C_4AF is 20% (Herfort D. *et al.* 2010). Tricalcium silicate ($3CaO.SiO_2$: C_3S) *i.e.* Alite is a synthesized product primarily responsible for the early strength, however a pure form of this mineral is not available, because of its impurities such as Fe, Al, Mg, Cr and Zn elements. The secondary constituent next to C_3S is Dicalcium silicate ($2CaO.SiO_2$: C_2S) *i.e.* Belite has polymorphs such as β-C_2S, α-C_2S, γ-C_2S *etc.* and in the impure form the Ca is replaced by Na, Al, Mg, K, Cr, and Mn. The Aluminate forms present in cement are Tri-calcium aluminate ($3CaO.Al_2O_3$: C_3A) *i.e.* Cellite and Tetra Calcium Aluminate Ferrite ($4CAO.Al_2O_3.Fe_2O_3$: C_4AF) *i.e.* Ferrite (Taylor H. F., 1997).

Before understanding the mechanical properties of PC, which are governed by PSD, the quantities of the major oxides, minor oxides are to be determined and analyzed. Three PC, which are PPC (IS 1489-1 (BIS, 1991)), OPC-43 (*IS* 8112 (BIS, 2013)) and OPC-53 (*IS* 12269 (BIS, 2013) are typically used across India. Among the three grades of cement (GoC) *PPC* has the least compressive strength (33 *MPa*) while OPC-53 has the highest compressive strength;

compressive strength of PPC is improved over time due to the presence of higher fly ash (15-35%) and calcined clay content. The significant advantages of *PPC* in comparison with *OPC* are lower heat of hydration, improved workability, reduction in segregation and bleeding, improvement in water tightness, better resistance to sulfates, chlorides and alkali-aggregate reaction. The pozzolanic material presence in cement reacts with gypsum ($Ca(OH)_2$) which produces cement compounds, thereby making the cement compounds denser and impermeable when compared to the other *OPC* (Taylor H. F. 1997). Because of all the advantages the PPC poses and the increase in production of electricity from thermal power plants, which produce a lot of fly ash, it has replaced *OPC*-33 cement used in the country.

In this work, *PPC, OPC*-43, and *OPC-53* bags are produced from the suppliers, and physical and chemical analysis are conducted to understand the variations among these PC. For understanding the variations in distribution particles size of PC, particle size distribution (PSD) analysis is conducted using the Laser Diffraction Spectroscopy (LDS) technique. For determining the chemical compositions of the PC, techniques such as XRF, XRD are used, while Spectroscopy studies using FTIR and FTRS are conducted for determining the chemical bond behavior of constituents present in cement. The above tests are performed to characterize the behavior of PPC, OPC-43, OPC-53 GoC for the unhydrated powder, 3, 7, 14, and 28 days as shown in Figure.3.1.

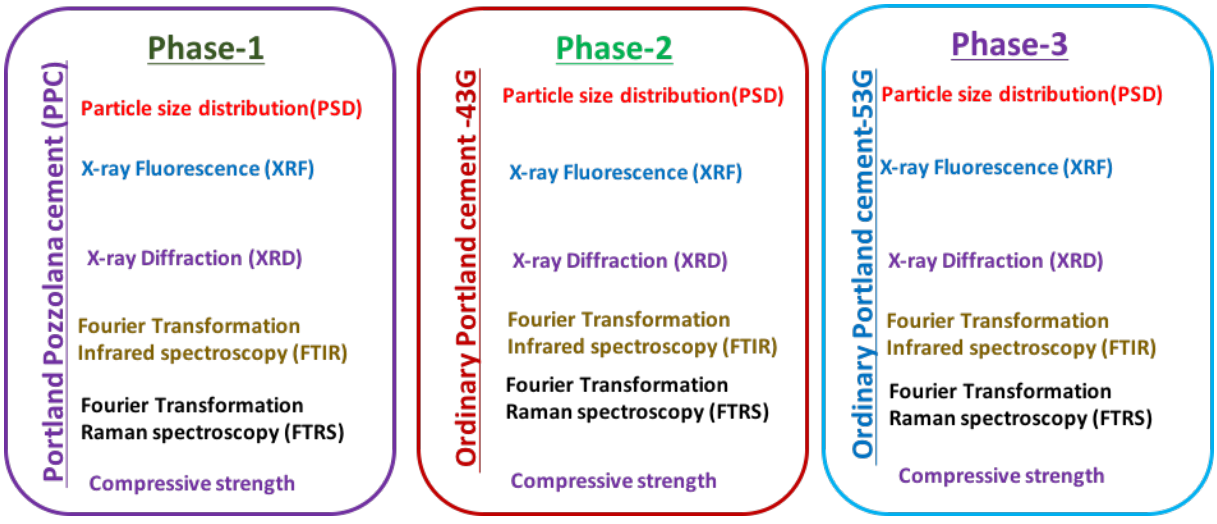

Figure 3.1. Various tests carried on PC specimens at different stages of hydration.

3.2. Sample preparation

Three GoC *i.e. OPC*-43, *OPC*-53, *PPC* are procured from retailers in the market. Three cubes of size 50 x 50 x 50 mm^3 are cast for each GoC with *w/c* 0.33, which is close to the normal

consistency of the PC. Three cubes were cast for each GoC for testing at 3, 7, 14, and 28 days. After casting the cubes are dried for one day and are placed in the curing tank for the corresponding duration and on the day of testing the cubes are dried under the sun. The specimens are tested for compressive strength in the compressive testing machine and the cores of the tested specimens are collected for further sample preparation for *XRD*, *FTIR*, *FTRS* testing. The collected samples are further pulverized in a planetary ball mill to obtain uniform fineness. 30 grams of the sample is placed in wiles with a sample to weight ratio of 1:10 and Touline is used for dispersing the particles. The revolutions are set for 300 rpm for a duration 5 min rotation and 5 min of rest for a total time of 30 minutes *i.e.* a mill time of 15 minutes and a rest time of 15 minutes. The extracted sample is dried at room temperature to obtain a dry powder, while the obtained sample is used for further studies.

3.3. Experimental investigation

The tests were carried on the three GoC *i.e.* PPC, OPC-43 and OPC-53, while the list of equipment used for the analysis is detailed below:

3.3.1. Particle Size Distribution (PSD)

PSD is essential in understanding the size, shape, and the surface characteristics of the cement. The PSD was obtained by using Malvern® Mastersizer 3000 which uses the concept of Laser Diffraction spectrometry to determine the particle sizes of cement powder by dry dispersion.

3.3.2. X-ray fluorescence (XRF)

Major and minor chemical oxidized present in the PC samples were determined using Bruker® S4 Pioneer for conducting XRF analysis.

3.3.3. X-ray Diffraction (XRD)

The chemical composition of the three Portland cement was found using PANalytical®, X'pert^3, which uses a graphite monochromator and Cu-Ka radiation. Tests are conducted on the Panlytical, powder expert equipment for the three Portland cements with the scans collected from 10° - 77^o (2θ) for a step size of 0.0167 seconds and 53.975 seconds as time per step as for a total duration of 30 minutes.

3.3.4. Fourier Transform Infrared Spectroscopy (FTIR)

The Infrared spectroscopy was conducted using Perkin-Elmer® Model 100 FTIR over a range of 400 to 4000 cm^{-1} with an accuracy of ± 2% with a transmission mode.

3.3.5. Fourier Transform Raman Spectroscopy (FTRS)

A laser source spectroscopy, i.e. FTRS tests were conducted on BRUKER® RFS 27, of scan range 50 to 4000 cm^{-1} with a resolution of 2 cm^{-1} for an excitation of 1064.

3.3.6. Compressive Strength

The compressive strength of the specimens is determined using compressive testing machine with a rate of loading of 140 kg/cm^2/min.

3.4. Results and Discussion

The PSD, XRD, XRF, FTIR, FTRS and compressive strength tests are carried out on the three GoC *i.e.* PPC, OPC-43, OPC-53. These tests are carried out on the samples of plain cement as well as cement with, 3-days, 7-days, 14-days and 28-days of hydration. The test results are discussed in the following sections:

3.4.1. PSD analysis of PPC, OPC-43 and OPC-53 cements

The size of particle present in PC ranges from 1-100 µm, the size of the particles present in PC governs the strength *i.e.* Particle size of diameter 1µm reacts in a day, while 10 µm reacts in a month and the particles size > 50 µm does not react entirely even with sufficient amount of water, while over fineness poses severe problems resulting in poor flowability (IDI, 2018). Even though chemical composition of the material remains same, the fineness to which the cement is ground and proportions of chemical oxides effects the behaviour of PC, due to an increase in the surface area to volume ratio chemcial reactionis occur primarliy on surface of phases. PSD governs the hydration of the cement and the depth of reaction (Sereda, P. J. et. al. 1981). The estimation of PSD can be carried out by mechanical methods such as dry sieving, wet sieving, optical microscopy, sedimentation rate (Andreasen apparatus), coulter counter size (for measuring the particle volume), Dynamic Light Scattering (DLS), scanning electron microscopy (SEM), Transmission Electronic Microscope (TEM), Atomic Force Microscope

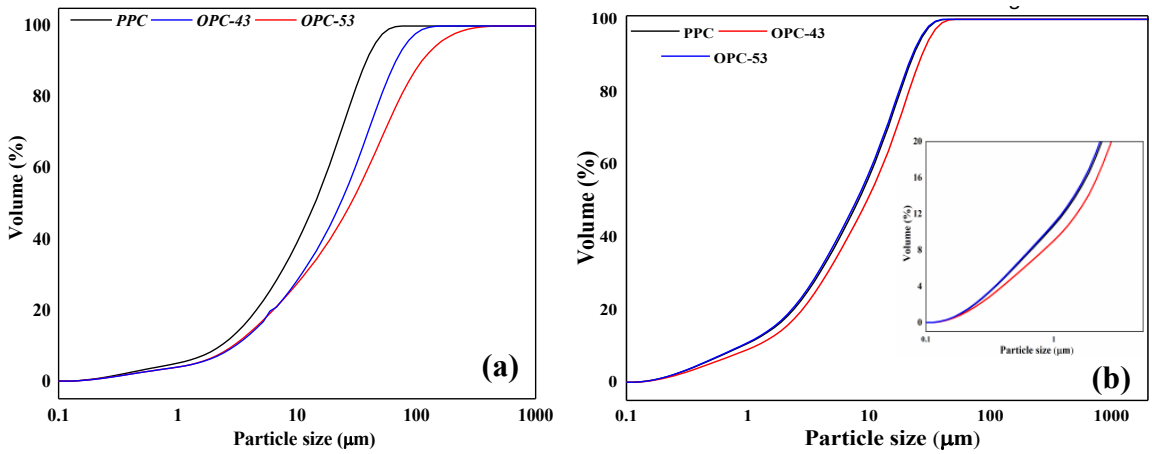

Figure 3.2. Particle size distribution of PPC, OPC-43 and OPC-53 (a) unhydrated cements (b) after grinding.

(AFM). The PSD plots of the PPC, OPC-43, and OPC-53, obtained using dry dispersion method are shown in Figure 3.2(a) for the dry cement powders. The D_{10}, D_{50}, and D_{90} which denote 10%, 50% and 90% of the cumulative mass are shown in Table. 3.1, where 'D' denotes the mass division diameter and D_{10} signifies the mass percentages of the particles below the corresponding diameter. An increase in fineness or specific surface area results in the improvement of compressive strength. For the cement of the same surface area, the narrower distribution in particle size yields higher strengths (Zhang Y. M. et. al. 1995).The cumulative mass from the *PSD* data shows that the PPC samples have the least amount of fine particles

Table 3.1. Cumulative mass of PPC, OPC-43 and OPC-53.

Cumulative mass	PPC	OPC-43	OPC-53
D_{10}	2.3	3.04	2.92
D_{50}	14	23	28.2
D_{90}	37.9	66.9	110
Specific Gravity	3.13	3.15	3.19

which are under the size of 10, while OPC-43 has the highest number particles with in the same range. At D_{50} and D_{90} PPC has the least number of particles and OPC-53 has the highest number of particels. However, after the grinding process, the distribution of the particle is shown in Figure.3.2(b) and a clear variation of particles is observed, *i.e.* OPC-43 has the highest number of particles at D_{10}, D_{50} and D_{90}, while OPC-53 has the least number of particles, while the cumulative distriubtion of PPC particles are almost similar to OPC-53, and the cumulative weight distribution is shown in Table. 3.2.

Table. 3.2. Cumulative weight retained of PC after grinding.

	PPC	OPC-43	OPC-53
D_{10}	0.9	1.16	0.874
D_{50}	8.15	9.61	7.87
D_{90}	23.2	27.2	22.7
D_{100}	45.3	51.7	40.1

3.4.2. XRF analysis of PPC, OPC-43 and OPC-53 cements.

The XRF results of the unhydrated samples for the GoC are shown in Table 3.3. According to the British code the concentrations of major and minor oxides are: SiO_2 is 21-22%, Fe_2O_3 is 0.5-5%, $SO_3 \leq 1.5\%$ and all the three GoC have exceeded the recommended values, while Al_2O_3 should be in the ranges of 3-8%. The PPC has exceeded the concentration limits as per the British code, While the CaO was less than the required i.e. 60-67% for PPC amd OPC-43. XRF analysis was conducted on four grades of cement and the following ranges and the results were were compared to ASTM C 150. The range of volume fraction is typically as follows CaO(60.2-66.3), SiO_2(18.6-23.4), Al_2O_3(2.4-6.3), Fe2O3(1.3-6.1), MgO(0.6-4.8), SO3(1.7- 4.6

), Na_2O& K_2O (0.05-1.20) (see ITI (2018)).The major oxides of the three grades of cement CaO (36.65-51.25), SiO_2(27.06-34.67), Al_2O_3 (3.86-11.8), Fe_2O_3 (6.99-8.64). The volume fraction of minor oxides concentrations for MgO (0.578-1.39) which exceed by 6%, SO_3 (4.41-6.41) which exceeds by 3% as the maximum requirements as per ASTM C 150, while alkali oxides are K_2O(1.16-1.28), Na_2O(0.142-0.216). The OPC-43 and OPC-53 has higher concentrations of CaO in comparison to PPC, and PPC has higher concentrations of SiO_2. This is due to the inclusion of fly ash in the concentrations of 15 - 35% during its manufacturing. However, the volume fraction of Al_2O_3 (11.8%) is greater for PPC, while CaO (66.86%) volume fraction are greater in OPC-53 when compared with the other two PC.

Table 3.3. XRF values of PPC, OPC-43 and OPC-53.

Chemical Composition	PPC	OPC-43	OPC-53
CaO	37.65	49.97	66.86
SiO_2	34.67	27.51	16.71
Al_2O_3	11.8	3.86	3.19
Fe_2O_3	6.99	8.64	5.69
SO_3	4.41	6.413	5.11
K_2O	1.28	1.16	0.5
TiO_2	1.02	0.341	0.295
MgO	0.578	0.851	1.02
Na_2O	0.216	0.142	0.07
MnO	0.146	0.198	0.115
P_2O_5	0.395	0.286	0.169
SrO	0.077	0.083	0.081

3.4.3. XRD analysis of PPC, OPC-43 and OPC-53 cements

The XRD analysis is carried on the PPC, OPC-43 and OPC-53 at various stages of hydration *i.e.* unhydrated, 3-days, 7-days, 14-days, and 28 days respectively. These PC consist of many phases, however only a few of the major phases of interest are discussed. The importance of the major phases and their volume percentages as per ASTM C 150-86 is shown in the Table

Table 3.4. Phases concentration in PC as per ASTM C 150-86.

Chemical Name	Chemical notation	Mass contents (%)
Tricalcium Silicate	$3CaO . SiO_2$	38-60
Dicalcium Silicate	$2CaO . SiO_2$	15-38
Tricalcium Aluminate	$3CaO . Al_2O_3$	4-12
Tetracalcium alumina ferrite	$4CaO . Al_2O_3 . Fe_2O_3$	10-18
Pentacalcium Trialuminate	$5CaO_3 .Al_2O_3$	1-3
Calcium sulphate dihyrate	$CaSO_4 .2H_2O$	2-5

3.4. The importance of these phases such as Alite, Belite, Portlandite *etc.* in PC are discussed, along with the observation made for the XRD analysis of the three GoC.

3.4.3.1. Alite

Alite indicates the impure form of the C_3S phases, and in the impure form this phase has other elements such as Mg^{2+}, Al^{3+}, and Fe^{3+}. It is a crucial phase which is present in the bulk of the cement and is responsible for early strength. It exists as three polymorphic forms in clinker represented by M1, M2, and M3. A peak occurring in between 51° - 51.50° are indication of the Alite phase in the clinker. A single peak at 51.7° represents the M1 polymorph, while a doublet peak is observed, is an indicator of M3. The triclinic polymorph is represented by a triplet peak, observed between 51° and 52°. The strong peaks observed at 30.40° and 51.7° are used for quantitative analysis (Stutzman P.E., 1996).

3.4.3.2. Belite

Belite is a predominant phase in industrial clinker, and it is the impure form of C_2S. It is also present in the gα and α^1 forms. Additionally, the γ-C_2S form also exists but it is not found in the industrial clinkers. It is not more reactive than Alite and it contributes to the later age strength. A resolvable peak is observed at 31°, and a noticeable weak peak at 35.2° is also observed. The estimation of quantity of Belite peak is hard as it is overlapped by Alite peaks (Stutzman P.E., 1996).

3.4.3.3. Aluminate

Aluminate phase is the most reactive phase and it incorporates impurities like Si^{4+}, Fe^{4+}, K^+, and Na^+. Cubic and orthorhombic are the two polymorphs that exists in industrial clinker, and is identified by the stronger peak at 33.3°. The cubic polymorph is identified by the stronger peaks at 33.3°, 47.7°, and 59.4°, while the splitting of the peak at 33.3° is observed for the orthorhombic phase. However, the peaks at 22° - 23° are also used to quantify the polymorphs of Aluminate (Stutzman P.E., 1996).

3.4.3.4. Ferrite

Ferrite phase is a mixture of C_3A and solid solutions series with the compositions range $Ca_2(Al_xFe_{1-X})_2\ O_5$, x ranges from 0 – 0.7. C_4AF is the representation of 1:1 ratio of Al:Fe ; $Ca_2(Al,Fe)_2O_5$ also known as Brownmillerite. It is recognised by the diffraction peaks at 12.1°

and 33.9°; As the qualitative estimate of the 33.9° peak is not possible, peaks occurring at 24.4° and 12.1° peak are used for the intensity measurements (Stutzman P.E. 1996).

3.4.3.5. Portlandite

The Calcium hydroxide also represented as Portlandite, which is also a crucial phase in the hydrated cement pastes. The peaks are observed at 18.01°, 28.67° and 34.10° (Stutzman P.E. 1996).

3.4.3.6. Tobermorite

Tobermorite is considered to be similar to CSH gel structure. It is stable at temperatures of ~ 80 °C – 150 °C, however it can be produced at temperatures exceeding 200 °C as a meta-stable solid. It exists in 3 polytypes *i.e.* 9Å, 11Å, and 14Å. The peaks observed at 29.1° and 30.1° peaks are helpful for the identification and quantification of the phase (Stutzman P.E. 1996).

3.4.3.7. Gypsum

Gypsum is a mineral that is added to clinker during the manufacture of PC to avoid flash setting. Depending on the amount of Gypsum added, relative humidity and temperature, to the clinker, various forms of Calcium Sulphate-water forms exists. The primary form is $CaSO_4$. $2H_2O$ - gypsum, $CaSO_4$. $0.5H_2O$ - Hemihydrate or Basanite, and $CaSO_4$ - Anhydrite are formed. The peaks for Gypsum are observed at 11.5° and 20.70°; for Basanite and Anhydrite the peak are observed at 14.74° and 25.48° (Stutzman P.E. 1996).

3.4.3.8. Calcium silicate hydrate (CSH)

It is the key phase existing in the hydrated cement, which plays a crucial role in the strength development of the PC. It is also responsible for the growth of the mineral Tobermorite and Gyrolite. The structure of the CSH gel is amorphous, and the peaks which are of significance are at 29.3° and 50.08° (Stutzman P.E. 1996).

3.4.3.9. Alkali sulfates

It is not a significantly occurring mineral but it effects the properties of early and later age strength. Common Alkali Sulfates are Aphthitalite, Arcanite, Calcium langbeinite. Aphthitalite major peaks are at 32.20°, 31.5° which run over by Ferrite and Aluminate. The peak at 22.39° is overlapped by minor Ferrite at 23° and cubic Aluminate at 21.77°. The 25.3° peak overlaps the minor peak of cubic Aluminate. Arcanite peaks are observed at 29.77°, 21.3°, 20.9° and 21°, For Calcium langbeinite a triple grouping peak is at 27.3° (Stutzman P.E. 1996).

Apart from these phases many other phases are present, however most of the PC properties are governed by those phase concentrations presented here. After the XRD plots are obtained for the three GoC at their respective duration, the analysis is carried using X'pert Highscore® software and the following steps are adopted:

Table 3.5. Phases identified from the JCPDF database and formulas.

Phases	Formulae	Crystal system notation	ICSD codes	Year	PDF codes
Alite	$3CaO.SiO_2$	Monoclinic/M_3	94742	2002	01-070-8632
		Monoclinic/M_1	-	2006	–
Belite	$2CaO.SiO_2$	Monoclinic/β	79550	1994	01-083-0460
		Orthorhombic/α'_H	81097	1995	01-086-0399
Aluminate	$Ca_3Al_2O_6$	Cubic	1841	1975	00-038-1429
	$Ca_{8.5}NaAl_6O_{18}$	Orthorhombic	1880	1975	00-032-0150
Ferrite	C_2AlFeO_5	Orthorhombic	9197	1971	01-071-0667
Lime	CaO	Cubic	75785	1994	43-1001
Portlandite	$Ca(OH)_2$	Rhombohedral	15471	1961	01-072-0156
Periclase	MgO	Cubic	104844	1984	45-946
Calcite	$CaCO_3$	Rhombohedral	79673	1989	01-083-0577
Dolomite	$Ca\ Mg\ (CO_3)_2$	Trigonal	31335	1983	01-075-1761
Quratz	α-SiO_2	Rhombohedral	200721	1978	01-083-2465
Gypsum	$CaSO_4.2H_2O$	Monoclinic	151692	2004	33-0311
Hemihydrate	$CaSO_4.0.5H_2O$	Monoclinic	380286	2009	41-224
Anh ydrite	$CaSO_4$	Orthorhombic	40043	1975	01-086-2270
Arcanite	K_2SO_4	Orthorhombic	2827	1972	01-070-1488
Aphthitalite	$K_3Na(SO_4)_2$	Trigonal	26018	1980	01-074-0398
Syngenite	$K_2Ca(SO_4)_2(H_2O)$	Monoclinic	157072	2005	00-28-0739

Step. 1. The .XRDML files are imported into the X'pert Highscore software,

Step.2. Imported plots background is removed

Step. 3. Strip Kα command is used,

Step.4. Peaks are searched

Step.5. Phases present in the XRD graphs are searched in (ICDD) database.

Step.6. Fit profile option is selected for proper fit and to measure the phase concentrations.

The above-mentioned steps are adopted for all the plots obtained from the XRD analysis. The phases matched in the data base, and their formulas are shown in Table. 3.5.

3.4.4. XRD analysis of PC samples

The plots obtained from XRD analysis of PPC, OPC-43 and OPC-53 of unhydrated cement, and also at 3, 7,14, 28 days of hydration were shown in Figure. 3.3 – 3.5. CaO and MgO mineral

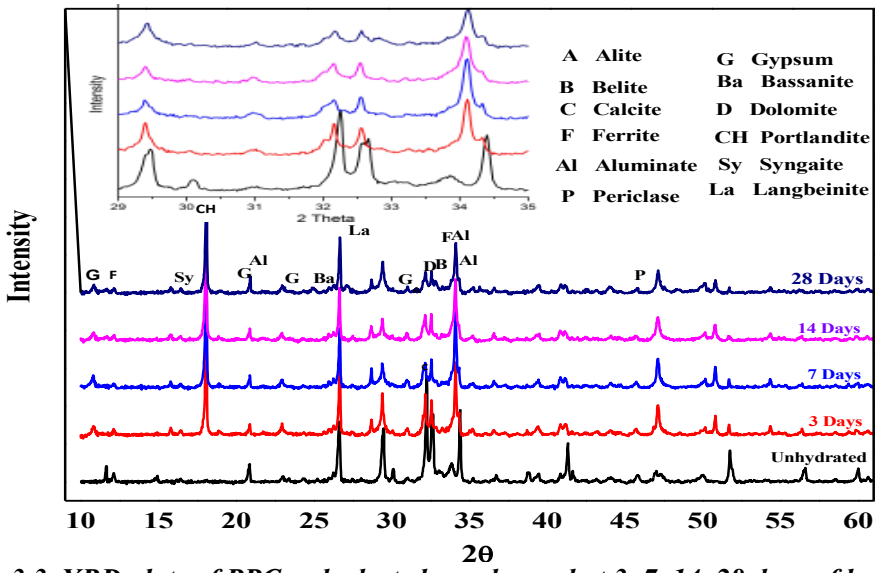

Figure 3.3. XRD plots of PPC unhydrated powder and at 3, 7, 14, 28 days of hydration.

are primary responsible for causing the expansion of mature concrete and also cause durability problems. Free lime peaks of CaO observed at 37.7° and 53.90° are used to identify the presence of the mineral and for measuring the quantity. Lime also reacts with moisture which produces carbonates and later on leads to formation of Calcite. An intense corresponding peak can be

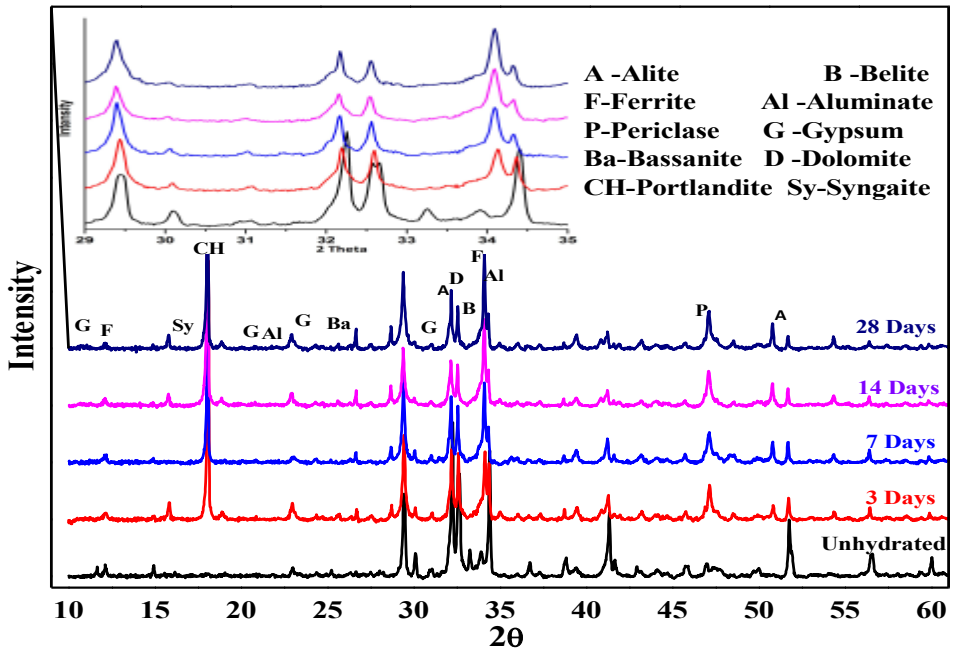

Figure 3.4. XRD plots of OPC-43 unhydrated powder and at 3, 7, 14, 28 days of hydration.

observed at 42.93°. As soon as the water is added to the cement, the hydration process begins and continues as long as Silicates and Aluminates are present. This hydration process gives rise to new hydrated compounds such as Calcium Hydroxide, Calcium Hydroaluminate, Hydro Ferrites in crystalline or gel form (Stutzman P.E. 1996, 2016).

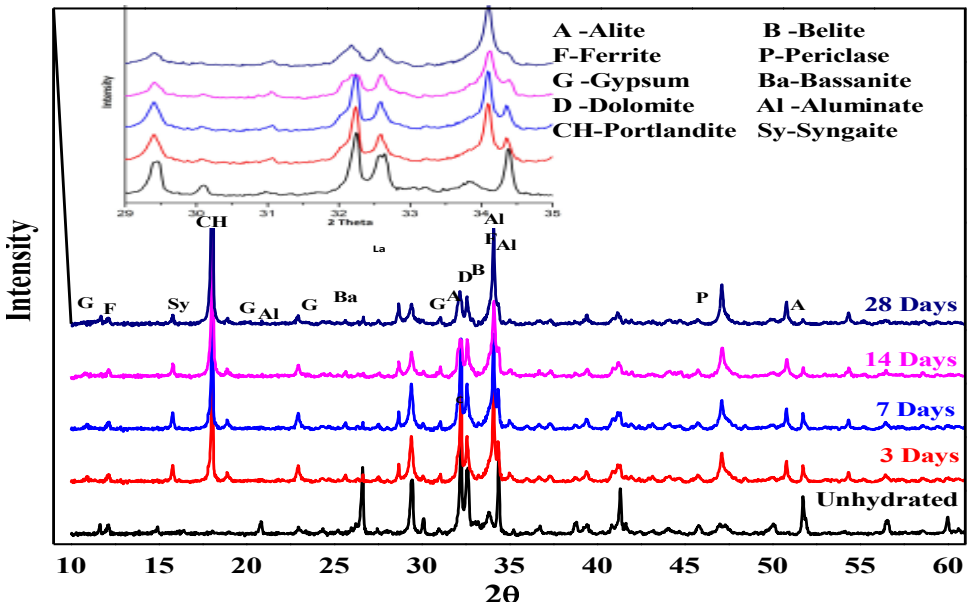

Figure 3.5. XRD plots of OPC-43 unhydrated powder and at 3, 7, 14, 28 days of hydration.

The reduction in the peak intensity of the important phases in all the grades of PC samples is shown in Figure 3.6. A reduction is observed in Peak intensities in the region of 32 - 33° which is indicative of Alite phase, while the concentration of Alite phase is higher for OPC-43 than rest of the PC at 28 days of hydration. Similarly the peak at 52° which is of C_3S has a gradually reduction in intensity with respect to the increase in the rate of hydration. Increase in the intensity of Belite after the hydration process has be initiated can be observed for all the three GoC at 47° and an increase in the phase concentration observed from XRD plots is plotted in Figure 3.6, however the peak intensities are lesser than alite for all the three GoC. Aluminate concentration are lower for PPC when compared to other two GoC i.e. OPC-43 and OPC-53 as shown in Figure 3.5. The increase in the Portlandite concentrations with the progress in hydration was observed for all the three GoC are as shown in Figure 3.6, and OPC-53 has higher concentration of Portlandite phase and PPC has lower concentrations of Portlandite phase, which is reponsible for the superior mechanical porperites of OPC-53 GoC. Calicte concentration are intially higher, and as the hydration progresses, a gradual reduction in peak intensites can be observed from Figure 3.6, however comparitively lower peak concentration of OPC-43 were observed in comparison to the rest of the GoC. The Lanbegnite peak intensities are observed for PPC, and from the XRD analysis the peak at 27.10° is the only

way one can differentiate between PPC and OPC GoC. The gypsum and aluminate phases peak at 21° is present for PPC (Figure 3.3); Such a peak was not observed in OPC-43 (Figure 3.4), however this peak which is present for plane cement of OPC-53 (Figure 3.5) is not present as there is a progress in hydration. The intensity of the peaks in between 29° - 34° is less for PPC when compared with OPC-43 and OPC-53.

3.4.5. Spectroscopy studies on PC samples

Chemical bonds can be related to oscillating springs whose distance can vary and is relaxed at equilibrium distance. Similarly, atoms within molecules can be idealized as balls, connected by springs. Any change in frequency causes the springs to vibrate depending on the mass and bond strength of the atoms. When the bond between the atoms is stronger, and the reduced mass is smaller, the vibrational frequency higher will be. The reduced mass is defined ($m_{reduced}$) by Equation 3.1.

$$m_{reduced} = (m_{atom1} + m_{atom2}) / (m_{atom1} + m_{atom2}) \text{ -------- } (3.1)$$

In the case of hydrogen atoms bonded with other elements, the $m_{atom1} << m_{atom2}$ reduced mass is equal to m_{atom1}. The connection between wavenumber (k) and frequency (f) is given by Equation 3.2.

$$f = c*k \qquad (3.2)$$

Where c – speed of light, while vibration occurs only at certain frequencies stated by quantum mechanics.

While the energies for these vibrations are obtained from the Equation 3.3.

$$E_{vib} = \frac{h}{2\pi}\sqrt{\frac{K}{m_{reduced}}} * \left(n + \frac{1}{2}\right) \qquad (3.3)$$

Where h – Planck's constant, K – bond strength between atoms while n is the integer. The atoms can go from one energy level to the other when there is a polarisation over the bond. The energy (ΔE) required for the transition of energy from initial level ($n_{initial}$) to final energy level (n_{final}) is given by the Equation 3.4.

$$\Delta E = \frac{h}{2\pi}\sqrt{\frac{K}{m_{reduced}}} * \left(n_{final} - n_{initial}\right) \text{ -------- } (3.4)$$

Transition between energy states can only take place when the electromagnetic radiation energy matches the difference in energy exactly. Hence the electromagnetic radiation estimated from the Equation 3.5.

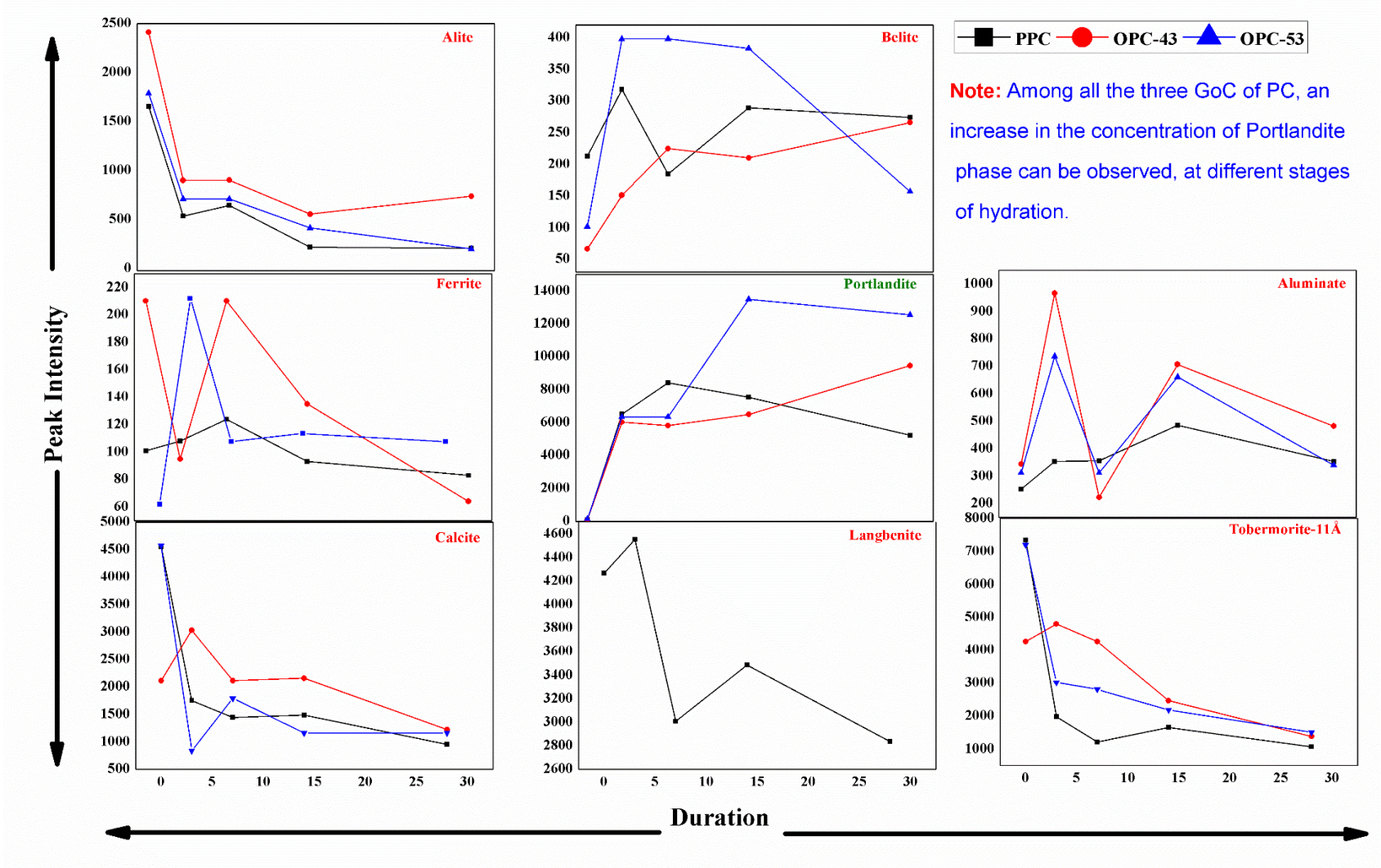

Figure 3.6. Peak intensities observed in XRD analysis of PPC, OPC-43 and OPC-53 samples corresponding unhydrated powder, 3, 7, 14 and 28 days of hydration.

$$\Delta E = hf \text{ -------- } (3.5)$$

Where h is frequency of the radiation. All the molecules will be in ground vibration state at room temperature *i.e.*($n_{initial}$ = 0), and as the majority of molecules reaches the first excitation state *i.e.* (n_{final} =1). The wavenumber (k) of light which can cause the excitation by vibration is obtained by combining the Equations 3.1, 3.3, 3.5 and the obtained formula is shown below:

$$k = \frac{h}{2\pi c}\sqrt{\frac{K}{m_{reduced}}} \text{ -------- } (3.6\ )$$

This wavenumber lies in the IR region of the electromagnetic spectrum. As the atoms which are involved in vibration are more than two, the vibration takes place in the 3D also, hence for 3N-6 vibration modes exists for non-linear molecule, where N denotes number of atoms in the molecule. However, if a group is linear, the vibration states are 3N-5.

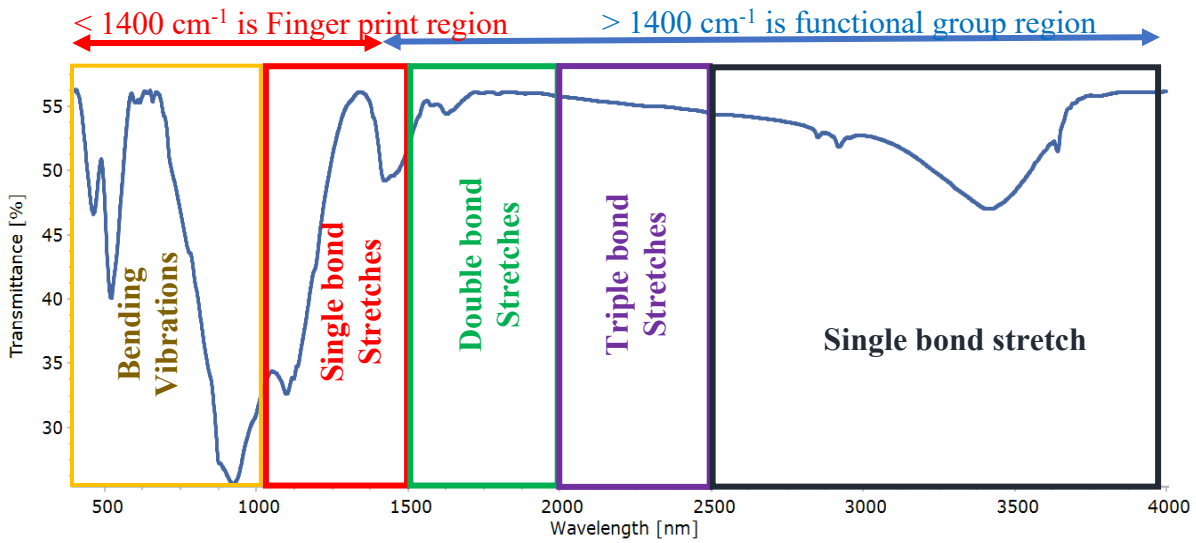

Figure 3.7. Loaction of the peaks in the IR spectrum.

The electromagnetic radiation is absorbed with characteristic frequencies, which can be used for the identification of a certain group of molecules present in the sample. The radiation of the electromagnetic waves of known frequencies are sent across the sample, and the changes in the intensities of the provided radiation provides the characteristics wavenumber of IR spectrum. The plots of spectrum of IR are intensities Vs the wave number, hence two substances which absorb the same wavenumber are mostly identical. Therefore the IR spectrum is called a finger print. Two regions exists in the IR spectrum (a) less than 1400 cm^{-1} which is a finger

print region and (b) greater than 1400 cm^{-1} is a functional group region. The detailed sketch showing the different region and bond stretches of the plots obtained from FTIR analysis Figure 3.7.

3.4.5.1. FTIR analysis of PPC, OPC-43 and OPC-53

The major advantage of using a FTIR for the study of PC is the advantage it has in identifying the amorphous phase, costs involved in sample preparation are low and data can be obtained very quickly. FTIR Spectrometer is used over a range of 400 - 4000 cm^{-1} with a accuracy of ± 2%, on transmission mode for the three GoC *i.e.* PPC , OPC-43, and OPC-53 cements for the samples obtained from unhydrated cement and at different stages of hydration such as 3-days,7-days,14-days and 28-days respectively. A specimen pellet is made using 250 mg of Potassium Bromide(KBr) and 3 mg of cement powder. The transmission plots are converted to absorbance plots for ease of analyzing the data. From the FTIR plots, a shift of wave number to higher values takes place if there is a decrease in bond length, while a decrease in bond length causes a reduction in wavenumber. Whereas an increase in peak intensity is an indication that there are higher concentrations of those bonds. A peak shift towards higher wave number is also an indication of the reduction in the mass of the molecule, as vibration frequency is proportional to mass of the vibrating molecule.

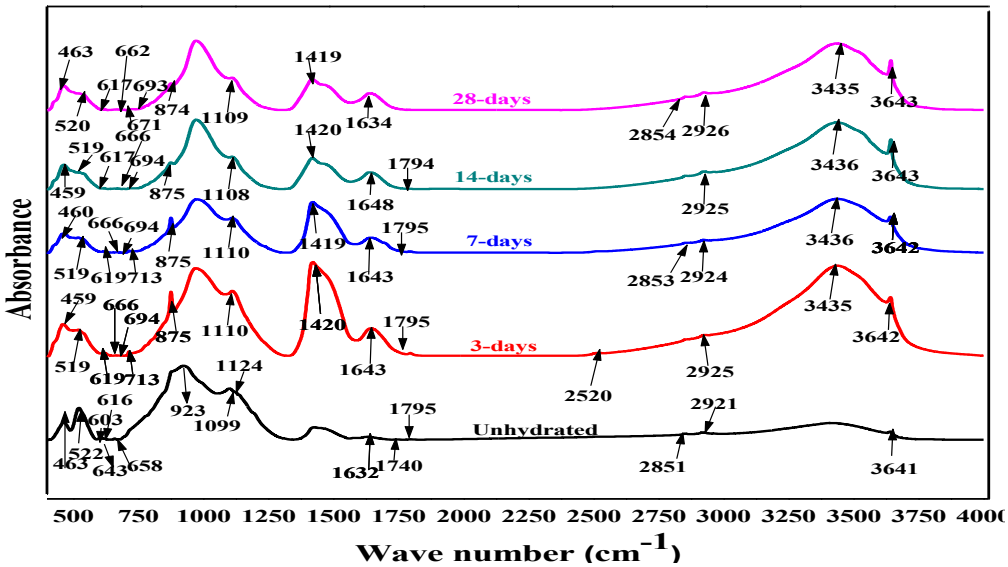

Figure 3.8. FTIR peaks of PPC samples of unhydrated cement and at 3, 7, 14, 28 days of hydration.

The FTIR plots PPC samples is shown in Figure 3.8, where the peaks in the finger print region are: peak 463 cm^{-1} of unhydrated cements shifts to 458 cm^{-1} at 3-days, 461 cm^{-1} at 7-days, 462 cm^{-1} at 14-days and to 463 cm^{-1} at 28 days with a gradual decrease in intensity as the

hydration progresses which is an indication of the C_3A phase. The peak 521 cm^{-1} unhydrated cement, 519 cm^{-1} (3 and 7-days of hydration), 520 cm^{-1}at 14 days and 518 cm^{-1} at 28 days of hydration a drop down in intensity is observed for C_3S or C_4AF phases. The peaks in the range of 500-700 are of C_4AF (Hughes T.L. *et al*. 1995). The peaks observed in the functional group region are: peaks 1643 cm^{-1} (3,7-days), 1634 cm^{-1} (14 days),1648 cm^{-1} (28 days) hence range of a limit of 1640-1680 is an indication Ettringite phase (Horgnies M. *et al.* 2013). The peaks at 2851 cm^{-1}, 2853 cm^{-1}, 2855 cm^{-1}, 2921 cm^{-1}, 2925 cm^{-1}, 2924 cm^{-1}, 2925 cm^{-1}, 2926 cm^{-1} are an indication of Calcium Carbonate (Hughes T.L. *et al.* 1995). The peaks at 3435 cm^{-1}, 3436 cm^{-1} (7 and 14-days), 3435 cm^{-1} (28-days) are also indicators of Ettringite phase as can be seen

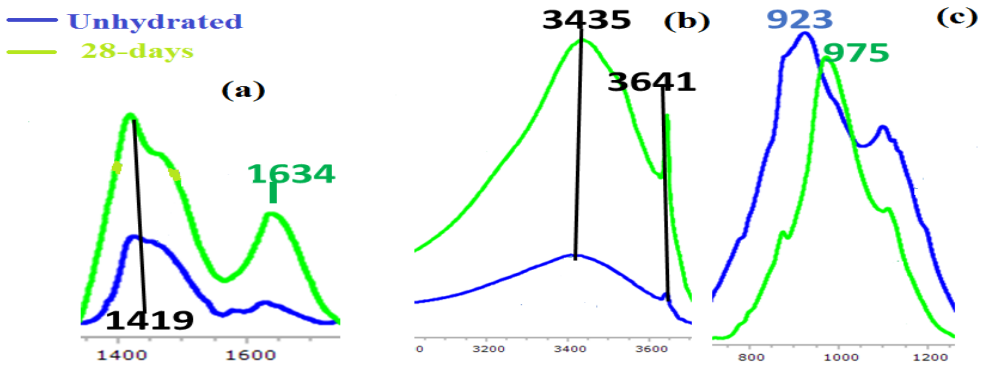

Figure 3.9. Peak variations observed in PPC samples of unhydrated cement and 28 days of hydration.

in Figure 3.9(b) and an increase in absorbance values with the increase in hydration period is observed (Horgnies M. *et al.* 2013). The peaks at 3641, 3642 cm^{-1} (3 and 7 days), 3643 cm^{-1} (14 and 28 days) are an indication of Portlandite and their intensity is increases with hydration (Horgnies M. *et al.* 2013) (Ylmén R. 2009). The variation in the peak intensities of unhydrated cements and at 28 days of hydration is shown in Figure 3.9. Increase in the intensity of absorbance peak at 1634 cm^{-1} is observed with increase in the hydration period. However, such an absorbance peak is not observed in the unhydrated sample as shown in Figure 3.9(a). An increase in the intensity of the absorbance band at 1419 cm^{-1} is corresponding to Calcite, is observed for unhydrated cement and 28 days of hydration, as shown in Figure 3.9(a). A shift in the peak intensity is observed from 923 cm^{-1} (β-C_2S) of unhydrated cement to 975 cm^{-1} (28 days) with increase in hydration as shown in Figure 3.9(c). The increase in the peak intensity of 3641 cm^{-1} from Figure 3.9(b) with the increase in hydration is in good agreement with the XRD data as detailed in section 3.4.

The FTIR plots of OPC-43 are shown in Figure 3.10. The peak at 403 cm^{-1} is an indication of C_3A is observed at 3-days of hydration and disappears at 7, 14, 28 days of hydration. The peak 463 cm^{-1} (unhydrated, 3 days) of C_3A shifted to 462 cm^{-1} at 7 days, 460

cm^{-1} at 14 days, and 463 cm^{-1} at 28 days of hydration. The peak 521 cm^{-1} closer to C_3A (522 cm^{-1}) and 520 cm^{-1}(C_3S) (Ghosh S. N. *et. al.*; 1974) shifted to 519 cm^{-1} at 3, 7, 14 days and 520 at 28 days. The peak range in between 500 -700 cm^{-1} indicating C_4AF (Ghosh S. N. *et. al.*; 1974) are observed for unhydrated cement and at all stages of hydration process *i.e.* at 618 (for unhydrated, 3,7,14,28 days), 596 cm^{-1} (unhydrated), 676 cm^{-1} (unhydrated)).

The decrease in peak intensity of Calcium Carbonate at 713 cm^{-1} was observed with the progress of hydration, this is in good agreement with XRD plots of OPC-43 samples shown in Figure 3.4. The peak at 873 cm^{-1} observed in unhydrated cement sample is an indicator of C_2S phase and slight shift is observed to 874 cm^{-1} (Ghosh S. N. *et. al.*; 1974) at all the stages of hydration. A shift in the peak of 924 cm^{-1} of unhydrated cement powder to 986 cm^{-1}(3 days), 971 cm^{-1}(7 days), 975 cm^{-1}(14 days) (Bayerite, Aluminium Hydroxide, 974 cm^{-1} (28 days) and

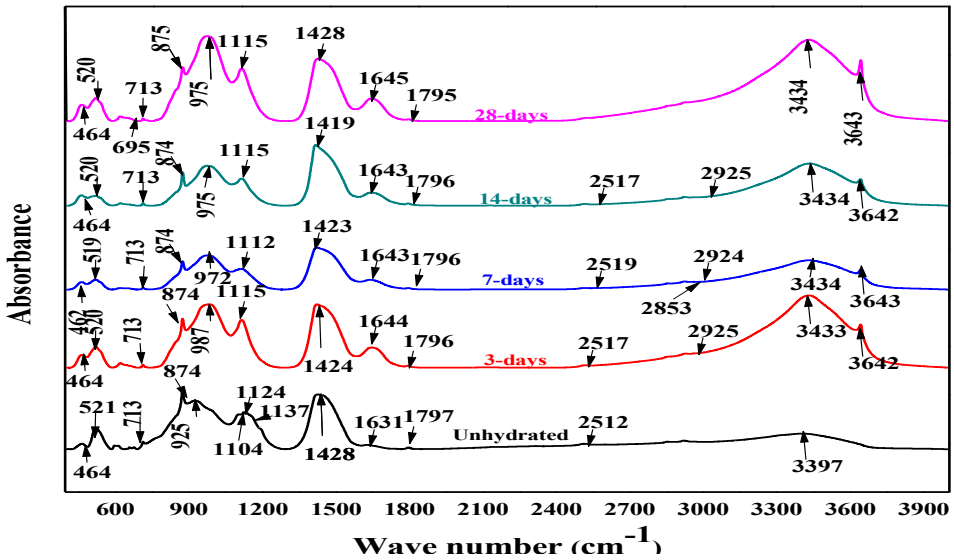

Figure 3.10. FTIR peaks of OPC-43 samples of unhydrated cement and at 3, 7, 14, 28 days of hydration.

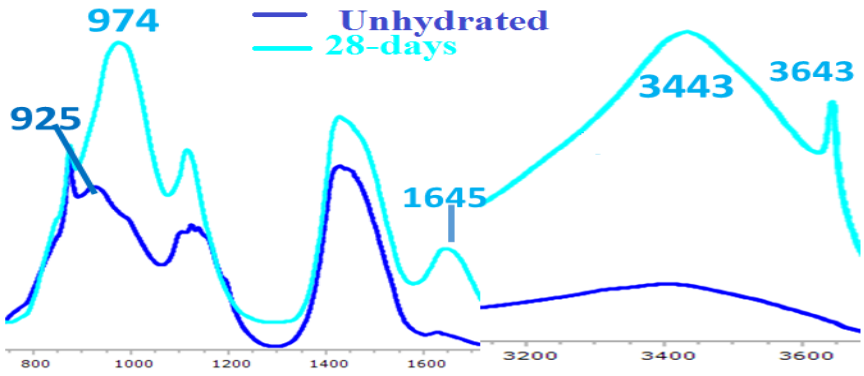

Figure 3.11. Peak variations observed in OPC-43 samples of unhydrated cement and at 28 days of hydration.

an increase in peak intensities is an indication of Tobermorite and Jennite. Peaks in the range of 1600 -2000 cm^{-1} correspond to C_3S, while 1600-2020 cm^{-1} corresponds to C_2S, and the peaks in the range of 500-700 cm^{-1} corresponds to C_4AF (Hughes T.L. *et al.* 1995). A peak at 1115 cm^{-1} at 3 days of hydration is an indication of Ettringite (Horgnies M. *et al.* 2013), has a shift 1112 cm^{-1} at 3 days, 1114 cm^{-1} at 14 days to 1116 cm^{-1} at 28 days. The peaks of 1428 cm^{-1},

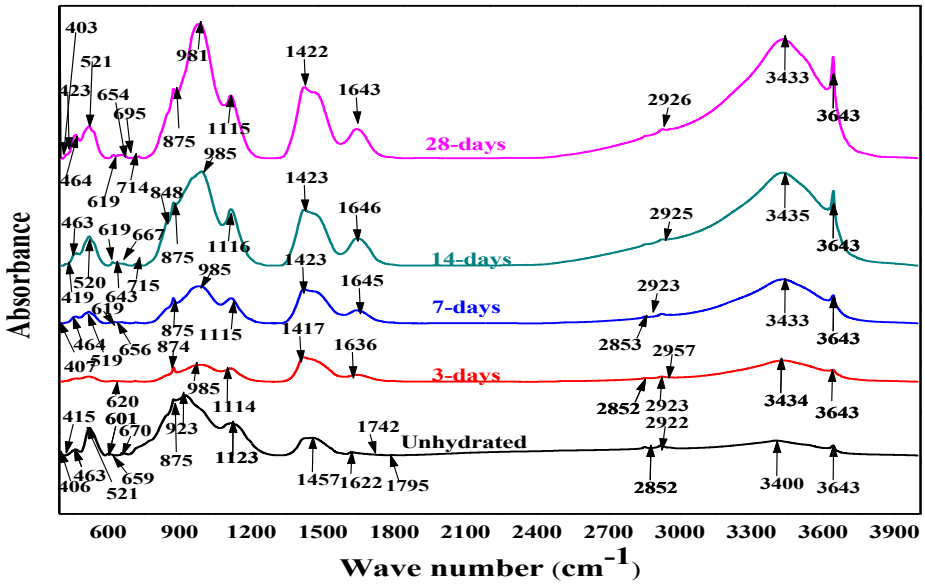

Figure 3.12. FTIR peaks OPC-53 samples of unhydrated cement and at 3, 7, 14 and 28 days of hydration.

1424 cm^{-1}, 1423 cm^{-1}, 1419 cm^{-1}, 1426 cm^{-1} from unhydrated to 28 days of hydration belong to Calcium Carbonate (Choudhary H.K. *et al.* 2015). The peaks of Ettringite occur at 1631 cm^{-1} for unhydrated cement, 1644 cm^{-1} at 3 and 7 days, 1642 cm^{-1} at14 days and 1645 cm^{-1} at 28 days of hydration (Horgnies. M. *et al.* 2013). The peak at 3432 cm^{-1} (3-days) is closer to 3435 cm^{-1} (7-days), 3434 cm^{-1}(14 and 28 days) which corresponds to Ettringite. The peak intensity at 3643 cm^{-1} of Portlandite and at 28 days of hydration has increased with hydration process as observed in Figure 3.11.

The FTIR plots of unhydrated cement, and hydrated cement at 3, 7, 14 and 28 days of hydration for OPC-53 samples are shown in Figure 3.12. The peak intensity of 463 cm^{-1} of C_3A for unhydrated cement is similar to OPC-43, a shift in absorbance peak of 465 cm^{-1} at 3 days of hydration and to 463 cm^{-1} for 7,14 and 28 days. Similarly, 521cm^{-1} which is closer to C_3A (522 cm^{-1}) and 520 cm^{-1} (C_3S) of unhydrated cement and at 3 days of hydration shifts to 519 cm^{-1} at 7 days and 520 cm^{-1} at 14 and 28 days. The peak at 1115 cm^{-1} which is of Ettringite is observed at 3 and 7 days of hydration has a shift to 1116 cm^{-1} at 14 days and to 1115 cm^{-1} at 28 days of hydration. The peak 521cm^{-1} unhydrated cement (C_4AF) has shift to 519 cm^{-1} (3, 7, 14

days) and back to 521 cm^{-1} at 28 days of hydration. The peak 659 cm^{-1} (C_4AF) for plane cement has 665 cm^{-1} (3-days), 656 cm^{-1} (7-days), 666 cm^{-1} (14-days). The peak 714 cm^{-1} is of Calcium Carbonate phase is observed at 3, 7,14 and 28 days of hydration. The peak of 923 cm^{-1} (β-C_2S) of unhydrated cement has reduced with the increase in hydration period, while a shift to 988 cm^{-1} at 3 days, 989 cm^{-1} at 7 days and 993 cm^{-1} and 991 cm^{-1} at 14 and 28 days is an indication of Tobermorite and Jennite. The peak 1456 cm^{-1}, 1418 cm^{-1}, 1422 cm^{-1}, 1423 cm^{-1}, of unhydrated cement, 3, 7,1 4, 28 respectively is an indication of Calcite phase. An increase in the intensity of Ettringite peak can be observed at 3433 cm^{-1} with respect to increase in the duration of the hydration, shown in Figure 3.15. The peaks at 3643 cm^{-1} (unhydrated cement), which is an indication of Portlandite phase, has a shift to 3644 cm^{-1} at 14 days and to 3643 cm^{-1} at 28 days of hydration. An increase in intensity can also be observed in Figure 3.13.

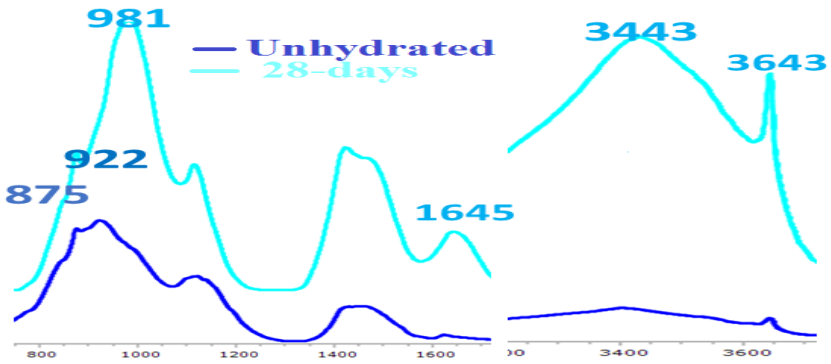

Figure 3.13. Peak variations observed in OPC-53 samples in unhydrated cement and 28 days of hydration.

3.4.5.2. Fourier Transform Raman Spectroscopy (FTRS)

FTRS tests were conducted on BRUKER® RFS 27, with a scan range 50 to 4000 cm^{-1} with a resolution of 2 cm^{-1} for a excitation of 1064. FTRS works on the functional principle of Raman Scattering, the excitation is UV visible NIR radiation of high intensity. Similar to FTIR, FTRS is helpful in determining the nuclear motion but it differs in the approach because in FTRS there should be a change in the molecule polarizability. So any variations which are weak or non existent in IR can be observed in RS and vice-versa (Bonen D. *et al.* 1994). Silicate bands which dominate the IR spectra are weak in RS, so trace elements can be detected. Sulfates gives a sharp peaks in RS. IR spectra is dominated by the ν_3 bands at 1000-1200 cm^{-1} region (Black L. *et al.* 2016). The RS is similar to NMR and FTIR which probe the local structure on the atomic nearest neighbour and next-nearest neighbour scale and hence provides unique information when compared with diffraction studies (Kirkpatrick R. J. *et al.* 1997). C_3S, Triclinic-C_3S, C_2S,

β-C_2S, γ-C_2S , C_4AF, CSH, Anhydrite phases are observed over the 50 to 4000 cm^{-1} region while the phases are observed for all the respective duration.

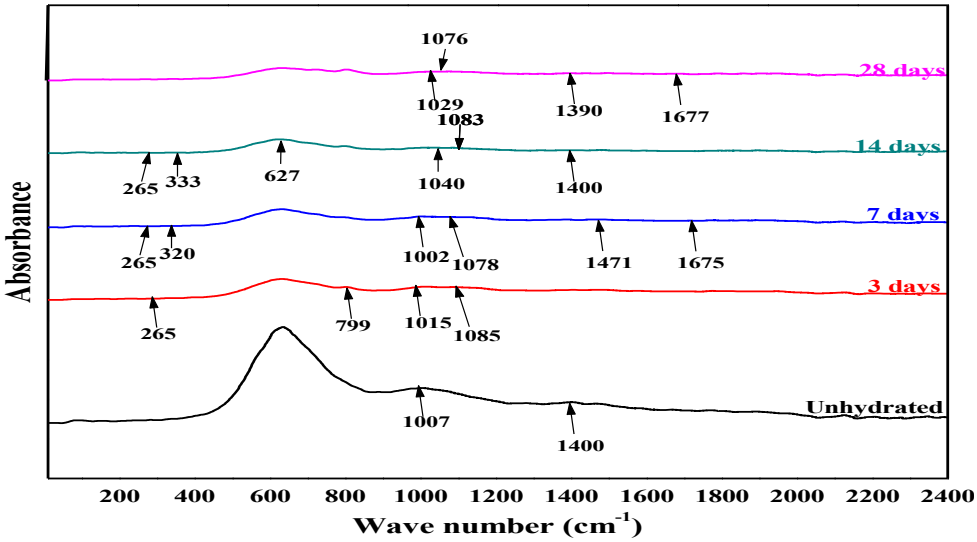

Figure 3.14. FTRS plots of PPC samples of unhydrated cement and 3, 7, 14, 28 days of hydration.

The FTRS plots of PPC samples at different stages of hydration are shown in Figure 3.14. The corresponding peaks observed for plain cement powder of PPC are 633, 1006, 1400, 1560, 2126, 2209, 2274, 2346, 2389, 2342, 2538, 2692, 2746, 2871 cm^{-1}. The peak 265 which is of fly ash (Bensted J. 1977). At 3-days of hydration a new peak at 336, 801 cm^{-1} are generated

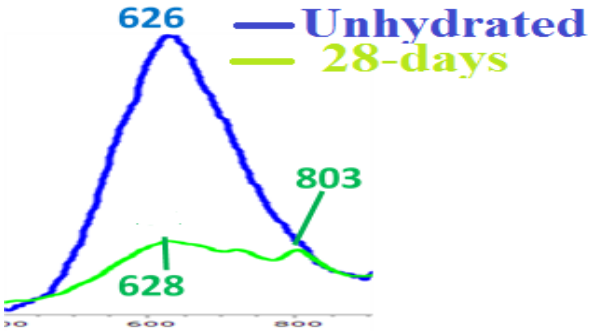

Figure 3.15. Variation in peak intensities of PPC samples of unhydrated cement and at 28 days of hydration.

and there was an increase in the absorbance values at 1085 cm^{-1} which is hemi carboaluminate has been initiated because of the hydration process (Newman S.P. *et al.* 2005). The peak at 333 cm^{-1} is an indicator of the development of CSH (Robertson K. *et al.* 2013) while 334 cm^{-1} peaks correspond to C_3S (Tarrida M. *et al.* 1995) and the peaks at 320, 336, 344 cm^{-1} correspond to CSH and C_3S phases. Increase in the peak intensity is observed at 722 cm^{-1} which is an indication of β-C_2S phase (Bonen D. *et al.* 1977). The peak at 803 cm^{-1} which is obtained at 28 days is developed over the 796 cm^{-1}, 801cm^{-1} which are the peaks of β-C_2S. The peak at 925

cm^{-1} at 14 days of hydration which is an indication of Alite phase (Bonen D. *et al.*1977). The oxidizing peak C_3S oxidizing peak 1040 cm^{-1} for 14 days of hydration in not observed at the

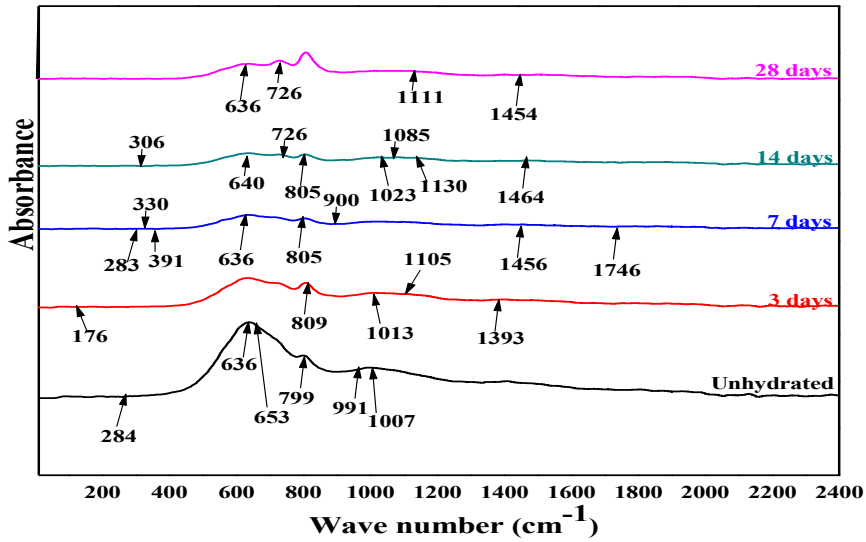

Figure 3.16. FTRS plots of OPC-43 samples of unhydrated cement, and 3, 7, 14, 28 days of hydration

end of the 28 days of hydration. The peaks 626 which is an indicator of triclinic C_3S (John B. *et al.* 1976) and the peaks that are closer by are 633, 631, 628 cm^{-1} should be an indicator of triclinic C_3S. The reduction in the peak intensity of C_3S with the increase in the hydration period is shown in Figure 3.16. The peak 1675 cm^{-1} earlier represented to Ettringite (Ghosh S.N. *et al.* 1980) is observed for PPC at 7 days and 1679 is at 3 and 28 days.

The FTRS peaks for OPC-43 samples at different days of hydration is shown in Figure 3.16, The peak at 306 cm^{-1} for 3 days of hydration is also an indicator for C_4AF, and the peaks

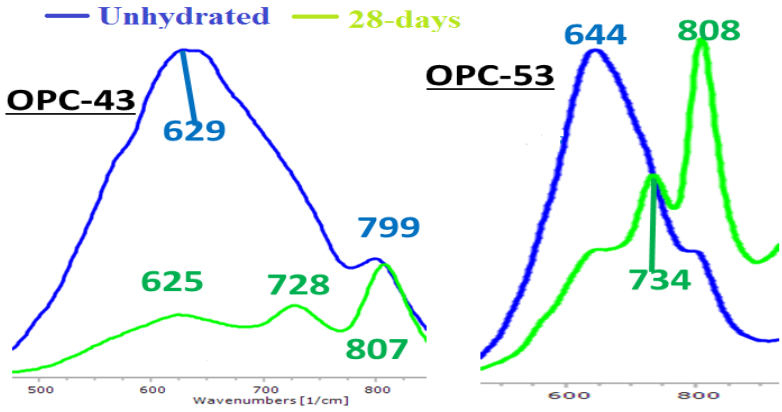

Figure 3.17. Variation in peak intensities of OPC-43 and OPC-53 samples of unhydrated cement and 28 days of hydration.

636, 634, 635, 637 cm^{-1} are indication of C_3S. Similar to peaks observed in PPC samples have gradually reduced with increase in hydration as shown in Figure 3.17. The peak at 330 cm^{-1} is an indication of CSH. The peaks at 799 cm^{-1} (unhydrated) which is β-C_2S, while the 807 cm^{-1} (3-days), 804 cm^{-1} (7-days), 805 cm^{-1} (14-days), 807 cm^{-1} (28-days) closer to 805 cm^{-1} represents the C_3S phase. The peaks of 730 cm^{-1}, 734 cm^{-1}, 722 cm^{-1},799 cm^{-1} represents the β-C_2S phase and these peaks are close to 728 cm^{-1}, 726 cm^{-1}, are observed and a development of

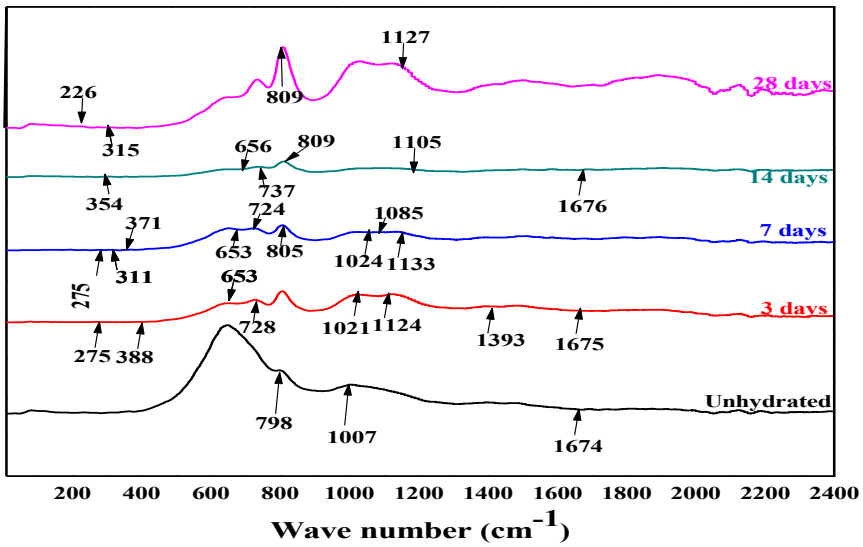

Figure 3.18. ***FTRS plots of OPC-53 samples of unhydrated cement and 3, 7, 14, 28 days of hydration***

peak intensities was observed in Figure 3.16 at 28 days of hydration. The peak at 1085 cm^{-1} correspond to Aragonite and also calcite is observed at 14 days of hydration for OPC-43. The peaks 3690 cm^{-1} which is closer to 3692 cm^{-1} is an indication of Calcium Aluminate Hydrate (CAH) observed in OPC-43. The FTRS peaks of OPC-53 at different stages of hydration is shown in Figure 3.18, peak 242, 288, 334, 361 cm^{-1} which is an indication of C_3S and the bands 243, 238, 290, 336 $cm^{-1}$are also an indicator of C_3S. The peak at 1674 cm^{-1} is an indicator of Calcite, and is observed at various stages of hydration similar to that observed in PPC and OPC-43 samples. The reduction in the peak intensities at 644 cm^{-1} of unhydrated cements, has gradually reduced with the increase in hydration as shown in Figure 3.17.

3.4.6. Compressive Strength

The compressive strengths obtained for these three GoC is shown in Figure 3.19. For each GoC a set of three samples are cast, at their respective durations *i.e.* 3, 7, 14 and 28 days of hydration. After the desired curing period, the samples are taken out of the curing tank and dried to open air, and tested for Compressive Testing Machine (CTM). The PPC samples has the least compressive strength at 28 days of hydration, while OPC-53 has the highest. From the PSA the OPC-53 has finer PSD, and PPC has the coarse particle size, while OPC-53 has higher

concentrations of CaO and lower concentrations of SiO_2 among major oxides and this is vice-versa for PPC. XRD analysis indicated higher concentrations of Portlandite for OPC-53 and the lowest for PPC cement samples. With all these variations observed, the OPC-53 cement has better compressive strength and PPC does not have relatively higher compressive strength. PSD, XRF and XRD analysis of OPC-43 samples indicated that the most of the mechanical properties shall range in between PPC and OPC-53. Hence, the

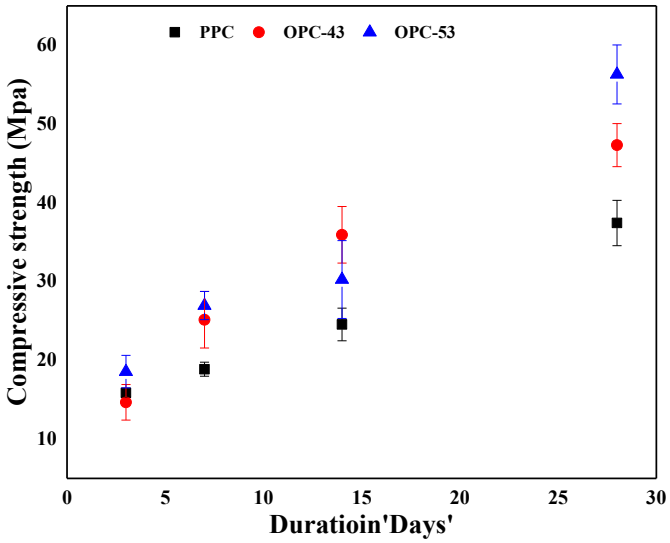

Figure 3.19. Compressive Strength of PPC, OPC-43, and OPC-53 at different days of hydration

compressive strength of OPC-43 ranges in between *i.e.* 33 MPa and 53 MPa**.**

3.5. Conclusions from this chapter

- The particle size distribution studies indicate that particle size of OPC-53 is finest while PPC is coarsest.
- From the XRF analysis it can be concluded that OPC-53 has higher concentration of CaO, and PPC has the least CaO concentration. CaO plays a crucial role in the formation of CSH gel and Portlandite. This confirms high early strength in OPC.
- Due to the inclusion of fly ash, the concentration of SiO_2 is greater in PPC sample compared to the two cements. The secondary CSH formation is due to this and hence later gain in compressive strength is observed in PPC.
- XRD studies indicate the same peaks for all the cements, however the major difference between PPC and OPC grade of cement is the Langbeinite peak, which is not found in the OPC samples. This peak is significant for PPC samples. Langbeinite which is a alkali sulphate increases the early strength and is a set-controlling agent.

- XRD analysis studies indicated the increase in concentrations of Portlandite, and a reduction in the concentrations of Calcite with the increase in the hydration periods for all the three cements. However, OPC-53 and OPC-43 has greater peak intensities of Portlandite when compared to PPC samples, indicating earlier strength gain.
- The FTIR spectroscopy analysis indicates an increase in the absorbance values of Belite, Ettringite, CSH, Portlandite and a decrease in Alite with the increase in the hydration periods.
- Fourier transform Infrared spectroscopy (FTIR) and Fourier transform Raman spectroscopy (FTRS) are useful in detecting the phases of Alite and Belite, as XRD peaks overlap in the region of 28°- 33°. From the spectroscopy studies a02t these regions it was noted that spectroscopy study is a good alternative for the detection of various amorphous phases present in cements.

Chapter-4

Thermal characterization of Portland cements at elevated temperatures

Chapter-4

Thermal characterization of Portland cements at elevated temperatures

4.1. General

The PSD, elemental concentrations, chemical oxides, and phase composition governs the mechanical properties of cement and thus of concrete. As indicated from the studies conducted on the unhydrated PC and hydrated samples at 3, 7, 14 and 28 days of hydration, , the OPC-53 has the highest compressive strength and PPC has the least among three GoC. The PSD indicates that OPC-53 has finer particle sizes Figure 3.1, while PPC has coarser particles. The XRF analysis indicate that PPC has higher concentration SiO_2 and OPC-43 and OPC-53 have higher concentrations of CaO. The XRD analysis studies indicate greater concentrations of Portlandite in OPC-53, and lower concentrations in PPC. The FTIR and FTRS analysis indicate the formation of new wavenumber and formation of new absorbance peak with the progress of hydration, which is an indication of higher concentration of new phases formed in PC. With the increase in hydration period the OPC-53 samples have shown superior compressive strength and PPC has the least shown in Figure 3.19. The effects of elevated temperatures on the hydrated PC samples of PPC, OPC-43 and OPC-53 after 28 days of hydration were investigated.

To understand the effects of temperature on the hydrated PC, thermal analysis tests such as Thermo gravimetric analysis (TGA), Differential thermal analysis (DTA) and Differential scanning calorimetry (DSC) tests are conducted for identifying the thermal response of PC to heat loads on the pulverised PC samples after 28 days of hydration. The variation in the heat flow and mass loss taking place at critical temperatures regions in the samples of PPC, OPC-43 and OPC-53 are considered and at those temperature regions further experimental investigation are carried using compressive strength, CHNS-O elemental

analysis, XRD, FTIR, FTRS tests are conducted at these temperatures, and the experimental program is shown in Figure 4.1.

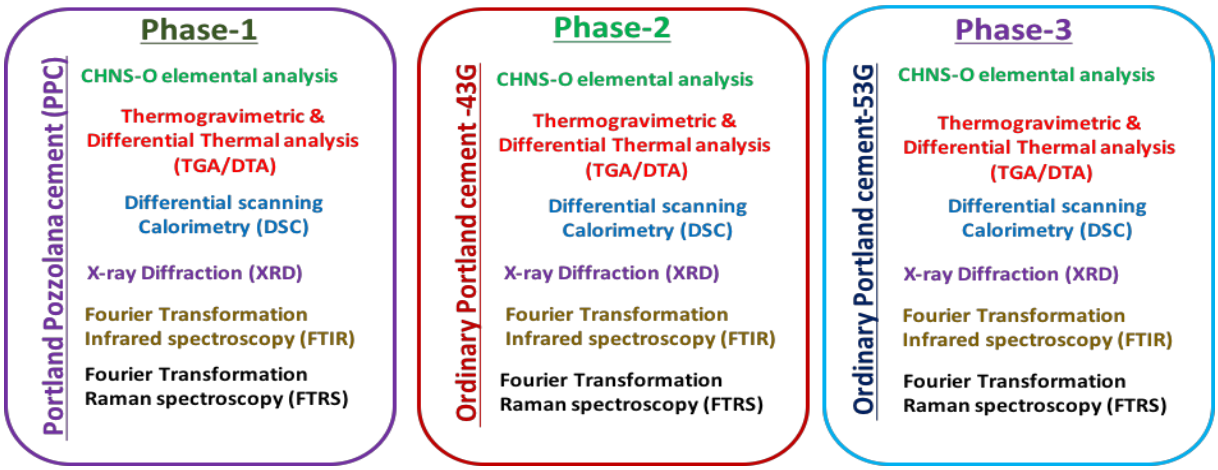

Figure 4.1. Various tests carried on PPC, OPC-43 and OPC-53 specimens subjected to elevated temperatures.

4.2. Experimental program

The tests are carried on the three GoC *i.e.* PPC, OPC-43 and OPC-53 at elevated temperatures for which the list of equipment is detailed below, apart from the new tests that are carried in this section:

4.2.1. CHNS-O elemental analysis

CHNS-O elemental analysis was carried out to determine the presence of elements such as carbon (C), Hydrogen (H), Sulphur (S), Nitrogen (N) and oxygen (O) present in PPC and OPC-53 by using Thermo Finnigan®, FLASH EA 1112 equipment.

4.2.2. Thermogravimetric Analysis (TGA)

TGA analysis of the samples are conducted with the help of a TG/DTA analysis using NETZSCH STA 2500 ® at a heating rate of 10 ºC/min in argon atmosphere with an initial temperature of 27 ºC to 800 ºC to determine their response (*i.e.*, the percentage weight loss with respect to the original weight).

4.2.3. Differential Thermal Analysis (DTA)

DTA of PC cast samples are conducted using NETZSCH STA 2500® at a heating rate of 10 ºC/min in an argon atmosphere with an initial temperature between 27 ºC going to 800 ºC. This analysis helps in estimating the endothermic or exothermic behaviour of the sample by recording the difference in the temperature between the sample and reference material (*i.e.*, Alumina).

4.2.4. Differential Scanning Calorimeter (DSC)

DSC analysis is carried on NETZSCH5 STA 449F1® at a heating rate of 10 ºC/min with a temperature range of 27 to 700 ºC.

Table 4.1. Difference between TGA, DTA and DSC analysis.

Aspect	TGA	DTA	DSC
Instrument	Thermo balance	DTA apparatus	Calorimeter
Graph	Mass Vs Temperature or Time	ΔT Vs Temperature	dH/dT Vs Temperature
Parameter Measured	Measures mass change as temperature (or) Time increasing during heating or cooling	Measures temperature differences during heating or cooling.	Heat observed during heating or cooling

4.3. Results and Discussions

The CHNS-O elemental analysis, TGA, DTA, DSC, XRD, FTIR, FTRS and compressive strengths tests are carried out on the three GoC *i.e.* PPC, OPC-43, OPC-53. These tests are carried out on the pulverised hydrated samples at elevated temperatures, and from these tests the obtained results are discussed:

4.3.1. Thermal analysis

Thermal analysis is the primary method for analysing and capturing the data obtained from the physical and chemical changes that take place in samples subjected to thermal treatments is thermal analysis. Among the thermal analysis techniques, three techniques such as TGA, DTA, and DSC used to conduct tests on the PPC, OPC-43 and OPC-53 samples. The obtained plots are shown in Figure. 4.2 – 4.4.

4.3.1.1. Thermo gravimetric analysis (TGA)

TGA estimates the absolute amount of change and the rate of change in the weight of the sample, which is a function of time or temperature in a controlled environment. Using TGA various properties such as thermal stability, atmosphere effects at different conditions, oxidative stability, moisture and volatile content, can be determined. The TGA plots showing the mass loss, obtained for the three different GoC samples are shown in Figure 4.2. The mass loss changes taking place in the PPC sample from room temperature (27 °C) to 150 °C (9.76%), is almost linear. A sudden mass loss of 5.55% occurs in the range 410 °C - 450 °C. After the sample exceeds the temperature of 500 °C the mass loss is not linear; at 600 °C - 700 °C the mass loss in the sample is 5.25%. At temperatures exceeding 700 °C the mass loss

is stable. The OPC-43 samples mass loss was shown in Figure 4.1. The mass loss taking place in the sample from room temperature to 150 °C is 8.65%. A sudden mass loss of 4.1% occurs in the sample at 410 °C - 450 °C, and at 650 °C - 680 °C the mass loss is 3.2%. For OPC-43 mass loss is stable in the sample after exceeding a temperature of 700 °C. The mass loss taking place in the sample is slightly higher for the OPC-43 sample, when compared to the other two GoC. The mass loss taking place in the OPC-53 samples at different temperatures

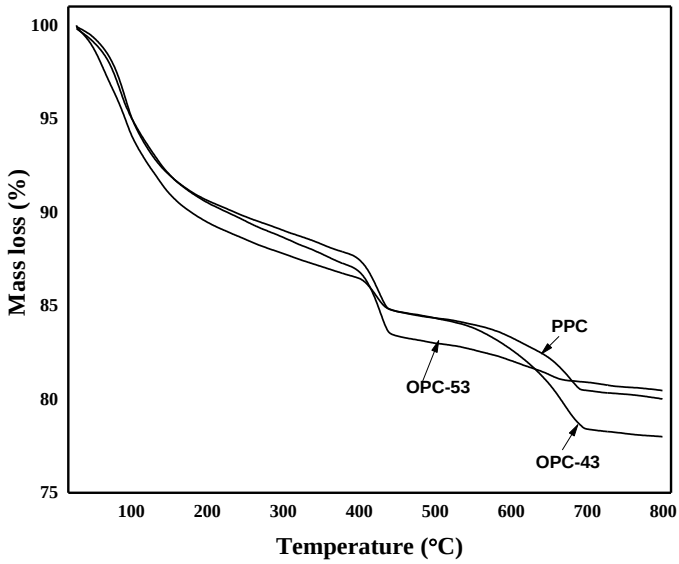

Figure 4.2. Mass loss of PC estimated using TGA.

is shown in Figure. 4.1.The mass loss is 8.39% that took place in the OPC-53 sample from room temperature to 150 °C, similar to the other two GoC a mass loss is observed in the region of 415 °C - 450 °C, and a mass loss of 4.13% is observed in the sample. A constant mass loss is observed in the sample after 450 °C, and no sudden mass loss is observed, which is not in the case of the other two GOC. The mass loss in OPC-53 sample is the least among the other two GOC, and OPC-43 has greater mass loss.

4.3.1.2. Differential thermal analysis (DTA)

The plots obtained from the DTA analysis of the PPC, OPC-43 and OPC-53 with respect to the standard sample in this case an aluminium crucible from room temperature to 800 °C is shown in Figure 4.3. The PPC samples has shown four regions of interest, and the first endothermic peak is at 63 °C, and the second being at 99 °C and these peaks are caused due to the evaporation of water and bound water from the samples. It is mentioned by other researchers that the water present in the hydrated cement paste can be completely evaporated from the samples at 120 °C (Alarcon-Ruiz, L. *et al.* 2005). It observed by (Alarcon-ruiz L. *et al.* 2005) that two endothermic peaks are observed at the temperatures ranges of 110 °C – 170 °C, due to the decomposition of Gypsum, Ettringite, and loss of water in the Carbo-

Aluminates, however such peaks are not observed in all the three GoC of cements. A continuous loss of mass takes place from 171 °C to 300 °C due to the decomposition of CSH, which releases the bound water present in the gel. This phenomenon can be observed from the TGA plots and this mass loss can have an effect on the heat flow that can be seen from DTA

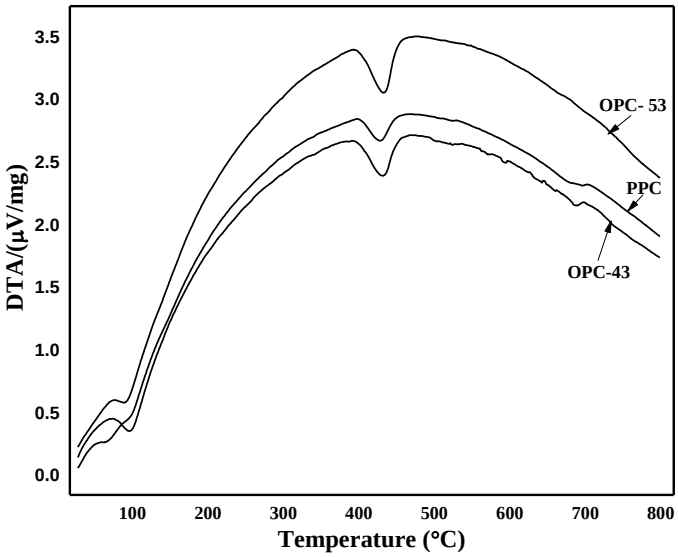

Figure 4.3. Differential temperatures of PC at varying temperatures using DTA.

plots. The third endothermic peak is observed in the PPC sample at 428 °C which is due to the de-hydroxylation of Portlandite from the hydrated cement paste. The fourth endothermic peak is observed in the sample at 702 °C for the PPC sample, this is endothermic peak is formed due to the de-carbonation of Calcium Carbonate and this followed by a mass loss observed in the TGA plot of PPC. Similar to the PPC analysis, the OPC-43 has shown three ROI, which is at 96 °C, 431 °C and 689 °C, while OPC-53 has shown two ROI that is at 87 °C, and 432 °C.

4.3.1.3. Differential scanning calorimeter (DSC)

DSC yields a graph of the heat flow between the sample and reference crucible at various temperatures. The DSC plots of the three GoC are shown in Figure 4.4. The endothermic reaction is indicated by a upward peak and the down peak indicates an exothermic reaction. After 28 days of hydration and pulverisation the sample is placed in the DSC apparatus for analysis. Two major peaks are observed in the plots obtained from the DSC analysis. The first endothermic peak observed at temperatures below 100 °C, is formed due to the loss of hydration water. From Figure 4.3 the variations in the heat flow of the samples can observed, wherein PPC sample has the least heat flow capability and OPC-53 has the highest. The second peak is formed in the region of 400 °C to 460 °C for all three GoC, due to the dehydroxylation of Portlandite, which is a major hydrated product. Apart from the peaks observed in the Figure 4.3, few peaks are also observed by other researchers, *i.e.* an

endothermic peak in between 165 °C – 205 °C, and 255 °C – 300 °C due to the decomposition of Ettringite and C_4AH_{13} which are the byproducts of C_3A. An endothermic peaks formed at 155 °C and 390 °C are due to the higher concentrations of iron- substituted

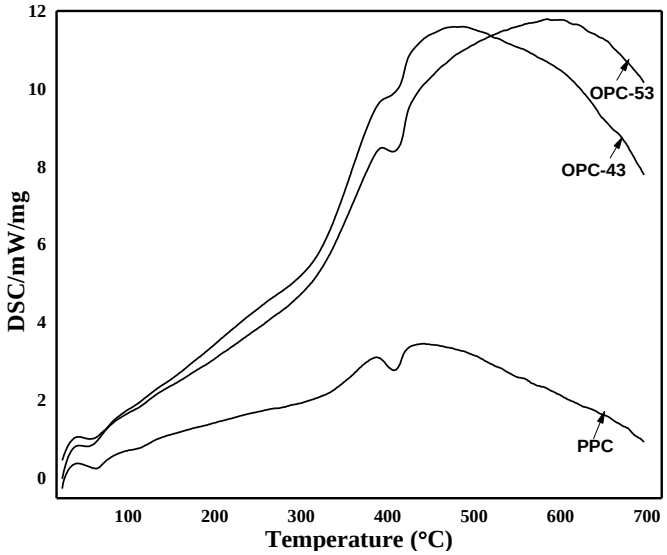

Figure 4.4. Heat flow taking place in PC samples using DSC.

ettringite and Fe_2O_3 solution being formed, and both of these products are formed from C_4AF (Sha W. *et al.* 1999). The thermal analysis carried out by (Stepkowska *et al.*, 2005) indicates the decomposition of Portlandite in Argon environment at 450 °C for OPC-33 and OPC-43. At temperatures 680 °C to 710 °C the variation in heat flow is due to the decomposition of Calcite in OPC-33 and OPC-43 GoC.

4.3.2. Temperature profiles of samples

The thermal analysis tests conducted on the PPC, OPC-43 and OPC-53 samples have indicated several regions of interest, indicate a significant decay in the chemical properties of hydrated cement. Four critical temperatures are selected, to understand the damage caused by these chemical changes on the physical and compressive strength of the hydrated cement. 27 °C, 100 °C, 400 °C, 500 °C and 800 °C are selected as temperatures of interest, at which the samples are exposed to dry heat in a muffle furnace. The temperature profile's to which these three grades of PC specimens are subjected to, are shown in Figure 4.5. The rate of temperature loading is 5 °C/min until the desired temperatures are reached, and once the desired temperatures are reached the temperature is sustained for a period as shown in Figure 4.4. As the temperature is increased the hold time is also increased. It is assumed by doing so a uniform saturation temperature is maintained within the sample *i.e.* at the periphery as well as the core of the sample. After the desired hold times have been achieved the samples are

cooled to room temperature inside the furnace and further analysis described in the section 4.3.3 – 4.3.8 is carried out.

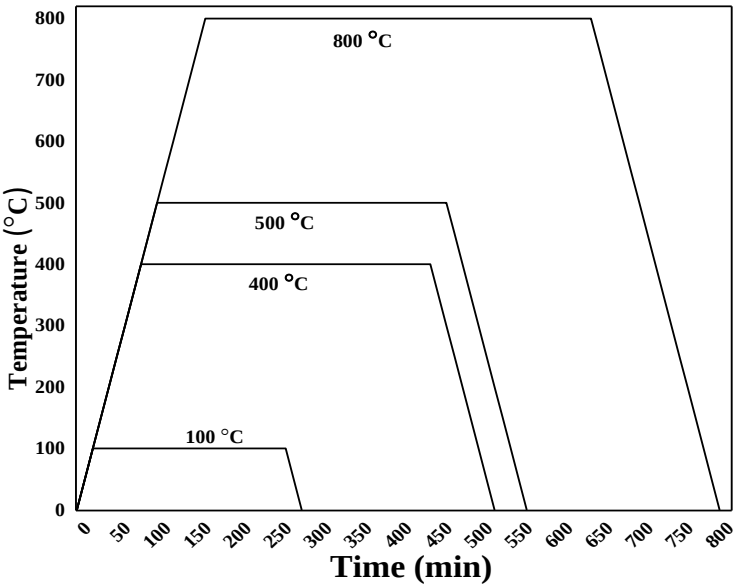

Figure 4.5. Temperature profile to which specimens are subjected.

4.3.3. Sample preparation of chemical analysis

After being subjected to the desired temperature as shown in Figure 4.5, cooled specimens are placed in a compressive testing machine (CTM). The crushed specimens are then pulverized for use in XRD, CHNS-O element analyses, FTIR, and FTRS analysis, all of which require powdered specimens. For pulverization, 25 grams of each specimen are collected, and care is taken to ensure that the powders are not collected from the surfaces of the specimens. The crushed specimens are combined with Toluene at a specimen to weight ratio of 1:10. Milling is performed with Tungsten Carbide balls for 30 minutes and is divided into three cycles, each of which consists of 5 minutes of milling time and 5 minutes of resting time. The wet specimens after milling are placed at room temperature for the Toluene within them to evaporate, the dry powder obtained after the drying at the respective temperatures are used for testing. The same procedure is repeated for all the samples at their respective temperatures. The sample preparation for the chemical analysis is similar to methodology described in Chapter-3, the major difference being that the samples are collected from the cores of the specimen which are subjected to different temperatures.

4.3.4. CHNS-O elemental analysis of PC samples

The elemental content present in the PC samples at temperatures of 100 °C and 800 °C for PPC, OPC-43 and OPC-53 samples is identified as shown in Table 4.2. The elemental percentages of oxygen content at 100 °C is higher for PPC samples, while OPC-53 has the

least amount of oxygen present at this temperature. The loss of elemental oxygen percent is 55.02%, 26.97%, and 21.62% for PPC, OPC-43 and OPC-53. Sulfur content is not observed for OPC-43 and OPC-53, while smaller concentrations are observed for PPC samples. No traces of nitrogen elements are observed in all the three 3 GoC in the range of 100 °C to 800 °C. PPC has higher concentrations of elemental carbon, in comparison to other two GoC, while OPC-53 has lower concentrations at 100 °C. The loss of elemental hydrogen is 84.41%, 72.43% and 68.73% for PPC, OPC-43 and OPC-53 respectively. The elemental carbon content increased with increasing temperatures from 100 °C to 800 °C, for the OPC-43 and OPC-53 samples, while a drop in elemental carbon is observed for PPC samples.

Table 4.2. CHSN-O elemental analysis of PC at 100 °C and 800 °C.

Elements	**PPC**		**OPC-43**		**OPC-53**	
	100 °C	**800 °C**	**100 °C**	**800 °C**	**100 °C**	**800 °C**
Carbon	2.119	0.966	1.871	1.996	1.568	1.605
Hydrogen	1.731	0.270	1.650	0.4551	1.976	0.618
Nitrogen	None	None	None	None	None	None
Sulfur	0.248	0.475	None	None	None	None
Oxygen	8.229	3.7018	6.212	4.599	4.683	3.671

4.3.5. Compressive strength of PC samples

From the thermal analysis conducted on the three GoC *i.e.* PPC, OPC-43 and OPC-53, four critical temperatures are selected, which are 100 °C, 400 °C, 500 °C and 800 °C, apart from room temperature. At each temperature three samples are selected for each GoC, for which

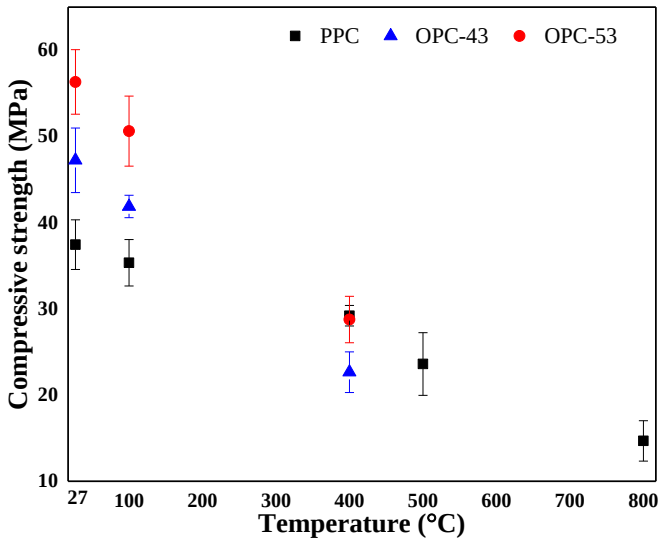

Figure 4.6. Compressive strength of PC samples at elevated temperatures.

samples of 50 x 50 x 50 mm^3 cubes are cast. Among the three GoC of cement PPC sample has the least compressive strength, while OPC-53 has the highest average compressive strength. Figure 4.6 shows the compressive strengths of PPC, OPC-43 and OPC-53 at various temperatures. Figure 4.6, 4.7 & 4.8 shows the surface pictures of the physical changes that the

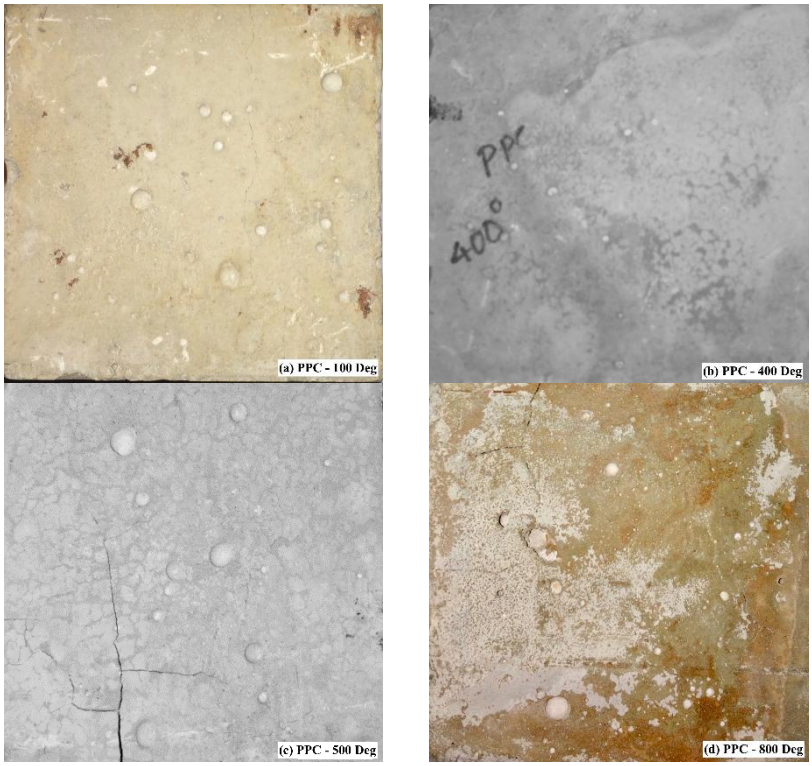

Figure 4.7. Surface behaviour of PPC samples subjected to different temperatures.

PPC, OPC-43 and OPC-53 samples undergo at 100 °C, 400 °C, 500 °C and 800 °C. PPC, OPC-43 and OPC-53 were able to withstand external loads up to 400 °C; the OPC-53, and OPC-43 specimens completely failed to carry any load after 400 °C, while PPC lost 61% of its compressive strength at 800 °C. In other research conducted by (Heikal, M., 2006) the fly ash specimens have shown superior compressive strength properties at 650 ºC in comparison to OPC. The loss in compressive strength of PPC is 5.61%, 22%, 37%, and 61% at temperatures of 100 °C, 400 °C, 500 °C and 800 °C. The physical changes taking place on the surface of the sample are shown in Figure 4.7. For the OPC-43 samples, the loss of compressive strength is 11% and 52% at 100 °C and 400 °C, while the physical changes on the surface of the samples are shown in Figure 4.8. Major variations in the chemical oxide concentrations obtained from XRF analysis, for the three GoC is as shown in Table 4.3. Similarly, for OPC-53 samples, the loss of compressive strength is 10% and 49% at temperatures of 100 °C and 400 °C, while the physical chances on the surface of the samples at 100 °C, 400 °C, 500 °C and 800 °C are shown in Figure 4.9. The OPC-43 and OPC-53

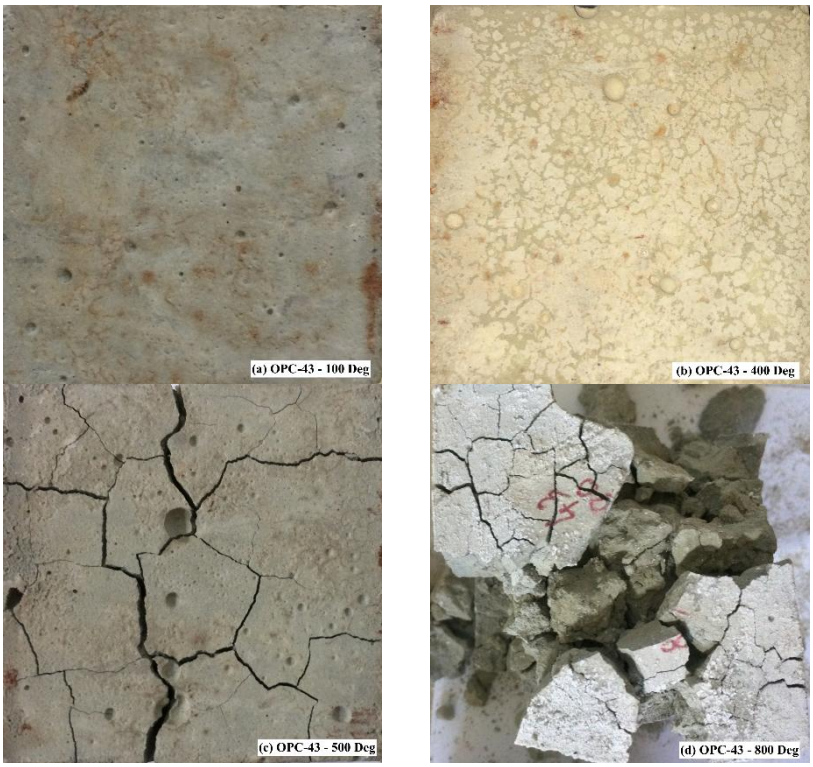

Figure 4.8. Surface behaviour of OPC-43 samples subjected to different temperatures.

specimens completely failed (or pulverized) at 400°C. Hairline fractures became visible in the PPC at 500 °C, however these cracks are only at the surface, while the crack widths

Table 4.3. Chemical Oxide concentrations in PPC, OPC-43 and OPC-53

GoC	CaO	SiO_2	Fly ash
PPC	35.95	34.67	30-50
OPC-43	49.97	27.51	15-30
OPC-53	66.86	16.71	15-30

of 1-2 mm and crack length extending from one end to the other are formed within OPC-43 and OPC-53 samples. At 800 °C, the OPC-43 and OPC-53 completely disintegrate and become unable to samples by (Mendes *et al.* 2008). The PPC specimen is able to carry a load the same temperature at 800 °C. Overall PPC performs better than OPC-43 and OPC-53 when the hydrated cubes samples are subjected to different heat cycles. An equation is proposed to predict the compressive strengths for the three GoC with respect to temperature, in Appendix-A.

4.3.6. XRD analysis of PC samples

The thermal analysis, carried on the three GoC, and four critical areas of interest are selected for the XRD analysis. These temperatures are 100 °C, 400 °C, 500 °C and 800 °C and for these temperatures the XRD analysis is carried for the three GoC. For the XRD analysis mineral phases such as Alite, Belite, Aluminate, Ferrite *etc.* are selected because of the

significant role they play in the formation of hardened cement paste during their hydration and the decay of these hydrated cement pastes during exposure to elevated temperatures.

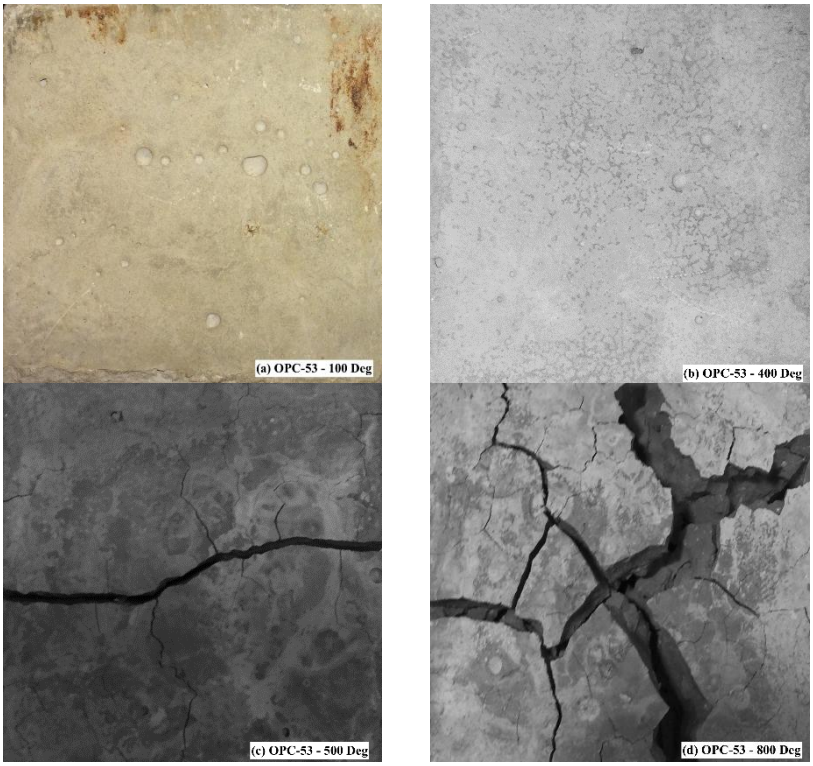

Figure 4.9. Surface behaviour of OPC-53 samples subjected to different temperatures.

4.3.6.1. XRD analysis of PPC

The XRD analysis of the PPC samples at different temperatures is shown in Figure 4.10, in the current study peak intensities less than 100 are not discussed, since the values less than that are assumed to be negligible. The Alite peak intestines are 208 at 27 °C, while the Belite peak intensity is observed at 27 °C which is 316. The Belite peak is not observed at other temperatures. The Portlandite phase is a major phase in the formation of hardened cement, and the relative peak intensities of this phase are 5222, 3055, 4330, 1251 at temperatures of 27 °C, 100 °C, 400 °C and 500 °C respectively. No peak intestines were observed for Portlandite phase at 800 °C from the Rietveld analysis. The peak intensities of CSH phase are 1631, 583, 490, 476, and 240 at 27 °C, 100 °C, 400 °C, 500 °C and 800 °C respectively. The relative peak intensities of gypsum are 686, 267, 214, 193 and 139 at 27 °C, 100 °C, 400 °C, 500 °C and 800 °C respectively. From the XRD tests, the peak intensities of Aluminate phase are in the range of 22°- 23° is observed at 27 °C and no significant peaks are observed at the remaining temperatures, while the variations in peak intensities of other phases are shown in Figure 4.12.

4.3.6.2. XRD analysis of OPC-43

The XRD analysis of the OPC-43 samples at different temperatures is shown in Figure 4.11. In the current study, peak intensities less than 100 are not considered. While Alite peak

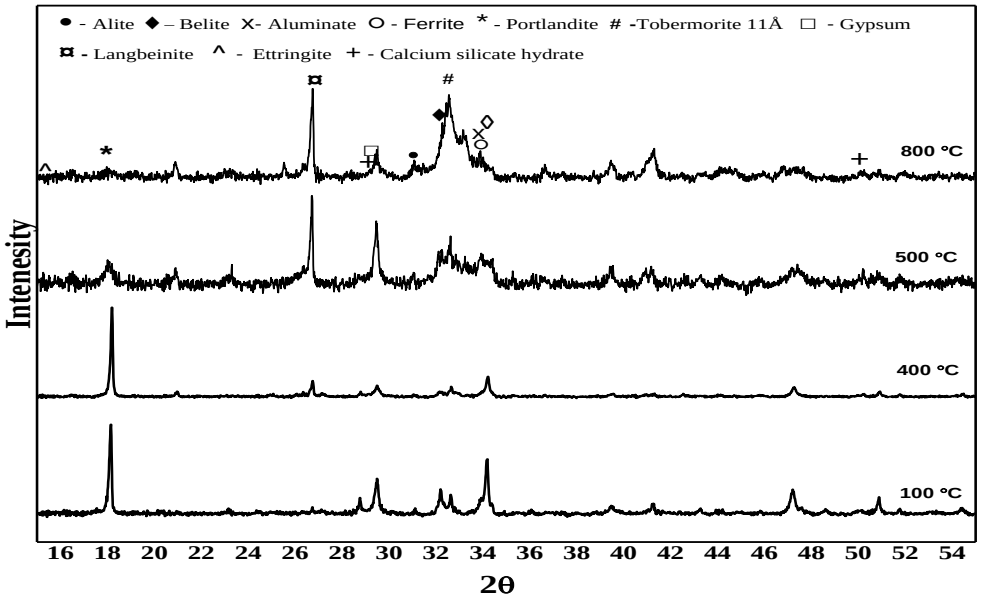

Figure 4.10. XRD analysis of PPC samples at different temperatures.

intensities are 2369, 920, 900, 866 and 559 at 27 °C, 100 °C, 400 °C, 500 °C and 800 °C respectively. The observed Belite peak intensities at 27 °C is 178, and this peak is not observed at other temperatures. The Portlandite phase is a major phase involved in the formation of hardened Cement and the relative peak intensities of this phase is 7603, 3080, 2233, 128 and 109 at temperatures of 27 °C, 100 °C, 400 °C, 500 °C and 800 °C respectively. The peak intestines of the Portlandite for OPC-43 are higher than PPC samples at room temperature, and the drop of peak intensities is slightly higher for OPC-43 sample. However, the peak intensities of OPC-43 for Portlandite was still observed at 800 °C, while this was not the case for the PPC samples. The peak intensities of CSH phase is 1184, 629, 944, 407, and 317 at 27 °C, 100 °C, 400 °C, 500 °C and 800 °C respectively. While the relative peak intensities of Tobermorite-11Å are 229 and 104 at 27 °C and 100 °C respectively. Similar, to PPC samples at elevated temperatures no peak intensities are observed for Aluminate phase other than room temperatures in OPC-43 samples, and the variations in peak intensities of other phases are shown in Figure 4.13.

4.3.6.3. XRD analysis of OPC-53

The XRD analysis of the OPC-53 samples at different temperatures is shown in Figure 4.12, in the current study peak intensities less than 100 are not considered. The Alite peak intestines are 1184, 629, 550, 417 and 307 at 27 °C, 100 °C, 400 °C, 500 °C and 800 °C respectively.

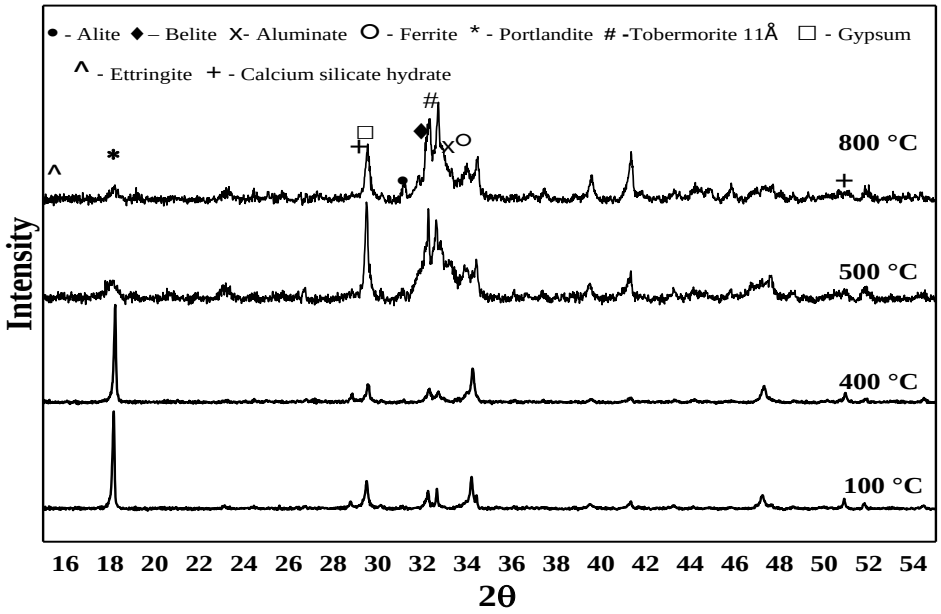

Figure 4.11. XRD plots of OPC-43 samples at elevated temperatures.

The Belite peak intensity observed at 27 °C which is 400, and this peak is not observed at other temperatures. The Portlandite phase being a major phase in the formation of hardened cement, the relative peak intensities of this phase is 17075, 2204, 1542, 120 and 178 at temperatures of 27 °C, 100 °C, 400 °C, 500 °C and 800 °C. The variations in peak intensities of other important phases is shown in Figure 4.13. The reduction in the peak intensities (is an indication of reduction in the phase concentration) was observed, with the increasing temperatures, as shown in Figure 4.13. These are not gradual, because the peak intensities of the phases are obtained from different samples tested at different temperatures. The peak intensities of the Portlandite is higher for OPC-53, samples at room temperature then the other two GoC, and the drop of peak intensities is greater for OPC-53 sample. However, the peak of intensities of Portlandite for OPC-53 is still observed at 800 °C, while this is not the case for the PPC samples. As mentioned earlier that the OPC-53 has the highest compressive strength among the three GoC, while the peak of Portlandite is also high, when compared two other two GoC. Hence one can say that Portlandite is crucial in governing the mechanical properties of PC when the samples are subjected to elevated temperatures. The peak intensities of CSH phase is 301 and 165 at 27 °C and 800 °C, while peak intensities re not observed at other

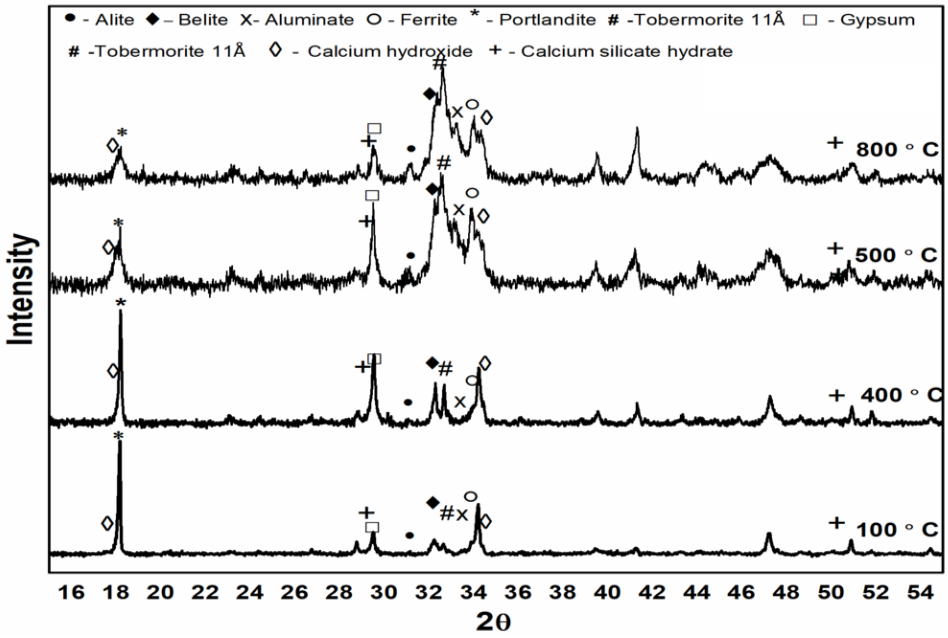

Figure 4.12. XRD plots of OPC-53 samples at elevated temperatures.

temperatures. Peak intensities are not observed at elevated temperatures for aluminate phase except at 27 °C, and the same observation is made with the other two GoC

4.3.7. FTIR analysis of PC samples

The infrared spectroscopy analysis of the three PC *i.e.* PPC, OPC-43, and OPC-53 are plotted in the Figure 4.14 - 4.18, at the temperatures of 100 °C, 400 °C, 500 °C and 800 °C respectively. Unlike the XRD analysis, the interpretation of the data obtained from FTIR plots is easier, as the changes taking place at the respective wave numbers. The wavenumber region of 400- 1000 cm^{-1} corresponds to bending vibrations, 1001 – 1500 cm^{-1} corresponds to single bond stretches, 1501 – 2000 cm^{-1} corresponds to double bond stretch, 2001 – 2500 cm^{-1} corresponds to triple bond stretch, and 2501 – 4000 cm^{-1} corresponds to Z-H single bond stretch such as O-H, N-H, and C-H bonds. From the three GoC of cements the following observations are made:

4.3.7.1. FTIR analysis of *PPC*

The FTIR plot of the PPC samples subjected to elevated temperatures of 100 °C, 400 °C, 500 °C, and 800 °C is shown in Figure 4.14. The absorbance value of 457 which is of C_3A shifted towards the higher wavenumber at 400 °C and is not observed after 500 °C and 800 °C. The wavenumber of 517 cm^{-1} which corresponds to C_3A or C_4AF, develops at temperatures of 500 °C and 800 °C, and increase in the absorbance values is also noticed. Two peaks are observed in the region of 870 – 1000 cm^{-1} at 100 °C; 874, 971 cm^{-1} which represent the β-C_2S and are

observed. As the temperatures increase to 800 °C four peaks are observed that is of 846, 875, 915 and 996 cm^{-1}. The peak 1109 cm^{-1} formed due to the S-O stretching of SO_4^{2-} observed in the sample at room temperature and is not observed at elevated temperatures ranging from 100 °C – 800 °C. With the increasing temperatures from 100 °C - 800 °C, there is a reduction in the absorbance intensity of the peak 1419 cm^{-1} which represents the Calcite (Ylmén, R. *et al.* 2009) in the sample. There is an increase in the absorbance peak intensity value at wavenumber 1468 cm^{-1} at temperatures of 500 °C and 800 °C for the PPC samples. A reduction in the intensity values of the Ettringite peak is observed at 3451 cm^{-1} at 100 °C, and decreases noticeably at 400 °C at a wavenumber of 3432 cm^{-1}. As the temperatures reach 500 °C and 800 °C the absorbance peaks were not observed in the samples. With the increasing temperatures from 100 °C - 800 °C, there was an increase in peak intensity of Portlandite phase at wavenumber of 3642 cm^{-1}.

4.3.7.2. FTIR analysis of OPC-43

The FTIR analysis of OPC-43 samples subjected to elevated temperatures of 100 °C, 400 °C, 500 °C, and 800 °C is shown in Figure 4.14. The peak absorbance value of 463 cm^{-1}, which is C_3A, is not observed after 400 °C (Ghosh S.N. *et al.* 1974). The peak absorbance values of 518 cm^{-1}, which belongs to C_4AF, has an increase in intensity with the increase in temperatures, and the increase in the formation of this peak intensity is shown in Figure. 4.14. The peak of C_4AF or Afwillite (Horgnies M., *et al.* 2013; Hughes T.L. *et al.* 1995) is observed at 618 cm^{-1}, and is observed at all temperatures. While the same is also observed for the polymorph of Calcium Carbonate at the wavenumber of 713 cm^{-1}. Two peaks are observed in the region of 874, 975 cm^{-1} which represents the β-C_2S and Aluminium Hydroxide (Ghosh S.N. *et al.* 1974; Fernández L. *et al.* 2012), found at 100 °C, at 400 °C. The absorbance peaks of 875 and 988, at 500 °C 874 and 935, as the temperatures reached 800 °C the peaks of 847, 874, and 917 were observed. The Ettrinigte peak at wavenumber 1114 cm^{-1} (Horgnies M. *et al.* 2013) is not observed after 100 °C. A new peak of 1141 cm^{-1} is formed once the temperatures reach 500 °C and 800 °C, which is not observed in the PPC samples at the corresponding temperatures. The Calcite peak of 1424 cm^{-1} observed at 100 °C has shifted towards the higher wavenumber with the increase in temperature, *i.e.* 1428, 1428, and 1471 cm^{-1} at 400 °C, 500 °C and 800 °C respectively. A similar behaviour of the Ettringite peak which was observed in PPC samples was observed in the OPC-43 samples. The wavenumber 3436, 3437 cm^{-1} of Ettringite phase at 100 °C and 400 °C, was not observed

after 500 °C. An increase in peak intensity of the Portlandite peak was observed with the increasing temperatures which can also be observed in the Figure 4.15.

4.3.7.3. FTIR analysis of OPC-53

The plots of OPC-53, at elevated temperatures of 100 °C, 400 °C, 500 °C and 800 °C obtained from the FTIR analysis is shown in Figure 4.16. The absorbance spectrum of OPC-53 increases with the increase in temperature, especially the wavenumber region in between the 800 – 1000 cm^{-1} shown in Figure. 4.16. The wavenumber of 713 cm^{-1} (Fernández L. *et al.* 2012) which is of Calcium Carbonate shifts towards the higher wavenumber region towards 719 cm^{-1} at 800 °C. As the temperatures increased from 100 °C - 800 °C an increase in the intensity of absorption values at wavenumber 519 cm^{-1} which represents C_3A phase was observed. Such a phenomenon is found to be common across the PPC and OPC-43. The adsorption values of 519 cm^{-1}, are higher for PPC and OPC-53 cements, in comparison to OPC-43 cements at 800 °C. The adsorption intensity of peak 1424 or 1474 cm^{-1} which correspond to Calcite, is higher than the peaks observed in the region of 800-1000 at 100 °C for OPC-43 and OPC-53 samples. However, with the increasing temperatures the adsorption intensities of 1424 or 1474 cm^{-1} reduce beyond 400 °C. such a phenomenon was not observed in the PPC samples at 100 °C. The adsorption peak of 1138 cm^{-1} is completely developed for OPC-53 at 800 °C, and shift towards the higher wavenumber at 1141 cm^{-1} is observed for OPC-43 cements, while for PPC the wavenumber of 1114 cm^{-1} is observed to shift towards the lower wavenumbers. The adsorption intensity is also lower in comparison to other two GoC. It is observed for all the three GoC that the wavenumber of 3433 cm^{-1} has higher adsorption intensities until the samples reaches temperatures of 400 °C, and then there is a reduction in the intensities. The adsorption peak of Portlandite observed at 3643 has the highest intensity at 800 °C, this can signify the higher concentration of Portlandite present in OPC-53 cements due to which the samples gains higher strength. The Figure 4.17 showing the major variations in the wavenumber values of 800-1000 cm^{-1} region. At 100 °C for all the three GoC two absorbance peaks are observed at 874 and 971 cm^{-1} for PPC; 874 and 975 cm^{-1} for OPC-43; and at 874 and 978 cm^{-1} for OPC-53. However as the temperatures reach 800 °C four absorbance peaks *i.e.* 846, 875, 915 and 996 cm^{-1} are observed for PPC; 847, 874, 917 and 997 cm^{-1} for OPC-43; 846, 875, 915 and 997 cm^{-1} for OPC-53 as shown in Figure 4.16. While the Figure 4.18 showing the major variations in the regions of 1400-1700 cm^{-1} are with the increase in temperature the absorbance peak at 1420 cm^{-1} (Calcite) at 100 °C, intensity reduces, since such peak is not observed at 800 °C. Such phenomenon is observed

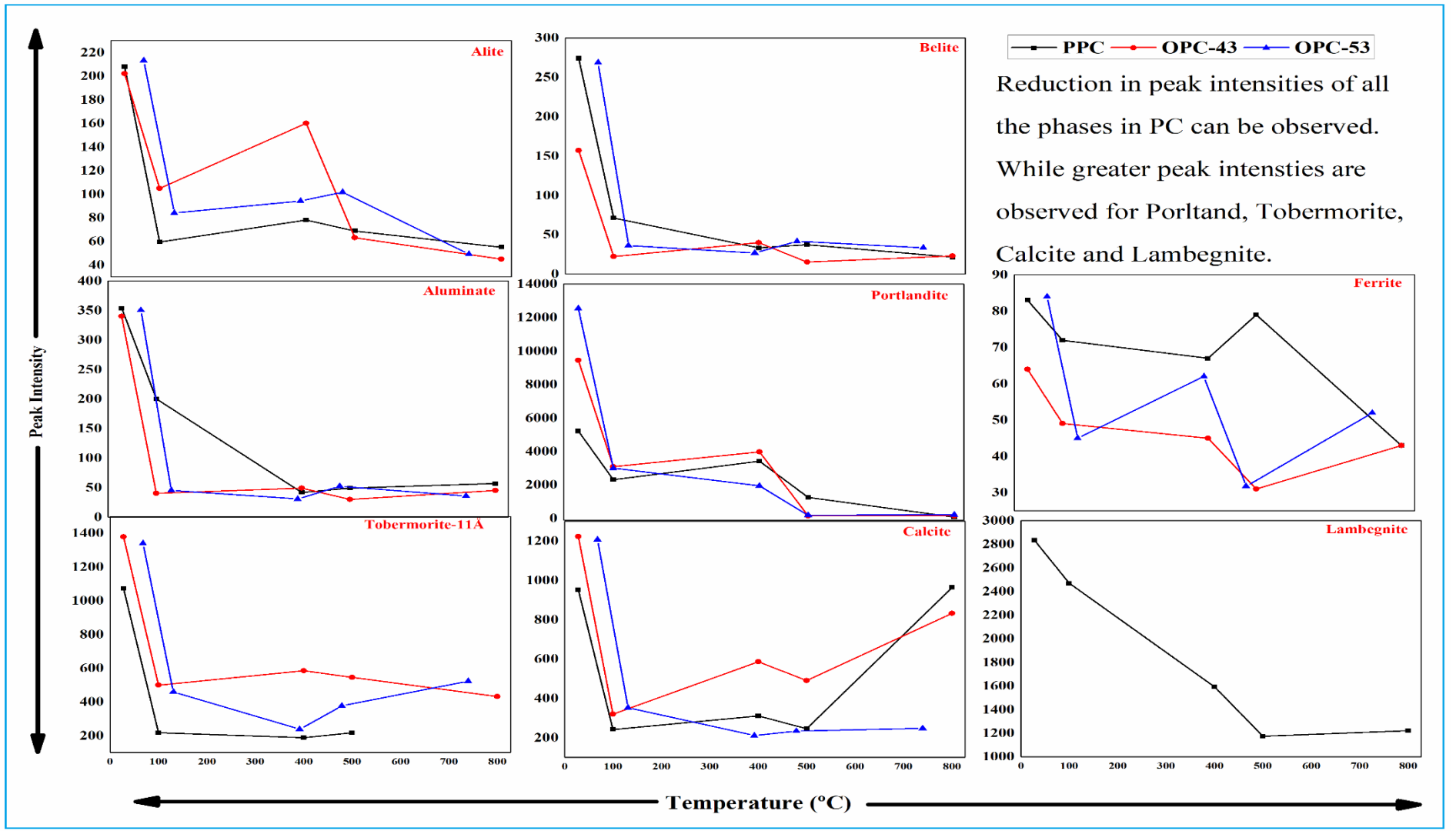

Figure 4.13. Variations in peak intensities of phases obtained from XRD analysis of samples at elevated temperature

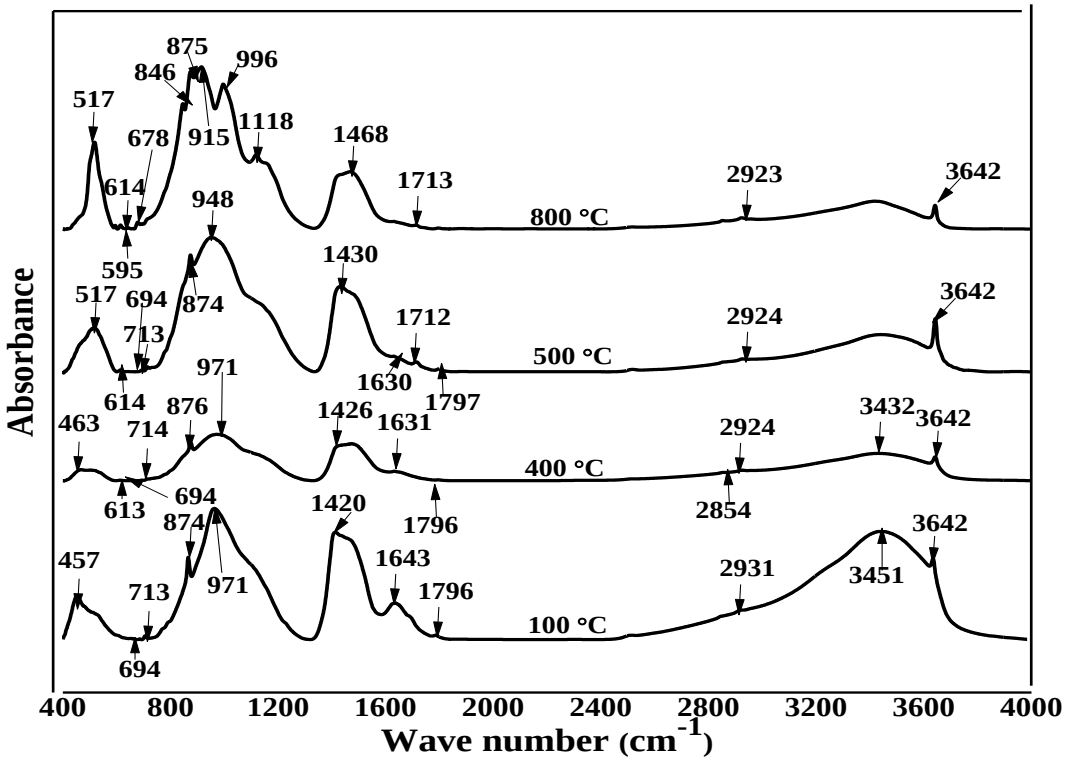

Figure 4.14. FTIR analysis of PPC samples at elevated temperatures.

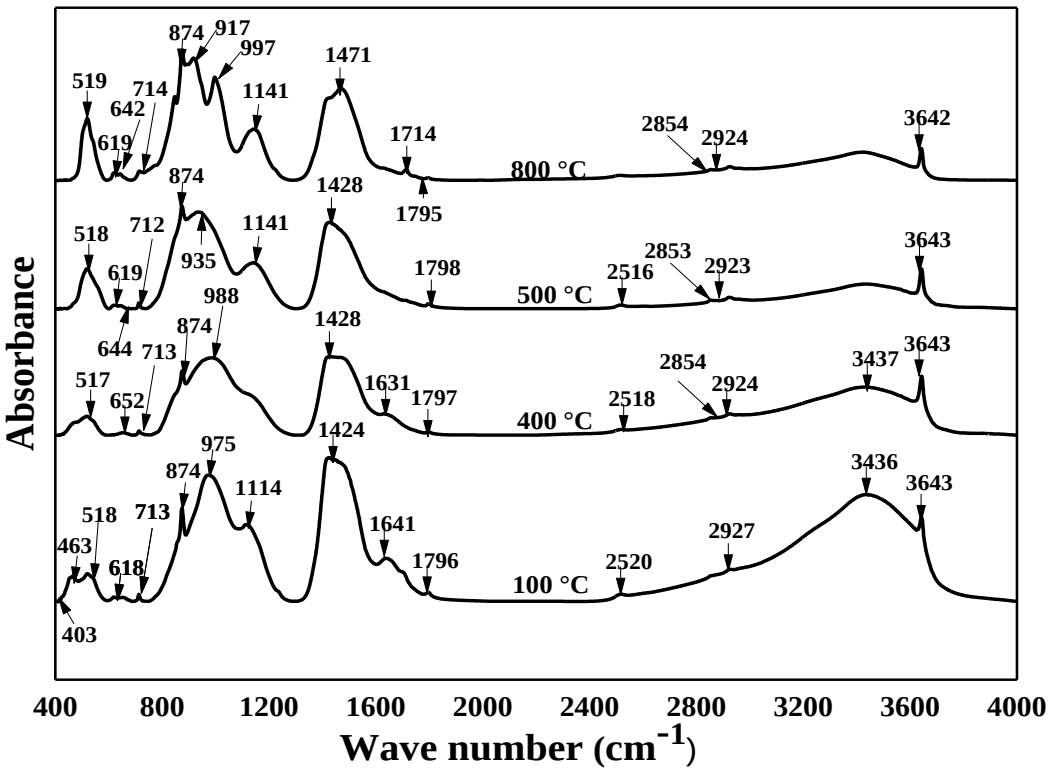

Figure 4.15. FTIR analysis of OPC-43 samples at elevated temperatures.

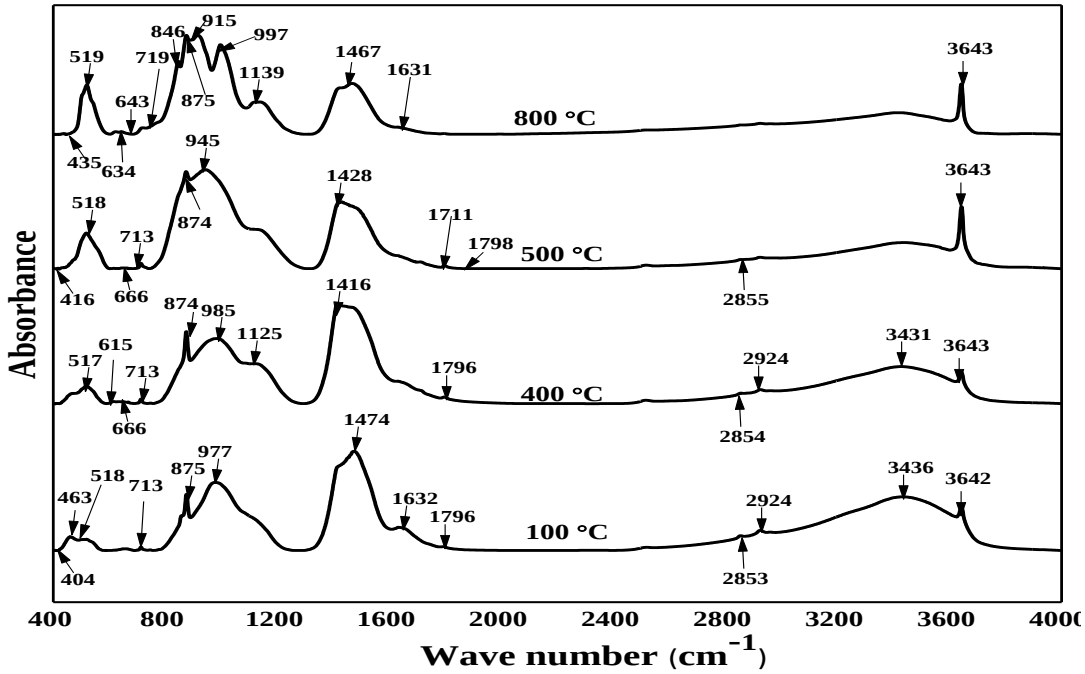

Figure 4.16. FTIR analysis of OPC-53 samples at elevated temperatures.

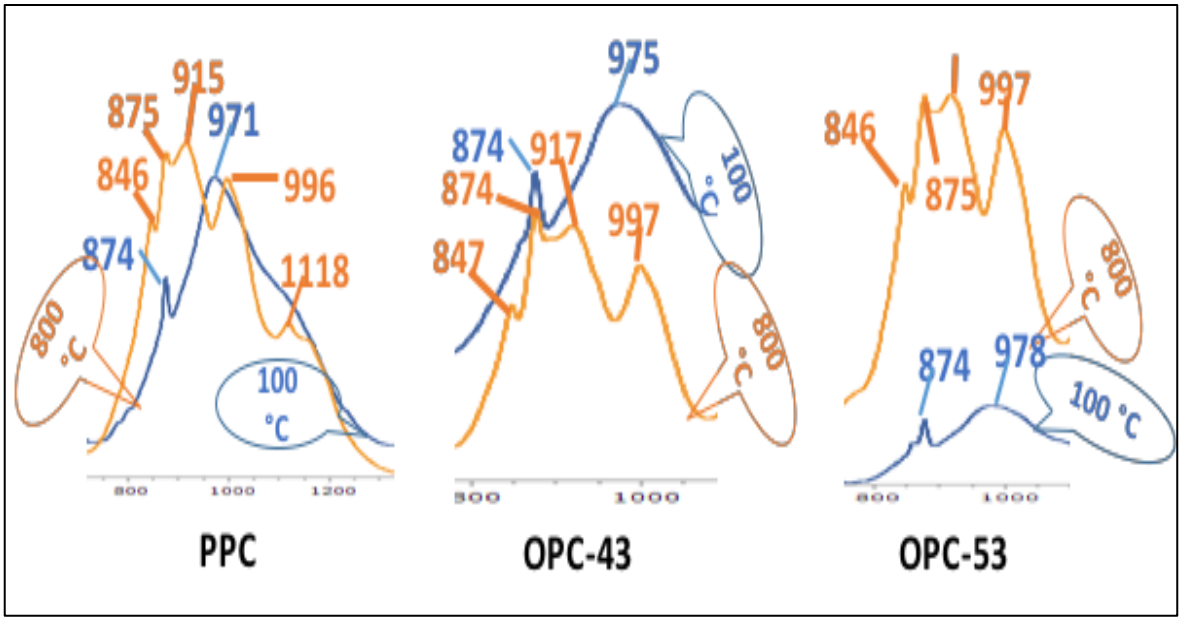

Figure 4.17. Variations in the absorbance values at 800 -1000 cm^{-1} of PPC, OPC-43, OPC-53 at 100 °C & 800 °C.

for PPC and OPC-43 samples. An increase in the absorbance values of 1643(CSH) was observed at 800 °C, and this peak is not observed at 100 °C for PPC and OPC-43 samples. PPC, OPC-43 and OPC-53 samples at 800 °C has four absorbance peak, hence from the FTIR analysis, one can predict the extent of damage to which the sample are subjected to.

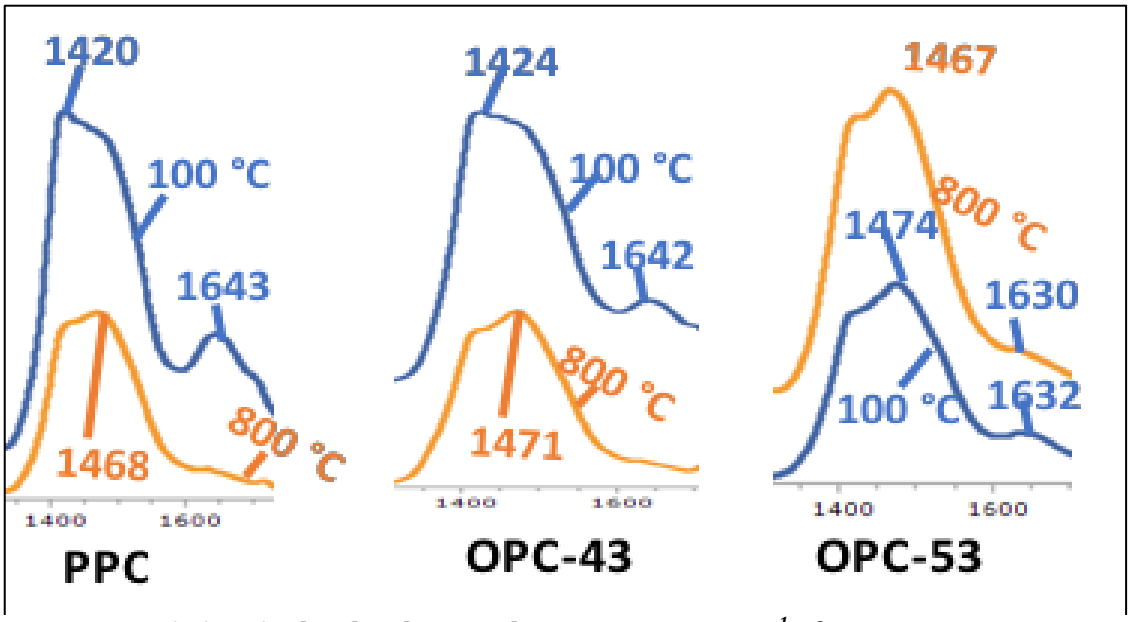

Figure 4.18. Variations in the absorbance values at 1400 -1700 cm^{-1} of PPC, OPC-43, OPC-53 at 100 °C & 800 °C.

Even though the XRD analysis can predict the quantities, the time consumed and cost of the equipment involved is greater, hence FTIR analysis is a suitable alternative method to estimate the extent of damage to which the samples are subjected.

4.3.8. FTRS analysis on PC samples

Similar to FTIR, FTRS is also helpful in determining the nuclear motion, but it follows a different approach which is the change in molecular polarizability. Hence the peaks that are not identified in Infrared Spectroscopy are visible in Raman Spectroscopy. The FTRS data are plotted obtained for the PPC, OPC-43 and OPC-53 with the excitation 1064 nm at temperatures of 100 °C, 400 °C, 500 °C and 800 °C is shown from Figure 4.19 – 4.21. The plots are plotted in the wavelength regions of 0 – 2000 cm^{-1} and the obtained results are discussed as follows:

4.3.8.1 FTRS analysis of PPC

The FTRS plots obtained at temperature intervals of 100 °C, 400 °C, 500 °C and 800 °C and these plots are shown in Figure 4.19. There was a reduction in the intensity of peak at 82 cm^{-1} from 27 °C - 800 °C. Peak at 632 cm^{-1} which is an indicator of CSH, is observed at 100 °C and shifted towards higher wavenumber *i.e.* 635 cm^{-1} at 400 °C. This peak is not observed in the temperature range from 500 °C to 800 °C. Peak 722 cm^{-1} (which is an indicator of β-C_2S) is found at 100 °C and 400 °C is not observed at 500 °C and 800 °C (Bonen D. *et*

*al.*1994).The peak 808 cm^{-1} (which is an indicator of C_3S) which is observed at 100 °C and 400 °C, has shifted towards the higher wavenumber *i.e.* 806 cm^{-1} at 500 °C, and to 817 cm^{-1} at 800 °C. The peak at 1007 cm^{-1} (which is an indicator of the presence of Gypsum) is observed at 27 °C and this peak is not observed between 100 °C to 800 °C (Bensted J. 1976). The peaks at 628 cm^{-1} which was observed at 27 °C, 632 peak at 100 °C, 635 peak at 400 °C which are in the range of 600-700 cm^{-1} (which is an indicator of CSH) are not observed at 500 °C and 800°C. Peak 1675 cm^{-1} (which is an indicator Ettringite) (Liu F. *et al.* 2014) at 27 °C was also observed at 100 °C, but between 400 °C, 500 °C and 800 °C this peak was not observed. In the PPC samples the peaks in between the wavenumber region of 630 – 650 cm^{-1}, peak intensity reduces with increasing temperatures. However, such a peak is not observed beyond 400 °C.

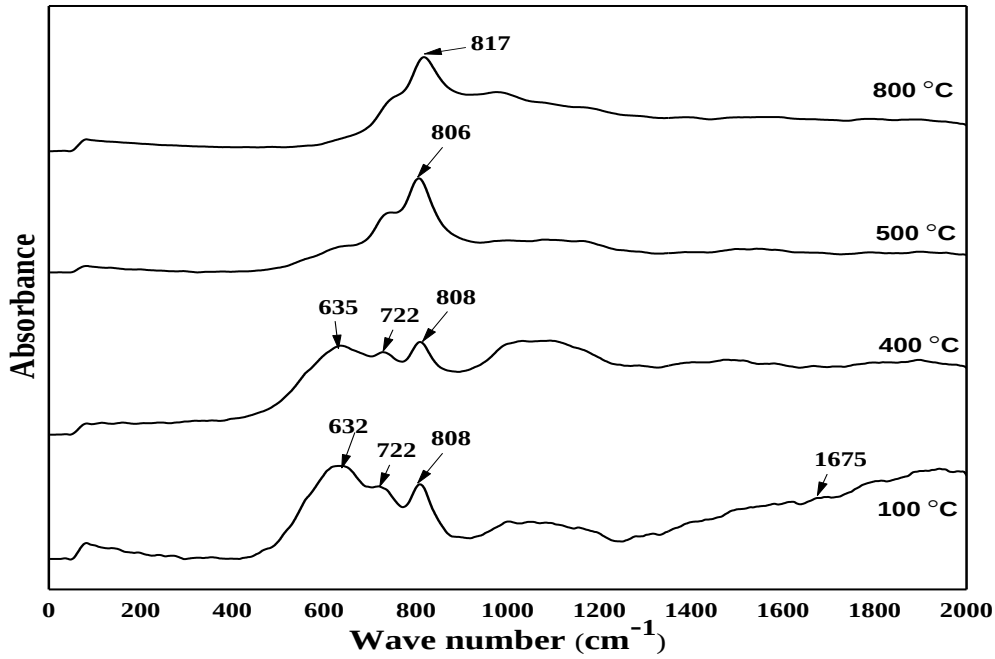

Figure 4.19. FTRS analysis of PPC samples at elevated temperatures.

4.3.8.2. FTRS analysis of OPC-43

The FTRS spectrum of the OPC-43 samples at different temperatures are shown in Figure 4.20. The absorbance peak at wavenumber 632 cm^{-1} is an indicator of CSH phase present in the sample at 100 °C and 400 °C; however with the increasing temperatures there is a shift towards the higher wavenumber *i.e.* 640 cm^{-1} and 647 cm^{-1} at 500 °C, and 800 °C respectively (Garg N. 2012). This phenomenon of shifting of wave number towards higher wavenumber is an indication of the mass being reduced, as the vibration frequency is inversely proportional to the vibrating mass. The absorbance peak at wavenumber 728 cm^{-1} is

an indicator of C_4AF phase and there is a shift towards the higher wavenumber which is 739 cm^{-1} at 800 °C. The wavenumber of 807 cm^{-1} at 100 °C is an indication of the C_3S phase, and 805 at 400 °C is an indication of C_2S phase. However after 400 °C a shift in the wavenumber towards higher wavenumber is 807 and 810 cm^{-1} at 500 °C and 800 °C is observed. With the increase in temperature there is an increase in the intensity at wavenumber region of 800 – 810 cm^{-1}. As the sample temperature reaches 800 °C the peaks in this region are the most predominant. While the peak in between wavenumbers of 630 – 650 cm^{-1} decreases. The wavenumber of 1029, 1021 cm^{-1} which represents the β-C_2S phase, is observed at 100 °C and 400 °C (Garg N. 2012), while the peak of 1081 cm^{-1} which is an indicator of Hemi-Carbo-Aluminate is observed at 800 °C.

4.3.8.3. FTRS analysis of OPC-53

The FTRS spectrum of OPC-53 samples subjected to different temperatures is shown in Figure. 4.21. The absorbance peak observed at wavenumber of 283 cm^{-1}, represents the C_2S phase at 100 °C. The wavenumbers 624 and 633 cm^{-1} represent the CSH phase in the samples at 100 °C and 400 °C. The 1033 and 1124 cm^{-1} represent the β-C_2S (which is C_2S polymorph), and C_2S at 100 °C. Among all the three GoC, the increase in the peak absorbance of the wavenumber 811 cm^{-1} (which is an indication of the C_3S phase) is a common phenomenon, along with the reduction of the wavenumber region of 630 – 650 cm^{-1}. Hence by observing these two crucial areas, one can predict the intensity of the fire, to which the specimens were subjected to. For the PPC samples the wavenumber region of 720 – 730 cm^{-1} is not observed at temperatures of 500 °C and 800 °C. The wavenumber 1009 cm^{-1} (which is an indicator of the C_3S triclinic phase) is observed at 400 °C (Garg, N., 2012), and 749 which represents the C_4AF phase at 800 °C was observed. As the chemical oxides present in the three GoC is same, the variation among the three GoC is the relative chemical composition and its particle size distribution. The FTRS plots of all the three GoC is the same, however certain variations have been observed among the samples. XRD equipment is very expensive, while interpreting the XRD data graphs require expensive software's. By using FTIR and FTRS spectroscopy studies which are less expensive, lesser sample preparation and scan time, one can determine the extent to what temperatures the concrete specimens were subjected to. However, the quantitative analysis cannot be carried out with the spectroscopy data. The variation in peak intensities of PPC, OPC-43 and OPC-53 sample

at wavenumbers less than 100 cm^{-1} and 700-1000 cm^{-1} is shown for PPC and OPC-43, while wavenumber less than 100 cm^{-1} is not shown for OPC-53 Figure 4.22. An increase in the

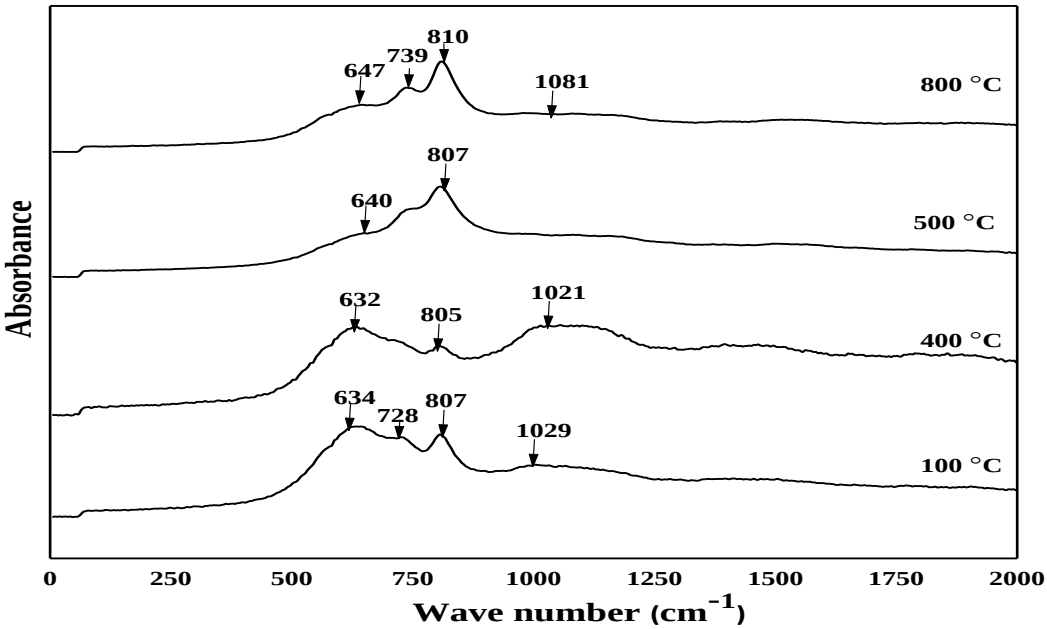

Figure 4.20. FTRS analysis of OPC-43 samples at elevated temperatures.

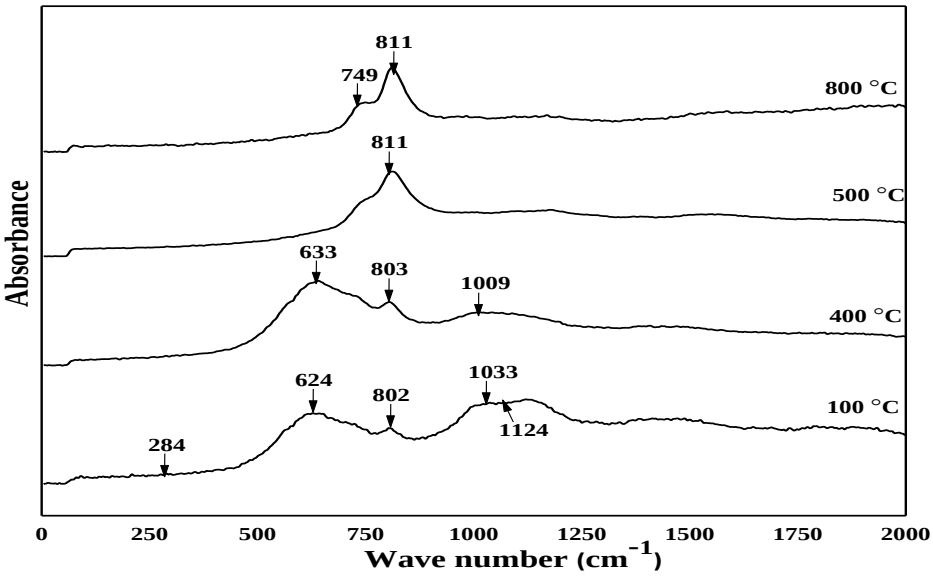

Figure 4.21. FTRS analysis of OPC-53 samples at elevated temperatures.

peak intensity of peak 82, 75 from 27 °C to 800 °C for both PPC and OPC-43 can be observed. The shift in the peak 800-817 cm^{-1} (C_3S) and increase in peak intensity was observed for all the three GoC with the increase in temperature. A peak shift towards higher wave number is also indication of the reduction in the mass of the molecule.

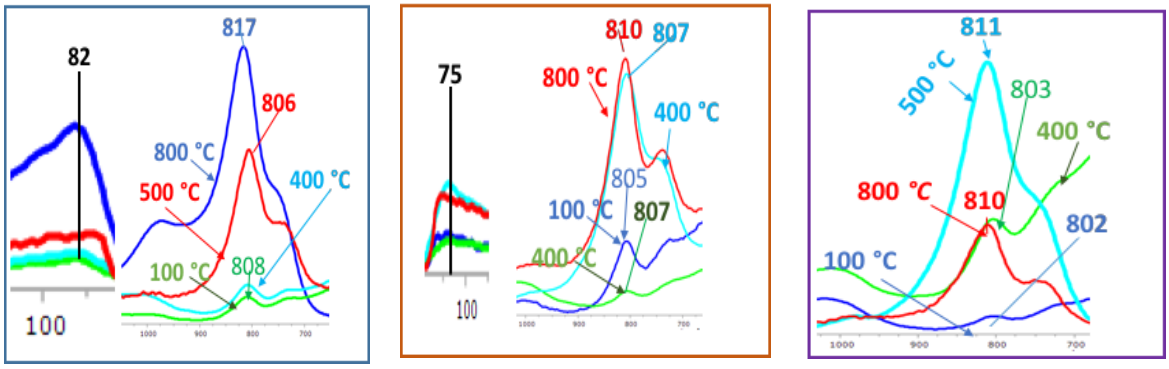

Figure 4.22. Variation in absorbance values observed at different temperatures for (a) PPC (b) OPC-43and (c) OPC-53

4.4. Conclusion from this chapter

- It was observed that there is a reduction in elemental concentrations of Hydrogen and Oxygen with increasing temperature. The elemental concentration of carbon increased with the increase in temperatures for OPC-43 and OPC-53 samples. This phenomenon is completely opposite for PPC sample. This is an advantageous point in favour of PPC.
- Thermo gravimetric analysis (TGA) indicated three critical regions of interest where the decomposition of the phases are present in the Portland Cement at i.e. 100 °C, 400 °C, 500 °C and 800 °C respectively.
- Differential thermal analysis (DTA) and differential scanning calorimetry (DSC) indicated a sudden drop in heat flow at 400 °C and 500 °C. This may be due to the reduction in the phase concentrations of Portlandite and is observed for all the three cements.
- The heat flow pattern obtained from differential thermal analysis is same for all the samples, while differential scanning calorimetry has indicated a slight variation in the heat flow for PPC samples.
- XRD tests carried at the temperatures of 100 °C, 400 °C, 500 °C and 800 °C indicate the deterioration of the all the phases with increase in temperatures.
- The Portlandite phase concentration increases with increase in hydration period. However, with increase in temperature there is a reduction in the peak intensities. Minor traces of Portlandite is noted after the temperatures exceeds 500 °C for all the samples.

- XRD results have also indicated a sudden drop in the Portlandite concentration at the temperature regions of 400 °C, and 500 °C, which is in good agreement with the TGA, DTA and DSC analysis.
- PPC samples are able to maintain the integrity and were able to withstand loads even at the temperatures of 800 °C, while OPC-43 and OPC-53 failed to do so. This means there is an improved performance of PPC at high temperatures.
- Fourier transform Infrared spectroscopy and Fourier transform Raman spectroscopy suitable analysis to predict the extent to which thermal loads damage the Portland Cements.
- This phase of study has brought out the differences in the composition between various types of cement and variation in concentrations due to temperature.
- Higher is the rate of gain in compressive strength, the rate of damage caused to cements due to thermal loads will also be high.

Chapter-5

Determination of pore network and porosity at mesoscale

Chapter-5

Determination of porosity and pore network at mesoscale

5.1. General

The thermal behavior of three grades of cements *i.e.* PPC, OPC-43 and OPC-53 is analyzed from 27 °C to 800 °C and results presented in chapter-4. From the thermal analysis four temperatures corresponding to significant mass loss are selected *i.e.* 100 °C, 400 °C, 500 °C and 800 °C, and the cast specimens are tested at these temperatures. The visual inspection and compressive strength of the samples indicate that PPC samples have superior thermal behavior under higher temperatures. However, the elemental tests conducted using CHNS-O indicate higher oxygen concentration along with hydrogen; while DSC studies indicate that the rate of heat flow in PPC is lower in comparison with OPC-43 and OPC-53. XRD tests on PPC indicate the presence of Langbeinite, which was not in other two GoC. The concentrations of Portlandite and CSH are lower in PPC when compared to other two GoC. The XRD analysis of the OPC-43 and OPC-53 samples indicates the higher concentrations of CSH and Portlandite present in them. OPC-43 and OPC-53 failed to carry any temperature load after 400 °C, while PPC samples are able to with stand the load even at 800 °C.

For understanding the superior behavior of PPC under thermal loading compared to the other two GoC, the internal pore structure of the samples needs to be analyzed. Porosity is simple to define but very difficult to quantify. An increase in pores within the volume of the structure effects the strength of the material and reduces thermal conductivity. The ratio of volume of voids (V_v) to volume of the bulk of the materials (V_T) is called Total porosity (ϕ) and is denoted by equation 5.1:

$$\phi = \frac{V_v}{V_T} \text{ ------ (5.1)}$$

Many methods are available for determining the air voids present in concrete. A few methods to analyze the porosity in the samples are shown in Figure. 5.1. There exists extensive literature on studies conducted by other researchers using indirect methods such as mercury intrusion porosimeter (MIP), nitrogen adsorption test, Brunauer, Emmett and Teller (BET) method. These methods are indirect and the sample size is restricted to few millimeters

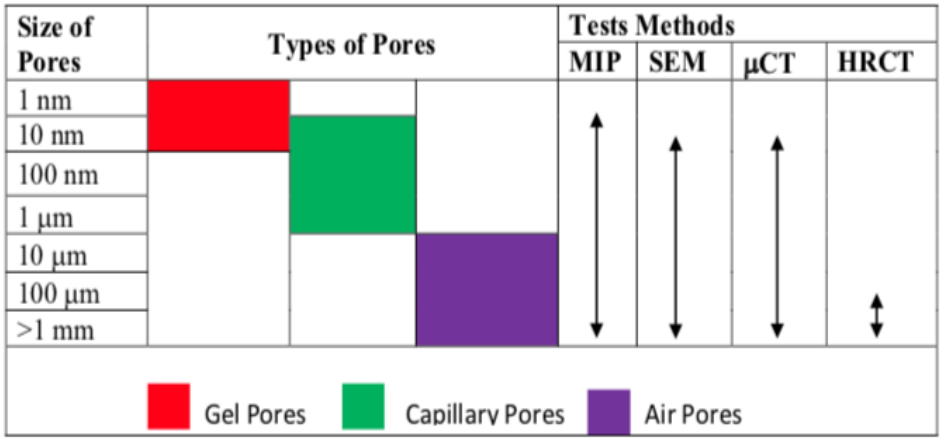

Figure 5.1. Different types of pores detected using various methods.

(2 mm – 3 mm). The pressure method based on Boyle-Mariotte law, can determine the air content in compacted fresh concrete. The air void analyser method cannot determine the air voids lesser than 50 µm. This method is suitable for air entrained concretes, and can also be used for non air entrained concretes. It can also determine the spacing factor and micro-air-void content, total air content and specific surface on an air void system. A stereoscopic microscope can be used to determine the air-void diameter and distribution of hardened concrete, spacing factor, micro-air-void content, total air content, specific surface area of an air void system, average pore diameter. It can estimate the pores of 1-4000 µm and can estimate the microscopic air pore.

Computed tomography (CT) is used to determine the spacing factor, micro-air-voids, total air content, specific surface area of an air void system and average pore diameter (Moravcova B. *et al.* 2016). The porosity analysis using indirect method cannot be conducted on the samples greater than > 3mm because of the limitation on the size of test samples.

Hence there is a need to quantify the pore structure and their distribution across the sample visually or analytically. The thermal effects causes the pores in the sample to expand and interconnect, thereby forming a network. when sufficient load acts on the samples or the thermal pressure acting inside the sample is equal to the amount of the external loads, the material fails by the external pressure or the internal stresses due to temperature loads as observed from Figure 4.7-4.9.

Hence, CT technique is a suitable option to characterize this phenomenon of the pores nucleation, expansion and interconnection of pores. The pores that are present in the sample are spread across the volume of the sample, and most of these pores cannot be seen with the naked eye. For larger sample sizes in this case the dimensions are 50 mm x 50 mm x 50 mm. The PC cubes made of PPC, OPC-43 and OPC-53 are subjected to various temperatures ranging from ambient temperature to 800 °C and studied using high resolution computer tomography (HRCT) typically used in medical applications.

5.2. Sample preparation

Three GoC commonly used in India which have different compressive strengths i.e. PPC, OPC-43, and OPC-53 are selected for the current analysis and no admixtures are used under room temperature. PPC has the least compressive strength among the three GoC, while OPC-53 has the highest. The PPC cement is mixed with a w/c of 0.33 corresponding to standard consistency. After mixing the sample is placed in a mold of dimension 50 x 50 x 50 mm^3, and compacted using a pan vibrator. After compaction, the samples are left to dry at room temperature for 24 hours. The air-dried samples are taken out of the mold and placed in a

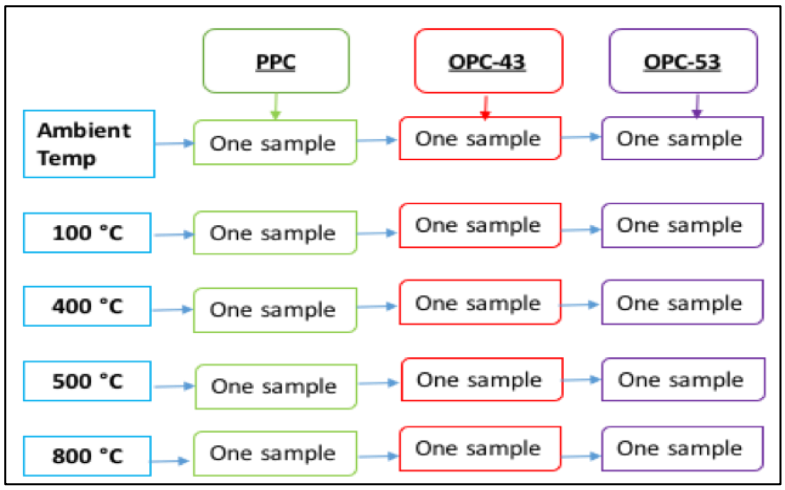

Figure 5.2. Samples scanned under HRCT.

After 28 days of curing the samples are left for air drying, and then subjected to thermal load. A set of 12 cubes are cast, i.e., three cubes each, are subjected to temperatures of ambient, 100 °C, 400 °C, 500 °C, 800 °C corresponding to significant mass loss as observed in Figure 4.2. during the TGA (section 4.3.3). Figure. 5.2 shows the number of specimens scanned under HRCT for different GoC. A single specimen is selected out of three samples, which were subjected to thermal loads in the furnace at their respective temperature, and is scanned under HRCT. The rate of temperature loading in the muffle furnace is 5 °C/min, and the temperature profile is plotted in Figure 5.3. After the desired temperatures have reached the samples are brought to room temperature inside the furnace, and the same process is adopted for the other two GoC.

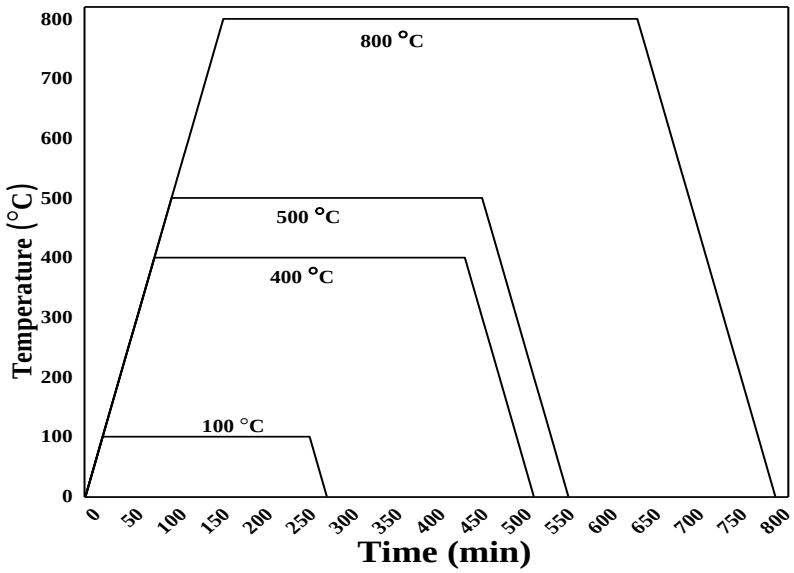

Figure 5.3. Temperature profile to which the samples were subjected.

5.3. Experimental procedure

5.3.1 CAT scan investigation

The number of slices used for image analysis are fixed for all the specimens at their respective temperatures. Figure 5.4. Shows a complete step by step procedure of image acquisition and processing. CT scan studies at elevated temperatures were carried using HRCT at Sai CT-Scan centre, Hanamkonda, Warangal, Telangana, India: Hispeed® scanner manufactured by GE® medical system with a voxel size of 0.488 X 0.488 x 0.70 mm. The specimen for the scan shown in step -1 of the Figure 5.4. is placed under an X-ray tube current of 130 KV, (constant for all the samples). The sample is placed on a table with x-y plane orientation, and

the scans are in the z-direction. A slice thickness of 0.7 mm is chosen for all the specimens as the sample length is 50 mm and a total of ±75 layers are generated during the scan. These scans produce 2D images in Digital Imaging and Communication in Medicine (DICOM) format shown in step-2 of the Figure 5.4. All the produced 2D slices are set to the actual size in OsiriX Lite pro® software and DICOM files are adjusted to visualise the pores present in the sample and these images converted into Tiff format for further analysis corresponding to step-3 of Figure 5.4. The saved 2D image stacks are converted into 8-bit images using ImageJ ®software, and these converted 8-bit images are analysed in MATLAB® by using Otsu's method (Otsu; 1979). Otsu's method used for optimum threshold, determines a threshold 't' value for the scanned images obtained from HRCT, and for these images, the values less than 't' were treated as pores and rest as a matrix as shown in step-4 of Figure.5.4. All the 2D images are stacked in the Z-direction as shown in step-5 of Figure 5.4, to produce a 3D view of the scanned sample shown in step-6 of Figure 5.4 using ImageJ® analysis, and step-7 was produced using Avizo® also shown in Figure 5.4.

5.3.2. 2D analysis

ImageJ® analysis was used to calculate the number of pores in the individual slices, for all the 2D slices obtained from Otsu's method as shown in step-4 of Figure 5.4. The images are imported using the image sequence option and cropped to the desired region of interest (ROI)

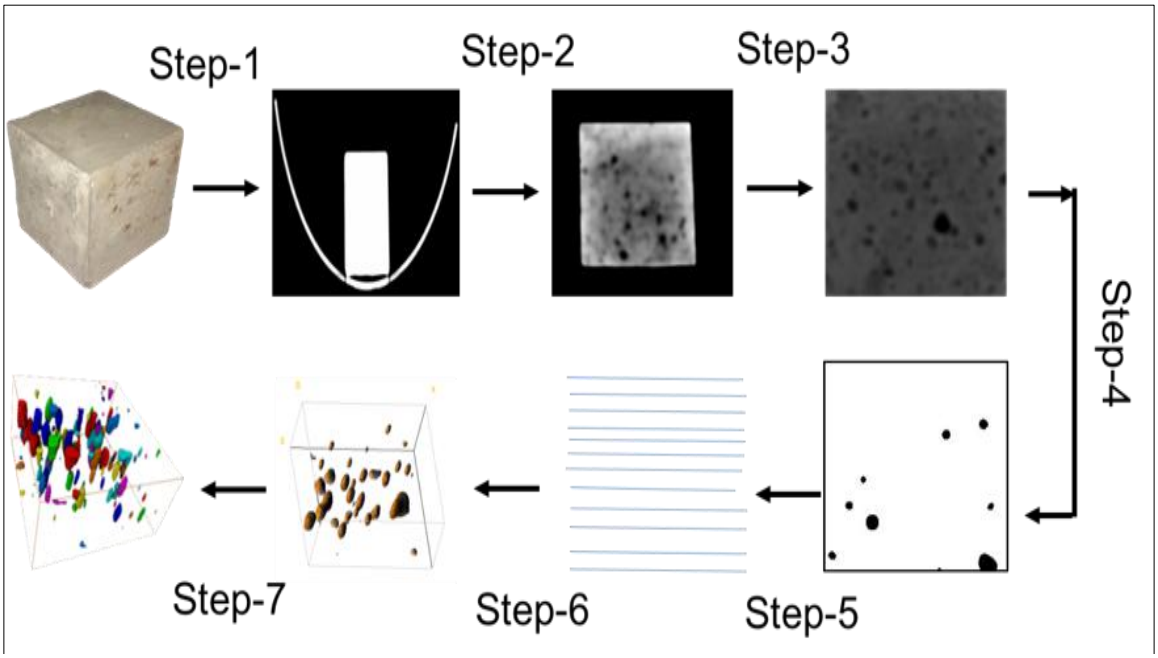

Figure 5.4. Flow chart of the image analysis for slices obtained from HRCT.

step.3 shown in the Figure 5.4. In the images a layer of thickness 5mm at the top and bottom considered. After the ROI is selected, voxel dimensions are set to 0.488 x 0.488 x 0.7 mm, which are input parameters from the HRCT scan. The threshold option is selected and set to "default" and the noise present in the images is filtered using the "median filter". The final analysis is carried out using "analyze particle" option from which the total number of pores are estimated in each slice.

5.4. Results and discussion

5.4.1. Radii of pores in PC samples

The DICOM images obtained from the HRCT scan are analysed using ImageJ® software as mentioned earlier in section 5.3.2. After completing the image analysis of the 2D slices, a set of 57 images are analysed and the pore areas are estimated along with other parameters such as effective radii of the pores using the area data obtained from ImageJ analysis, assuming that the pores are circular in shape.

5.4.1.1. Radius of pores in PPC

The variation in the radius of pores in PPC samples with respect to temperature is plotted in Figure 5.5 and indicates that the porosity as well as the number of pores in all the slices increase with temperature. The radii of pores in specimen subjected to ambient temperature (27°C)

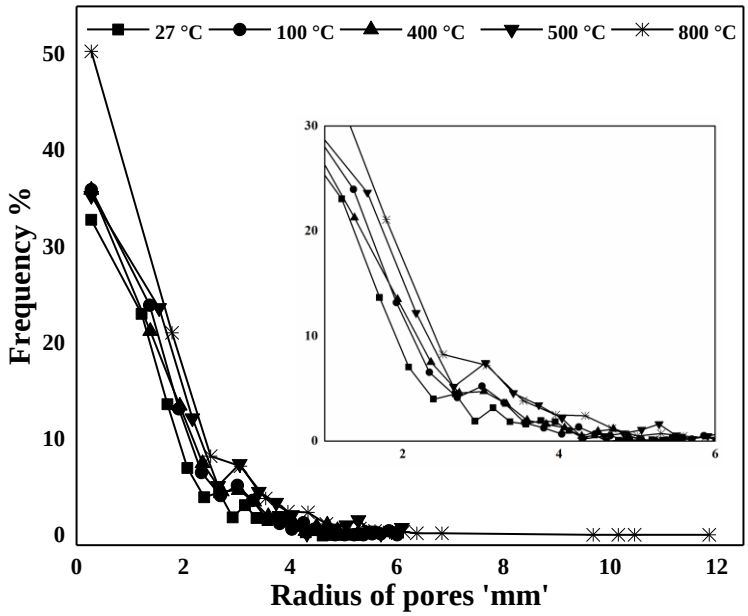

Figure 5.5. Radii of pores in PPC sample obtained from HRCT at various temperatures.

ranges from 0.28 mm (32.81%) to 5.58 mm (0.34 %), where the corresponding percentage volume fraction of a specific pore size is provided in parenthesis alongside the particle radius. In specimens subjected to standard peak temperature (SPT) of 100 °C, the radii of pores ranged from 0.28 mm (35.96 %) to 6.00 mm (0.08 %). In specimen subjected to SPT 400 °C, the radii of pores ranged from 0.28 mm (35.93%) to 5.42 mm (0.20 %). In specimen subjected to SPT beyond 400 °C the thermo-gravimetric analysis showed a sharp change in mass loss and in specimen subjected to SPT 500 °C, the radii of pores ranges from 0.28 mm (35.32 %) to 6.09 mm (0.80 %). In specimens subjected to SPT 800 °C, with the radii of pores ranges from 0.28 mm (50.32 %) to 11.85 mm (0.08%). Figure 5.5 shows the distribution of the radius of pores in these ranges.

5.4.1.2. Radii of pores in OPC-43

The variation in the radius of pores in OPC-43 samples with respect to temperature is plotted in Figure 5.6, and indicates that the porosity and the number of pores in all the slices increase with temperature. The radii of pores in specimen subjected to 27°C ranges from 0.28 mm (41.55 %) to 5.80 mm (1.59 %). In specimen subjected to SPT 100 °C, the radii of pores range from 0.28 mm (40.52 %) to 5.68 mm (0.42 %). In specimen subjected to SPT 400 °C,

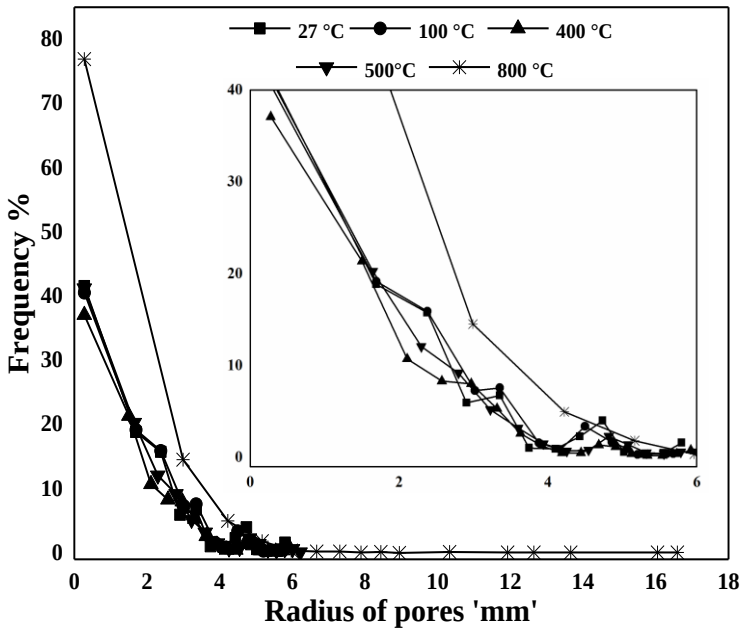

Figure 5.6. Radii of pores in OPC-43 sample obtained from HRCT at various temperatures.

the radii of pores ranged from 0.28 mm (37.06 %) to 5.92 mm (0.77 %). In specimen subjected to SPT 500 °C, the radii of pores ranges from 0.28 mm (41.21 %) to 6.21 mm (0.01 %). In specimens subjected to SPT 800 °C, with the radii of pores ranges from 0.28 mm (76.93 %) to 16.59 mm (0.08%). Figure 5.6 shows the distribution of the radius of pores in between these ranges.

5.4.1.3. Radii of pores in OPC-53

The variation in the radius of pores with respect to temperature is plotted in Figure 5.7, and indicates that the porosity and the number of pores in all the slices has increased with temperature. The radii of pores in specimen subjected to 27°C ranges from 0.28 mm (52.29%) to 2.88 mm (1.91%), where the corresponding percentage volume fraction of a specific pore size is provided in parenthesis alongside the particle radius. In specimen subjected to SPT 100 °C, the radii of pores ranged from 0.28 mm (42.49%) to 2.48 mm (0.85%). In specimen subjected to SPT 400 °C, the radii of pores ranged from 0.28 mm (37.43%) to 5.35 mm (0.079%). The radii of pores ranges from 0.28 mm (45.41%) to 4.59 mm (0.14%). In specimens subjected to SPT 800 °C, with the radii of pores ranges from 0.28 mm (68.70%) to 4.20 mm (0.05%). Figure 5.7 shows the distribution of the radius of pores in between these ranges.

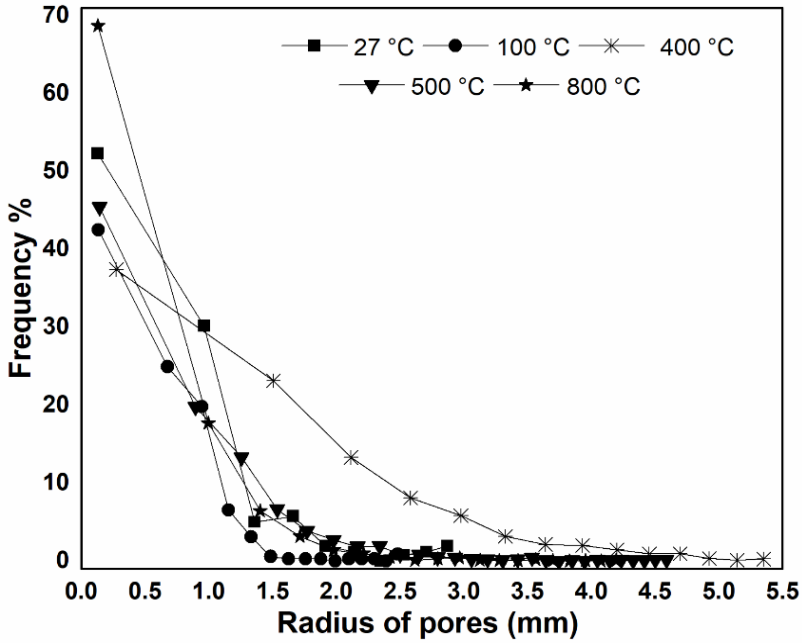

Figure 5.7. Radii of pores in OPC-53 sample obtained from HRCT at various temperatures.

5.4.2. Circularity of pores

Circularity, which is a dimensionless quantity used to describe the shape of the pores present in the samples is a function of perimeter and area of the pores present in the sample. The following equation (5.2) is used to estimate the circularity:

$$C = 4 \pi A / P^2 \qquad \text{----------} \quad (5.2)$$

Where 'C' is the circularity, 'A' is the area and 'P' is the perimeter. Spherically shaped pores are visible as circular holes in the 2D slices. Non-spherical (elongated) pores do not produce circular shaped holes in every layer. The circularity analysis is conducted for each of these slices to quantify the interconnection of pores. The elongated pores indicate increased probability of interconnection. Hence, even though circularity of pores within slice is a 2D quantity, an overview of the nature of the porosity and pore network in the 3D volume can be obtained from value of circularity.

5.4.2.1. Circularity of pores in PPC

The circularity of the pores is calculated for HRCT data obtained from PPC samples after image processing and plotted in Figures 5.8. where '1' on the X-axis indicates the pores are a perfect circle and '0' indicates the pores are highly elongated in shape. Figure 5.8 indicates that 60.44 % the pores present in the meso-scale HRCT specimen have a circularity of 0.971 at 27 °C. In meso-scale specimen subjected to SPT of at 100 °C, 58.08 % the pores have a

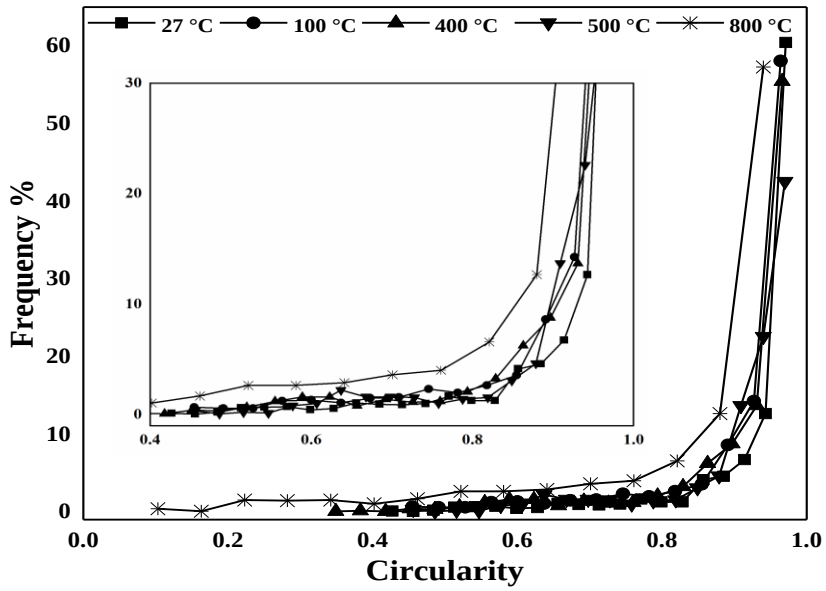

Figure 5.8. Circularity of pores in PPC samples at different temperatures.

circularity of 0.964. While, specimen subjected to SPT of 400, 500 and 800 °C the circularity percentage are 55.44, 42.56 and 57.30 for the circularity values of 0.966, 0.970, and 0.940.

The circularity values on the lower end, which are closer to '0', indicate the pores are elongated. In meso-scale specimen subjected to SPT of 27 °C, 0.11% of the meso-pores have an elongation value of 0.427 and in the specimen subjected to SPT of 100 °C, 0.67% of the meso-pores have an elongation value of 0.455. At SPT of 400 and 500 °C, the percentage are 0.33 and 0.40% and their elongation polygons with a circularity of 0.45 and 0.103. It is evident from the graph in Figure 5.8 that the pores changed shape from circular to elongated polygons as the temperature increases from 27 °C to 800 °C.

5.4.2.2. Circularity of pores in OPC-43

In meso-scale specimens of OPC-43, the circularity indicate that the pores are circular in shape closer to '1' on the higher end as shown in Figure. 5.9. 42.69 % of the pores present in the meso-scale HRCT specimen have a circularity of 0.972 at 27 °C. In the meso-scale specimen subjected to SPT 100 °C, 41.05 % the pores have a circularity of 0.977. At SPT of

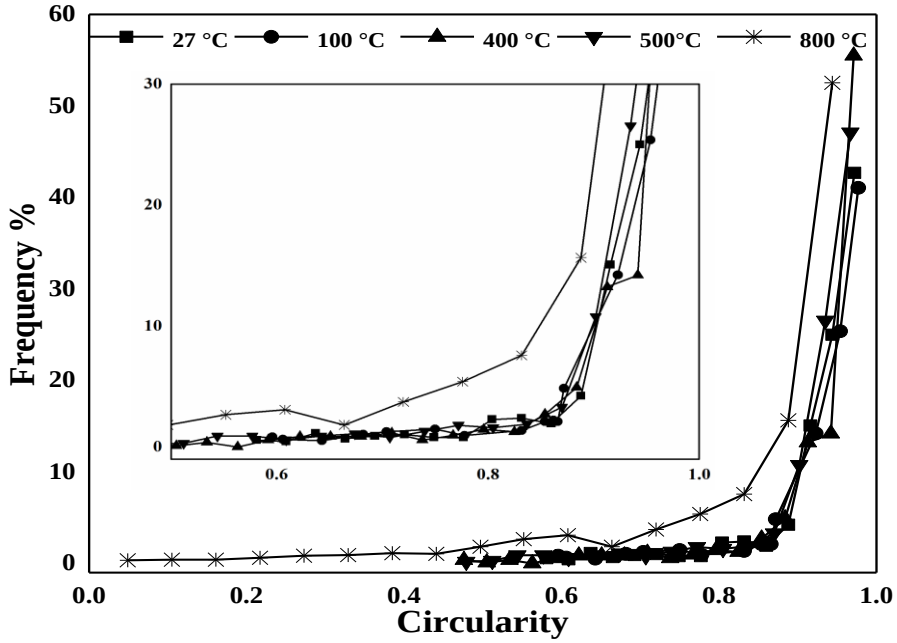

Figure 5.9. Circularity of pores in OPC-43 samples at different temperatures.

400, 500, and 800 °C, the percentages are 55.50, 47.10 and 52.53 % for a circularity of 0.971, 0.967 and 0.944.

The circularity values on the lower end, which are closer to ‘0’, indicates the pores are elongated. In meso-scale specimen subjected to SPT of 27 °C, 0.58% of the meso-pores have an elongation value of 0.581 and in meso-scale specimen subjected to SPT of 100 °C, 0.84% of the meso-pores have an elongation value of 0.596. In meso-scale specimen subjected to SPT of 400 °C, 0.39% of the meso-pores have an elongation value of 0.476. At an SPT of 500 and 800 °C, the percentage of elongated polygons are 0.20 and 0.35% for a circularity of 0.48 and 0.49. It is evident from the graph in Figure 5.9 that the pores change shape from circular to an elongated polygon as the temperature increases from 27 °C to 800 °C.

5.4.2.3. Circularity of pores in OPC-53

The circularity of the pores is calculated for HRCT data obtained from image processing and plotted in Figures 5.10. where ‘1’ on the X-axis indicates the pores are a perfect circle and ‘0’ indicates the pores are highly elongated in shape. Figure 5.10 indicates that 72.90 % of the pores present in the meso-scale HRCT specimen have a circularity of 0.947 at 27 °C. In meso-scale specimen subjected to SPT of at 100 °C, 75.22 % the pores have a circularity of 0.929. At an SPT of 400, 500 and 800 °C the circularity values are 0.946, 0.944 and 0.941, and their percentages are 53.14, 44.73 and 50.81%.

The circularity values on the lower end, which are closer to ‘0’, indicates the pores are elongated. In meso-scale specimen subjected to SPT of 27 °C, 0.38% of the meso-pores have an elongation value of 0.048. At an SPT of 100, 400, 500 and 800 °C the cruciality values for

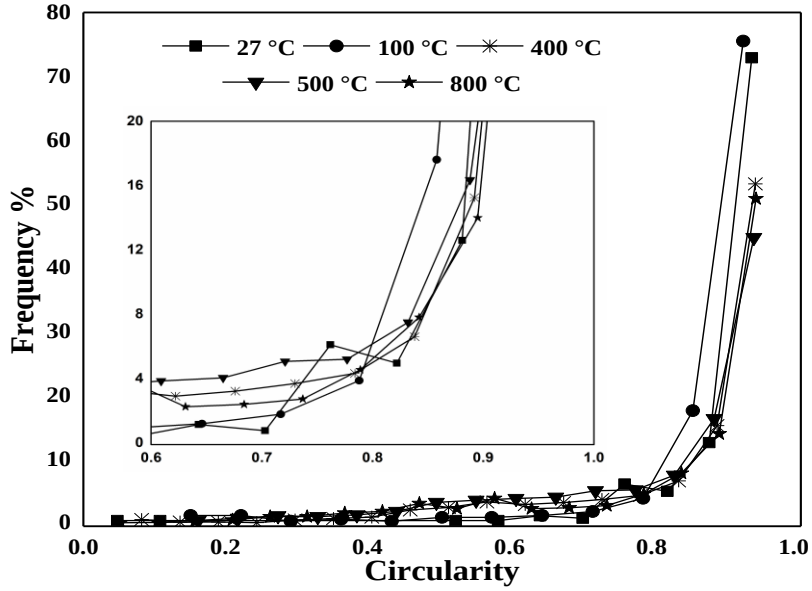

Figure 5.10. Circularity of pores in OPC-53 samples at different temperatures.

5.4.3. Nearest neighbor distance (NND)

NND is used to calculate the distance between pores so that the distribution of the pore network and their nearest neighbors in a porous medium can be estimated (Haeri, 2015). The NND and their distribution of pore network obtained from HRCT testing is shown in Figure. where NND value of '0' indicates the pores are clustered and values greater than '0' indicate that the pores are dispersed.

5.4.3.1. NND of pores in PPC

The results of CT scans and image analysis indicate that the number of pores increases with increase in temperature. This leads to generation of new pores, which causes a growth in pore radius, and thereby an increase in the pore network. The estimated NND values of PPC samples at their respective temperatures is shown in Figure 5.11. In PPC sample at 27 °C, for an NND value of '0' it is 77.02% of pores are present together while the maximum distance or distribution value is '8.47' and their percentage is 0.06. While the value closer to '0' is

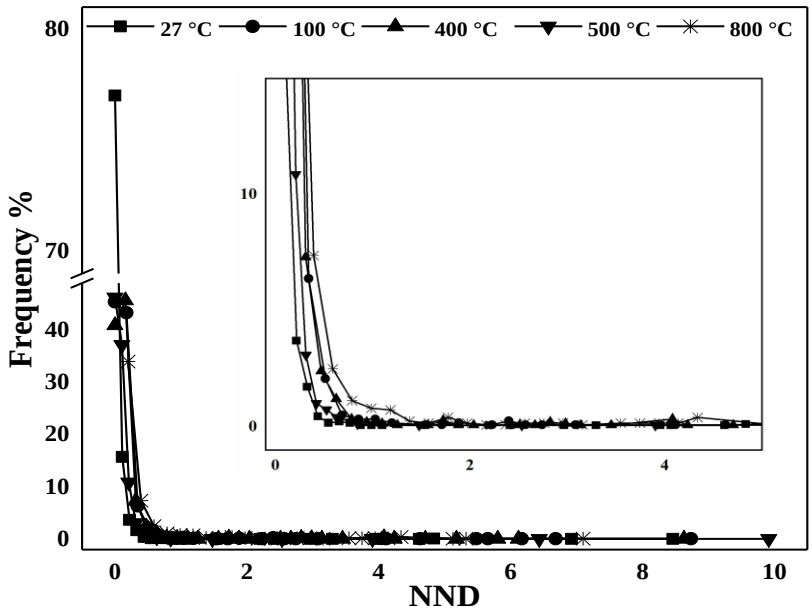

Figure 5.11. Distribution of NND of pores in PPC samples.

0.11 and its percentage is 15.75 respectively. In specimen subjected to SPT of 100 °C of PPC sample, for an NND of '0' the volume fraction is 45.41% and maximum NND value is '8.74' and its percentage is 0.08; the spatial extent of the pore network is not relatively high, and the inter-pore distance is high as observed in Figures . However, in specimen subjected to SPT of 400 °C for the pores having NND of '0' (*i.e.*, highly clustered pores) the volume fraction is

40.90 and the maximum NND value is 8.63 for a volume fraction of 0.07, and next value closer to a NND of ‘0’ is ‘0.16’ for a volume fraction of 45.68. In specimen subjected to SPT of 500 °C the volume fraction of the pores having NND of ‘0’ is 46.24% and volume fraction corresponding to pores having NND of 0.10 is 37.20%.

In specimen subjected to SPT of 800 °C the volume fraction corresponding to pores having NND of ‘0’ is 50.48%, and volume fraction corresponding to pores having NND of 0.197 is 33.97%, indicating the increase in spatial extent of pore network in the sample with increase in temperature. The NND values closer to ‘0’ are spaced far apart, which is an indication that the pores presnt in the sample are spaced apaprt, since the pores are spaced apart the internal pressure caused by the heat did not effect the integrity of the sample.

5.4.3.2. NND of pores in OPC-43

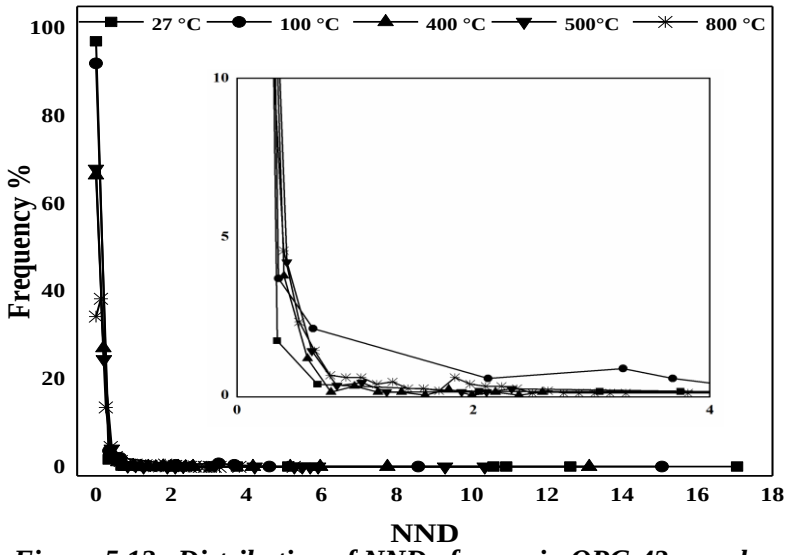

Figure 5.12. Distribution of NND of pores in OPC-43 samples

The NND values of the OPC-43 subjected to different temperatures is plotted in Figure 5.12. For OPC-43 sample at 27 °C, for an NND value of ‘0’ the volume fraction is 97.03, which indicated the pores are clustered, while the maximum distance or distribution value is 17.06 and its volume fraction is 0.12. In OPC-43 specimen subjected to SPT of 100 °C, for an NND of ‘0’ the volume fraction is 92% and maximum NND value is 15.05 and its volume fraction is 0.11, while the value next to ‘0’ is 0.35 and its volume fraction is 3.68; the spatial extent of the pore network is not relatively high, and the inter-pore distance is high as observed in Figure 5.12. However, in OPC-43 specimen subjected to SPT of 400 °C,there is an increase in the spatial extent of the pore network; for the pores having NND of ‘0’ the volume fraction

reduces to 66.50 and for pores having NND value of 0.20 the volume fraction is 27.13%, while the maximum NND value is 13.12. In specimen of OPC-43 subjected to SPT of 500 °C the volume fraction of the pores having NND of '0' is 67.97% and volume fraction corresponding to pores having NND of 0.211 is 24.50%, while the maximum NND value is 10.35. In specimen OPC-43 subjected to SPT of 800 °C the volume fraction corresponding to pores having NND of '0' is 34.30%, a gradually reduction in the NND value of '0' can be observed, which indicates the pores are well spread across the sample. This distribution of pores eventually acts a failure network, which initates the failure in the specimen. The next two values close to '0' are 0.132 and 0.283 and their volume fractions are 38.35 and 13.60 respectively, while the maximum NND value is 5.26. With the increase in tempearture the maximum NND values started to decrease, this is due to the formation of new pores across the samples, and thereby a decrease in the NND value is observed.

5.4.3.3. NND of pores in OPC-53

At 27 °C, the pores are very dense, *i.e.* at the NND value of '0' it is 97.32% of pores are present while the maximum distance or distribution value is 7.12. In specimen subjected to SPT of 100 °C, for an NND of '0' the volume fraction is 95.18% and maximum NND value is 7.48; the spatial extent of the pore network is not relatively high, and the inter-pore distance is high as observed in Figures 5.13 . However, in specimen subjected to SPT of 400 °C,there is

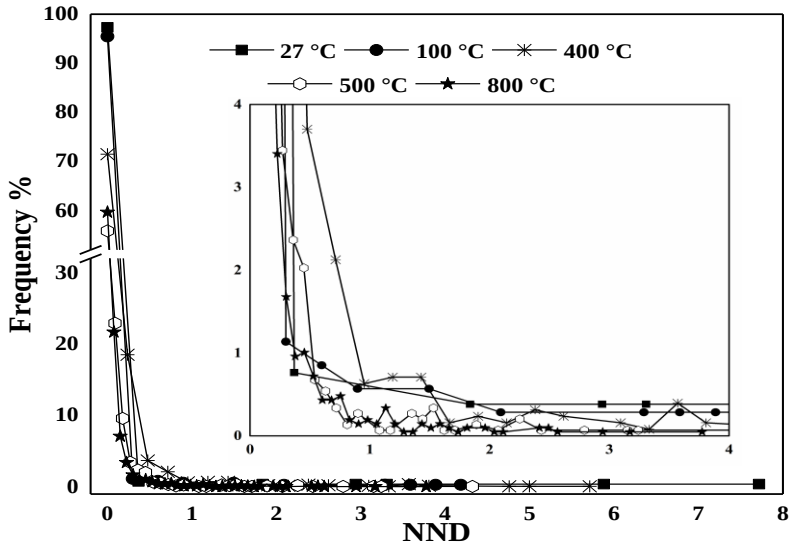

Figure 5.13. Distribution of NND of pores in OPC-53 samples.

an increase in the spatial extent of the pore network; for the pores having NND of '0' (*i.e.*, highly clustered pores) the volume fraction reduces to 71.38 and for pores having NND value of 0.24 the volume fraction is 18.48%; in specimen subjected to SPT of 500 °C the volume fraction of the pores having NND of '0' is 55.87% and volume fraction corresponding to

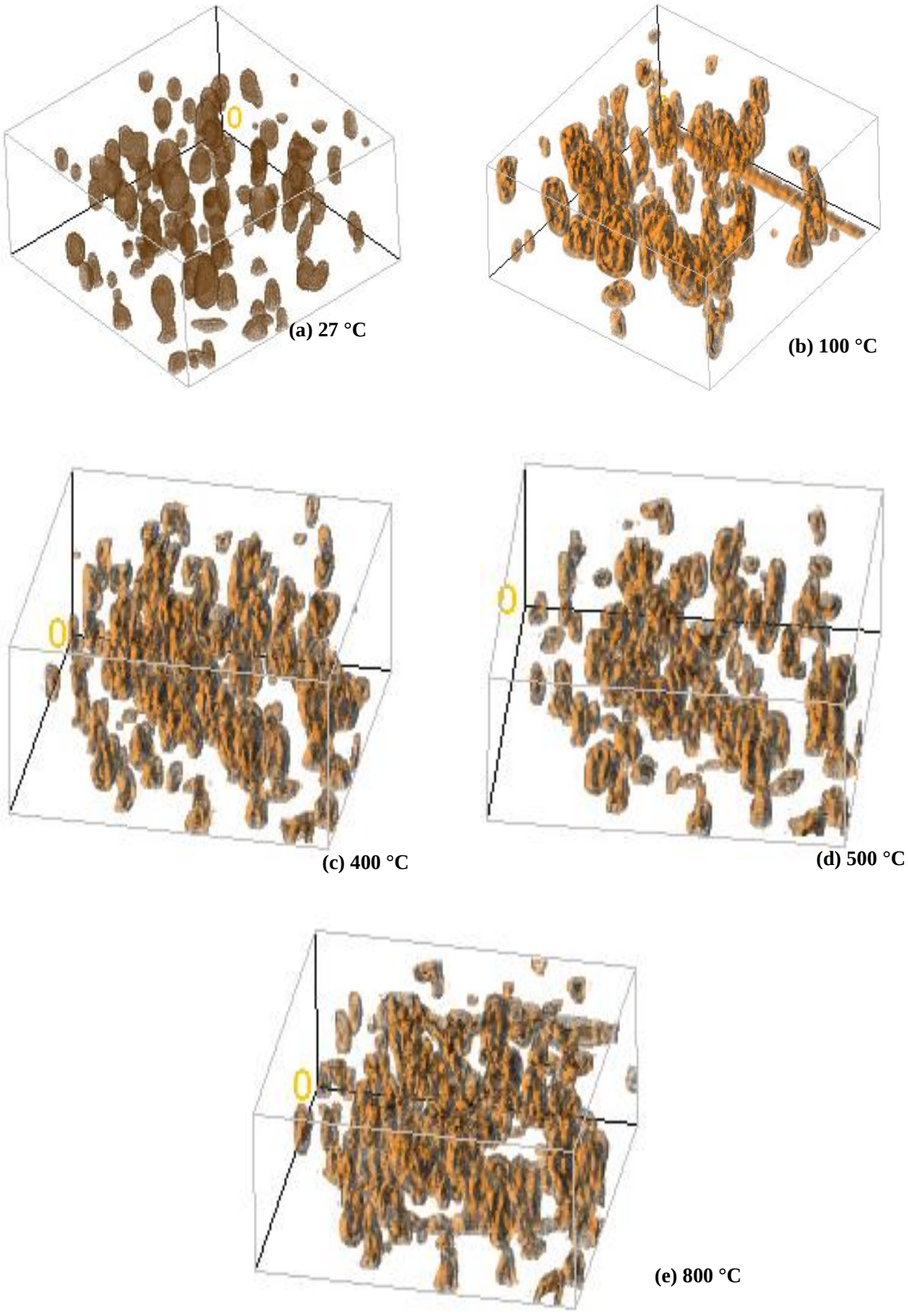

Figure 5.14. 2D to 3D reconstructed samples of PPC at different temperatures using HRCT.

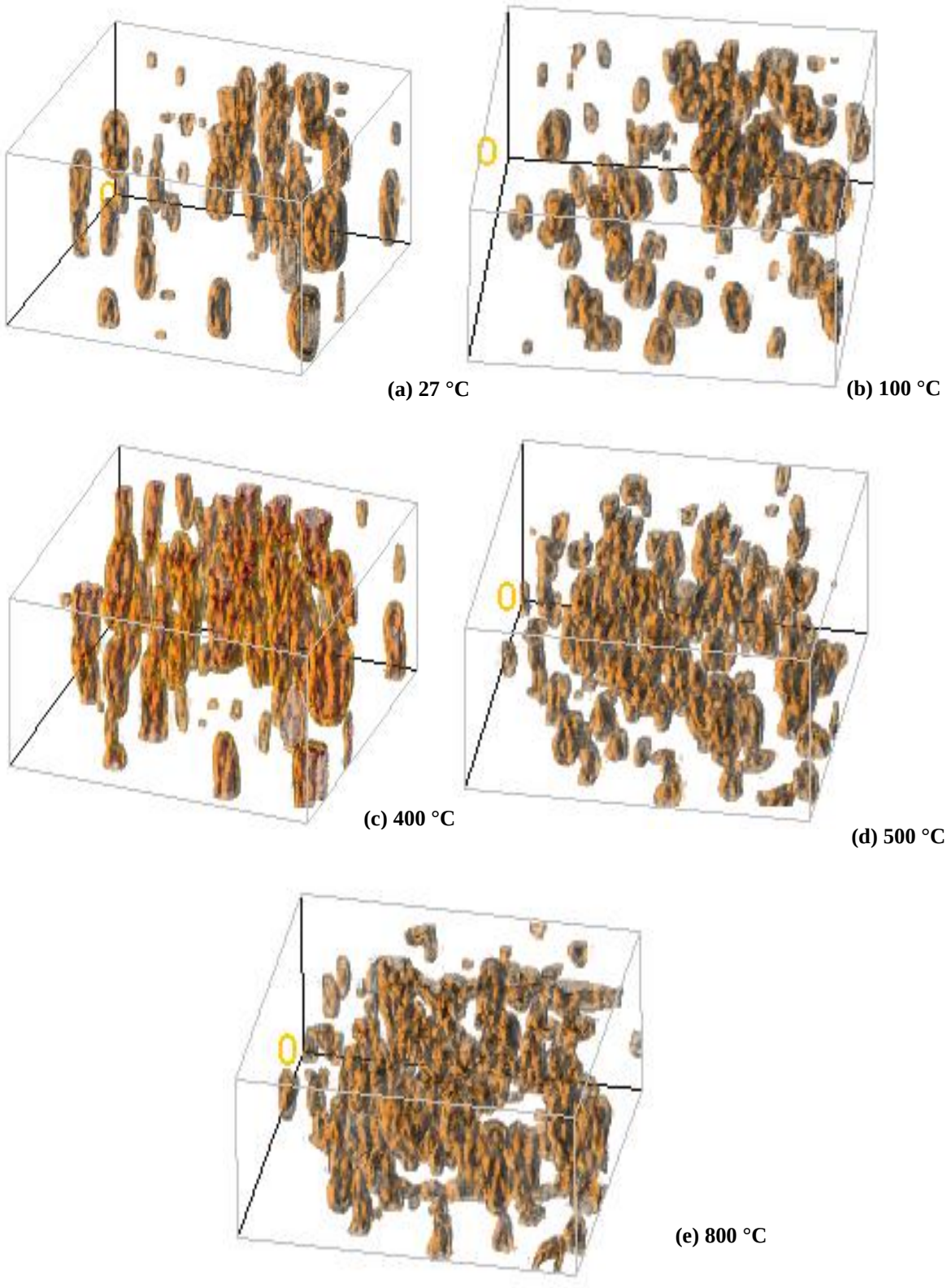

Figure 5.15. 2D to 3D reconstructed samples of OPC-43 at different temperatures using HRCT.

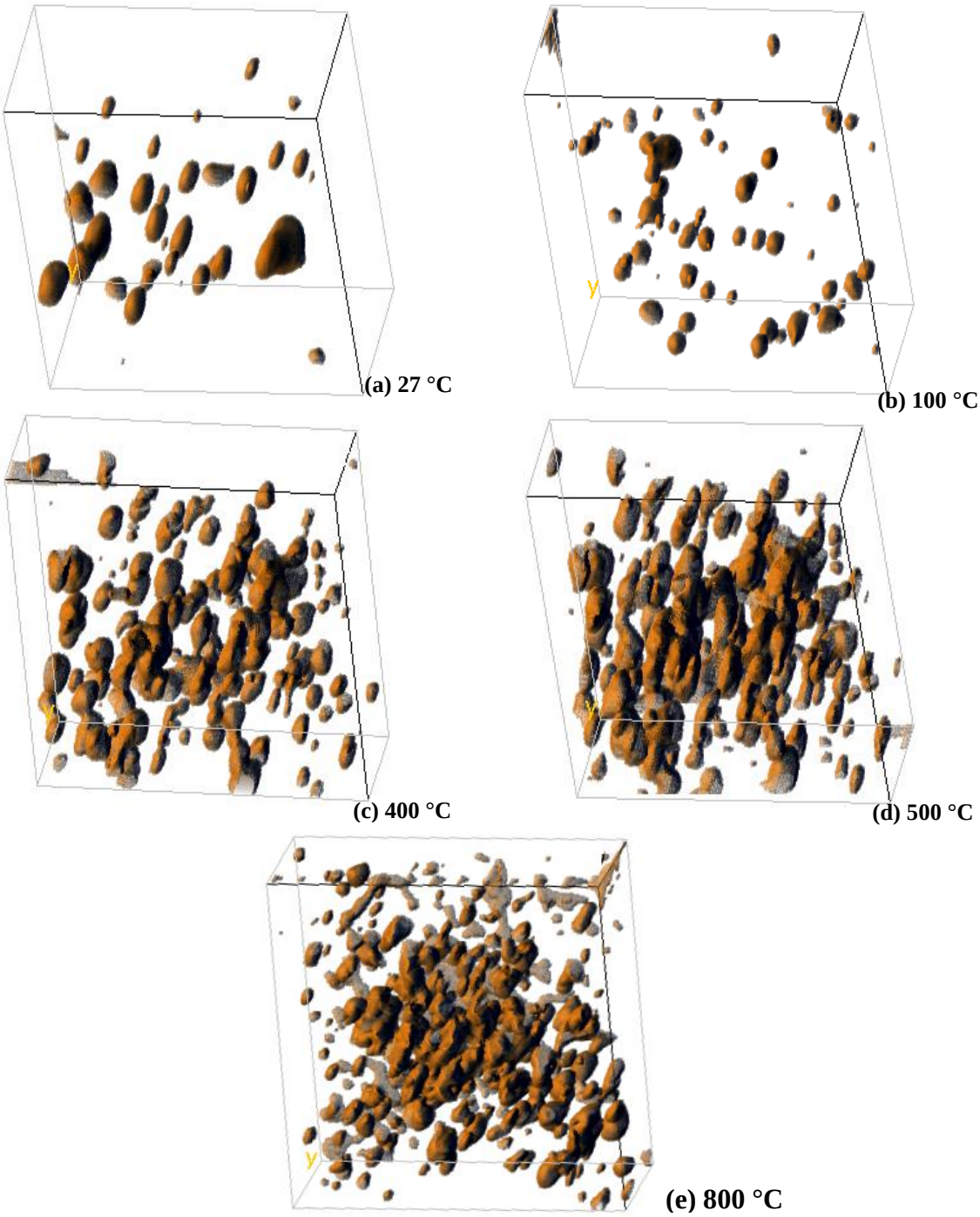

Figure 5.16. 2D to 3D reconstructed samples of OPC-53 at different temperatures using HRCT.

pores having NND of 0.09 is 22.90%. In specimen subjected to SPT of 800 °C the volume fraction corresponding to pores having NND of '0' is 59.71%, and volume fraction corresponding to pores having NND of 0.076 is 21.68%, indicating the increase in spatial extent of pore network in the sample with increase in temperature.

5.4.4. 2D-3D reconstructed images

The 2D slices obtained from the HRCT scan, are constructed into 3D volume to obtain the distribution of the pores in the samples, by stacking the 2D slice one over the other. The *"volume viewer"* plugin is used for the 3D reconstruction using ImageJ®.

5.4.4.1. 3D reconstructed PPC samples

The 3D reconstructed images in the Figure 5.14. show the distribution of the pore network across the samples of PPC at the temperatures of 27 °C, 100 °C, 400 °C, 500 °C, and 800 °C. When comparing the images of Figure 5.14(a) at 27 °C the pores and their distribution is not well spread across the sample, i.e. each pore is spaced apart. However, with the increasing temperatures the spread of pores across the lateral and longitudinal direction can be noticed in Figure 5.14(e) at 800 °C and also in the other samples at their respective temperatures as shown in Figure 5.14(b)-(d), which is the primary reason for the reduction in compressive strength.

5.4.4.2. 3D reconstructed OPC-43 samples

The 3D reconstructed images of the OPC-43 samples are shown in the Figure 5.15 (a)-(e) at the temperatures of 27 °C, 100 °C, 400 °C, 500 °C, and 800 °C. The image analysis of the 2D slices indicates less number of pores than the PPC samples, however the area of pores is larger in comparison to PPC samples. The pores in OPC-43 sample at 27 °C shown in Figure. 5.15(a) are spread deeper than the PPC samples at the 27 °C as shown in Figure 5.14(a). Similar to PPC samples, with the increase in temperature the pores in OPC-43 has also increased, as is evident in the Figure 5.15(c) & 5.15(d) at temperatures of 400 °C and 500 °C.

5.4.4.3. 3D reconstructed OPC-53 samples

The 3D reconstructed images of the OPC-53 samples are shown in the Figure 5.16 (a)-(e) at the temperatures of 27 °C, 100 °C, 400 °C, 500 °C, and 800 °C. Unlike the samples of PPC and OPC-43, the OPC-53 samples have the least number of pores at 27 °C and 100 °C which can be observed in the Figure 5.16(a) & (b). However, as the temperatures increase to 400 °C the number of pores has also increased as evident in Figure. 5.16(c), and as the temperatures increase the pore concentration is higher at 500 °C and 800 °C as observed in Figure 5.16(d) & (e).

5.4.5. 3D analysis

Avizo® software is used to estimate the values of pores in the cube, i.e., equivalent diameter, volume, and the sphericity of pores. The images that are analysed in ImageJ® are loaded into the Avizo® software. Voxel properties of 0.488 x 0.488 x 0.7 mm are given as input properties; and "*ortho slice"* option is selected so that the process of thresholding becomes simpler. The *"Interactive threshold"* module is chosen to distinguish the pores and matrix, with the help of Orth slices the selected pore region is visualized in each pore region that was selected across the x-y-z-axis. Label analysis modules is selected for carrying out 3D interpretation to measure, i.e., equivalent diameter, area, and sphericity of pores in the sample

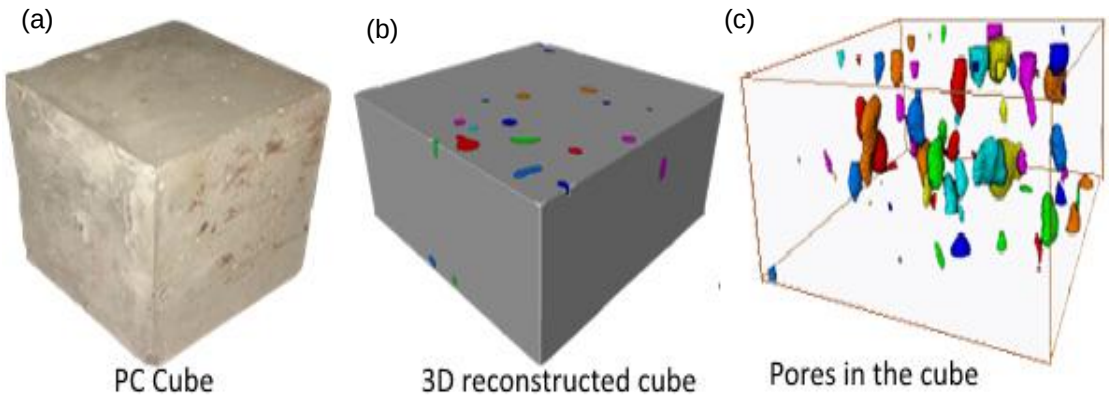

Figure 5.17. Image analysis of hydrated PC cube.

at respective temperatures. The PC cube that placed under the scan shown in Figure 5.17(a), the 3D reconstructed PC cube using Avizo® analysis, with matrix and the pores shown in Figure 5.17(b), while the matrix from the sample has been removed to visualize the pores in the cube shown in Figure 5.17(c).

5.4.6. Volume of pores in PC samples

The pores existing in the cube and the volume of these individual pores can be determined, using the 3D image analysis. 2D image analysis indicated a growth in the number of pores per slice. From the image analysis of the following results were obtained:

5.4.6.1. Volume of pores in PPC

The PPC sample has a total number of 119, 99, 114 and 110 pores at 27 °C, 400 °C, 500 °C, and 800 °C respectively. The PPC sample at 27 °C has pores of volume ranging from 50.49 mm^3 to 957.26 mm^3, and the pore percentages are 75.63 and 0.84, while the pores of volume

151.24 mm^3 and 252 mm^3 have pore percentages of 9.24 and 3.36. At 400 °C the sample has pore volumes ranging from 63.58 mm^3 to 1078 mm^3 for pore volume percentages of 75 and 1 respectively, while the pores 190.42 mm^3 and 317.26 mm^3 pore percentages are 16.16 and 1 respectively. The volume of pores in the sample at 500 °C ranges from 64.08 mm^3 to 1214 mm^3, and the pore volume percentages are 78.07 and 0.87 respectively, while pore volumes of 191.87 mm^3 and 319.67 mm^3 has pore volume percentages of 7.01 and 7.89 respectively. At 800 °C the pore volume ranges from 68.37 mm^3 to 7710 mm^3, and the pore volume percentages are 58.18 and 0.90 respectively, and the pores of 92.43 mm^3 and 190 mm^3 has pore volume percentages of 19.09 and 12.72 respectively.

5.4.6.2. Volume of pores in OPC-43

In OPC-43 at 27 °C the volume of pores range from 97.54 mm^3 to 1263 mm^3 for a pore volume percentage of 76.19 to 1.38, while the pore volume range of 292 mm^3 to 486 mm^3 have pore volume percentages of 14.28 and 4.76. At 400 °C the pore volumes range from 78.76 mm^3 to 1179 mm^3 for pore percentages of 75.47 and 1.88, while the pores of volume 236 mm^3 and 393 mm^3 and the pore percentages are 11.94 and 7.96 respectively. At 500 °C the specimen fails to show resistance to the external load in the compressive testing machine. The pore volume in the sample are in the range of 77.23 mm^3 to 1310 mm^3 for a pore volume percentage of 72 and 1.08 respectively, while the volumes of 231.36 mm^3 and 345.45 mm^3 have pore volume percentages of 11.86 and 11.95 respectively. However, at 800 °C the specimen disintegrates entirely due to thermal load. The volume ranges are 110.34 mm^3 to 12552 mm^3 for volume percentages of 80.64 and 1.07, while the pores of volume 240.56 mm^3 and 450.32 mm^3 has pore percentages of 9.67 and 4.30 respectively.

5.4.6.3. Volume of pores in OPC-53

The OPC-53 samples have a total number of 118, 124, 104 and 153 pores at 27 °C, 400 °C, 500 °C, and 800 °C respectively. The OPC-53 sample at 27 °C has a pore volume ranging from 42 mm^3 to 805 mm^3, and the volume percentages are 83.05 and 0.84 respectively, while the pore volumes of 128 mm^3 and 211 mm^3 have pore volume percentages of 11.10 and 3.39 respectively. At 400 °C the pore volume ranges between 139 mm^3 to 2897 mm^3 and the pore volume percentages are 82.25 and 0.80 respectively, while the pore volumes of 414 mm^3 and 690 mm^3 have a pore volume percentage of 8.87 and 1.62 respectively. At 500 °C the

specimen failed to show any resistance to external loads in the compressive testing machine. The corresponding pore volume in the sample is in the range of 160.68 mm^3 to 3031 mm^3 for pore volume percentages of 83.65 and 0.96, while the pores of volume 480 mm^3 and 798 mm^3 have pore volume percentages of 9.61 and 2.88 respectively. However, at 800 °C when the OPC-53 sample disintegrates due to thermal load, the sample has pores of volume ranging from 182.32 mm^3 to 10828 mm^3 for pore volume percentages of 72 and 0.62 respectively, while the pores of 470 mm^3 and 3295 mm^3 have pore volume percentages of 26.14 and 6.35. A gradual increase in the pore volume and along with the growth in the maximum volume of pores can be observed at their respective temperatures. The OPC-43 has a total of 63, 67, 92, and 93 pores at 27 °C, 400 °C, 500 °C and 800 °C respectively.

5.4.7. Sphericity

Sphericity (Ψ) is defined as the ratio of the surface area of a sphere to the particle surface area which are obtained from the following equation 5.3 in which 'V' is the volume of the particle, 'A' is the surface area.

$$\Psi = \frac{\pi^{1/3} * 6V^{2/3}}{A} \quad \text{---------- (5.3)}$$

Sphericity is indicated on a scale of '0' to '1' wherein '1' indicates a perfect sphere and '0' indicates the pores are elliptical and the obtained plot shown in the Figure. (Note: sphericity computed can be greater than 1 for smaller pores which are composed of fewer voxels) the values above '1' sphericity are neglected.

5.4.7.1. Sphericity of pores in PPC

For PPC sample at 27 °C the sphericity values lie between 0.61(2.52%) and 1(4.20%), while the maximum percentage is 49.57 for sphericity of 0.92. PPC at 100 °C the sphericity values lie between ranged 0.69 (9.09%) and 1 (10.10%), while the maximum percentages of 58.58 for a sphericity value of 0.90. For PPC at 400 °C the sphericity values lie between 0.69 (9.09%) and 1(10.10%), while the maximum percentage is 58.58 for sphericity value of 0.90. For PPC at 500 °C the sphericity values lie between 0.61 (7.89%) and 1(4.38%), while the maximum percentage is 39.47 for sphericity value of 0.92. For PPC at 800 °C the sphericity values lie between 0.34 (0.97%) and 1 (20.90%), while the maximum percentage value is

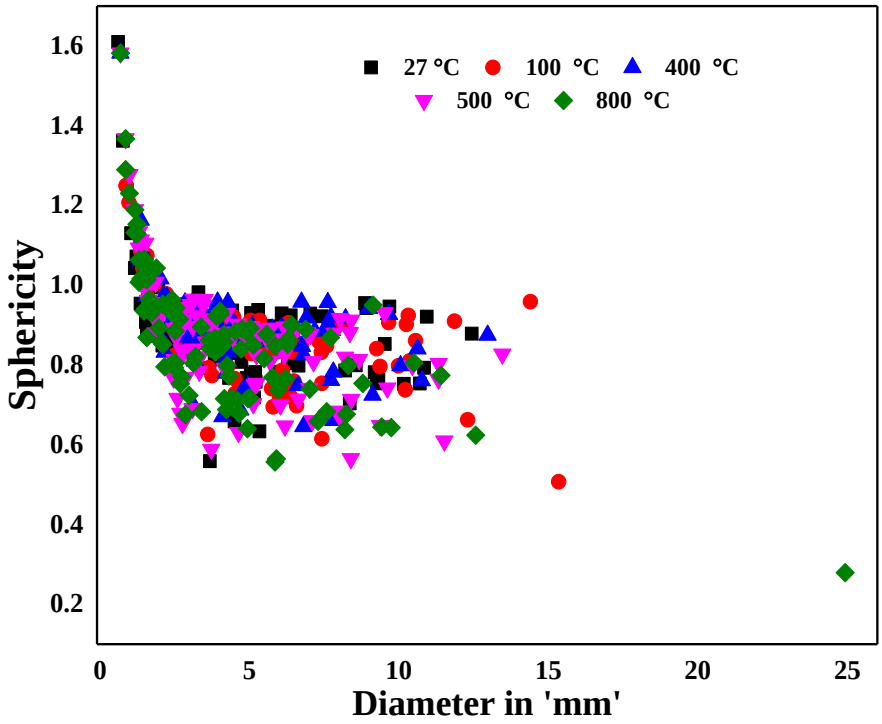

Figure 5.18. Sphericity of pores in PPC samples.

34.54 for a sphericity of 0.86. The data in Figure 5.18 reveals that, with the increase in temperature, the pores which are initially in spherical shape have turned into elliptical pores due to the interconnection between the existing pores. It can also be observed from Figure 5.18 that as the diameter of the pores increased with temperature the sphericity values decreased. The pores of smaller diameter remain spherical in shape.

5.4.7.2. Sphericity of pores in OPC-43

For OPC-43 sample at 27 °C the sphericity values lie between 0.71 (6.3%) and 1.02 (6.34%), while the maximum percentage is 47.6 for sphericity of 0.86. For OPC-43 at 400 °C the sphericity values lie between 0.74 (7.4%) and 1 (1.49%), while the maximum percentage is 50.74 for sphericity of 0.85. For OPC-43 at 500 °C the sphericity values lie between 0.67(3.26%) and 1 (15.21%), while the maximum percentage is 54.34 for sphericity value of 0.88. OPC-43 at 800 °C the sphericity values lie between 0.36(1.07%) and 1 (3.22%), while the maximum pore percentage is 37.63 for a sphericity value of 0.95.

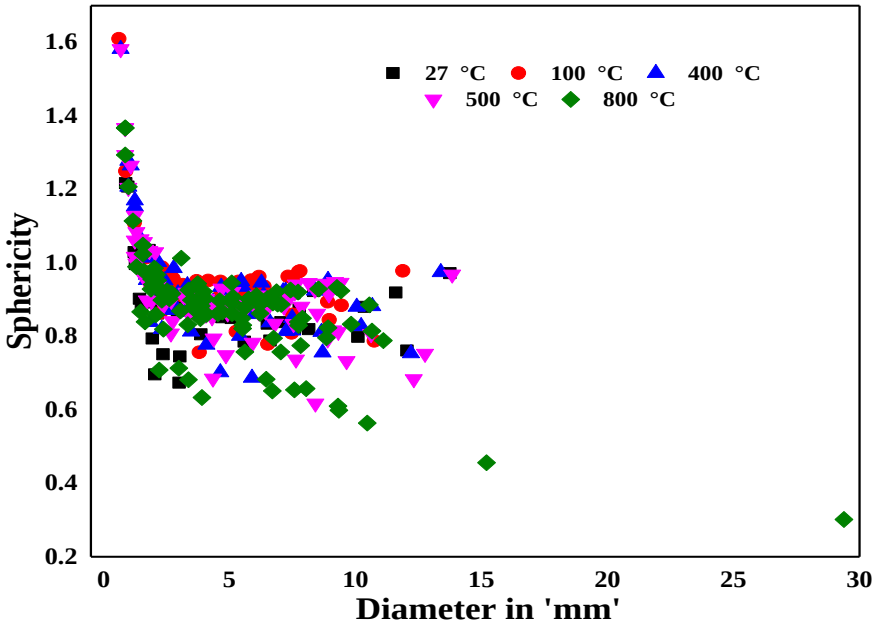

Figure 5.19. Sphericity of pores in OPC-43 samples.

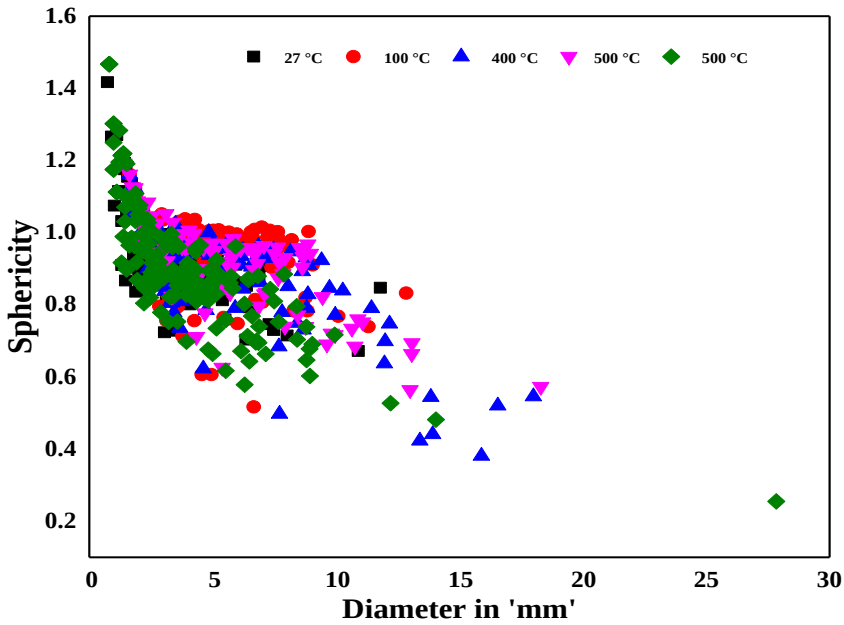

Figure 5.20. Sphericity of pores in OPC-53 samples.

5.4.7.3. Sphericity of pores in OPC-53

For OPC-53 at 27 °C, the sphericity lies between 0.70 (5.08%) and 1 (12.72%), while the highest sphericity of 0.85 with 39.83. For OPC-53 at 400 °C the sphericity values lie between 0.41 (2.41%) and 1(2.90%), while the maximum sphericity is 0.94 with 38%. For OPC-53 at between 0.30 (0.65%) and 1 (12.41%), while the maximum percentage of 31.37 for a sphericity of 0.91.

5.4.8. Relationship between Compressive strength Vs Porosity

The tests conducted using HRCT for the samples exposed to the elevated temperatures, indicate that the air voids existing in the samples have gradually increased with temperature. As the increase in temperature progresses, the porosity of the samples increase drastically, leading to failure of the samples due to internal stresses at 500 °C and 800 °C. A certain variation in the pore propagation exists between the PPC, OPC-43 and OPC-53 samples exists as discussed below:

5.4.8.1. Compressive strength Vs porosity for PPC

The variation in the number of pores in all the samples with respect to 2D analysis (slices), 3D analysis (entire sample), temperature, compressive strength and porosity is plotted in Figure 5.21. The DSC plots shown in Figure 4.4 indicate the rate of heat flow in PPC sample is lower than OPC-43 and OPC-53 samples. The plots in the Figure 5.21 indicate an increase

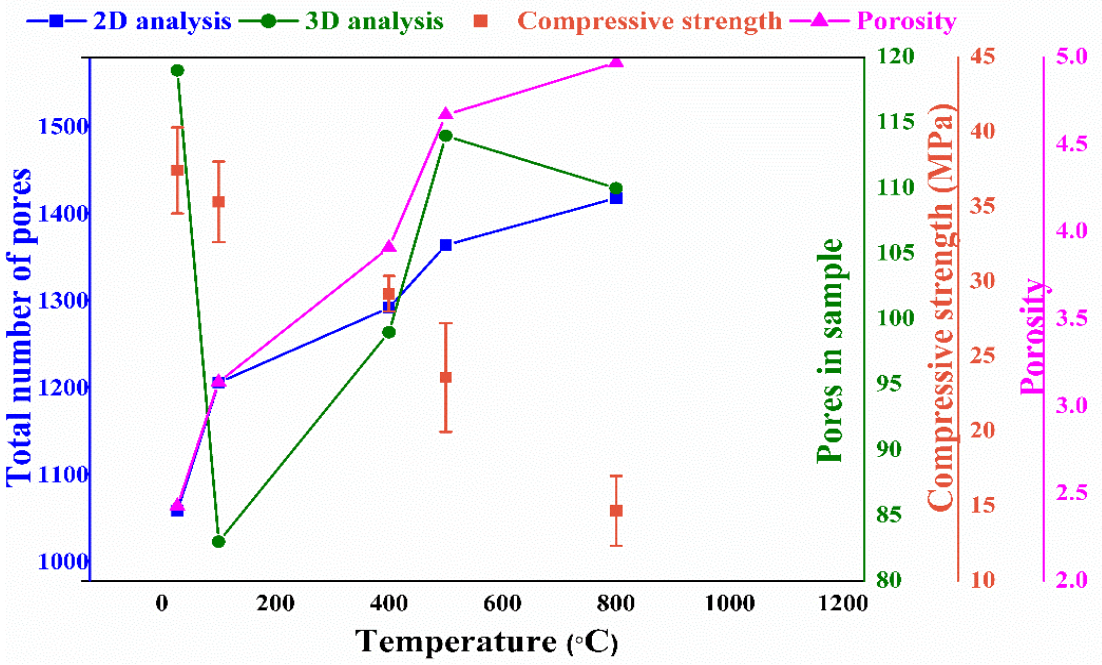

Figure 5.21. Porosity Vs Temperature Vs compressive strength of PPC

in the number of pores per slice with increasing temperature. In the region between 400 °C - 500 °C a drastic increase in the number of pores was observed from both 2D and 3D analysis. However, the 2D image analysis studies indicate an increase in the number of pores per slice. The overall number of pores in the sample (3D image analysis) decreased slightly, due to the other GoC interconnectivity among the pores. The porosity in the PPC samples is the least in comparison if the number of pores are higher the greater will the possibility of interconnection which causes a pore network leading to failure of the samples. The Figure

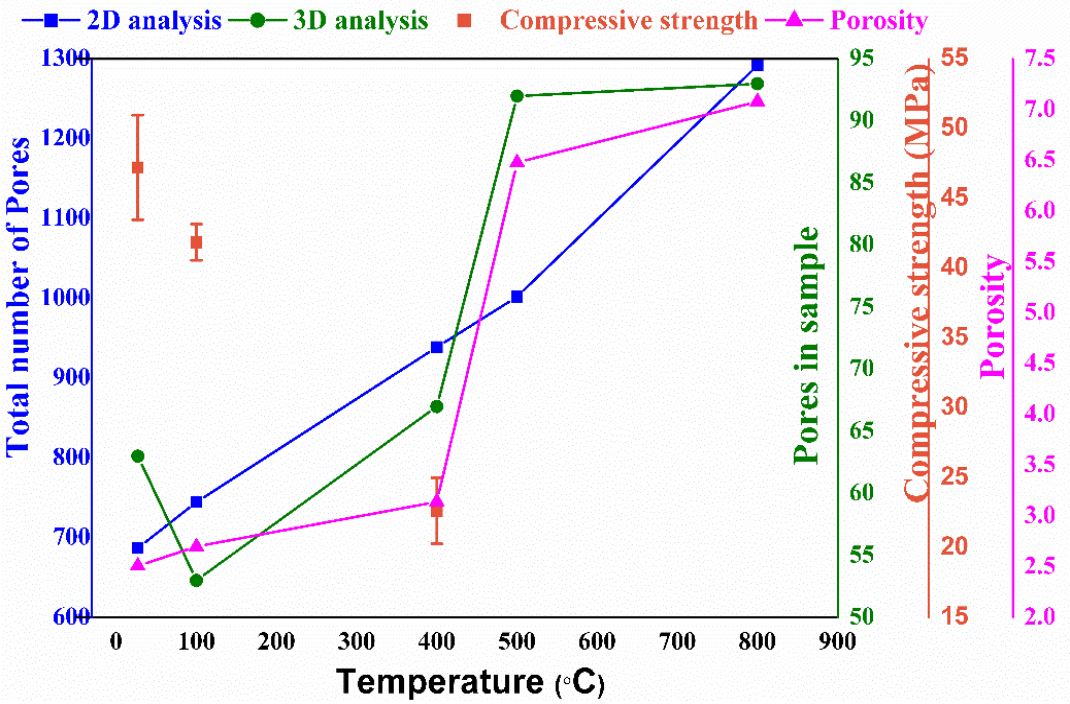

Figure 5.22. Porosity Vs Temperature Vs compressive strength of OPC-43

5.24 indicates pores spread across the samples at all temperatures, while Figure 5.24 (e) shows a less dense pore network with the rest of the samples of OPC-43 i.e. Figure 5.25(e) and OPC-53 i.e. 5.26(e).

5.4.8.2. Compressive strength Vs porosity for OPC-43

The variation in the number of pores in all the samples of OPC-43 with respect to slices (2D analysis), entire sample (3D analysis), temperature, compressive strength and porosity is plotted

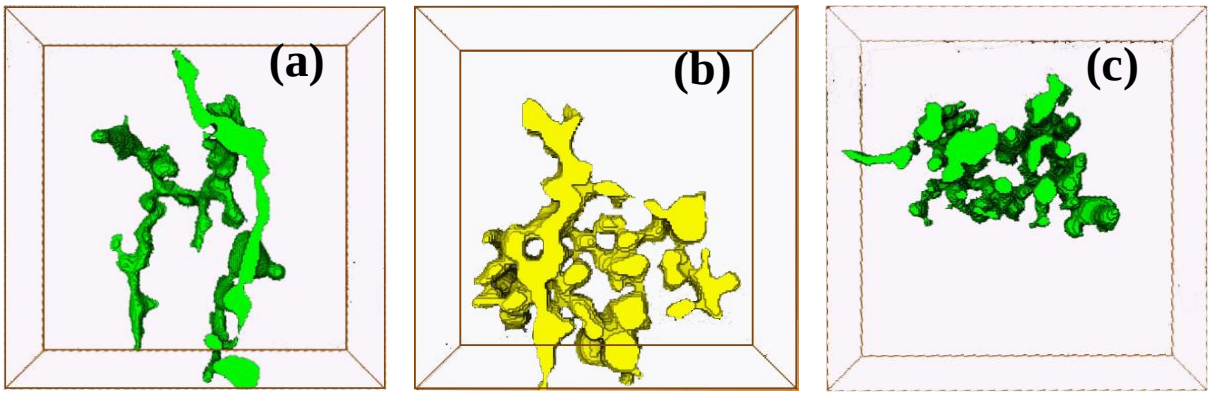

Figure 5.23. Pore network spread across the PPC, OPC-43 and OPC-53 samples at 800 °C

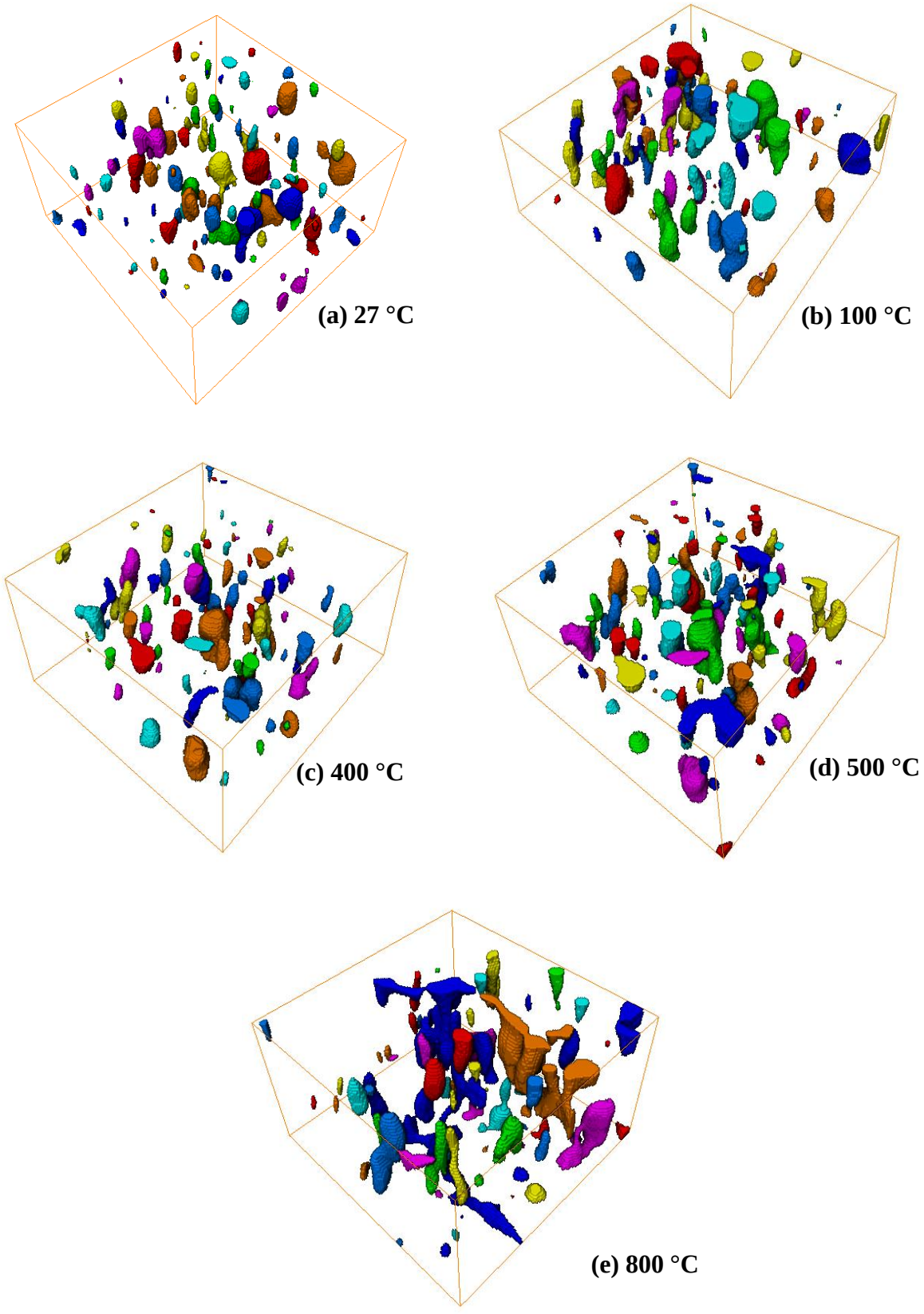

Figure 5.24. 3D reconstruction of the PPC samples, identifying the pores individually at different temperatures.

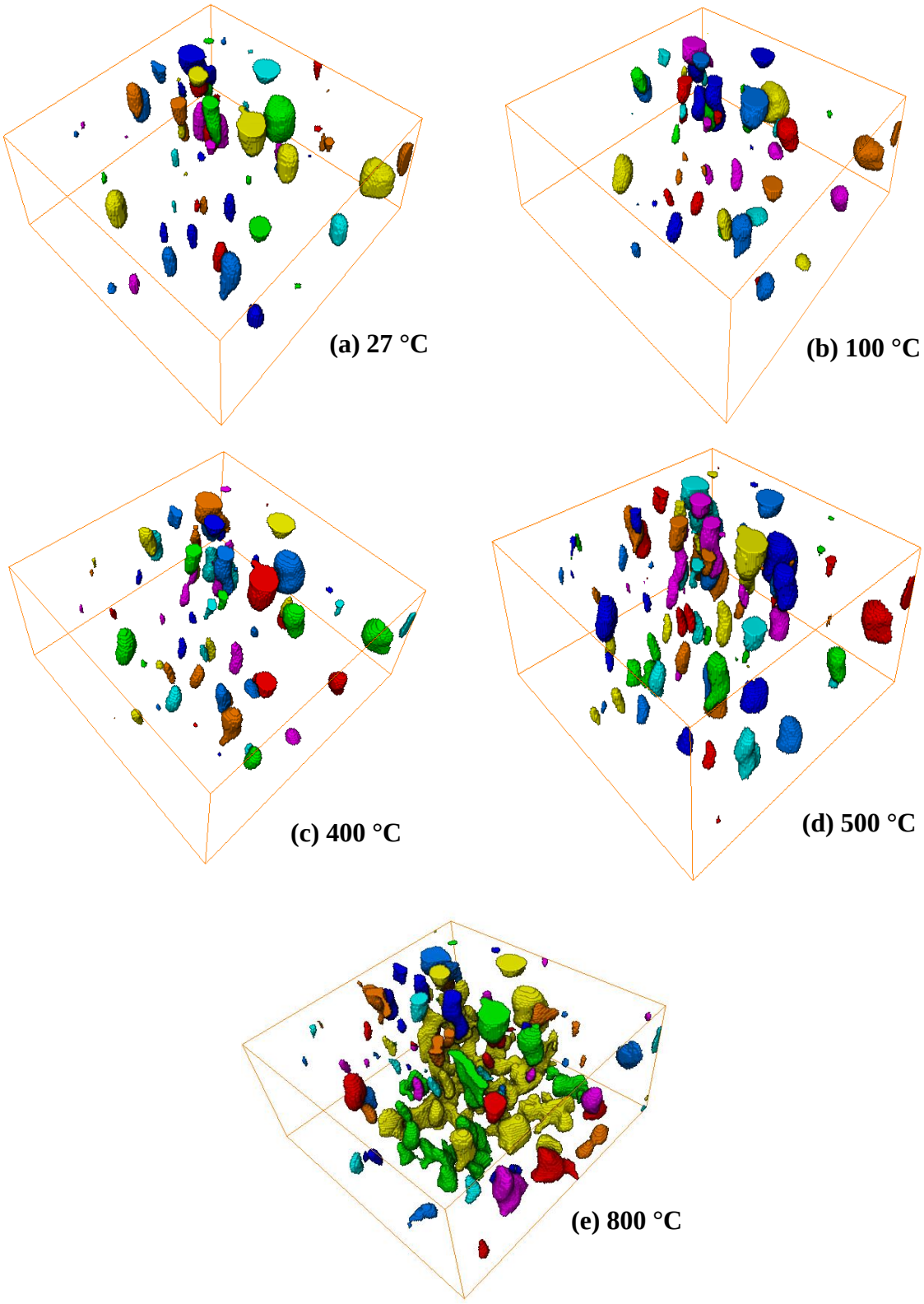

Figure 5.25. 3D reconstruction of the OPC-43 samples, identifying the pores individually at different temperatures.

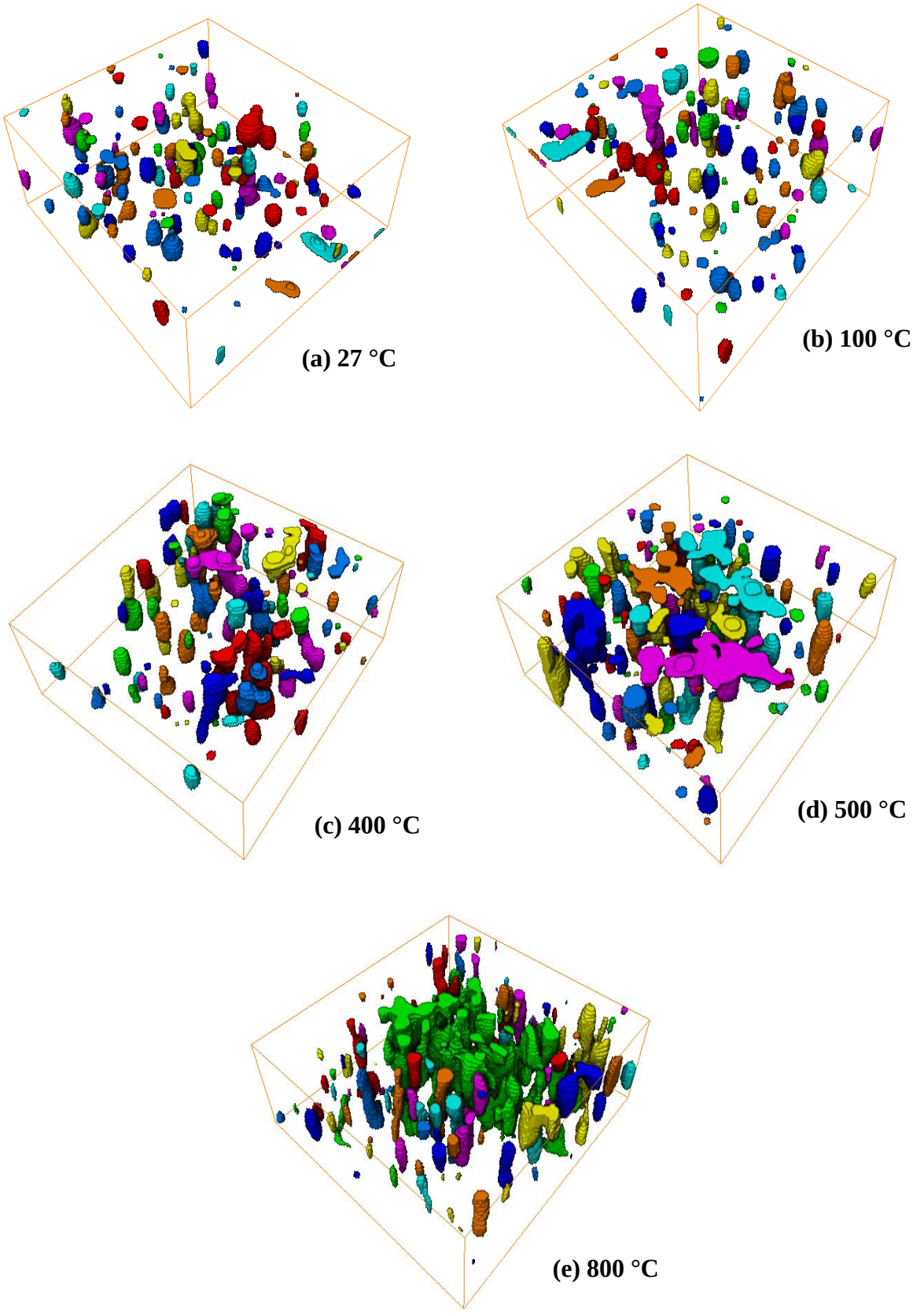

Figure 5.26. 3D reconstruction of the OPC-53 samples, identifying the pores individually at different temperatures.

in Figure 5.22. The heat flow taking place in OPC-43 samples is higher in comparison to the PPC samples, as shown in Figure 4.4. The pores in the number of slices of the samples after 2D image analysis and 3D analysis increased with temperatures. The rate of increase in the number of pores per slice (2D) and in the sample (3D) and also the obtained porosity is higher when compared with PPC samples. The PPC and OPC-43 sample shown in Figure 2.4(e) and 2.5 (e) after 3D image analysis indicates that OPC-43 has denser pores and pore network, and the pore diameters are larger in comparison to PPC samples. The porosity values reported for OPC-43 are higher than PPC samples. The Figure 5.23 (a) & (b) shows the variation in the pore network for PPC and OPC-43 samples, the spread of pore network across the sample is one of the primary reason for the disintegration of the OPC-43 sample.

5.4.8.3. Compressive strength Vs porosity for OPC-53

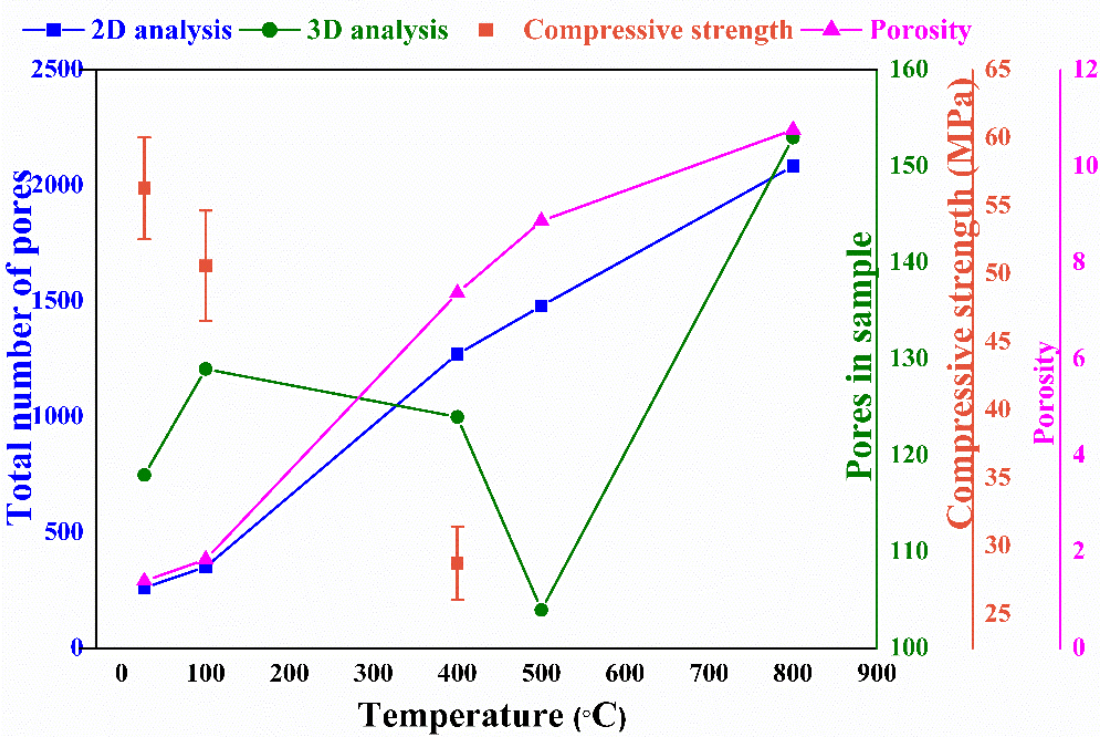

Figure 5.27. Porosity Vs Temperature Vs compressive strength of OPC-53

The variation in the number of pores in all the samples of OPC-53 with respect to 2D analysis (slices), 3D analysis (entire sample), temperature, compressive strength and porosity is plotted in Figure 5.27. Similar to OPC-43, the OPC-53 samples failed to maintain integrity at 500 °C. The pore distribution in the slices after 3D image analysis is shown in Figure 5.26. Similar to the OPC-43 sample there is a sudden increase in the number of pores per in all the slices.

However, the OPC-53 samples are able to form a pore network even at 500 °C, which is one of the reason that the sample has lower compressive strengths. A part of the pore network formed at 800 °C is shown in Figure 5.23(c). Among the three GoC, the pore network formed at 800 °C is lower for PPC sample. The porosity values are the highest for OPC-53 samples. By comparing the images of 5.24(e), 5.25(e), 5.26(e) one can conclude that the formation of pore network and rapid increase in the number of pores is the primary reason for the reduction in the compressive strengths for PPC, OPC-43 and OPC-53 samples.

5.4.8.4. Relationship between porosity and compressive strength

HRCT studies conducted on the samples of PPC, OPC-43 and OPC-53 subjected to an increase in temperature indicate a reduction in compressive strengths. The porosity of the samples has gradually increased with temperature as indicated in Figure 5.21, 5.22 and 5.27

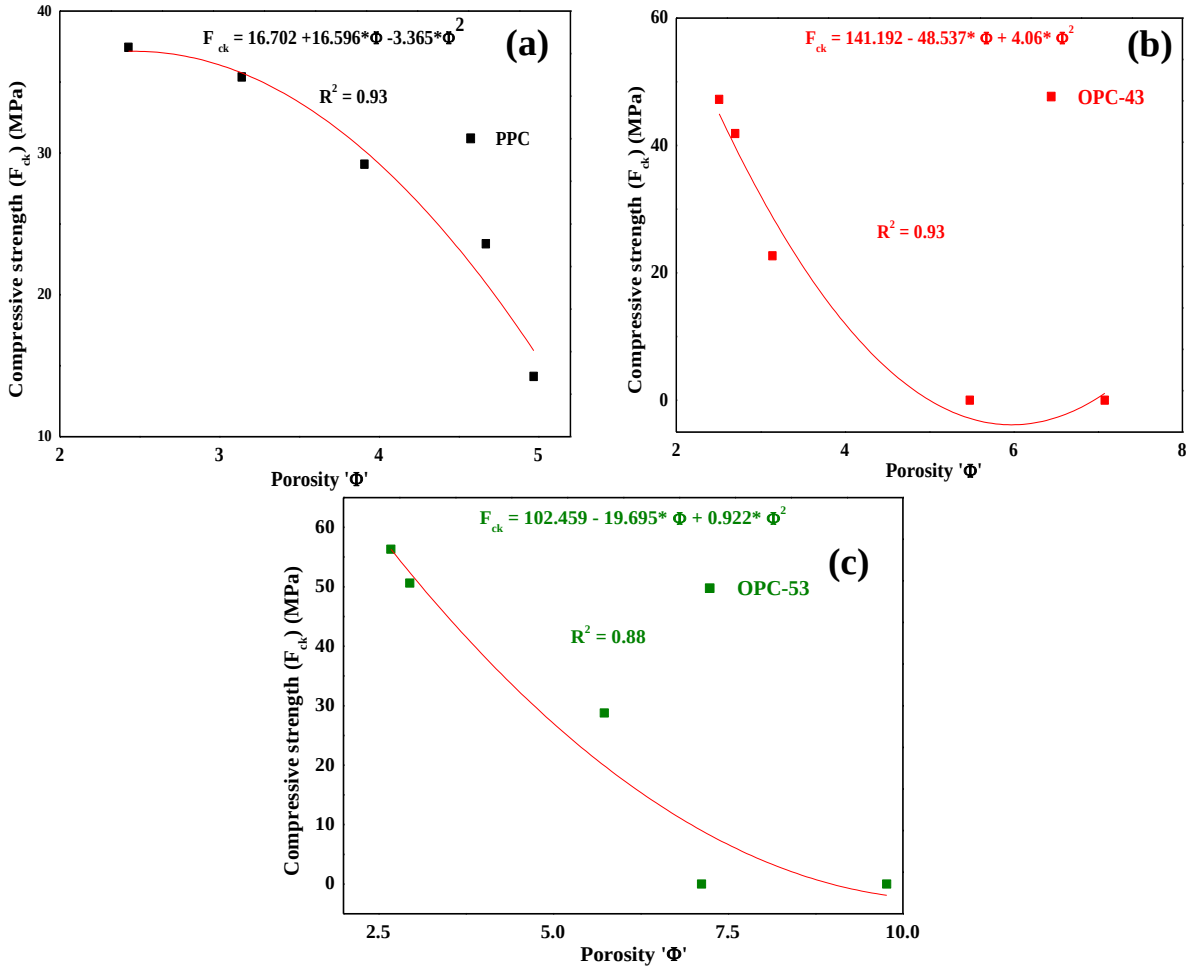

5.28. Porosity Vs compressive strength for (a) PPC, (b) OPC-43 and (c) OPC-53

for all the three GoC. The reduction in the compressive strengths with the increase in porosity are shown in Figure 5.28 for all the three GoC. The samples of OPC-43 and OPC-53 have porosity greater than 5%, and at this porosity the samples disintegrated due to temperature loads. Depending on the GoC a polynomial equation is developed to estimate the compressive strength (F_{ck}) from the porosity (Φ) values at mesoscale for PPC, OPC-43 and OPC-53 samples as shown in Figure 5.28(a - c). As mentioned earlier the OPC-43 and OPC-53 samples failed to withstand any temperature loads at 500 °C hence the compressive strength (F_{ck}) values are zero. However, the porosity values increased with the increasing temperatures, this lead to disintegration of the sample. Equations are proposed to estimate the compressive strength from the estimated porosity values for all the three GoC. Higher the GoC (i.e. compressive strength), severe is the effects of porosity with the increase in temperature. The porosity (Φ) values are severely effected as the temperature went beyond 400 °C. Regression analysis was carried and a polynomial expression was developed for the PPC, OPC-43 and OPC-53, with the regression values of 0.93, 0.93 and 0.88 respectively. The polynomial equations 5.24, developed for the PPC, OPC-43 and OPC-53 at meso-scale are shown below:

$$F_{ck} = 16.702 + 16.596(\Phi) - 3.396\,(\Phi)^2 \quad \text{---- 5.24}$$

$$F_{ck} = 141.192 - 48.537(\Phi) + 4.06\,(\Phi)^2 \quad \text{---- 5.25}$$

$$F_{ck} = 102.459 - 19.695(\Phi) + 0.992\,(\Phi)^2 \quad \text{---- 5.26}$$

5.5. Conclusion from this chapter

- High resolution computer tomography (HRCT) is an appropriate crucial test to understand the evolution of pores with increase in temperature and these studies enabled monitoring the changes in meso structure taking place in various cement sample.
- At meso-scale, the number of pores increased gradually with increase in temperature. A sudden increase in the number of pores is observed as the temperatures switch from 400 °C to 500 °C. This is the threshold temperature at which the interconnected porosity is observed.
- The circularity of pores shifted to elongated pores with increasing temperatures, indicating interconnection between them. Larger pore diameters tend to be in elliptical

in shape rather than spherical shape, which is observed from the sphericity of the samples.

- The nearest neighbour distance (NND) analysis indicated an increase in a strong pore network with increasing temperatures, and as the pore network increased the pore propagation has become much easier, leading to coalescence of pores into cracks.
- PPC samples were intact because of less extensive pore network, while this was not the case with OPC-43 and OPC-53. Among all the three grades of cement, PPC samples has better resistance to thermal loads even at 800 °C, while OPC-43 and OPC-53 failed to do so at 500 °C.
- The formation of pores and interconnection of pores at different temperatures in different types of cement was understood. This is important to understand the possible durability related deterioration in samples.

Chapter-6

Determination of pore network and porosity at microscale

Chapter-6

Determination of pore network and porosity at microscale

6.1. General

High resolution computer tomography tests are carried on the three GoC samples of dimensions 50 x 50 x 50 mm^3. The pores present in the samples at elevated temperatures are analysed, and the pores of sizes greater than 0.48 mm at meso-scale are studied. All the three samples has shown signs of the pore growth with the increase in temperature, and with the increase in temperature the pores get interconnected. The estimation of the pores in the samples is very much governed by the beam resolution of the X-ray used under the HRCT. The pores present in the sample are spread across multiple scale of the sample, and the pore concentration should vary across the scales of the samples being analysed. To analyse the pores at smaller scales, the X-ray beam intensity of smaller scales needs to be used, because the beam intensity of medical HRCT is 0.48 mm. In order to study the pores in the samples at smaller scales micro tomography tests are conducted on the samples at smaller scales of ± 3 mm x 3 mm x 10 mm. While the resolution of the micro tomography facility is 4.5 x 4.5 x 4.5 μm^3, due to which the number of slices and pores of smaller diameter can be estimated. So far various studies have been carried out by other researchers on the hydrated cement pastes to estimate the hydration reaction at different stages of hydration, effects of water cement ratios on hydration and to determine tortuosity etc.

6.2. Experimental investigation

The effects of temperature on the samples at micro scale are investigated in this study. The samples for the micro tomography scan are collected from the core of the specimens, scanned under HRCT. The micro tomography enables estimation of the changes in porosity and its parameters, with respect to temperatures in the three GoC i.e. PPC, OPC-43 and OPC-53 at room temperature, 100 °C, 400 °C, 500 °C, and 800 °C. The number of samples scanned is

shown in Figure 6.1, and the experimental investigation carried for the current study is shown in Figure 6.2.

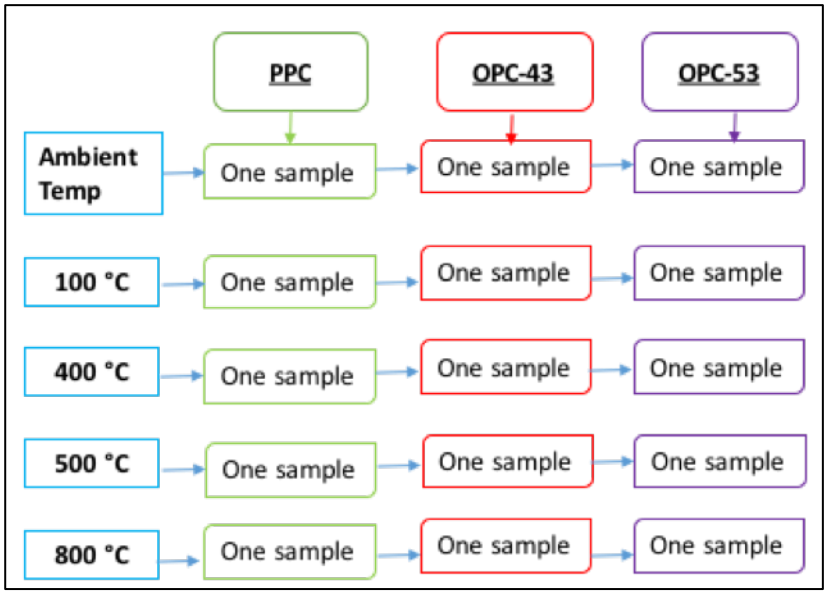

Figure 6.1. Samples scanned under micro tomography.

6.2.1. Synchrotron micro tomography

The experimentation facility for micro tomography consists of storage ring energy of 2.5 GeV, and its maximum current is 135 mA. Unfocused monochromatic x-ray beam with an energy of 20 Kev, and a cross-sectional area of 100 x 5.25 mm^2 is used for irradiation. The voxel size resolution for the current scan is 4.5 x 4.5 x 4.5 µm, and the sample is mounted on a stage that allows the rotation and translation movement, and the data sets are obtained from the Micro-

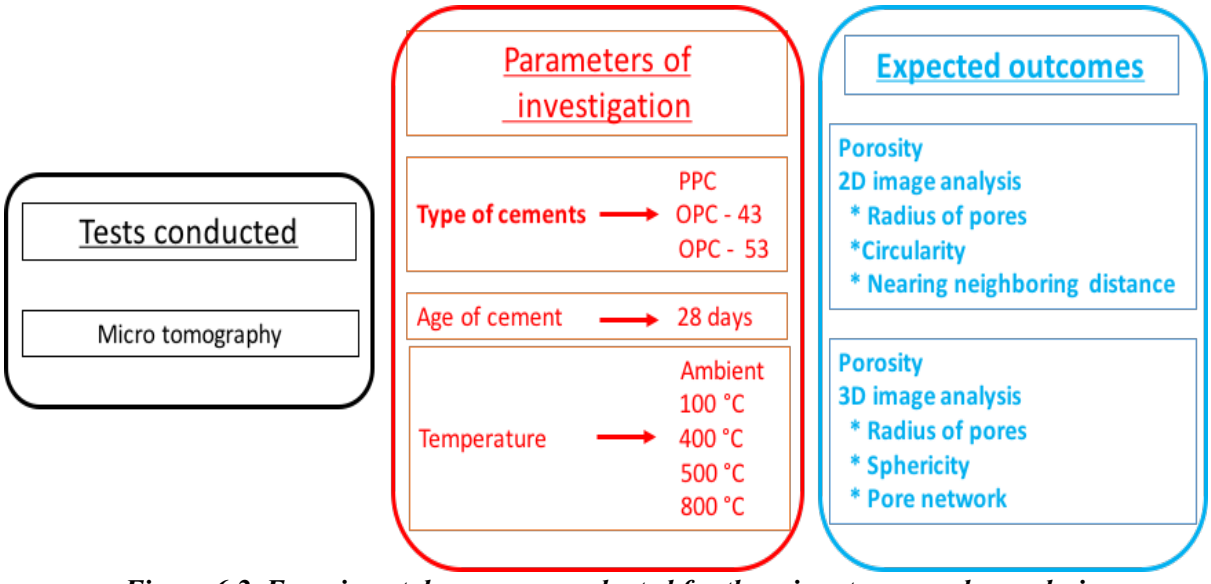

Figure 6.2. Experimental program conducted for the micro tomography analysis

tomography scans. The cross-sectional images obtained from the micro tomography are reconstructed using Octopus® 3D reconstruction software which uses the filtered back projection algorithm (Kak A. C. *et al.* 1988). Data sets obtained from the micro tomography scans are processed to remove beam noise and temporal fluctuations, and the normalized obtained images are cropped to the ROI. After the normalization, the sinogram is built; then parallel beam reconstruction module is chosen, and the sinogram images are processed to remove any smears that are present in the image using the rotation axis option. After removing the smears, the volume reconstruction process is initiated and once the reconstruction is completed a histogram is generated. The upper and lower limit for the histogram is applied to the image and it is converted into an 8-bit image; this process is repeated for all the samples at the respective temperatures.

6.2.2. 2D image processing

The 2D images obtained from the Synchrotron micro tomography are analyzed using ImageJ® software. A total of 900 to 1100 images are produced from the scan of depending on the sample size, and the scanned images are analyzed using image processing technique to estimate the porosity, pore distribution, circularity, and NND. The threshold of the images and beam hardening effects play a significant role in image quality for quantifying the parameters mentioned above using Otsu's method (Otsu, 1979). Otsu's method defines a threshold 't' value for converting grayscale images to a binary image. This method is dependent on determining an ideal 't' value that is achieved by minimizing the variance of the two-pixel group. Once the threshold value is determined, the voxel with threshold value lower than 't' are selected as pores and the rest as solids. The threshold images are imported into ImageJ® using the "*import image sequence"* option.

For the current analysis, 500 images are considered while neglecting the image layers at the top and bottom. This method is adopted so that the internal structure of the sample can be determined. For these imported images, ROI is selected by omitting the external area of the sample, i.e., for all the samples dimensions of ± 1.1 mm x 1.1 mm x 2.2 mm is selected. After the ROI is selected the voxel parameters of 4.5 x 4.5 x 4.5 µm are given as the image properties, and the threshold is set to default for separating the pores and the matrix of the sample for estimating the quantity of porosity. *"Analyze particles"* option is selected to obtain the values of the area of pores, and circularity. After the area of pores is calculated, the NND plugin is used to estimate the pore network. The effective radius of the pore is determined assuming that

the area of the pores obtained from image analysis are in circular shape. The 3D view is obtained by stacking 2D slices in the z-direction using *"volume viewer"* plugin.

6.2.3. 3D image processing

2D analysis is useful in determining the pores present in the sample per slice as the analysis does not give the number of pores in the sample which is a 3D quantity. Avizo® software is used as this software treats the pores present in the immediate slice at the same coordinates as a single pore. Hence Avizo® software is used to estimate the pore parameters such as diameter, area, volume and sphericity in the sample. For the 3D analysis, the threshold images that are analyzed in ImageJ® software, are imported into Avizo® software, and the voxel parameters of 4.5 x 4.5 x 4.5 µm are given as the image properties for the image sequence. *"Interactive threshold"* module is selected for separating the pores and matrix; the *"ortho slice"* option enables observation of the pores being threshold across the x-y-z-axis. To quantify pores in the cube, *"label analysis"* module is selected to calculate the diameter, area, volume, sphericity, and porosity of the sample and this procedure is repeated for all the samples at the respective temperatures.

6.3. Results and discussion

The radii of pores, area, volume, circularity, sphericity, and NND values of the slices obtained from micro tomography after performing 2D and 3D image analysis are shown below:

6.3.1. Radii of pores in PC samples

6.3.1.1. Radii of pores in PPC samples

The radii of pores at corresponding temperatures are plotted in Figure. 6.3, the radii of pores which contribute to greater than 1% of total volume only are considered. At 27 °C the radii of

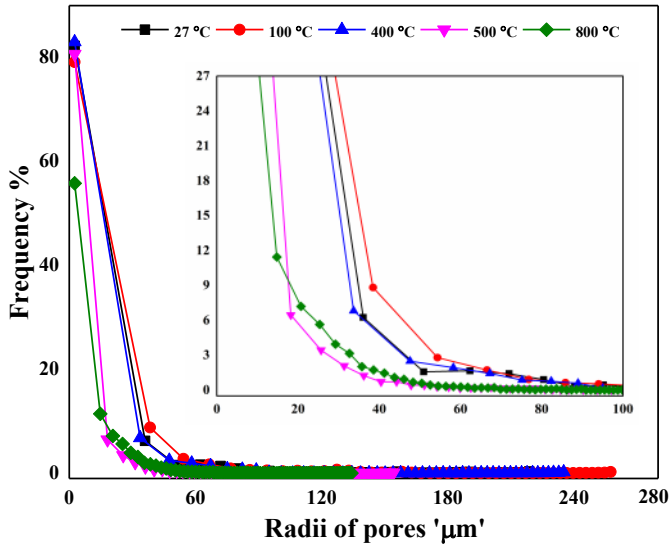

Figure 6.3. Radii of pores in PPC samples at elevated temperatures.

pores range from 2.54 µm to 218.86 µm corresponding to volume percentages of 82.24 and frequency bins (of radii distribution) are centred on 38.46 µm, 54.33 µm, 66.51 µm and the relative volume percentages are 8.82, 2.79, and 1.72 respectively. At both these temperatures, the pores are spaced far apart. The 3D reconstructed samples after 2D image analysis at 100 °C

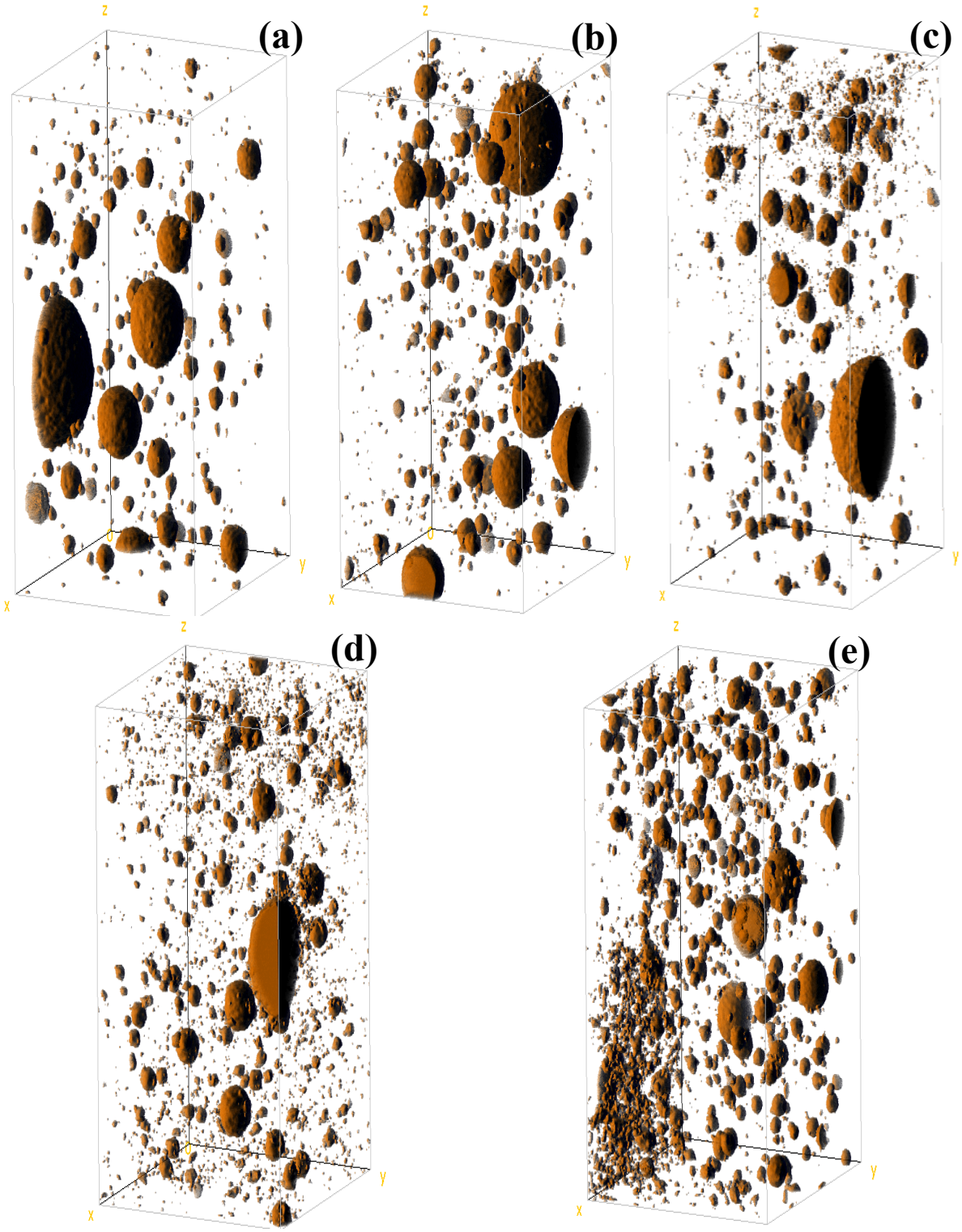

Figure 6.4. 3D reconstructed 2D slices of PPC samples at (a) 27 ℃ (b) 100 ℃ (c) 400 ℃ (d) 500 ℃ (e) 800 ℃

is shown in Figure 6.4(b).At 400 °C the radii of pores range from 2.54 µm to 235.14 µm corresponding to volume percentages of 83 and 0.22 respectively; at this temperature the size of pores tend to get reduced, i.e. they attain values of 33.69 µm, 47.57 µm, 58.23 µm, and 67.23 µm and the relative volume percentages of these pores are 6.82, 2.48, 1.93, and 1.43. The far end of the distribution of pore radii are centred on 218.8 µm (27 °C), 235.14 µm (100 °C), and 257.70 µm µm to 154.16 µm with relative volume percentages of 80.77 and 0.07 respectively; while the frequency bins (of radii distribution) which contribute to greater than 1% of total volume are 18.22 µm, 25.64 µm, 31.35 µm, 36.17 µm and the volume percentages are 6.46, 3.43, 2.08, and 1.24 respectively. The 3D reconstructed samples after 2D image analysis at 400 °C and 500 °C is shown in Figure 6.4(c) & (d). At 400 °C, the radii of pores range from 2.54 µm to 134.18 µm with a volume percent of 55.81 to 0.02, while the volume percentage greater than 1% of total volume are 14.77 µm, 20.73 µm, 25.33 µm, 29.22 µm, 32.62 µm, 35.74 µm, 38.58 µm, 41.24 µm, and 43.73 µm; and the relative volume percentages are 11.44, 7.19, 5.64, 3.95, 3.15, 2.01, 1.73, 1.46, and 1.08. At 500 °C the radii of pores range from 2.54 µm to 154.16 µm with relative volume percentages of 80.77 and 0.07 respectively. The volume percentages greater than 1% of total volume are 18.22 µm, 25.64 µm, 31.35 µm, 36.17 µm and the volume percentages are 6.46, 3.43, 2.08, and 1.24 respectively. At 800 °C the radii of pores range from 2.54 µm to 134.18 µm with a volume percent of 55.81 to 0.02. The volume percentages greater than 1% of total volume are 14.77 µm, 20.73 µm, 25.33 µm, 29.22 µm, 32.62 µm, 35.74 µm, 38.58 µm, 41.24 µm, and 43.73 µm; and the relative volume percentages are 11.44, 7.19, 5.64, 3.95, 3.15, 2.01, 1.73, 1.46, and 1.08 respectively. A sudden drop in the frequency of pores of radii around 2.54 µm is observed at 800 °C in Figure 6.3 this is due to the pore expansion which increases the size of existing pores accompanied by an increase in the number of finer pores.

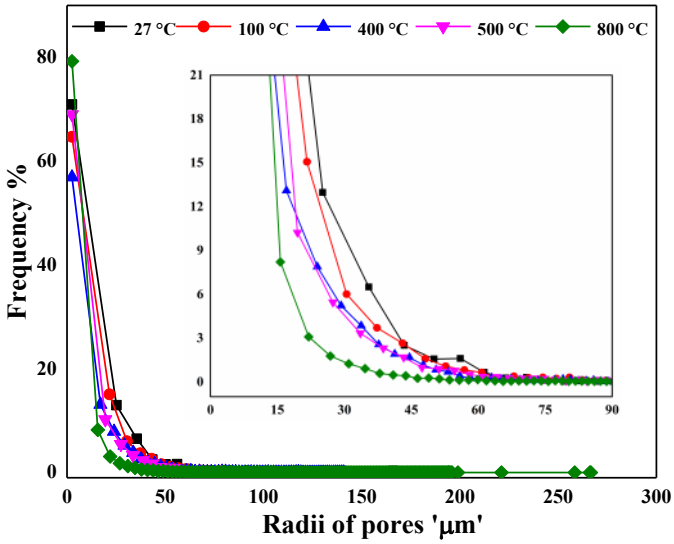

Figure 6.5. Radii of pores in OPC-43 samples at elevated temperatures.

6.3.1.2. Radii of pores in OPC-43 samples

The radii of pores in OPC-43 samples obtained from 2D image analysis is shown in Figure 6.5. The pores of radius 2.54 µm to 56.00 µm contributes to 96.10% of total pores at 27 °C, at 100 °C the pore radius ranged from 2.54 µm to 52.68 µm contributes to 94.13 % of total pores, 2.54

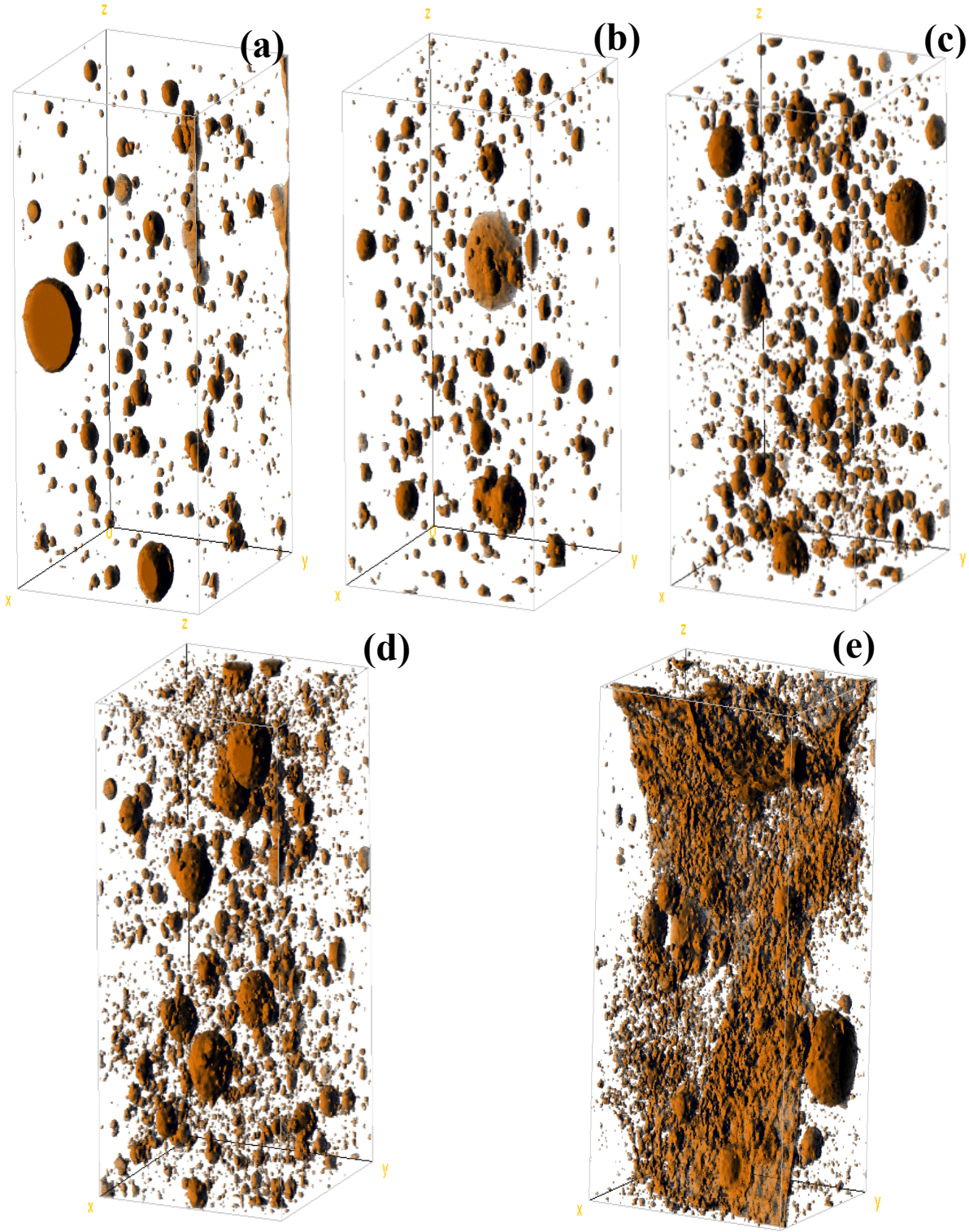

Figure 6.6. 3D reconstructed 2D slices of OPC-43 samples at (a) 27 ℃ (b) 100 ℃ (c) 400 ℃ (d) 500 ℃ (e) 800 ℃

µm to 47.61 µm contributes to 94.31% of the total pore radius present in the sample at 400 °C, we can observe the reduction in the radius of pores with respect to temperature, at 500 °C the pores range has become finer i.e. from 2.54 µm to 43.28 µm, which constitutes to 92.07% of

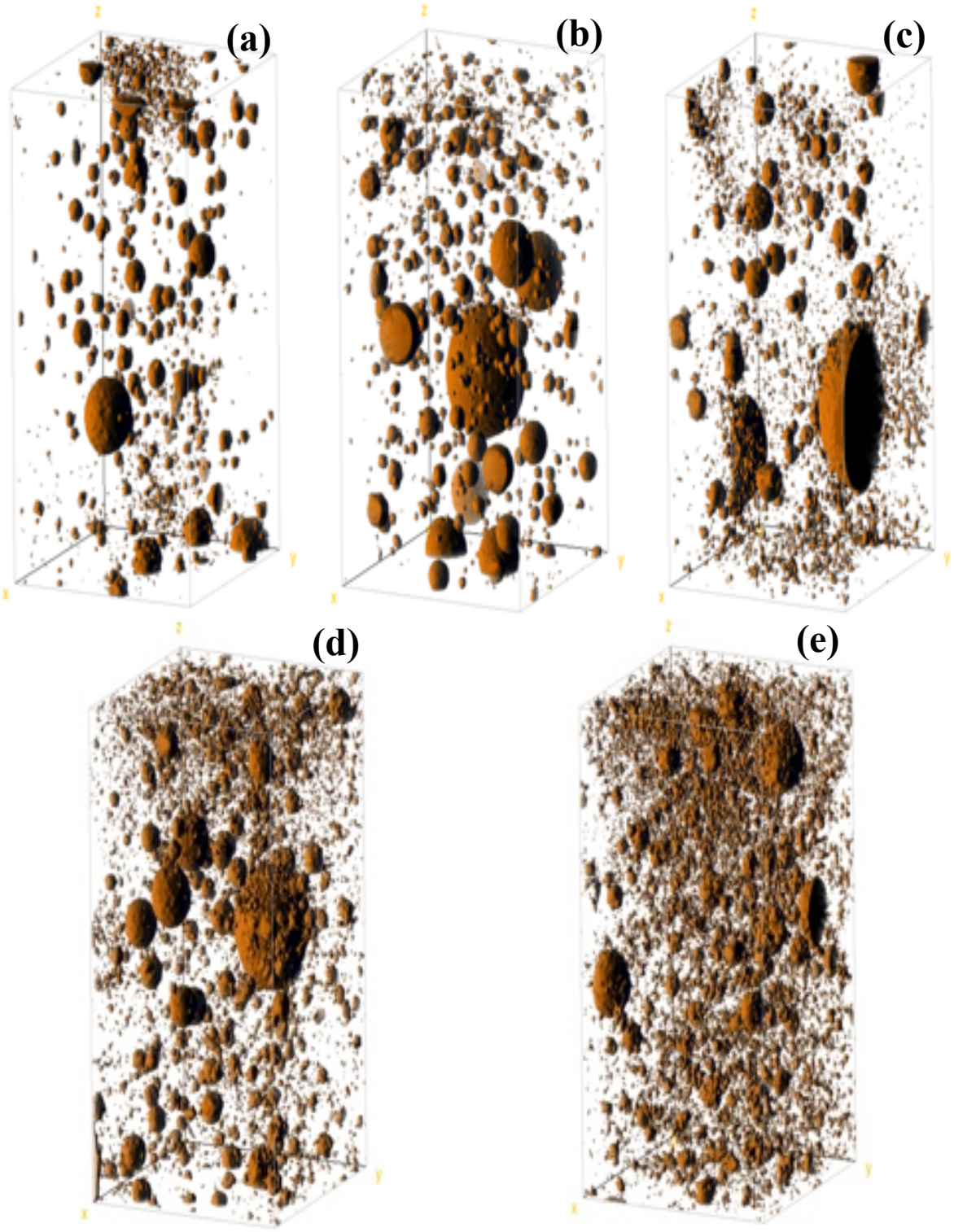

Figure 6.7. 3D reconstructed 2D slices of OPC-53 samples at (a) 27 ℃ (b) 100 ℃ (c) 400 ℃ (d) 500 ℃ (e) 800 ℃

the total radius of pores and at 800 °C the radius of pores are 2.54 µm to 30.99 µm which is 93.59%. PPC has pore radii ranging from of 2.54 µm to 43.73 µm at 800 °C while OPC-43 the pore radii ranging from is 2.54 µm to 30.99 µm. From this we can conclude that the radii of pores is a primary reason for the failure of OPC-43. The radii of pores and the number of pores are higher for OPC-43 in comparison with PPC, for OPC-43 the pores are very much small in comparison to PPC and this can be observed in the Figure 6.5 and also at 800 °C temperature. The 3D reconstructed samples after 2D image analysis for OPC-43 samples at 27 °C, 100 °C, 400 °C, 500 °C and 800 °C is shown from Figure 6.6(a)-(e).

6.3.1.3. Radii of pores in OPC-53 samples

The 3D reconstructed samples after 2D image analysis for OPC-53 samples at 27 °C, 100 °C, 400 °C, 500 °C and 800 °C is shown from Figure 6.7(a)-(e). The radii of pores in OPC-53 samples after the 2D image analysis is shown in Figure 6.8. The radius of pores at 27 °C ranged

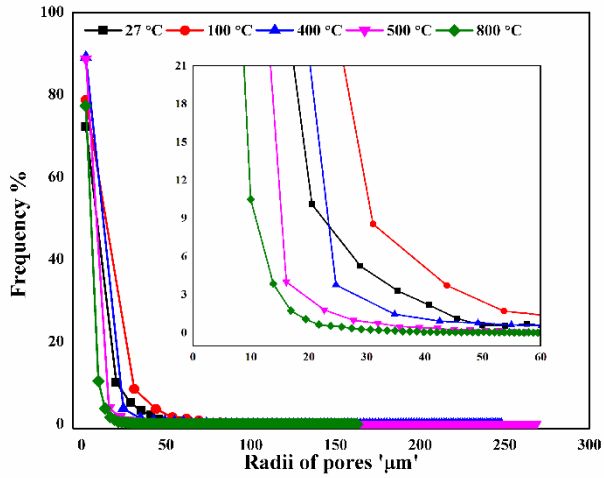

Figure 6.8 Radii of pores in OPC-53 samples at elevated temperatures.

from 2.54 µm to 170 µm while the pores of 2.54 µm to 45.59 µm contributes to 94.26% of pore volume fraction. The radii of pores at 100 °C ranges from 2.54 µm to 243 µm, while the pores of 2.54 µm to 61.98 µm contributes to 94.13 % of total pores contribute to 89% of total pores. The pores of radius 2.54 µm to 247 µm, while the pores of radius 2.54 µm to 34.81 µm contributes to 94.38% of the total pores present in the sample at 400 ºC. The endotherm peak from DTA was observed at 430 °C, and at 410 °C from DSC analysis. The rate of heat flow in OPC-53 is higher in comparison to PPC samples obtained from DSC analysis shown in Figure 4.4. At 500 ºC the radius of pores range 2.54 µm to 22.61 µm constitutes to 94.51% of the total pores. At 800 ºC the radius of pores are 2.54 µm to 19.46 µm which is 94.52% of the total pores. In OPC-53 the radius of pores are having less radius in comparison to PPC, however due to the limitation of the image resolution, majority of the pores are under the radius of 2.54 µm.

6.3.2. Circularity of pores in PC samples

6.3.2.1. Circularity of pores in PPC samples

The circularity of the pores in the PPC samples at elevated temperatures after image analysis is shown in Figure 6.9. The circularity of pores for PPC samples at 27 and 100 °C, circularity ranges from 0.97-0.27 and 0.97-0.26, while their respective percentages are 45 - 0.01% and 37 - 0.03%. At 400 and 500 °C, circularity range from 0.97 - 0.24 and 0.98 - 0.20, while their respective percentages are 46 - 0.01% and 53.84 - 0.01%. However, at 800 °C for a circularity range from 0.97 - 0.11 and the respective percentages are 34 - 0.01%. The circularity Vs the area of the pores spread across the height of the specimen is shown in Figure 6.10. The numbers 1, 2, and 3 in Figure 6.11 at 27 °C, 100 °C, 400 °C represent a single pore and the gradual increase and decrease in area, because its area changes in every image slice, and this pores is a perfect circle.

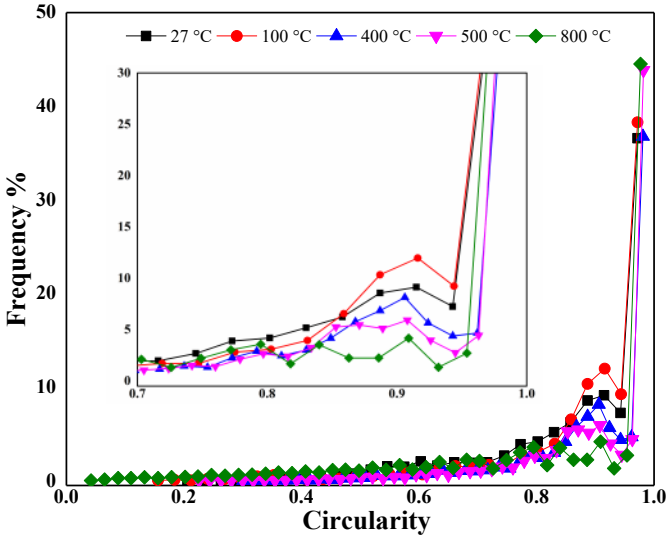

Figure 6.9. Circularity of pores in PPC samples at elevated temperatures.

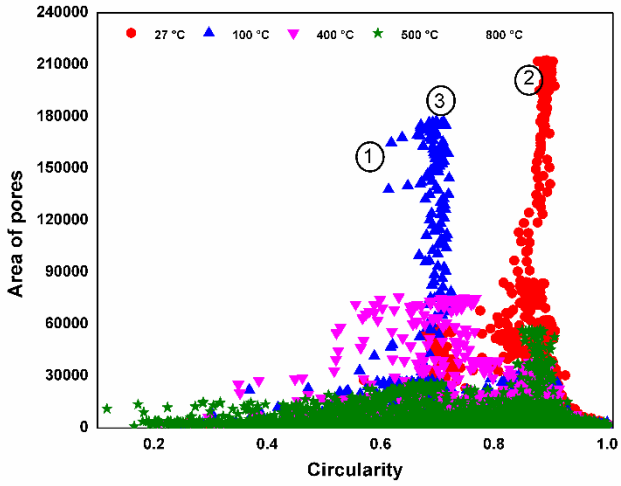

Figure 6.10. Circularity Vs area of pores in PPC samples at elevated temperatures.

With the increase in temperature, the pores get elongated, which is an indication of the interconnection of pores. The elongated pores causes the failure of the specimen, and with the increase in temperature, such elongated pore are spread across the sample causing the disintegration of the samples at elevated temperatures.

6.3.2.2. Circularity of pores in OPC-43

The circularity of the pores in OPC-43 samples at elevated temperatures is shown in Figure 6.11. With increase in temperature the mean circularity of the samples varies from 0.17 to 0.98. The OPC-43 sample at 27 °C has circularity ranging from 0.20 to 0.97 and the volume percentages are 0.03 and 36.58. At 100 °C the circularity ranges from 0.15 to 0.97 and the respective volume percentages are 0.03 and 38.28. The pores present in the sample have increased and thereby the shift in the circularity towards elongated pores can be observed in Figure 6.11. At 400 °C the circularity ranges from 0.30 to 0.98 and the volume percentages are 0.01 and 36.77. As the sample reaches 500 °C the cracks are visible on the surface of the OPC-43 samples. At this temperature the circularity of the samples range from 0.22 to 0.98 and the volume percentages are 0.01 and 43.84. As the sample is subjected 800 °C the disintegration in

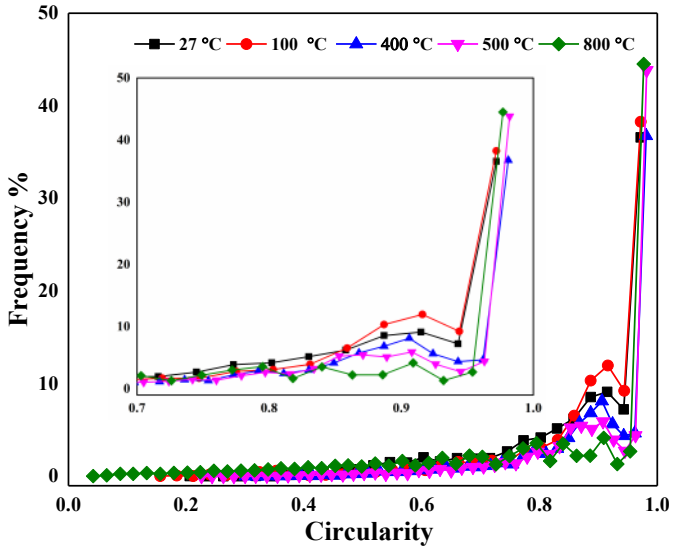

Figure 6.11. Circularity of OPC-43 samples at elevated temperatures.

the samples can be observed and at this temperature the circularity range from 0.04 to 0.97 and the volume percentages are 0.03 and 44.51. From the data one can observed the shift of the value closer '0' which indicates the pores are elongated. Even though the volume percentage of these pores is small, their contribution cannot be neglected. The circularity values closer to '0' are higher at smaller length scales.

6.3.2.3. Circularity of pores in OPC-53

The circularity of pores in the OPC-53 samples at elevated temperatures is shown in Figure 6.12. The circularity of the pores range vary from 0.13 to 0.98, when the temperature increases from 27 °C to 800 °C. At 27 °C the circularity ranges from 0.97 to 0.26 and the percentages are

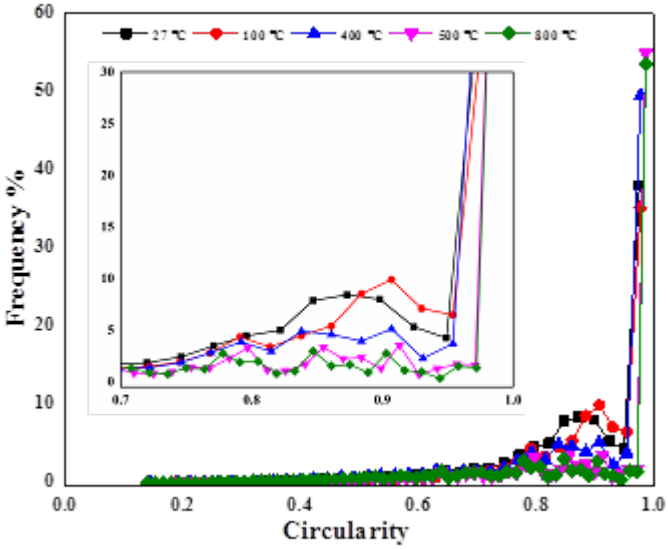

Figure 6.12. Circularity of pores in OPC-53 samples at elevated temperatures.

37.95 and 0.01; at 100 °C the circularity ranges from 0.97 to 0.18 and the percentages are 35.18 and 0.09; at 400 °C the circularity ranges from 0.97 to 0.14 and the percentages are 49.5 and 0.01; at 500 °C the circularity ranges from 0.98 to 0.18 and the percentages are 54.9 and 0.01;

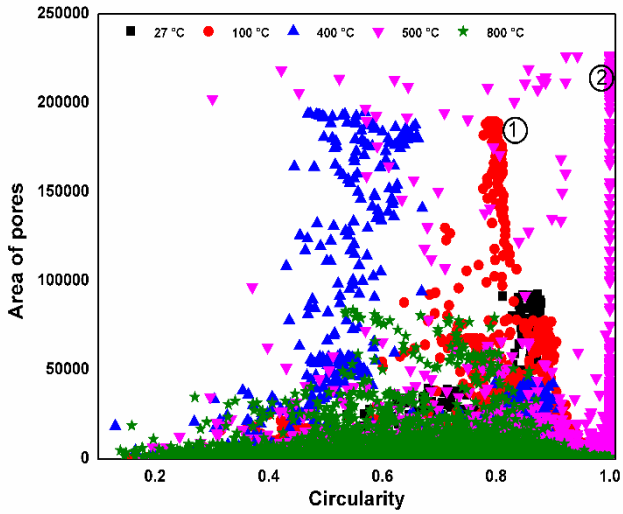

Figure 6.13. Circularity Vs area of pores in OPC-53 samples at elevated temperatures.

at 800 °C the circularity ranges are 0.98 to 0.13 and the percentages are 53.45 and 0.01. The PPC samples have the least circularity value of 0.11 at 800 °C. While for OPC-53 the samples least circularity values range from 0.15 to 0.13 from 100 °C. A pore perfectly circular in shape interconnects with the surrounding pores to form a elongated pore which are crucial for the crack initiation. Among the three samples the OPC-43 samples has a circularity value of 0.04

closest to ‘0’, while all the samples have shown a shift of circularity values indicative of elongated pores, which can be observed in the Figure 6.12. The circularity with respect to area of the pores are shown in Figure 6.13, the clustering of points at the number 1 and 2 are indication of a single pore spread across multiple layers along the depth of the sample at 100 °C and 800 °C.

6.3.3. Nearest neighbouring distance (NND)

NND enables quantification of the pore network distribution across the sample. An NND value of ‘0’ indicates the pores are clustered, while values above ‘0’ indicate the pores are dispersed.

6.3.3.1. NND of pores in PPC

The distribution of the NND values in PPC samples at elevated temperatures is shown in Figure 6.14. At 27 °C the NND value ranges from 0 µm to 56 µm and the corresponding volume percentages are 34.71 and 0.01; the volume percent greater than 2 % are 1.11 µm, 2.22 µm, 3.33 µm, 4.44 µm, 5.55 µm, 6.66 µm and their volume percentages are 21.14, 14.50, 7.42, 5.02, 3.22, and 2.31 respectively. At 100 °C the NND range is 0 µm to 74 µm for corresponding volume percent are 53.70 and 0.02; while the distribution of NND contributing individually to more than 2 % volume of porosity are in the range of 1.19 µm, 2.39 µm, 3.59 µm, and 4.79 µm and the volume percentages are 22.97, 8.78, 5.61, and 2.17. At 400 °C the distribution of NND values are in the range of 0 µm to 51.04 µm for a volume percent of 21.71 to 0.012; the volume

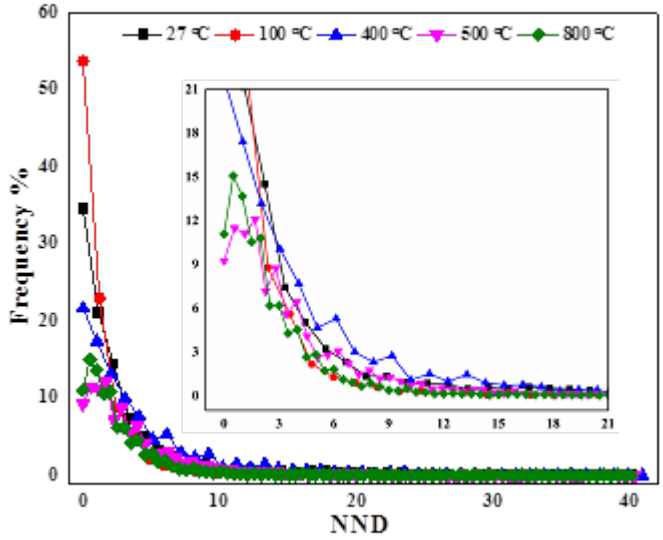

Figure 6.14. NND of pores in PPC samples at elevated temperatures.

percentages greater than2% of total volume are 1.02 µm, 2.04 µm, 3.06 µm, 4.08 µm, 5.10 µm and the volume percentages are 17.41, 13.19, 10.05, 7.69, 4.66 respectively (the values with volume percent greater than 4%). At 500 °C and 800 °C the volume percent of NND values closer to 0 µm decreased to 9.04% and 11.09%; at 500 °C the NND values in the range of 0 µm

to 4 µm, while the distribution of NND values are 0.56 µm, 1.13 µm, 1.70 µm, 2.27 µm, 2.83 µm, 3.40 µm, and 3.97 µm for volume percentages of 11.50, 11.11, 12.08, 7.16, 8.74, 5.59, and 6.44 respectively. One can observe from the frequency of NND ranges that the distance between the pores reduce with an increase in temperature. At 800 °C the NND values in the range of 0µm to 4µm and their distribution are 0.50 µm, 1.00 µm, 1.5 µm, 2 µm, 2.5 µm, 3 µm, 3.5 µm, and 4 µm while the volume percentages are 15.06, 13.68, 10.54, 10.82, 6.18, 6.18, 4.28, and 4.53 respectively. As the number and diameter of pores increase with the increase in temperature, this forms a dense pore network which enables the interconnection of pores due to external or internal stressed.

6.3.3.2. NND of pores in OPC-43

The distribution of the NND values in OPC-43 samples at elevated temperatures is shown in Figure 6.15. At 27 °C the NND value ranges from 0 µm to 40.10 µm and their corresponding volume percent is 47.67 and 0.01. The volume percent greater than 2 % of total volume are 1.18 µm, 2.36 µm, 3.54 µm, 4.72 µm, and their volume percent is 24.30, 9.85, 5.41 and 2.88 respectively. At 100 °C the NND range is 0 µm to 40.30 µm for corresponding volume percent of 37.61 and 0.01; while the distribution contributing individually to more than 2 % are in the

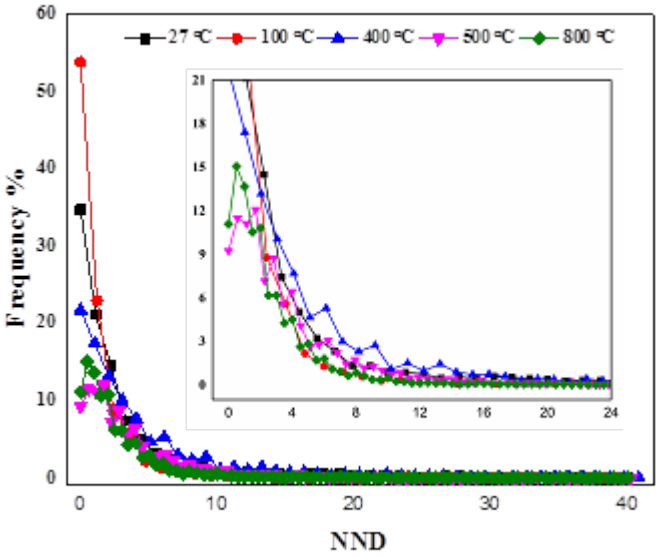

Figure 6.15. NND of pores in OPC-43 samples at elevated temperatures.

ranges is 0.91 µm, 1.83 µm, 2.75 µm, 3.66µm and 4.58 µm and the volume percentages are 26.49, 14.06, 6.88, 4.04, and 2.24. However, at 400 °C the distribution has become finer i.e. the NND range is 0 µm to 40.19 µm for a volume percent of 21.15 to 0.01; the NND contribute to volume percent greater than 3% are 0.61 µm, 1.23 µm, 1.85 µm, 2.47 µm, 3.10 µm, 3.71 µm and 4.32 µm, and their volume percentages are 21.21, 13.65, 10.64, 6.05, 5.75, 3.47 and 3 respectively. At 500 °C and 800 °C the volume percent of NND values closer to 0 µm decreased

to 16.16% and 3.21%; at 500 °C the NND values in the range of 0 µm to 4 µm, and their distribution are 0.59 µm, 1.18 µm, 1.77 µm, 2.37 µm, 2.96 µm, and 3.55 µm for volume percentages of 18.09, 13.20, 12.22, 7.67, 6.72, and 4.44 respectively. One can observe from the frequency of NND ranges, that the distance between the pores reduce with an increase in temperature. At 800 °C the NND values in the range of 0µm to 2 µm and their distribution are 0.23 µm, 0.46 µm, 0.69 µm, 0.92 µm, 1.51 µm, 1.38 µm, 1.61 µm, and 1.84 µm while the volume percentages are 1.64,2.81, 4.22, 5.05, 4.48, 5.46, 5.13, and 5.08 respectively. As the number and diameter of pores increase with the increase in temperature, this forms a dense pore network which enables the interconnection of pores due to external or internal stresses. The difference with the NND distribution values of OPC-43 is higher when compared to PPC samples.

6.3.3.3. NND of pores in OPC-53

The distribution of the NND values in OPC-53 samples at elevated temperatures is shown in Figure 6.16. At 27 °C the NND value ranges from 0 µm to 87.51 µm and their corresponding volume percent is 32.45 and 0.01; the NND values contributing to volume percent greater than 3 % of total volume are 0.96 µm, 1.92 µm, 2.88 µm, 3.84 µm, 4.81 µm and 5.77, while their volume percent is 22.02, 12.34, 8.34, 6.25, 3.93, and 3.36 respectively. At 100 °C the NND range is 0 µm to 55.57 µm for corresponding volume percent of 32.60 and 0.01; while the distribution of radii contributing individually to more than 4 % volume of porosity between

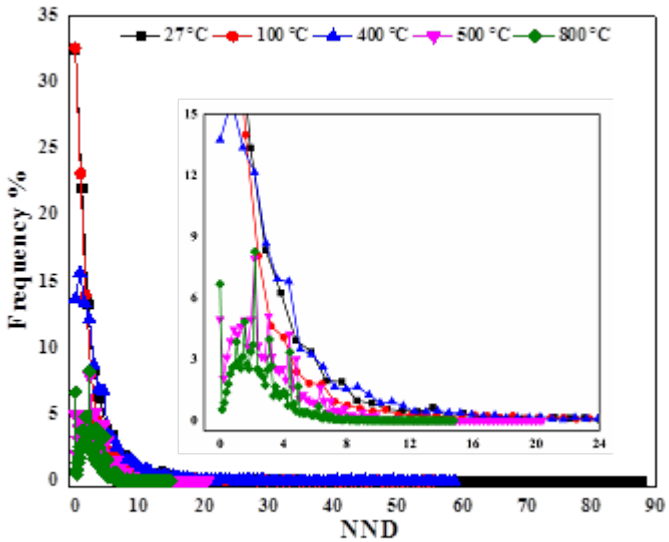

Figure 6.16. NND of pores in OPC-53 samples at elevated temperatures.

these ranges are 0.80 µm, 1.61 µm, 2.41 µm, 3.22 µm and 4.02 µm and the volume percentages are 23.14, 13.99, 8.05, 4.63 and 4.07. But at 400 °C the distribution has become finer while the same trend was observed in OPC-43 sample, *i.e.* the NND range is 0 µm to 58.67 µm for a

volume percent of 1.73 to 0.01; the NND distribution which contribute to greater than 8% of total volume are 0.72 µm, 1.44 µm, 2.17 µm, 2.98 µm, and 3.62 and 4.34 µm and their volume percentages are 15.67, 13.36, 12.14, 8.68, and 8.92 respectively. At 500 °C and 800 °C the volume percent of NND values closer to 0 µm decreased to 4.95% and 6.68%. At 500 °C the NND values in the range of 0 µm to 1 µm, and the values are 0.21 µm, 0.43 µm, 0.65 µm, 0.87 µm, and 1.09 µm for volume percentages of 2.05, 3.08, 3.89, 4.46 and 4.21 respectively. One can observe from the frequency of NND ranges, that the distance between the pores reduce with an increase in temperature because the distribution of the NND has become finer. At 800 °C the NND values in the range of 0µm to 1 µm are centred on frequency bins 0.13 µm, 0.26 µm, 0.39 µm, 0.52 µm, 0.65 µm, 0.788 µm, 0.91 µm, and 1.04 µm while the volume percentages are 0.54, 0.87, 1.39, 1.78, 2,28, 2.60, 2.68 and 3.84 respectively. As the number and diameter of pores increase with the increase in temperature, this forms a dense pore network which enables the interconnection of pores due to external loading taking place or due to the internal stresses generated. The difference with the NND distribution values of OPC-43, and OPC-53 is higher when compared to PPC samples, hence the PPC samples have shown better performance under thermal loads.

6.3.4. Pores in PC samples

The 2D analysis discussed above for data obtained from 500 2D slices characterizes the frequency distribution of NND, circularity and radii of pores within the plane of the 2D slice. Further, these 2D slices are integrated in the 3D analysis wherein the volume, area and sphericity of pores in the cube are estimated. The porosity estimated in 2D analysis is identical to that obtained from the more complex 3D analysis for the same image set. The 3D analysis treats the pores present in the next slice centred at the same coordinates as a single pore for estimating the total number of pores in the sample.

6.3.4.1. Number of Pores in PPC

The total number of pores in the PPC sample corresponding to each temperature are: 27 °C (317), 100 °C (629), 400 °C (2811), 500 °C (4979) and 800 °C (3361). There is a sudden increase in the total number of pores after 100 °C, due to increase in the number of smaller pores in the sample. However, there is a drop in the number of pores at 800 °C which is due to the increase in the pore diameter leading to the merging of the separate pores. To investigate the reasons for the sudden reduction in the pore numbers, 3D analysis is conducted and the diameter, area and volume of the pores are analysed in the following sections.

6.3.4.2. Number of Pores in OPC-43

The total number of pores present in the OC-43 corresponding to each temperatures are 27 °C (878), 100 °C (827), 400 °C (2304), 500 °C (2828) and 800 °C (5359). The OPC-43 samples have shown signs of increase in pores with respect to temperatures. Unlike the PPC samples, the total number of pores in OPC-43 samples is greater at all temperatures. The total number of pores in OPC-43 at 800 °C is higher in comparison to PPC samples.

6.3.4.3. Number of Pores in OPC-53

The total number of pores in OPC-53 corresponding to each temperatures are 27 °C (562), 100 °C (1356), 400 °C (2899), 500 °C (3498) and 800 °C (31254). All the 3 GoC have shown indications of the pore growth with temperature. Among the three GoC, PPC has the least number of pores, while OPC-43 has greater number of pores at 800 °C. As the pores get interconnected and form a failure network, the observed number of pores in OPC-43 are less than OPC-53 samples.

6.3.5. Diameter of pores

The total number of pores are determined in the samples using 3D image analysis for all the three GoC at elevated temperatures. 3D image analysis is useful in differentiating the pore distribution frequencies. For the estimation of the pore diameters the following equation (6.1) is used:

$$\text{Equivalent diameter} = \sqrt[3]{\frac{6 * Volume3D}{\pi}} \quad \text{---------- (6.1)}$$

where V – Volume of pores , A – Surface area of the pores.

6.3.5.1. Diameter of pores in PPC

From the 3D analysis of the PPC samples at elevated temperatures, the diameter of pores range from 7.93 µm to 520 µm. The distribution of the diameter of the pores in PPC samples at elevated temperatures after 3D analysis of pores is shown in Figure 6.17. The pores in the PPC sample at 27 °C range from 20.35 to 493 µm with corresponding volume percentages of 60.88 and 0.31. The volume fraction of pores which contribute to greater than 1% of total volume are centred on 49.88 µm, 79.42 µm, and 108.98 µm and the volume percentages are 22.98, 10.09, and 1.92, and the PPC sample at 27 °C after 3D reconstruction and image analysis is shown in Figure 6.18 (a). At 100 °C the diameter of the pores are between 15.73 to 502.80 µm and the volume percentages are 65.65 to 0.15. The volume fraction of pores which contribute to greater

than 1% of total volume are centred on 36.02, 56.32, and 76.61 µm and the volume percentages are 14, 7.95, and 5.56 respectively, after 3D reconstruction and image analysis is shown in

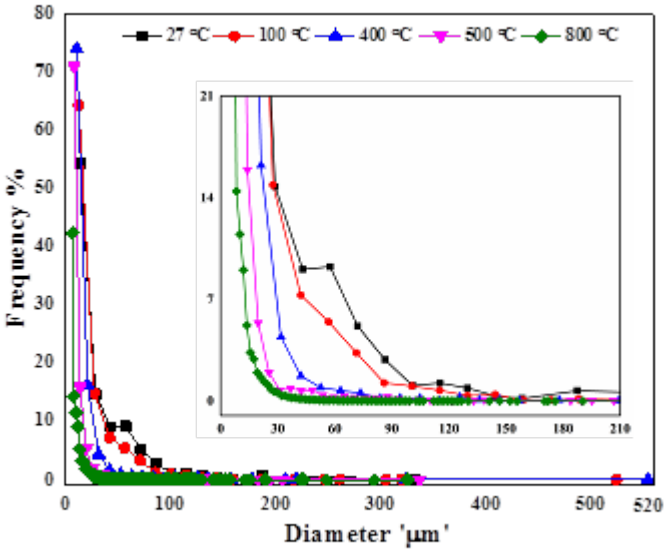

Figure 6.17. Diameter of pores in the PPC samples at elevated temperatures.

Figure 6.18 (b). At 400 °C there is reduction in the diameter ranges which is 10.48 and 520 µm respectively, and volume percentages are 84.24 and 0.03. The distribution of pore diameters has become small with an increase in temperature, and the preceding values of higher percentages are for pores 20.28 and 30.07 µm, and the volume percentages are 8.44 and 2, the after 3D reconstruction and image analysis is shown in Figure 6.18 (c). Over 500 °C the minimum diameter of pore size reduces to 8.26 µm for 59.10% of pores and 377.76 µm for 0.02% of pores, while the distribution of the pores diameters 13.61, 18.97, and 24.32 µm for a volume percentage of 20.57, 9.87, and 4.70 respectively are shown in Figure 6.18(d). At 800 °C the distribution of diameters is 7.93, 12.61, 17.30, and 21.97 µm for volume percent of 50.67, 16.22, 8.13, and 5.10 respectively. The maximum diameters of is 270.17 µm which has a corresponding volume percent of 0.03. From Figure 6.18(e) it is observed that the reduction in the distribution of the diameter of pores for the region of 20.35 µm at 27 °C volume has been reduced to 7.93 µm at 800 °C. Overall it is observed that the pore diameter decreases with increase in temperature.

6.3.5.2. Diameter of pores in OPC-43

From the 3D analysis of the OPC-43 samples, the overall diameter of pores range from 8.49 µm to 575 µm, and the distribution in the diameter of the pores in the samples at elevated temperatures is shown in Figure 6.19. The pores in the OPC-43 sample at 27 °C range from

11.78 to 358 µm with corresponding volume percentages of 64.12 and 0.03. The volume fraction of the diameter of pores which contribute to greater than 3 % of total volume are 24.19

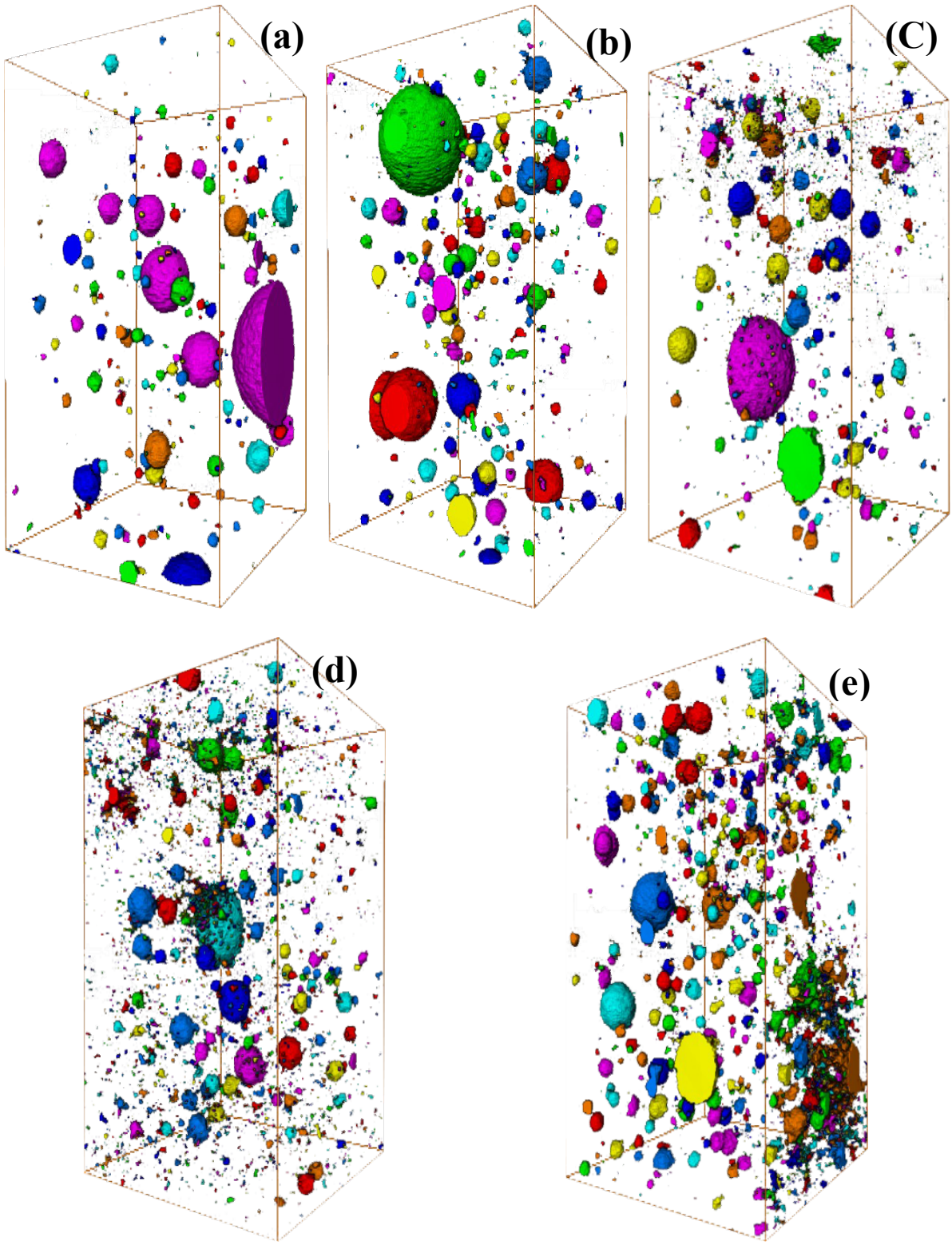

Figure 6.18. Pore distribution in PPC samples at elevated temperatures using 3D analysis.

µm, 36.60 µm, and 49 µm and the volume percentages are 14.12, 6.26, and 5.69, and the OPC-43 sample at 27 °C after 3D reconstruction and image analysis is shown in Figure. 6.20(a). At 100 °C the diameter of the pores are between 10.70 to 287.30 µm and the volume percentages

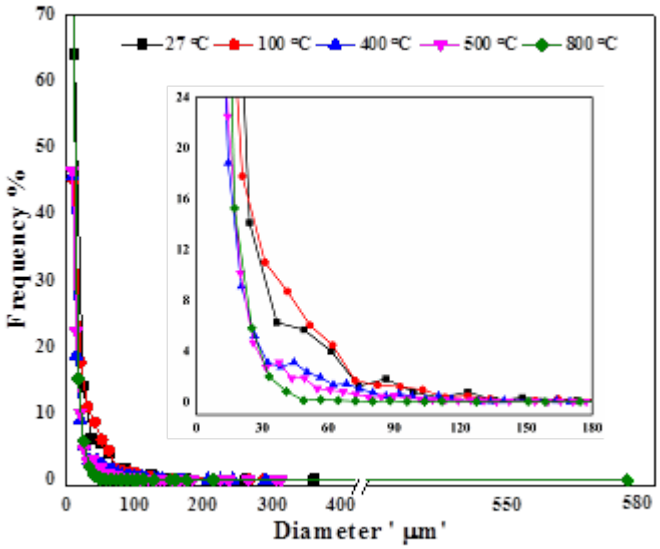

Figure 6.19. Diameter of pores in the OPC-43 samples at elevated temperatures.

are 45.10 to 0.12. The volume fraction of the diameter of pores which contribute to greater than 4% of total volume are centred on 20.95, 31.20, 41.44, 51.68 and 61.93 µm and the volume percentages are 17.78, 11, 8.70, 6.04 and 4.48 respectively, after 3D reconstruction and image analysis is shown in Figure. 6.20(b). At 400 °C there is reduction in the diameter ranges which is 8.57 and 289 µm respectively, and volume percentages are 45.79 and 0.04. The distribution smaller diameter of pores in the sample is represented pictorially in Figure. 6.20(c), while the distribution of the volume percent greater than 3% whose pore diameters are 14.31, 20.12, and 25.94 µm for a volume percentage of 22.48, 10.15, and 4.67 respectively. At 800 °C in sample of OPC-43 the diameters distribution is 9.51, 17.36, 25.22, 33.07 µm for a volume percentages of 75.12, 15.26, 5.82 and 2.01 respectively (The volume percentages greater than 2% are mentioned). The maximum diameter of pore is 575 µm which has a corresponding volume percentage of 0.019. From Figure 6.19 it is observed that the reduction in the distribution of the diameter of pores for the region 11.78 µm at 27 °C volume has been reduced to 9.51 µm at 800 °C. Overall it is observed that the pore diameter decreases with increase in temperature, and the increase in the number of pores after 500 °C is high, when compared with the sample of temperatures less 500 °C.

6.3.5.3. Diameter of pores in OPC-53

The 3D analysis carried on the samples obtained from the micro tomography images of the OPC-53 samples. From these tests the diameter of pores range in samples at elevated temperat-

ures range from 8.49 µm to 575 µm, and the distribution in the diameter of the pores in the samples at elevated temperatures is shown in Figure 6.21. The pores in the OPC-53 sample at

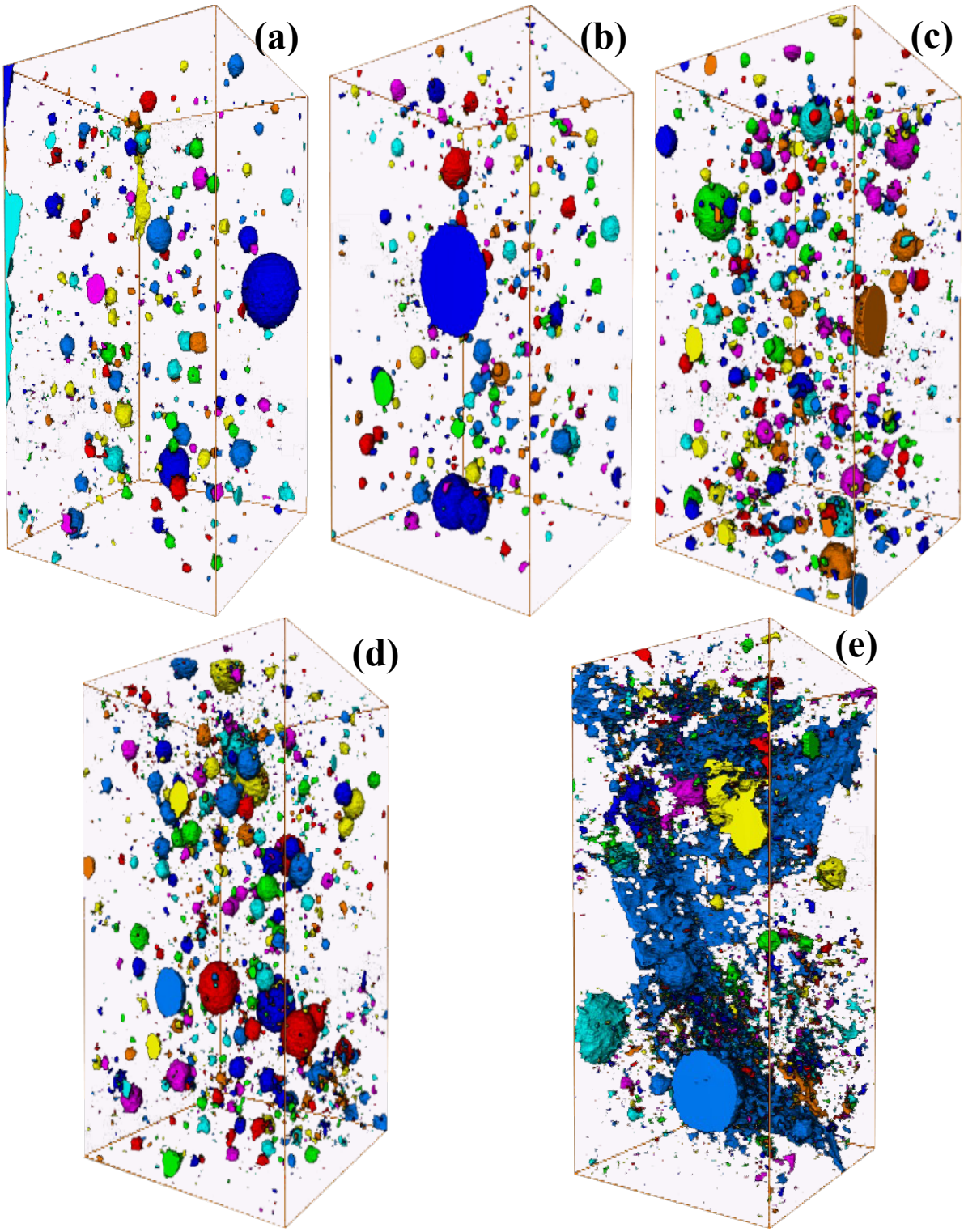

Figure 6.20. Pore distribution in OPC-43 samples at elevated temperatures using 3D analysis.

27 °C range from 14.25 to 331.28 µm with corresponding volume percentages of 54.27 and 0.17. The volume fraction of the diameter of pores which contribute to greater than 5% of total

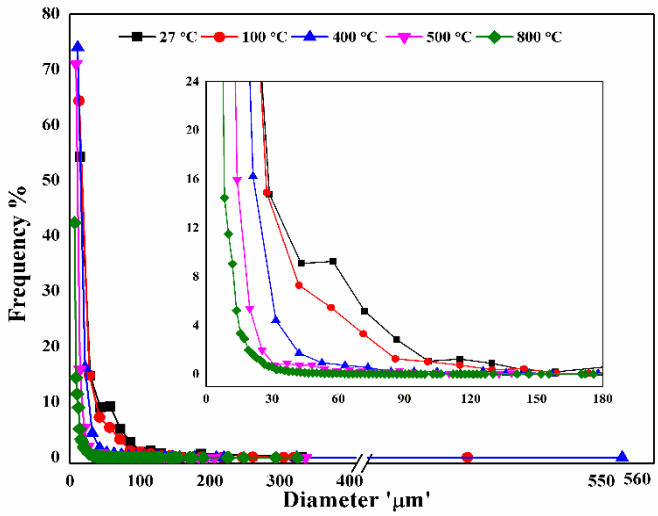

Figure 6.21. Diameter of pores in the OPC-53 samples at elevated temperatures.

volume are 28.68 µm, 43.12 µm, 57.55 µm and 71.99 µm and the volume percentages are 14.76, 9.07, 9.25 and 5.16, and the OPC-53 sample at 27 °C after 3D reconstruction and image analysis is shown in Figure. 6.22(a). At 100 °C the diameter of the pores are between 12.88 to 524.31 µm and the corresponding volume percentages are 64.38 to 0.07. The volume fraction of the diameter of pores which contribute to greater than 4%, and their distribution are 27.50, 42.11, and 56.72 µm and the volume percentages are 14.90, 7.30, 5.46 respectively. At 400 °C there is reduction in the diameter ranges which is 10.80 and 553 µm respectively, and volume percentages are 74.02 and 0.03. The distribution of diameter of pores has increased with an increase in temperature, and the diameter values whose pore percentages greater than 4% of total volume are 21.25 and 31.60 µm and the volume percentages are 16.25, and 4.41 respectively. It is observed physically in the samples of OPC-53, cracks are visible on the 50 x 50 x 50 mm^3 samples at 500 °C, while the results indicate further reduction in the pore diameter values. At 500 °C the minimum diameter of pore size reduces to 8.41 µm for 71.04% of pores and 336.83 µm for 0.02% of pores, the finer diameter of pores distribution in the sample is represented pictorially in Figure. 6.22(c), while the distribution of the volume percent greater than 1% are 14.07, 19.74, and 25.04 µm for a volume percentage of 15.92, 5.37, and 1.92 respectively are shown in Figure. 6.21. At 800 °C the diameters distribution is 6.49, 8.31, 10.13, 11.95, and 13.73 µm for volume percentages of 42.40, 14.46, 11.49, 9.03, and 5.21 respectively (The volume percentages greater than 4 are mentioned). The maximum diameter of pore is 325 µm which has a volume percent of 0.03. From Figures 6.22(a)-(e) it is observed that the reduction in the distribution of the diameters of pores i.e. at 27 °C the minimum diameter of pores is 14.25 µm, however at 800 °C the minimum diameter of pores is 6.49 µm respectively.

Similar to the other PPC and OPC-43 samples there is a reduction in the overall pore diameter with the increase in temperature.

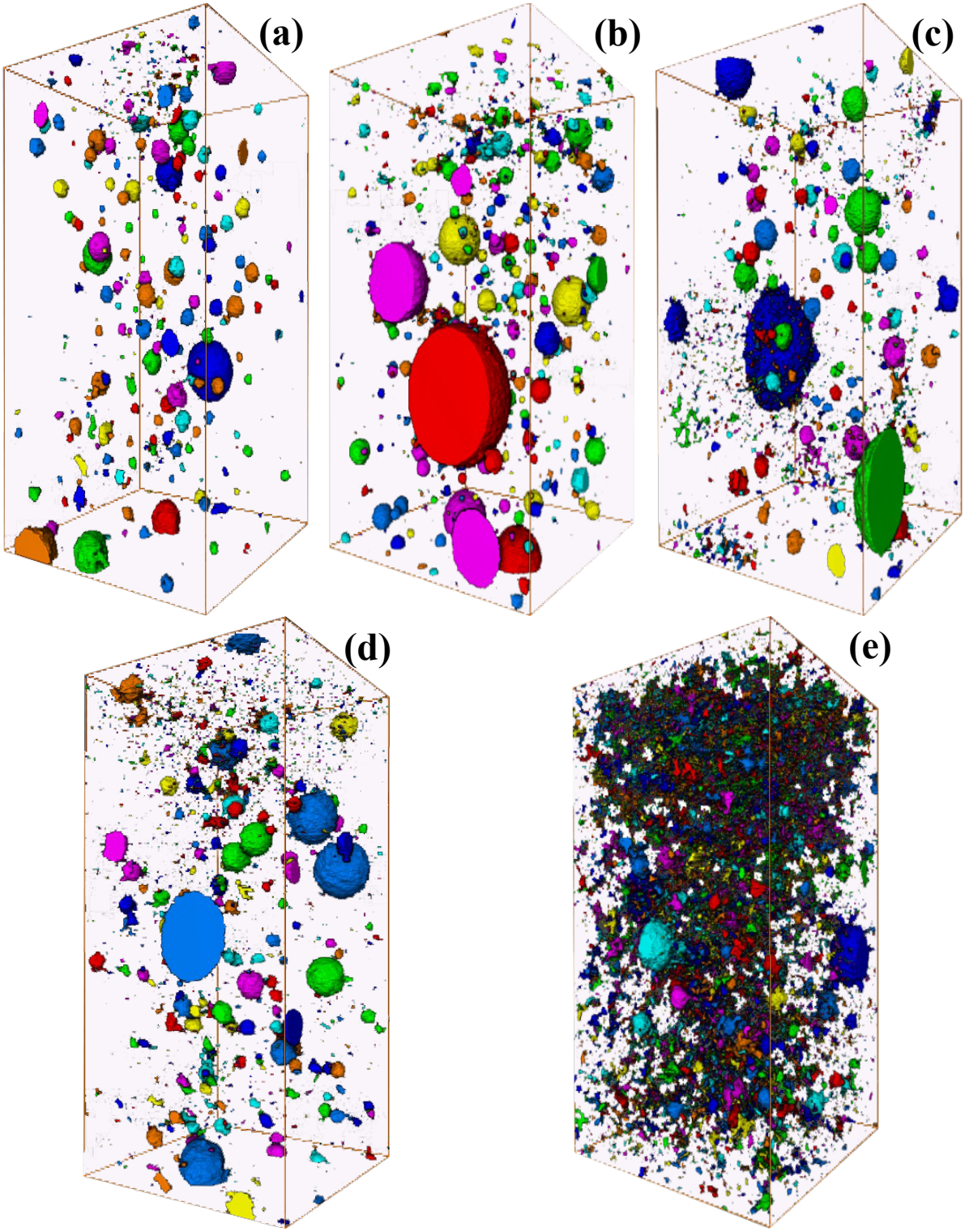

Figure 6.22. Pore distribution in OPC-53 samples at elevated temperatures using 3D analysis.

6.3.6. Sphericity

Sphericity (Ψ) is a 3D quantity defined as the ratio of the surface area of a sphere to the particle surface area obtained from formula given below shown in equation (6.2):

$$\Psi = \frac{\pi^{1/3} * 6V^{2/3}}{A} \text{ ---------- (6.2)}$$

where V and A are the volume, and surface area of the pore. Sphericity is indicated on a scale of '0' to '1' where 1 indicates a perfect sphere. The plots for PPC, OPC-43 and OPC-53 samples are shown in Figure 6.23 – 6.25. Sphericity may be greater than '1' if smaller pores consisting of fewer voxels exist in the sample, this is a resolution artefact due to low resolution. As the temperature increases the number of pores with sphericity '1' also increases.

6.3.6.1. Sphericity of PPC

The sphericity in PPC at elevated temperatures is shown in Figure 6.23. In PPC sample at 27 °C, pores of sphericity '1' occur with a volume percentage of 4.20%; for a similar sphericity at 800 °C the volume percent is 20.90%. At 27 °C the least sphericity value of '0.61' is obtained for a volume percent of 2.52%. At 800 °C the sphericity is '0.34' where the volume percent is 0.90%. As the sample reaches 500 °C there is a shift in the sphericity values, similar to the trend observed in circularity values section 6.3.2. At 27 °C the pores which have sphericity of 0.97 occur with a volume percent of 28.70%. However, at 100 °C, 400 °C, 500 °C, and 800 °C for sphericity values of 0.96, 0.99, 0.98, and 0.97 the volume percentages are 21.63%, 2.49%, 3.12

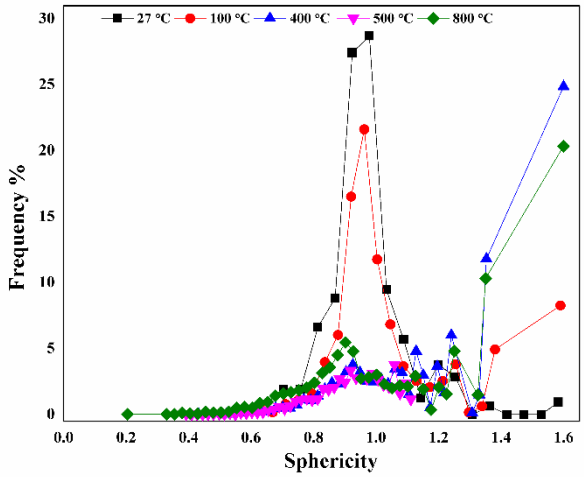

Figure 6.23. Sphericity of PPC samples at elevated temperatures.

%, and 2.82% respectively. It is observed from the data that the pores are not spherical in shape, which may be due to the interconnectivity of the individual pore with neighbouring pores. With an increase in temperature, the smaller pores which consist of fewer voxels also increase in

frequency *i.e.* for a sphericity value of 1.58 the volume percent is 0.94% at 27 °C. Whereas at 800 °C the sphericity value is 1.58, for a volume percent of 20.35%.

6.3.6.2. Sphericity of OPC-43

The sphericity in OPC-43 at elevated temperatures is shown in Figure 6.24. The sphericity of OPC-43 sample at 27 °C varies from 0.40 to 1.58 and the frequency percentages are 0.12 and 9.34 respectively. As stated earlier, the sphericity values may be greater than '1' if the pore consists of fewer voxels. The volume fraction of 8.88 was observed having a sphericity values of '1' which indicates these pores are shaped very close to a perfect sphere. At 100 °C the sphericity values range from 0.55 to 1.59 and the corresponding volume fractions are 0.24 and 9.07 respectively. For a sphericity value of '1' the volume percentage is 7.01. For OPC-43 the sphericity values range from 0.56 to 1.59 and the respective volume fraction are 0.56% and 14.19%, while the volume fraction correspond to the sphericity value of '1' the volume percent-

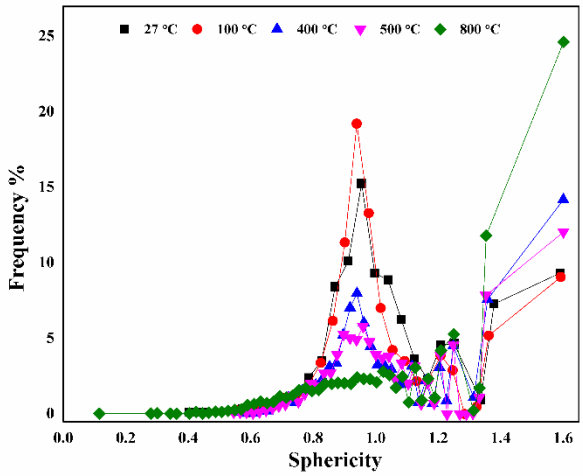

Figure 6.24. Sphericity of OPC-43 samples at elevated temperatures.

age is 3.25. It is observed from the Figure 6.24 that with increasing temperatures the pores which are spherical closer to '1' tend to decrease and they shift towards elongated ellipsoids. For the samples at 500 °C the sphericity values ranges from 0.54 to 1.60, while the volume percentages are 0.11% and 12.05%, while the sphericity value of '1' it is 3.92%. With increasing temperatures the volume percentages of pores which are of fewer voxels has also increased as observed in Figure 6.24. The sphericity values of OPC-43 samples at 800 °C ranges from 0.11 to 1.60 and the corresponding volume percentages are 0.018% and 24.65%, while the pores for a sphericity of '1' are 2.10%. From Figure 6.24 it can be observed that a shift in the sphericity towards the left hand side, which is an indication of the elongated ellipsoids was

observed. Such a shift indicates that the pores are increasingly interconnected and hence they tend to lose their shape.

6.3.6.3. Sphericity of OPC-53

The sphericity of OPC-53 samples at elevated temperatures is shown in Figure 6.25. The overall sphericity values in the OPC-53 samples at elevated temperatures range from 0.17 to 1.60. The sphericity values of OPC-53 sample at 27 °C range from 0.59 to 1.34 and the corresponding volume percentages are 0.53 to 2.49, while the sphericity values of '1' the volume percentage is 7.47%. The sphericity values at 100 °C range from 0.44 to 1.59 and the volume percentages are 0.14% and 10.84%, while the pores of sphericity '1' are 6.12. The sphericity values at 400 °C range from 0.36 to 1.60 and the volume percentage range from 0.03 to 18, while the sphericity values of '1' the volume percentage is 3.13%. The OPC-53 samples have indicated a reduction in the spherical particles with increase in temperature, and the volume of fewer voxels has also increased Similar to PPC and OPC-43 samples. For OPC-53 samples at 500 °C the sphericity values range from 0.41 to 1.60 and the percentages are 0.02% and 26.90% respectively. The disintegration of the samples at was observed 800 °C and at this temperature

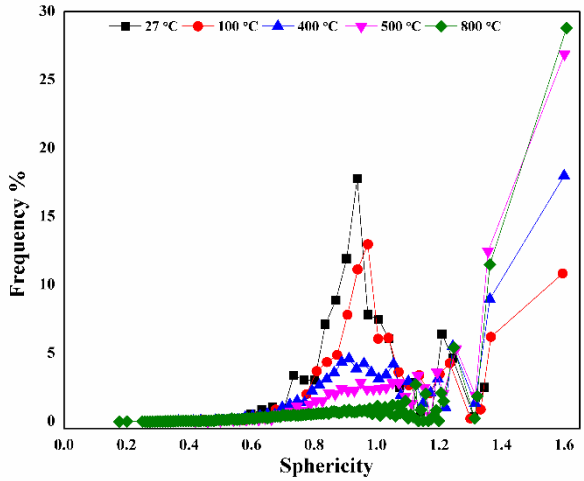

Figure 6.25. Sphericity of OPC-53 samples at elevated temperatures.

the sphericity in the OPC-53 samples range from 0.17 to 1.60 and the corresponding volume percentages range from 0.01% to 28.81%, while the pores which are perfect spherical in shape indicated by '1' has a volume fraction of 1.13. When comparing the mean sphericity values of the three GoC, the OPC-53 has the least sphericity value of 0.11 and the PPC has the highest sphericity value of 0.20. All the three GoC have shown indications of the reduction in the pores of perfect spherical shape, similarly an increase in the volume fraction of pores consisting of

fewer voxels has also increased. All the three GoC have indicated a shift towards the sphericity of '0' and it can be seen in all the samples at 800 °C.

6.3.7. Relation between compressive strength, porosity and temperature of PC

Porosity is spread across the samples at multiple scales, as indicated by the studies carried using micro tomography of the samples. The PPC samples have shown superior compressive strength behaviour at elevated temperatures, the studies conducted on the images obtained from HRCT indicate that porosity in PPC sample is less when compared to the OPC-43 and OPC-53 samples. However there is a pore network formed between the pores due to the increasing temperatures, which is an indication that there should be an increase in the extent of the pore network at smaller scales i.e. micro scale and below (current study is limited to micro scale) which was investigated in the current chapter and the obtained results are summarised in the Figure 6.26 – 6.28.The porosity at micro scale are compared to the compressive strength results obtained from the samples of 50 x 50 x 50 mm^3 for all the three GoC i.e. PPC, OPC-43 and OPC-53 respectively:

6.3.7.1. Porosity, temperature Vs compressive strength for PPC

The variation in the number of pores in all the 2D slices, of PPC samples, compressive strength and porosity is shown in Figure 6.26. The estimated porosity values varied a lot as the samples analysed under micro tomography are varied. However, the increase in the number of pores per slice was evident with the increase in temperature. Similar to the HRCT studies a sudden increa-

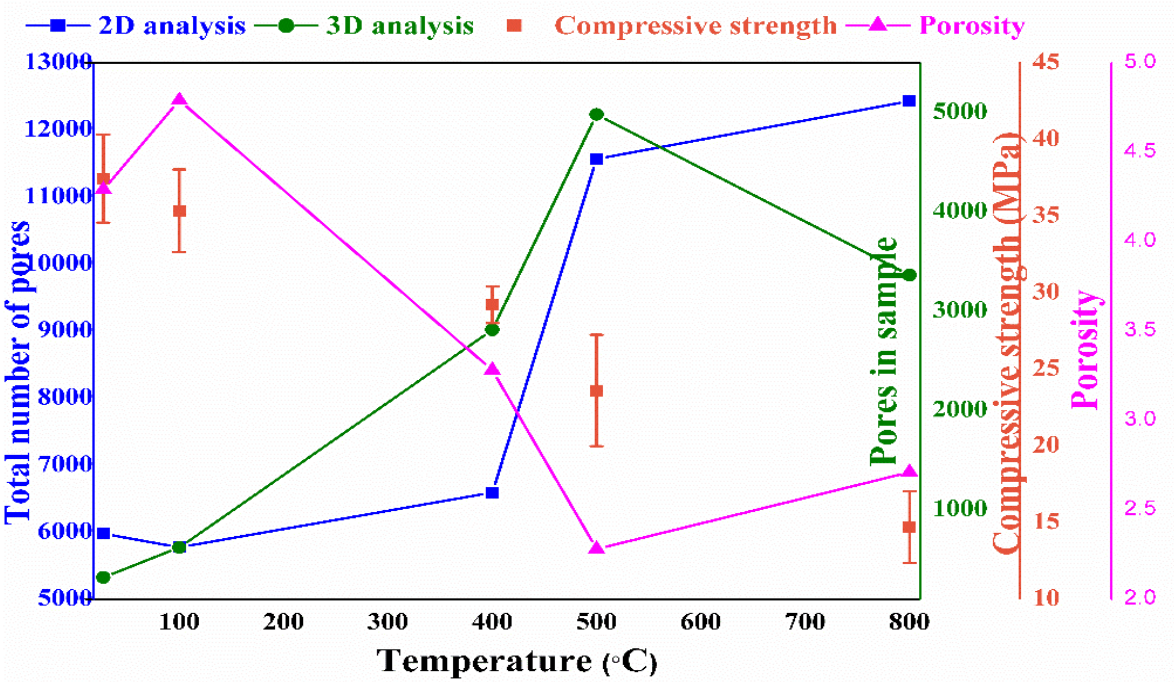

Figure 6.26. Compressive strength Vs Porosity Vs temperature for PPC samples

se in the number pores was also observed at the temperatures of 400 °C – 500 °C. The reported number of pores in 2D slices of the sample are relatively small, in comparison to the OPC-43 and OPC-53 samples. The obtained microstructure is less porous than the other two GoC samples, indicating the coalescence of the pores in forming a network did not take place. The porosity values of PPC samples at 500 °C and 800 °C is the lower than the other two GoC, which is one of the reason that PPC samples were relatively intact.

6.3.7.2. Porosity, temperature Vs compressive strength for OPC-43

The variation in the number of pores in all the 2D slices, across the sample, compressive strength and porosity of OPC-43 samples is shown in Figure 6.27. The porosity estimated for the samples of OPC-43 is higher than the other two GoC at 800 °C. An interconnectivity of pore network was observed in the samples at 800 °C, due to which the number of pores in the samples are less. It should be noted that the 3D analysis considers an interconnection of pores in the same layer and the depth of the sample as a single pore. Due to the increasing temperatu-

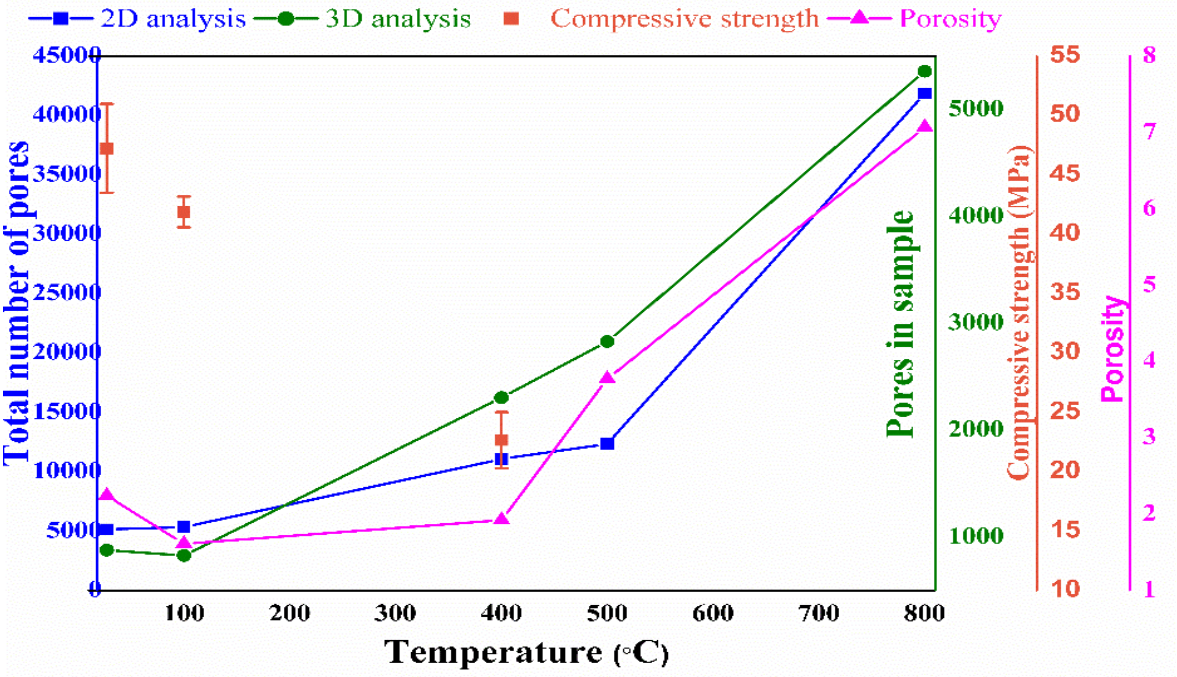

Figure 6.27. Compressive strength Vs Porosity Vs temperature for OPC-43 samples

res, the number of pores increases and NND decreases, which leads to pore network formation due to coalescence of pores. This also leads to increased pore pressure, which causes further extension of failure planes which can be observed in Figure. 6.20(e). An increase in the porosity and number of pores can be observed in Figure 6.27 and this is responsible in causing a reduction in compressive strength.

6.3.7.3. Porosity, temperature Vs compressive strength for OPC-53

The variation in the number of pores in all the 2D slices, across the sample, compressive strength and porosity of OPC-53 samples is shown in Figure 6.28. All the three GoC have shown a sudden increase in the number of pores at the temperatures of 400 °C and 500 °C. The OPC-53 samples has greatest number of pores in all the slices of sample at 800 °C. As the number of pores are greater the internal stresses generated due to the thermal loads would help

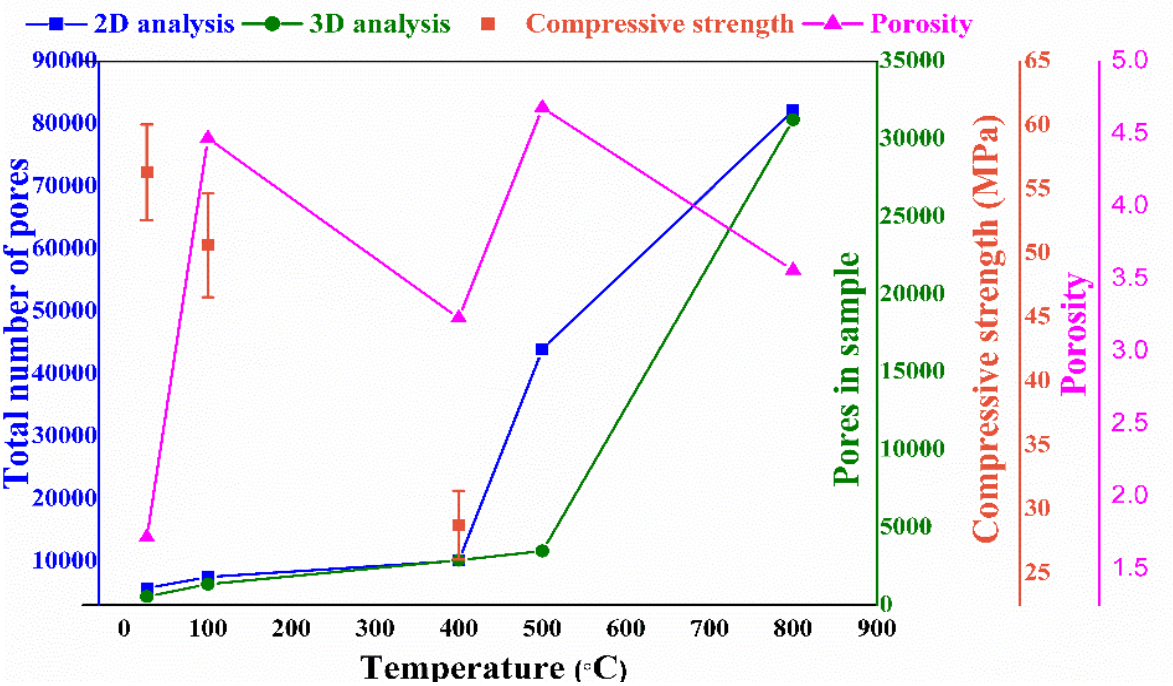

Figure 6.27. Compressive strength Vs Porosity Vs temperature for OPC-53 samples

in the coalescence of pores, forming a pore network. The coalescence of pores and formation of a pore network can be seen in the larger samples scanned under HRCT at 500 °C and 800 °C in Figure 5.26(d) & (e), due to which the samples disintegrate.

6.4. Conclusions from this chapter

- Micro tomography studies enable capturing the physical changes taking place in a 2D slice of 4.5 µm thickness. The number of pores detected are greater and have smaller dimensions.
- The 3D images of the sample obtained from combining the 2D slices, has enabled us to quantify the less extensive pore network that exists in PPC samples compared to OPC-43 and OPC-53.
- Micro tomography enables in capturing the coalescence of pores into cracks in OPC-43 samples at 800 °C, due to which the OPC-43 samples loose integrity and strength at lower temperature when compared to OPC-53 samples. OPC-43 and OPC-53 samples

have indicated lower circularity and NND values for pores in comparison to PPC samples.

- It is observed from the data that the pores are not spherical in shape, which is due to the interconnection of the individual pore with neighbouring pores. This implies that even though the number of larger pores decreases, the overall porosity increases.
- With the increase in temperature, the smaller pores, which consist of fewer voxels have also increased in frequency.

Chapter-7

Conclusion and scope of future research

Chapter-7
Conclusions and scope of further research

7.1. Conclusions

The experimental investigation carried on the three GOC (PPC, OPC-43 and OPC-53), that are exposed to thermal loading from the temperature ranges of 27 °C – 800 °C, indicated that the PPC samples has shown a superior behavior as compared to OPC-43 and OPC-53 samples. The following tests are carried for determining the variations taking place in the hydrated PC specimens with respect to hydration and thermal loads : PSD (PSA), Elemental changes (CHNS-O analysis), Chemical oxides (XRF), Phases present (XRD), bond behavior (FTIR and FTRS analysis), Thermal analysis *i.e.* TGA, DTA and DSC. To capture the internal changes taking place in the PC specimens, subjected to thermal loading Computer Tomography studies are performed. The changes taking place in the specimens at meso scale due to thermal loads, of specimens sizes 50 x 50 x 50 mm^3 are investigated using HRCT. While, internal changes taking place at micro scale, in the specimens of size 1.1 x 1.1 x 2.2 mm^3 are investigated using Micro tomography. The data set of images obtained from Computer Tomography are further analysed using 2D and 3D image analysis. After the images analysis was completed All these tests conducted on the hydrated cement samples the following conclusion emerged, in understanding the better behavior of PPC over the OPC-43 and OPC-53 cements:

(1) OPC-53 has finer particle size distribution (PSD) in comparison to PPC and OPC-43 grades of cement, which is responsible for higher 28 days strength, under room temperature. X-ray diffraction (XRD) studies has indicated higher concentrations of Portlandite (which is a major phase next to calcium silicate hydrate (CSH) after

hydration), in OPC-53 compared to the other grades of cement. This contributes to the dense microstructure and rapid development of compressive strength in Portland Cement.

(2) The reductions in the elemental percentages of oxygen and hydrogen (which are major elemental constituents of CSH & Portlandite) play crucial roles in the disintegration of the OPC-53, OPC-43 and PPC samples. Since the reduction of these critical elemental concentrations, contribute to the weakening of the hydrated structure, there by the materials mechanical properties .

(3) OPC-43 and OPC-53 samples begin to disintegrate at a threshold temperature of 400 °C.

(4) Among the three grades of cement, PPC showed a superior performance under thermal loading at temperatures of 800 °C compared to OPC-43 and OPC-53. From the HRCT and micro tomography studies it is evident that OPC- 53 & OPC-43 contains more pores than PPC at all temperatures.

(5) The images captured from Micro tomography and HRCT analysis, after 3D reconstruction indicated that a large number of inaccessible pores are observed in all the samples for all the three GOC, subjected to temperatures ranging from room temperature to 800 °C.

(6) The variations in heat flow and mass loss taking place at temperatures of 100 °C, 400 °C, 500 °C and 800 °C in hydrated PPC, OPC-43 and OPC-43. However, the heat flow in PPC is slightly lower when compared to OPC-43 and OPC-53 cements as observed from differential scanning calorimetry.

(7) The evolution of pores with temperature was observed to be a continuous process; after 400 °C, there is an interconnection between the pores, which lead to an increase in the pore volume. As the pore volume increases due to the thermal loads, the load carrying capacity the samples decreases, due to the formation of a failure plane because of the diffusion process under thermal energy.

(8) The chemical changes taking place due to the decomposition of phases such as Portlandite and CSH has weakened the microstructure of OPC-43 and OPC-53 cements. Micro tomography is a useful tool to capture these microstructure changes across the volume of the sample.

(9) The porosities of OPC-53 & OPC-43 are higher than that of PPC. The distribution of smaller pores plays a crucial role in forming a network of cracks. Hence, from the current tests and with a limited amount of research, we can conclude that the utilization of PPC under thermal loading is a good alternative to OPC-43 & OPC-53.

(10) The nearest neighbour distance (NND) analysis indicates an increase in spatial distribution of pore network with temperature expressed as an increase in the number of pores per 2D slice.

(11) The circularity of pores decreases with an increase in temperature, due to interconnection of the pores, which further causes an increase in the frequency of elongated pores.

(12) With the increase in temperature from 500 °C to 800 °C, there is an increase in the pore parameters i.e. diameter, area and volume. This is also associated with interconnected pores causing a reduction in sphericity.

(13) When a critical external load or internal stress due to increase in temperature is achieved, these pores get interconnected to form preferential failure planes along pore networks.

(14) At meso and micro scale, the distribution of inaccessible pores is observed to increase with temperature in the sample. The mean porosity values observed from this study at meso and microscale, may reveal better pore parameters than mercury intrusion porosimetry (MIP) test.

7.2. Further research

Understanding the concrete behavior is challenging because of heterogeneity, diversity and impurities of elements and chemical oxides it contains. However, an attempt was made to understand the internal phenomena at elevated temperatures in hydrated sample and these studies needs to be carried on. Many aspects need to be studied to holistically understand concrete behavior and make concrete a better material under fire:

- Meso and microstructure changes taking place in the material from room temperature to 800 °C at intervals of 50 °C and at least a set of three to six samples (minimum) needs to studied so that better understanding of air voids and thermal variation growth can be predicted.
- The current research work focused on understanding the meso and micro structure changes taking place in PPC, OPC-53 and OPC-43 cements. Studies can be further carried on the mortar and concrete samples made up of different kinds of mineral and chemical admixtures.
- Effects of carbon nanotubes, and how can it restrict the pore and crack propagation in hydrated cements needs to be studied.

- Computational models need to be generated, from the experimentally obtained data so that the coupled thermos-mechanical load effects on the evolving meso and microstructure may be understood.

Bibliography

Bibliography

Abell, A.B., Willis, K.L. and Lange, D.A., 1999. Mercury intrusion porosimetry and image analysis of cement-based materials. *Journal of colloid and interface science*, *211*(1), pp.39-44.

Alarcon-Ruiz, L., Platret, G., Massieu, E. and Ehrlacher, A., 2005. The use of thermal analysis in assessing the effect of temperature on a cement paste. *Cement and Concrete research*, *35*(3), pp.609-613.

Arioz, O., 2007. Effects of elevated temperatures on properties of concrete. *Fire safety journal*, *42*(8), pp.516-522.

Artioli, G., Cerulli, T., Cruciani, G., Dalconi, M.C., Ferrari, G., Parisatto, M., Rack, A. and Tucoulou, R., 2010. X-ray diffraction microtomography (XRD-CT), a novel tool for non-invasive mapping of phase development in cement materials. *Analytical and bioanalytical chemistry*, *397*(6), pp.2131-2136.

Barret (1854) "On the French and other methods of constructing iron floors", Civil Engineering and Architect's Journal, Vol XVII, pp 94.

BIS(Bureau of Indian Standards), 1991. IS 1489-1: Portland Pozzolana Cement-Specification. BIS, New Delhi, India.

BIS(Bureau of Indian Standards), 2013. IS 12269: 53 grade ordinary Portland cement. BIS, New Delhi, India.

BIS(Bureau of Indian Standards), 2013. IS 8112: Ordinary Portland cement, 43 grade - specification. BIS, New Delhi, India.

Black, L., Breen, C., Yarwood, J., Deng, C.S., Phipps, J. and Maitland, G., 2006. Hydration of tricalcium aluminate (C 3 A) in the presence and absence of gypsum—studied by Raman spectroscopy and X-ray diffraction. *Journal of Materials Chemistry*, *16*(13), pp.1263-1272.

Buchanan, A.H. and Abu, A.K., 2017. *Structural design for fire safety*. John Wiley & Sons.

Bonen, D., Johnson, T.J. and Sarkar, S.L., 1994. Characterization of principal clinker minerals by FT-Raman microspectroscopy. *Cement and Concrete Research*, *24*(5), pp.959-965.

Bossa, N., Chaurand, P., Vicente, J., Borschneck, D., Levard, C., Aguerre-Chariol, O. and Rose, J., 2015. Micro-and nano-X-ray computed-tomography: A step forward in the characterization of the pore network of a leached cement paste. *Cement and Concrete Research*, *67*, pp.138-147.

Bensted, J., 1977. Raman spectral studies of carbonation phenomena. *Cement and Concrete Research*, *7*(2), pp.161-164.

Bensted, J., 1976. Uses of Raman spectroscopy in cement chemistry. *Journal of the American Ceramic Society*, *59*(3-4), pp.140-143.

Bernardes, E.E., Carrasco, E.V.M., Vasconcelos, W.L. and de Magalhães, A.G., 2015. X-ray microtomography (μ-CT) to analyze the pore structure of a Portland cement composite based on the selection of different regions of interest. *Construction and Building Materials*, *95*, pp.703-709.

Bonen, D., Johnson, T.J. and Sarkar, S.L., 1994. Characterization of principal clinker minerals by FT-Raman microspectroscopy. *Cement and Concrete Research*, *24*(5), pp.959-965.

Black, L., Breen, C., Yarwood, J., Deng, C.S., Phipps, J. and Maitland, G., 2006. Hydration of tricalcium aluminate (C 3 A) in the presence and absence of gypsum—studied by Raman spectroscopy and X-ray diffraction. *Journal of Materials Chemistry*, *16*(13), pp.1263-1272.

Chan, Y.N., Peng, G.F. and Anson, M., 1999. Residual strength and pore structure of high-strength concrete and normal strength concrete after exposure to high temperatures. *Cement and Concrete Composites*, *21*(1), pp.23-27.

Choudhary, H.K., Anupama, A.V., Kumar, R., Panzi, M.E., Matteppanavar, S., Sherikar, B.N. and Sahoo, B., 2015. Observation of phase transformations in cement during hydration. *Construction and Building Materials*, *101*, pp.122-129.

Delhomme, F., Ambroise, J. and Limam, A., 2012. Effects of high temperatures on mortar specimens containing Portland cement and GGBFS. *Materials and structures*, *45*(11), pp.1685-1692.

Diamond, S., 2000. Mercury porosimetry: an inappropriate method for the measurement of pore size distributions in cement-based materials. *Cement and concrete research*, *30*(10), pp.1517-1525.

Du Plessis, A., Olawuyi, B.J., Boshoff, W.P. and Le Roux, S.G., 2016. Simple and fast porosity analysis of concrete using X-ray computed tomography. *Materials and Structures*, *49*(1-2), pp.553-562.

Du Plessis, A., le Roux, S.G. and Guelpa, A., 2016. Comparison of medical and industrial X-ray computed tomography for non-destructive testing. *Case Studies in Nondestructive Testing and Evaluation*, *6*, pp.17-25.

Esteves, L.P., 2011. On the hydration of water-entrained cement–silica systems: combined SEM, XRD and thermal analysis in cement pastes. *Thermochimica Acta*, *518*(1-2), pp.27-35.

Fernández Carrasco, L., Torrens Martín, D., Morales, L.M. and Martínez Ramírez, S., 2012. Infrared spectroscopy in the analysis of building and construction materials (pp. 357-372). InTech.

Gabrovšek, R., Vuk, T. & Kaučič, V. 2006. Evaluation of the hydration of Portland cement containing various carbonates by means of thermal analysis. Acta Chim. Slov, 53, pp.159-165.

Garg, N., 2012. Raman spectroscopy for characterizing and determining the pozzolanic reactivity of fly ashes.

Gary, M. (1911) “Brandproben an Eisenbetongbasuten”, Deutcher Ausschlutss für Eisenbetong, Heft 11, Berlin, Germany,(in German).

Gary, M. (1916) “Brandproben an Eisenbetongbasuten”, Deutcher Ausschlutss für Eisenbetong, Heft 33, Berlin, Germany, (in German).

Gary, M. (1918) “Brandproben an Eisenbetongbasuten”, Deutcher Ausschlutss für Eisenbetong, Heft 41, Berlin, Germany”, (in German).

Gallucci, E., Scrivener, K., Groso, A., Stampanoni, M. and Margaritondo, G., 2007. 3D experimental investigation of the microstructure of cement pastes using synchrotron X-ray microtomography (μCT). *Cement and Concrete Research*, *37*(3), pp.360-368.

Gallucci, E., Zhang, X. and Scrivener, K.L., 2013. Effect of temperature on the microstructure of calcium silicate hydrate (CSH). *Cement and Concrete Research*, *53*, pp.185-195.

Georgali, B. and Tsakiridis, P.E., 2005. Microstructure of fire-damaged concrete. A case study. *Cement and Concrete composites*, *27*(2), pp.255-259.

Ghosh, S.N. and Chatterjee, A., 1974. Absorption and reflection infra-red spectra of major cement minerals, clinkers and cements. *Journal of Materials Science*, *9*(10), pp.1577-1584.

Ghosh, S.N. and Handoo, S.K., 1980. Infrared and Raman spectral studies in cement and concrete. *Cement and Concrete Research*, *10*(6), pp.771-782.

Haeri, M. and Haeri, M., 2015. ImageJ plugin for analysis of porous scaffolds used in tissue engineering. *Journal of Open Research Software*, *3*(1).

Hager, I., 2013. Behaviour of cement concrete at high temperature. *Bulletin of the Polish Academy of Sciences: Technical Sciences*, *61*(1), pp.145-154.

Han, J., Sun, W., Pan, G., Wang, C. and Rong, H., 2012. Application of X-ray computed tomography in characterization microstructure changes of cement pastes in carbonation process. *Journal of Wuhan University of Technology-Mater. Sci. Ed.*, *27*(2), pp.358-363.

Handoo, S.K., Agarwal, S. and Agarwal, S.K., 2002. Physicochemical, mineralogical, and morphological characteristics of concrete exposed to elevated temperatures. *Cement and Concrete Research*, *32*(7), pp.1009-1018.

Heikal, M., 2006. Effect of temperature on the structure and strength properties of cement pastes containing fly ash alone or in combination with limestone. *Ceramics Silikaty*, *50*(3), p.167.

Henry, M., Hashimoto, K., Darma, I.S. and Sugiyama, T., 2016. Cracking and chemical composition of cement paste subjected to heating and water re-curing. *Journal of Advanced Concrete Technology*, *14*(4), pp.134-143.

Hasenjager (1935) “Über das Verhalten des Betons und Eisenbetons im Feuer und die Ausbildung von Dehnungsfugen im Eisenbetonbau” Dissertation, Techniche Hochschole Braunschweig, cited in Meyer-Ottens C. (1972) “Zur Frage der Abplatzungen an Betonbauteilen aus Normalbeton bei

Brandbeanspruchung”, PhD-thesis, Braunshweig, Germany, 1972.

Herfort, D., Moir, G.K., Johansen, V., Sorrentino, F. and Arceo, H.B., 2010. The chemistry of Portland cement clinker. *Advances in Cement Research*, *22*(4), pp.187-194.

Heikal, M., 2006. Effect of temperature on the structure and strength properties of cement pastes containing fly ash alone or in combination with limestone. Ceramics Silikaty, 50(3), p.167.

Helfen, L., Dehn, F., Mikulik, P. and Baumbach, T., 2005. Three-dimensional imaging of cement microstructure evolution during hydration. *Advances in Cement Research*, *17*(3), pp.103-111.

Henry, M., Darma, I.S. and Sugiyama, T., 2014. Analysis of the effect of heating and re-curing on the microstructure of high-strength concrete using X-ray CT. *Construction and building materials*, *67*, pp.37-46.

Hull W. (1920) “Fire tests of concrete columns”, Proceedings of the Sixteenth Annual Convention, American Concrete Institute, Chicago, USA.

Horgnies, M., Chen, J.J. and Bouillon, C., 2013. Overview about the use of Fourier transform infrared spectroscopy to study cementitious materials. *WIT Trans. Eng. Sci*, *77*, pp.251-262.

Hughes, T.L., Methven, C.M., Jones, T.G., Pelham, S.E., Fletcher, P. and Hall, C., 1995. Determining cement composition by Fourier transform infrared spectroscopy. *Advanced Cement Based Materials*, *2*(3), pp.91-104.

Ichikawa, Y., 2000. Prediction of pore pressures, heat and moisture transfer leading to spalling of concrete during fire.

ITI (Infrastructure Technology Institute) (2018) The Fineness and Particle Size Distribution of Portland Cement. ITI, Evanston, IL, USA. See http://iti.northwestern.edu/cement/monograph/Monograph3_7.html (accessed 26/02/2018).

Ingle J. (1866) “Recent improvements in the application of concrete to fire-proof constructions”, London Civil Engineering and Architects’ Journal.

Jaffer S.J., Lemaire C., Hansson, C.M. and Peemoeller, H., 2007. MRI: A complementary tool for imaging cement pastes. *Cement and concrete research*, *37*(3), pp.369-377.

Kak A. K. and Malcolm Slaney, Principles of Computerized Tomographic Imaging, (1988). http://www.slaney.org/pct/pct-toc.html (accessed July 8, 2018)

Kendall, K., Howard, A.J. and Birchall, J.D., 1983. The relation between porosity, microstructure and strength, and the approach to advanced cement-based materials. *Phil. Trans. R. Soc. Lond. A*, *310*(1511), pp.139-153.

Kirkpatrick, R.J., Yarger, J.L., McMillan, P.F., Ping, Y. and Cong, X., 1997. Raman spectroscopy of CSH, tobermorite, and jennite. *Advanced Cement Based Materials*, *5*(3-4), pp.93-99.

Kim, K.Y., Kang, D.H. and Yun, T.S., 2012. Evaluation of air void parameters for hardened concrete paste using 3D X-Ray CT images. *Advances in Civil, Environmental, and Materials Research*, pp.26-30.

Kim, K.Y., Yun, T.S., Choo, J., Kang, D.H. and Shin, H.S., 2012. Determination of air-void parameters of hardened cement-based materials using X-ray computed tomography. *Construction and Building Materials*, *37*, pp.93-101.

Kim, K.Y., Yun, T.S. and Park, K.P., 2013. Evaluation of pore structures and cracking in cement paste exposed to elevated temperatures by X-ray computed tomography. *Cement and Concrete Research*, *50*, pp.34-40.

Lee, J., Xi, Y., Willam, K. and Jung, Y., 2009. A multiscale model for modulus of elasticity of concrete at high temperatures. *Cement and Concrete Research*, *39*(9), pp.754-762.

Li, M., Qian, C. and Sun, W., 2004. Mechanical properties of high-strength concrete after fire. *Cement and concrete research*, *34*(6), pp.1001-1005.

Li, Q., Li, Z. and Yuan, G., 2012. Effects of elevated temperatures on properties of concrete containing ground granulated blast furnace slag as cementitious material. *Construction and Building Materials*, *35*, pp.687-692.

Lu, S., Landis, E.N. and Keane, D.T., 2006. X-ray microtomographic studies of pore structure and permeability in Portland cement concrete. *Materials and Structures*, *39*(6), pp.611-620.

Lu, H., Peterson, K. and Chernoloz, O., 2018. Measurement of entrained air-void parameters in Portland cement concrete using micro X-ray computed tomography. *International Journal of Pavement Engineering*, *19*(2), pp.109-121.

Lublóy, É., Balázs, G.L., Kapitány, K. and Barsi, Á., 2017. CT analysis of core samples from fire-damaged concrete structures. *Magazine of Concrete Research*, *69*(15), pp.802-810.

Liu, F., Sun, Z. and Qi, C., 2014. Raman spectroscopy study on the hydration behaviors of Portland cement pastes during setting. Journal of Materials in Civil Engineering, 27(8), p.04014223.

Liu, Z., Wang, J., Zhang, Y., Lv, H., Fu, P. and Li, A., 2016. In situ characterisation of the depth and mass of water intrusion in unsaturated cement pastes via X-ray computed tomography. *Advances in Cement Research*, *29*(3), pp.91-100.

Masse, S., Vetter, G., Boch, F. and Haehnel, C., 2002. Elastic modulus changes in cementitious materials submitted to thermal treatments up to 1000 C. *Advances in Cement Research*, *14*(4), pp.169-177.

Merlino, S., Bonaccorsi, E. and Armbruster, T., 1999. Tobermorites: Their real structure and order-disorder (OD) character. *American Mineralogist*, *84*(10), pp.1613-1621.

Merlino, S., Bonaccorsi, E. and Armbruster, T., 2001. The real structure of tobermorite 11Å: normal and anomalous forms, OD character and polytypic modifications. *European Journal of Mineralogy*, *13*(3), pp.577-590.

Mendes, A., Sanjayan, J. and Collins, F., 2008. Phase transformations and mechanical strength of OPC/Slag pastes submitted to high temperatures. Materials and structures, 41(2), p.345.

Moravcova, B., Possl, P., Misak, P. and Blazek, M., 2016. Possibilities of determining the air-pore content in cement composites using computed tomography and other methods. *Materiali in tehnologije*, *50*(4), pp.491-498.

Henry, M., Hashimoto, K., Darma, I.S. and Sugiyama, T., 2016. Cracking and chemical composition of cement paste subjected to heating and water re-curing. *Journal of Advanced Concrete Technology*, *14*(4), pp.134-143.

Monteagudo, S.M., Moragues, A., Gálvez, J.C., Casati, M.J. and Reyes, E., 2014. The degree of hydration assessment of blended cement pastes by differential thermal and thermogravimetric analysis. Morphological evolution of the solid phases. *Thermochimica Acta*, *592*, pp.37-51.

Newman, S.P., Clifford, S.J., Coveney, P.V., Gupta, V., Blanchard, J.D., Serafin, F., Ben-Amotz, D. and Diamond, S., 2005. Anomalous fluorescence in near-infrared Raman spectroscopy of cementitious materials. *Cement and concrete research*, *35*(8), pp.1620-1628.

Neville, A., 2003. How closely can we determine the water-cement ratio of hardened concrete?. *Materials and Structures*, *36*(5), pp.311-318.

Otsu, N. 1979. A threshold selection method from gray-level histograms. *IEEE transactions on systems, man, and cybernetics*, *9*(1), pp.62-66.

Parisatto, M., Dalconi, M.C., Valentini, L., Artioli, G., Rack, A., Tucoulou, R., Cruciani, G. and Ferrari, G., 2015. Examining microstructural evolution of Portland cements by in-situ synchrotron micro-tomography. *Journal of materials science*, *50*(4), pp.1805-1817.

Peškova, Š.Á.R.K.A., Machovič, V.L.A.D.I.M.Í.R. and Prochazka, P., 2011. Raman spectroscopy structural study of fired concrete. *Ceramics–Silikáty*, *55*(4), pp.410-417.

Piasta, J., Sawicz, Z. and Rudzinski, L., 1984. Changes in the structure of hardened cement paste due to high temperature. *Matériaux et Construction*, *17*(4), pp.291-296.

Piasta, J., 1984. Heat deformations of cement paste phases and the microstructure of cement paste. *Matériaux et Construction*, *17*(6), pp.415-420.

Preston F. W., White H. E. (1934) "Observations on spalling" Journal of the American Ceramic Society, Volume 17, Issue 1-12, pp 137-144.

Provis, J.L., Myers, R.J., White, C.E., Rose, V. and van Deventer, J.S., 2012. X-ray

microtomography shows pore structure and tortuosity in alkali-activated binders. *Cement and Concrete Research*, *42*(6), pp.855-864.

Robertson, K. and Bish, D., 2013. Constraints on the distribution of CaSO4· nH2O phases on Mars and implications for their contribution to the hydrological cycle. *Icarus*, *223*(1), pp.407-417.

Ramaswamy, K.P. and Santhanam, M., 2017. A study of deterioration of cement paste due to acid attack using X-ray computed micro-tomography. *Advances in Cement Research*, *30*(3), pp.123-138.

Su, Y.M., Hou, T.C., Lin, L.C., Chen, G.Y. and Pan, H.H., 2016, April. The nondestructive evaluation of high temperature conditioned concrete in conjunction with acoustic emission and x-ray computed tomography. In *Nondestructive Characterization and Monitoring of Advanced Materials, Aerospace, and Civil Infrastructure 2016* (Vol. 9804, p. 98040L). International Society for Optics and Photonics.

Sereda PJ, Feldman RF and Ramachandran VS (1981) Physical Factors Controlling Structure and Strength Development. National Research Council Canada, Division of Building Research, Ottawa, ON, Canada.

Senapati, M.R., 2011. Fly ash from thermal power plants- waste management and overview. *Current Science(Bangalore)*, *100*(12), pp.1791-1794.

Sha, W., O'Neill, E.A. and Guo, Z., 1999. Differential scanning calorimetry study of ordinary Portland cement. *Cement and Concrete Research*, *29*(9), pp.1487-1489.

Stutzman, P.E., 1996. *Guide for X-ray powder diffraction analysis of Portland cement and clinker*. US Department of Commerce, Technology Administration, National Institute of Standards and Technology, Office of Applied Economics, Building and Fire Research Laboratory.

Stutzman, P.E., Feng, P. and Bullard, J.W., 2016. Phase analysis of Portland cement by combined quantitative X-ray powder diffraction and scanning electron microscopy. *J Res (NIST JRES)*, *121*, pp.47-107.

Stepkowska, E.T., Blanes, J.M., Justo, A., Aviles, M.A. and Perez-Rodriguez, J.L., 2005. Thermo XRD-analysis of two aged cement pastes. *Journal of thermal analysis and calorimetry*, *80*(1), pp.193-199.

Sitek, L., Bodnarova, L., Soucek, K., Stas, L. and Gurkova, L., 2015. Analysis of inner structure changes of concretes exposed to high temperatures using micro X-ray computed tomography. *Acta Geodynamica et Geromaterialia*, *12*(1), pp.79-90.

Taylor, H.F., 1997. *Cement chemistry*. Thomas Telford.

Tarrida, M., Madon, M., Le Rolland, B. and Colombet, P., 1995. An in-situ Raman spectroscopy study of the hydration of tricalcium silicate. *Advanced Cement Based Materials*, *2*(1), pp.15-20.

Van Oss, H.G. and Padovani, A.C., 2002. Cement manufacture and the environment: part I: chemistry and technology. *Journal of Industrial Ecology*, *6*(1), pp.89-105.

Vodák, F., Trtık, K., Kapičková, O., Hošková, Š. and Demo, P., 2004. The effect of temperature on strength–porosity relationship for concrete. *Construction and building materials*, *18*(7), pp.529-534.

Valentini, L., Dalconi, M.C., Parisatto, M., Cruciani, G. and Artioli, G., 2011. Towards three-dimensional quantitative reconstruction of cement microstructure by X-ray diffraction microtomography. *Journal of Applied Crystallography*, *44*(2), pp.272-280.

Wan, K. and Xu, Q., 2014. Local porosity distribution of cement paste characterized by X-ray micro-tomography. *Science China Technological Sciences*, *57*(5), pp.953-961.

Woolson I. (1905) "Investigation of the Effect of Heat Upon the Crushing Strength and Elastic Properties of Concrete", Proceedings of the American Society for Testing Materials, Philadelphia, USA.

Wong, R.C.K. and Chau, K.T., 2005. Estimation of air void and aggregate spatial distributions in concrete under uniaxial compression using computer tomography scanning. *Cement and Concrete Research*, *35*(8), pp.1566-1576.

Xiao, J. and König, G., 2004. Study on concrete at high temperature in China—an overview. *Fire safety journal*, *39*(1), pp.89-103.

Ylmén, R., Jäglid, U., Steenari, B.M. and Panas, I., 2009. Early hydration and setting of Portland cement monitored by IR, SEM and Vicat techniques. *Cement and Concrete Research*, *39*(5), pp.433-439.

Ylmen, R. and Jäglid, U., 2013. Carbonation of Portland cement studied by diffuse reflection Fourier transform infrared spectroscopy. *International Journal of Concrete Structures and Materials*, *7*(2), pp.119-125.

Zeng, Q., Li, K., Fen-Chong, T. and Dangla, P., 2015. Pore structure of cement pastes through NAD and MIP analysis. *Advances in Cement Research*, *28*(1), pp.23-32.

Zhang YM and Napier-Munn TJ (1995) Effects of particle size distribution, surface area and chemical composition on Portland cement strength. Powder Technology 83(3): 245–252.

Zhang, W.M., Sun, W. and Chen, H.S., 2010. 3D visualisation of pore structures in cement-based materials by LSCM. *Advances in Cement Research*, *22*(1), pp.53-57.

Zhang, Q. and Ye, G., 2011. Microstructure analysis of heated Portland cement paste. *Procedia Engineering*, *14*, pp.830-836.

APENDIX-A

The reduction in strength with respect to temperature is modelled using the following equation, which enables future inclusion in the Johnson-Cook rate dependent model:

$$\boldsymbol{\sigma_c = \sigma_r(1 - aT^{*m})}$$

where :

σ_c = Concrete strength at temperature T $^{\circ}$C

σ_r= Concrete strength at room temperature (27 ^{O}C)

$$T^* = \frac{T - T_r}{T_m - T_r}$$

T_r = room temperature

T_m = maximum temperature

a, m = material constants

Table A1: Temperature vs compressive strength data

TEMP	Compressive strength		
	PPC	OPC-43	OPC-53
27	37.44	47.23	56.32
100	35.34	41.87	50.62
400	29.2	22.65	28.76
500	23.6	0	0
800	14.25	0	0

Model fitting (Least sum of squares fitting) using Excel spreadsheet:

PPC			
TT	**PPC-Fit**	**residual**	**residual^2**
0.000	**37.440**	0.000	0.000
0.094	**36.139**	-0.799	0.638
0.483	**27.886**	1.314	1.727
0.612	**24.668**	-1.068	1.140
1.000	**14.159**	0.091	0.008
		SS	**3.513**

OPC-43			
TT	**OPC-43 Fit**	residual	residual^2
0.000	**47.230**	0.000	0.000
0.196	**38.128**	3.742	14.002
1.000	**17.148**	5.502	30.268
1.268	**11.428**	-11.428	130.610

2.072	**-4.085**	4.085	16.684
		SS	191.564

	OPC-53		
TT	**OPC-53 Fit**	residual	residual^2
0.000	**56.320**	0.000	0.000
0.196	**46.240**	4.380	19.186
1.000	**21.278**	7.482	55.978
1.268	**14.307**	-14.307	204.693
2.072	**-4.821**	4.821	23.241
		SS	**303.098**

Curve fitting parameters:

	σ_r	T_r	T_m	m	a
PPC	37.44	27	800	1.222	0.622
OPC-43	47.23	27	400	0.733	0.637
OPC-53	56.32	27	400	0.764	0.622

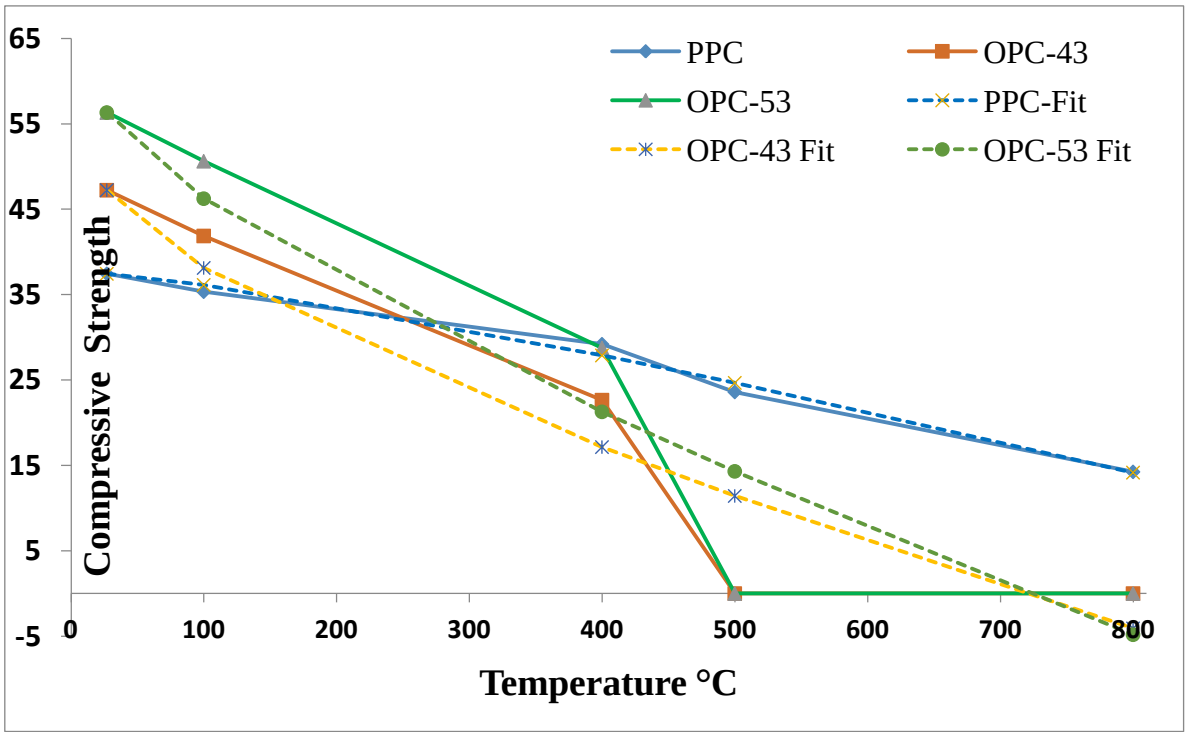

Figure: A1 Curve fitting carried for the PPC, OPC-43 and OPC-53.